

Preparation and Physical Characterization of Carbon Nanotubes-SU8 Composites

THÈSE N° 5248 (2011)

PRÉSENTÉE LE 23 DÉCEMBRE 2011

À LA FACULTÉ DES SCIENCES DE BASE

LABORATOIRE DE PHYSIQUE DE LA MATIÈRE COMPLEXE

PROGRAMME DOCTORAL EN PHYSIQUE

ÉCOLE POLYTECHNIQUE FÉDÉRALE DE LAUSANNE

POUR L'OBTENTION DU GRADE DE DOCTEUR ÈS SCIENCES

PAR

Marijana MIONIĆ

acceptée sur proposition du jury:

Prof. O. Schneider, président du jury

Prof. L. Forró, directeur de thèse

Prof. D. Damjanovic, rapporteur

Prof. K. Hernadi, rapporteur

Prof. J.W. Seo, rapporteur



ÉCOLE POLYTECHNIQUE
FÉDÉRALE DE LAUSANNE

Suisse
2011

Abstract

This thesis firstly describes the synthesis and characterisation of carbon nanotubes (CNTs). We focused our research on the growth conditions of CNTs synthesized by chemical vapour deposition (CVD). In particular, the effect of the support surface structure, composition and size of the catalyst precursor, relation of catalyst size with the size of its precursor and the diameter of synthesized CNTs, as well as CNTs diameter distribution were investigated. It was found that the support surface structure strongly influenced the size, shape and chemical composition of the catalyst precursor. Moreover, the size of the catalyst was found to be not always dependent on the size of the catalyst precursor. The best graphitized CVD CNTs were produced from the completely amorphous catalyst precursor in the form of micrometer-sized lumps. Thus, it was found that the growth of CVD CNTs proceeds from the *in-situ* formed catalyst grains, which were often found unrelated with the support due to the precursor large size and lack of available support's surface sites favourable for the precursor binding. We optimized the CVD CNTs synthesis method towards CNTs diameter controlled growth. Furthermore, well-structured CNTs comparable with arc-discharge CNTs were synthesized for the first time by the CVD method. In particular, catalyst particles were not found in such CNTs which were closed on both ends. CNTs, few-layered graphene and graphene were successfully synthesized by the CVD method without the presence of the transitional metal catalyst. We developed the method of controlled cutting of CNTs to the prescribed length by the planetary ball milling.

The second part describes preparation and physical characterisation of the composite made of the SU8 polymer and CVD CNTs previously optimized for this purpose. At first, we have optimized the preparation conditions (including the appropriate solvents, surfactants and all steps of the preparation process). CNTs dispersion in the SU8 matrix was characterized by the transmission electron microscopy (TEM) of the microtome composite and by the impedance measurements. The homogeneous CNTs-SU8 composites have been obtained and the results of the mechanical (hardness and Young's modulus), electrical (four-point measurement and resistivity as a function of temperature) and thermal characterization (thermal conductivity and thermo power) of the prepared composites were measured. The increase in hardness of 122% and in the Young's modulus of 56% (for 0.8 wt% of CNTs in SU8) and thermal conductivity of 3.7 times (for 10wt% of CNTs in SU8) was achieved for composites containing randomly oriented CNTs. Moreover, all prepared composite samples were electrically conductive.

In the third part, processing of the obtained composites was successfully optimized for the ink jet printing process, photolithography and screen printing. Especially, photopatterning was optimized at each processing step in order to minimize their drawbacks.

Keywords: carbon nanotubes, catalyst precursors, chemical vapour deposition, growth mechanism, graphene, composites, electrical and mechanical characterisations, photolithography processing

Zusammenfassung

Die vorliegende Doktorarbeit beschreibt zum einen die Synthese und die Charakterisierung von Carbon Nanotubes (CNTs). Hierbei standen die Wachstumsbedingungen von CNTs, welche durch chemische Gasphasenabscheidung (CVD) synthetisiert wurden, im Mittelpunkt unserer Forschungsbemühungen. Die Arbeit untersucht dabei im Besonderen den Effekt der unterstützenden Oberflächenstruktur, die Zusammensetzung und die Grösse des Katalysatorvorläufers, das Verhältnis zwischen Katalysator- und Vorläufergrösse und den Durchmesser synthetisierter CNTs, sowie deren Durchmesserverteilung. Hierbei konnte festgestellt werden, dass die unterstützende Oberflächenstruktur massgebend Grösse, Form und chemische Zusammensetzung des Katalysatorvorläufers beeinflusst. Ferner konnte festgestellt werden, dass die Grösse des Katalysators nicht zwangsläufig von der Grösse des Katalysatorvorläufers abhängt. Die besten graphitisierten, durch chemische Gasphasenabscheidung synthetisierten CNTs wurden mittels vollständig amorpher Katalysatorvorläufer in Form von Mikrometergrossen Klümpchen hergestellt. Demzufolge konnte festgestellt werden, dass das Wachstum von CVD CNTs von *in-situ* geformten Katalysatorkörnchen ausgeht, bei welchen vielfach festgestellt werden konnte, dass sie unabhängig von Support aufgrund von der Grösse des Vorläufers und einem Fehlen von vorhandener Oberflächenunterstützung, welche sich günstig auf Vorläuferbindung auswirken. Hierbei wurde die CVD CNTs-Synthesemethode hinsichtlich eines kontrollierten Wachstums der CNTs-Durchmesser optimiert. Fernerhin wurden gutstrukturierte CNTs, vergleichbar mit Bogenentladungs-CNTs, erstmalig mittels der CVD Methode synthetisiert. In den auf diese Weise synthetisierten CNTs wurden keine Katalysatorteilchen gefunden, die an beiden Enden geschlossen sind. CNTs, mehrlagiges Graphen und Graphen wurden erfolgreich mittels der CVD Methode ohne das Vorhandensein von Übergangsmetallkatalysatoren synthetisiert. In der vorliegenden Arbeit wurde hierfür eine Methode entwickelt, mit der CNTs mit Hilfe einer planetarischen Kugelmühle in einer vorher bestimmten Länge kontrolliert geschnitten werden können.

Im zweiten Teil der vorliegenden Doktorarbeit wurde die Herstellung und physikalische Charakterisierung eines Verbundwerkstoffs aus einem SU8 Polymer und CVD CNTs, welche zuvor hinsichtlich ihres Zwecks optimiert wurden, dargestellt. Zuerst wurden hierfür die Herstellungsbedingungen optimiert (einschliesslich geeigneter Lösungsmittel, Surfactante und allen Stufen des Herstellungsprozesses). Die CNTs Dispersion in der SU8 Matrix wurde mittels des Transmissionselektronenmikroskops (TEM) und mittels Impedanzmessungen charakterisiert. Homogene CNTs-SU8 Verbundwerkstoffe konnten dadurch hergestellt werden. Die Ergebnisse von mechanischer (Härte und Young's modulus), elektrischer (Vierletermessung und Resisitivität als Funktion der Temperatur) und thermischer Charakterisierung (Wärmeleitfähigkeit und Thermoelektrizität) dieser Verbundwerkstoffe wurden gemessen. Ein Härteerhöhung von 122% und eine Erhöhung des Young's modulus von 56% (für 0.8 wt% an CNTs in SU8) und eine 3.7 fache Wärmeleitfähigkeit (für 10wt% an CNTs in SU8) konnte hierbei für Verbundwerkstoffe, welche willkürlich ausgerichtete CNTs beinhalten, erzielt werden. Ferner waren sämtlich hergestellte Verbundwerkstoffproben elektrisch leitfähig.

Im dritten Teil dieser Arbeit wurden die hergestellten Verbundwerkstoffe erfolgreich für eine Anwendung in Tintenstrahldruckern, in Photolithographie und in Siebdruck

optimiert. Vor allem wurde hierbei das Photopatterning in jeder Prozessstufe optimiert, um zwangsläufig auftretende Hemmnisse zu minimieren.

Schlüsselwörter: Carbon Nanotubes, Katalysatorvorläufer, chemische Gasphasenabscheidung, Wachstumsmechanismus, Graphen, Verbundwerkstoffe, elektrische und mechanische Charakterisierungen, Photolithographie

List of Abbreviations

1M2P	- 1-methyl-2-pyrrolidone
3D	- three-dimensional
AFM	- atomic force microscope
CCVD	- catalytic chemical vapour deposition
CVD	- chemical vapour deposition
CNT	- carbon nanotube
EDX	- energy dispersive X-ray spectroscopy
GBL	- gamma-butyrolacton
HAR	- high aspect ratio
HR	- high resolution
IPA	- isopropanol (Isopropyl alcohol)
LIGA	- L ithographie, G alvanoformung, A bformung (Lithography, Electroplating, Molding)
MEK	- methyl-ethyl ketone
MWCNT	- multi walled carbon nanotube
NNDMAA	- N,N-Dimethylacetamide
PDMS	- polydimethylsiloxane
PEB	- post-exposure baking
PGMEA	- propylene glycol methyl ether acetate
PI	- photoinitiator
PMMA	- poly(methyl methacrylate)
SB	- soft baking
SEM	- scanning electron microscope
STM	- scanning tunnelling microscope
SWCNT	- single walled carbon nanotube
TEM	- transmission electron microscope
UV	- ultra violet
XRD	- X-ray Diffraction
XRPD	- X-ray Powder Diffraction

Table of content

1. Introduction	1
<i>References</i>	4
2. Materials	7
2.1 SU8	7
2.1.1 Historical background	8
2.1.2 Overview of SU8 processing techniques.....	9
2.1.3 Physical properties	11
2.1.4 Composition	13
2.1.5 UV-induced cationic ring opening polymerisation	14
2.1.6 Problems related with SU8	22
2.2 Fillers	22
2.3 CNTs	24
2.3.1 Basic morphologies of CNTs	24
2.3.2 Historical background	25
2.3.3 Synthesis of CNTs	29
2.3.3.1 Arc-discharge growth.....	29
2.3.3.2 Laser-ablation method	30
2.3.3.3 CVD growth	30
2.3.4 Theory of catalytic growth of CNTs	32
2.3.5 Properties of CNTs.....	33
2.3.5.1 Electronic properties and chirality of CNTs	33
2.3.5.2 Mechanical properties	34
2.3.5.2.1 Defects and deformations in CNTs	34
2.3.6 Potential applications	36
2.3.6.1 Problems related to CNTs	37
<i>References</i>	38

3. Experimental techniques.....	45
3.1 CNTs	45
3.1.1 Supported catalyst precursor for CVD MWCNTs synthesis.....	45
3.1.1.1 Catalyst support.....	45
3.1.1.2 Catalyst precursor	47
3.1.2 CVD MWCNTs synthesis.....	47
3.1.2.1 Furnace	47
3.1.2.2 Synthesis conditions.....	48
3.1.3 CNTs post-synthesis treatment.....	48
3.2 CNTs-SU8 composites.....	50
3.2.1 Composites 1.....	50
3.2.1.1 Characterization of composites 1.....	51
3.2.2 Composites 2.....	52
3.2.2.1 Characterization of composites 2.....	54
3.2.3 Composites 3.....	57
3.3 Processing techniques.....	57
3.3.1 Photolithography.....	57
3.3.2 Inkjet printing.....	58
3.3.3 Screen printing.....	60
<i>References</i>	60
4. Optimization of properties of CVD-synthesised CNTs.....	61
4.1 Optimization and insights into the CVD synthesis of CNTs.....	61
4.1.1 Support.....	63
4.1.2 Supported catalyst precursor and synthesized CNTs.....	68
4.1.2.1 Fe and Co salts in calcite aqueous suspensions.....	68
4.1.2.2 Obtained precipitates, their characterisation and synthesized CNTs..	69
4.2 CVD – towards high-quality CNTs, graphene... ..	85
4.3 Optimization of the lengths of CVD CNTs.....	91
4.3.1 Results and discussions.....	93
4.3.2 Conclusions.....	102
<i>References</i>	103

5. CNTs-SU8 composites and their preparation.....	107
5.1 CNTs-SU8 composites 1.....	110
5.1.1 Dispersion of CNTs in SU8.....	110
5.1.2 Nanoindentation.....	111
5.1.3 Microscopy.....	114
5.1.4 Impedance spectroscopy.....	115
5.1.5 Resistivity as a function of temperature.....	117
5.1.6 Thermoelectric power as a function of temperature.....	118
5.2 CNTs-SU8 composites 2.....	119
5.2.1 Dispersion of CNTs in SU8.....	120
5.2.2 Microscopy.....	120
5.2.3 Thermal conductivity as a function of temperature.....	121
5.2.4 Nanoindentation.....	122
5.2.5 Four Point Resistivity Measurements.....	124
5.2.6 Resistivity as a function of temperature.....	126
5.3 CNTs-SU8 composites 3.....	127
5.3.1 Microscopy.....	127
5.3.2 Thermal conductivity as a function of temperature.....	128
5.3.3 Resistivity as a function of temperature.....	129
5.4 Conclusions.....	130
<i>References.....</i>	<i>131</i>
6. CNTs-SU8 composites processing.....	133
6.1 Photolithography.....	133
6.2.1 Results of CNTs-SU8 composite photolithography.....	135
6.1.1.1 Results of cut CNTs-SU8 composite photolithography.....	139
6.1.1.2 Stripping.....	143
6.1.2 Conclusions.....	144
6.2 Inkjet printing of CNTs-SU8 composites.....	144
6.2.1 Inkjet printing of CNTs-SU8 composites 2C inks onto flexible polyester substrates.....	145

6.2.2 Resistivity measurements.....	146
6.2.3 Conclusions.....	149
6.3 Screen printing.....	150
6.3.1 Process description.....	151
6.3.2 Results and discussions.....	151
<i>References</i>	154
7. Conclusions.....	157
Appendix 1: Statistical analysis of the length distributions of cut CNTs.....	161
<i>References</i>	168
Appendix 2: Optimization of photolithography processing of CNTs-SU8 composites 2 and 2C.....	171
A2.1 Spin-coating.....	171
A2.2 Soft baking.....	176
A2.3 UV-exposure.....	183
A2.4 Post-exposure baking (PEB).....	194
A2.5 Development.....	202
A2.6 Hard baking.....	204
A2.7 Conclusions.....	204
<i>References</i>	205
Appendix 3: Optimization of inkjet printing of CNTs-SU8 composites 2C.....	209
A3.1 Applications and related problems.....	211
A3.2 Inkjet printing process optimization.....	214
A3.3 Conclusions.....	231
<i>References</i>	231
Curriculum Vitae.....	235

List of publications and patent.....	236
Acknowledgements.....	238

Chapter 1

Introduction

The new advanced technologies need new materials with improved characteristics, like lower weight, higher resistance to environmental exposures, lower production costs, higher strength and durability. In order to fulfil these requirements, scientists strive to find solutions among more sophisticated materials, *i.e.* composites. Composites are systems “composed” of two or more physically distinguishable components that combine the individual properties of their constituents and yield new features and better performances (1). For example, many flexible composite materials with high strength are composed of stiff fibres embedded in a lower stiffness (usually lightweight) matrix. Alignment of these fibres provides maximum stiffness in the direction of the alignment. One of the most common examples of the naturally-occurring fibrillar composites is wood, which consists of cellulose fibres bonded together with lignin (2). Human and animal bones are also composite materials made of organic fibres of collagen and small rod-shaped inorganic crystals of hydroxyapatite (2). In addition to naturally occurring composites there are synthetic man-made composites. In one of the earliest man-made composite materials, straw and mud were mixed to form bricks. This ancient brick-making process can still be seen on Egyptian tomb paintings. Another well known composite construction material is concrete which consists of gravel and sand held together by cement (2). Clearly, synthetic man-made composites overwhelm our everyday life.

Although the concept of composite materials has been known for thousands of years, recent advances in this field are particularly appealing. The origin of the renaissance of composites lies in the progress of the synthesis of nanoparticulate materials as fillers, resulting in new properties. Therefore, the today’s composites offer a great variety of properties and find numerous applications in various industrial branches, including: aerospace, automotive, electronics, construction, energy, bio-medicine, just to name a few of them. Furthermore, composite materials have improved the properties of a plethora of

everyday products. Recently, flexible roll-printed solar cells for using solar energy (NanoSolar Inc., CA, USA) have become commercially available (Fig. 1.1 (a)). Bicycles and tennis rackets became lighter due to carbon fillers. The running shoes “Lone Star” from Adidas AG were the first-ever to use carbon nanotubes (CNTs) (Fig. 1.1 (b)) - reinforced plates, thus reducing their thickness and weight, by about 30 and 50 percent, respectively (Fig. 1.1 (c)). Moreover, CNTs increased the structural integrity and durability of plates (3; 4).

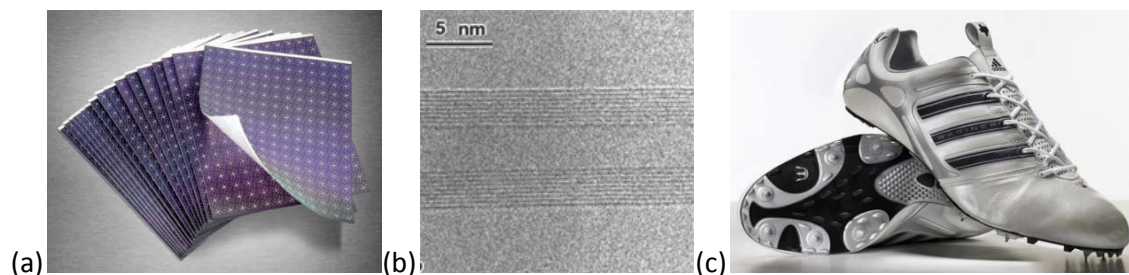


Figure 1.1: (a) Flexible roll-printed solar cells developed by NanoSolar Inc. (From the ref. (5)). (b) High resolution electron microscopy image of the carbon nanotube (CNT), a very popular component of new class of composites. (c) Spike running shoes (model “Lone Star”) with the first-ever CNTs-reinforced full-length continual plate brought to the market by Adidas AG (From the ref. (3)).

The synthesis and applications of new nanostructured materials, which could be embedded into matrices to give new composite materials, were the actual inspiration of this thesis. Clearly, the emerging field of nano-structured composites represent now attractive basic and applied research directions. This rapidly moving interdisciplinary field is also particularly interesting since development of composites requires expertise from various domains. In addition, for a physicist, “nanoworld” is motivating for studying the physical phenomena atypical for macroscopic world. The world “down there” on the nanoscale level has become accessible due to the development of electron microscopy (6), scanning probe microscopies (7; 8), and microfabrication techniques (9). Consequently, different nano-objects become accessible for observation, study and even manipulation.

This thesis relies on breakthrough developments in nano-scale science and technology of the last decades. Synthetic routes towards obtaining the composite material based on SU8 epoxy and CNTs, as well as its thorough characterisation were the main goals of this thesis. SU8 epoxy is a well-established polymer which is massively used in lithography, whereas CNTs, nanoscale carbon cylinders, represent a whole number of extraordinary physical properties. In particular, SU8 is a negative tone, epoxy functional near-UV photoresist, which, upon exposure to near-UV light, polymerises *via* cationic ring-opening polymerisation and forms highly stable bonds, thus providing outstanding chemical stability. This allows structuring of SU8 into highly complex patterns, which can be 2 or 3 dimensional, deposited on substrates or even free standing (Fig. 1.2).

A further advantage of SU8 is that it can be used for ultra-thick layer deposition and structuring. All these properties have led to significant interest in SU8 for the use in microfabrication applications. Besides these attractive features, SU8 has few drawbacks: it is an electrically-insulating material, with very low thermal conductivity, and it is also quite brittle. Clearly, for a number of applications, good electrical and thermal conductivities are often necessary. Therefore, it would be desirable to synthesise the SU8-based composite material without these drawbacks. In order to achieve this, our strategy was to prepare SU8 composite with CNTs.

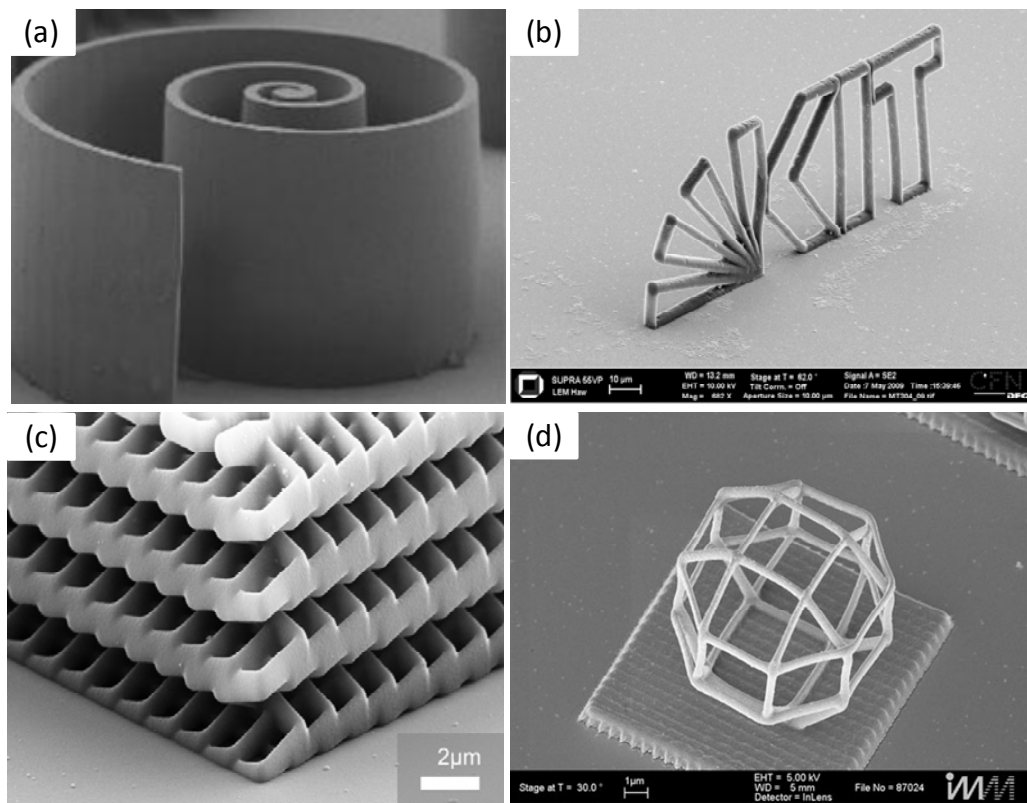


Figure 1.2: Various structures made of SU8 photoresist. High aspect ratio structures with curved vertical side walls (a) (From the ref. (10)) or with rounded lines in 3D (b) (From the ref. (11)). 3D square spiral structure (c) (From the ref. (12)) and wire frame written in SU8 (d) (From the ref. (13)).

CNTs are considered as the most suitable candidates to reinforce composites, especially polymer composites. This is because of their outstanding electrical, mechanical, thermal and optical properties together with their extraordinary chemical stability, low density and very high and tuneable aspect ratio. This is the reason why composite materials containing CNTs have recently attracted so much attention. Such composite materials are expected to have improved mechanical strength and become electrically conductive owing to the inherent high electrical conductivity of CNTs.

This project was full of challenges, like, *e.g.* how to control properties of produced nanoscopic objects (CNTs), how to design novel composite materials with a prescribed set of properties, how to study and understand physical parameters, or how to process the composite for specific applications.

The specific goal of this thesis was to produce a new photosensitive CNTs-SU8 composite material, which would be electrically and thermally conductive in combination with improved mechanical properties, high flexibility, good adhesion to a large variety of substrates, tuneable transparency, and, *at last but not least*, with the well-preserved abilities of SU8 epoxy for facile processing and photo-patterning.

The dissertation is structured as follows. After this general introduction, a more detailed introduction to the subject of the constituents of the composite material (i.e. the matrix and the filler) is given in Chapter 2. Experimental techniques used in this study are presented in Chapter 3. Optimization of the crucial technological parameters of CNTs synthesized by chemical vapour deposition (CVD), *i.e.* their diameters and lengths is presented in Chapter 4. Chapter 5 describes the fabrication and characterization of CNTs-SU8 composites. In particular, in this chapter, different factors influencing the dispersion of CNTs in SU8 are discussed. This discussion is then followed by an overview of the physical properties of the prepared composites. The study of the electrical and thermal transport properties is given in detail, as well as the results of the mechanical characterisation of the composites prepared by different solvents and/or with different CNT load. Finally, processing of the obtained composites by customized standard microtechnical techniques, like photolithography, inkjet, and screen printing, are presented in Chapter 6. Conclusions and outlook are given in Chapter 7.

References

Note to the references: Throughout the whole text of this dissertation, the citations of publications stemming from my thesis work are clearly marked by [MMX], where X indicates the publication number according to the list of publications given at the end of the thesis.

1. **D. Hull.** *An introduction to composite materials.* Cambridge : Cambridge University Press, 1981. Vol. Cambridge Solid State Science Series.
2. **F. L. Matthews and R. D. Rawlings.** *Composite materials: Engineering and science.* Cambridge : Woodhead publishing limited, 1994.
3. <http://www.nano.org.uk/news/aug2008/latest1540.htm>. [Online] [Cited: 8. 7. 2011.]
4. <http://news.adidaslookbook.com/394-jeremy-wariner-s-lone-star-spike>. [Online] [Cited: 8. 7. 2011.]
5. [En ligne] Nanosolar. [Citation : 22. 11. 2011.] <http://www.nanosolar.com/>.
6. *The development of the electron microscope and of electron microscopy.* **E. Ruska.** 1987, Reviews of Modern Physics, Vol. 59, p. 627.

7. *Surface studies by scanning tunneling microscopy*. **G. Binnig, H. Rohrer, C. Gerber, and E. Weibel**. 1982, *Physical Review Letters*, Vol. 49, p. 57.
8. *Atomic force microscope*. **G. Binnig, C. F. Quate and C. Gerber**. 1986, *Physical Review Letters*, Vol. 56, p. 930.
9. **C. Y. Chang and S. M. Sze, [ed.]**. *ULSI Technology*. s.l. : McGraw–Hill, 1996.
10. [Online] LAAS. [Cited: 21. 11. 2011.] <http://www2.laas.fr/laas/2-6870-Photolithography.php>.
11. [Online] Gersteltec. [Cited: 21. 11. 2011.] <http://www.gersteltec.ch/Application/>.
12. [Online] Nanoscribe. [Cited: 21. 11. 2011.] <http://www.nanoscribe.de/?id=439&language=en>.
13. [En ligne] [Citation : 21. 11. 2011.] <http://www.imm-mainz.de/959.html>.

Chapter 2

Materials

Composite materials are mixtures of two or more physically distinct components (1; 2). More precisely, composites can be defined as “multiphase materials obtained through the artificial combination of different materials in order to attain properties that the individual components by themselves cannot attain” (3). Composites differ from other multiphase materials that reveal naturally formed multiple phases, resulting from chemical processes or phase transformations, like, *e.g.* alloys (2; 3). The properties of composites can be tailored by the adequate choice of components. In this work, as constituents of the composite material, we have chosen an epoxy-based polymer (SU8) as the matrix and CNTs as the filler. In the following sections, a more detailed insight into the properties of the composite’s components, SU8 and CNTs, will be given.

2.1 SU8

SU8 is epoxy-based, negative-tone, near-UV-sensitive photoresist. The development of this material was related to the rapid progress in micro-engineering in the second half of the 1980s and the early 1990s, which required high aspect ratio (HAR) thick film resist. Today, SU8 is considered as the most suitable photoresist for HAR lithography (4; 5). In recent years, broad applications of SU8 in the field of UV- photolithography are extended into other domains, like X-ray or E-beam lithography. SU8 is the most widely utilised photoresist in low-cost LIGA microengineering processing (6). (The acronym LIGA originates from the German name of the processes: **L**ithographie, **G**alvanoformung, **A**bformung; means: Lithography, Electroplating, and Molding.) LIGA is a fabrication technology that is commonly used to create HAR microstructures (7). SU8, due to its high thermal stability of a fully cross-linked polymer, can be used as a mask for prolonged reactive ion etching, thus

yielding HAR patterning with vertical sidewalls (8). Moreover, rather high chemical and mechanical stabilities of the fully cross-linked SU8 allows for its applications as a direct template in LIGA-based electroplating of metals (9; 10). In addition, SU8 can be exploited in soft lithography in conjunction with thermosetting elastomers, like PDMS (11; 4). In the next section of this Chapter, we will briefly present, in chronological order, the most important events which brought SU8 to the industrial stage.

2.1.1 Historical background

In order to apply a polymer in microengineering, the key requirement is the possibility to tailor it into desired shapes. Therefore, two conditions are prerequisite: (i) the polymer has to be in the liquid state to be spreadable as a layer, and (ii) the polymer has to be processable to allow for selective hardening.

Clearly, the first condition (fluidity at room temperature) can be easily fulfilled for various epoxy polymers. The major difficulty is related to the second condition (hardening processing). In the '60s, after more than three decades of using the traditional thermally cured, solvent-based, electrically insulating enamel, scientists tried to find an alternative. Firstly, Licari and Crepeau (12), followed by the work of Schlessinger (13), had shown that aryldiazonium salts could be used as photoinitiators for the cationic ring-opening polymerisation of epoxides (14). In spite of the promising beginning, aryldiazonium salts could never be industrially used because of their intrinsic thermal instability and the generation of nitrogen gas as a product of the photolysis reaction (14). An alternative way to photochemically induce cationic polymerisations by generating either cationic species directly or indirectly, was found by J. V. Crivello (15; 16) in the form of onium salts (17; 18). The first synthesised onium salts were iodonium salts reported in 1894 by Hartmann and Meyer (19; 20). In 1965, Ptitsyna et al. first observed that diaryliodonium salts are photosensitive (21). This inspired Crivello (14) who first patented triarylsulphonium salts as photoinitiators (15; 16). Almost at the same time, Smith patented photoinitiators based on diaryliodonium salts (22; 23). Finding of the appropriate polymerisation mechanism was then followed by an intensive search for a suitable polymer, weakly absorbing UV light and providing a large number of epoxy groups per monomer. Such a combination was necessary to strengthen the cross-linking density and make possible patterning structures with vertical walls. In 1980, Skarvinko patented the first epoxy molecule with 8 epoxy groups per formula under the name of EPI-REZ SU8 as a possible candidate for photosensitive patternable coatings (24). The final composition of the photo-patternable SU8 was developed in the end of the '80s and in the early '90s, by the group of J. D. Gelorme at IBM-Rueschlikon (25; 26; 27). They introduced SU8 to the scientific community as a negative tone photoresist (28; 29). The IBM team continued the further characterisation of this new material in collaboration with the group of Prof. Philippe Renaud from the Ecole Polytechnique in Lausanne (30; 31). In particular, in 1998, Hubert Lorenz from this latter group completed his

PhD thesis on fabrication of SU8-based microstructures (32). Commercially available photosensitive formulation based on SU8 epoxy resin products were introduced for the first time by MicroChem in 1996 (4). The further development of SU8 photoresist and broadening of its applications still continues.

2.1.2 Overview of SU8 processing techniques

Nowadays, SU8 is well-established as an engineering material for microfabrication. One of the biggest advantages of SU8 is that it can be processed towards obtaining 3D submicron HAR patterns. The most common process of fabrication of HAR patterns is UV-assisted photolithography. This fabrication consists of a combination of thermal- and UV-curing. The process flow includes the following steps: substrate pre-treatment, coating, soft baking in order to remove the solvent, UV exposure, post-exposure baking to continue curing and development, rinsing, drying and hard-baking. The specificities of all technological steps will be considered in details in Chapter 6 and Appendix 2. By careful optimization of UV lithography conditions, the aspect ratio up to 40 was achieved (4; 33). The actual limitation of the aspect ratio in this case was due to the diffraction effects and broadening of the UV light beam within the air gap between the mask and photoresist. Compensation of the air gap can, in principle, be achieved by a perfect match of the refractive index of the liquid placed in the gap separating the mask and the SU8 photoresist. In fact, the practically achieved compensations of the diffraction effects enabled one to fabricate structures with an impressive aspect higher than 190 (Fig. 2.1) (34). The relatively high aspect ratios of up to 100 were also obtained by X-ray exposure (35). In particular, the X-ray exposure method is convenient for HAR structures with vertical sidewalls because X-rays penetrate deeply into SU8 due to their short wavelengths, 7–12 Å. The practical applications are rather seldom because the availability of the X-ray photolithography equipment is limited (4).

Although initially developed for optical lithography, SU8 is more and more used as a highly sensitive negative-tone E-beam resist for nanopatterning (4). In comparison to other E-beam resists, SU8 has usually 150 times higher sensitivity and hence shorter exposure times than standard PMMA-based E-beam resists (36). The low energy of electrons restricts E-beam patterning on the resist layers of a thickness up to 200 nm, which limits the aspect ratio of the structures (4). Scattering of the impinging electrons causes loss of resolution of E-beam patterning (so called 'proximity effect'). Although this electron scattering theoretically limits the attainable resolutions to >10 nm, in practice line widths of 75 nm with a pitch of 300 nm in a 200 nm thick SU8 layer were obtained (37). The lowest achieved line width was of 24 nm for lines with a pitch of 300 nm patterned with 100 kV E-beam lithography in 99 nm thick SU8 (38).

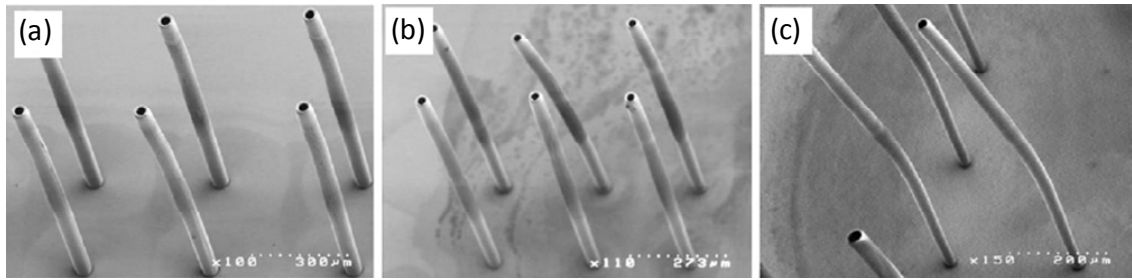


Figure 2.1: 1150 μm high microcylinders of SU8 obtained using different matching refractive index liquids for gap compensation (4). (a) 10 μm wall thickness and 45 μm internal diameter obtained using a filtered light source and no gap compensation. (b) 8 μm wall thickness and 30 μm internal diameter obtained using broadband exposure and glycerin gap compensation. (c) 6 μm wall thickness and 20 μm internal diameter obtained using PMMA filter and gap compensation with optical index matching liquid. As the wall thickness is reduced, the physical strength becomes too low to maintain the freestanding positions (From the ref. (34)).

Recently, a new direct writing lithographic technique was developed. This technique, called proton beam lithography, is using the ability of high-energy ions, such as Ga^+ , H^+ or He^+ , to deeply penetrate a resist without any significant deviation in their trajectory. Structures with well-defined smooth side walls can be directly patterned when the focused MeV proton beam is scanned over the layer of SU8 resist (39).

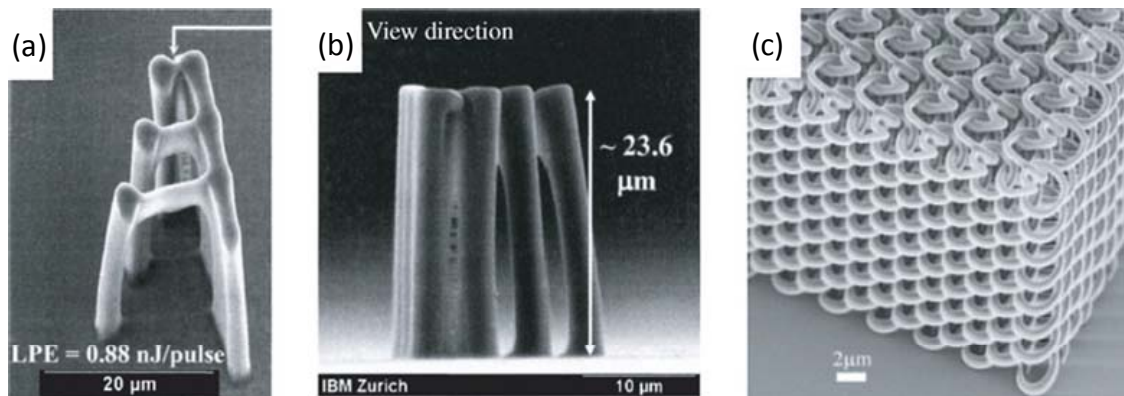


Figure 2.2: (a), (b) 3D constructs prepared from SU8 with HAR values up to 50 obtained by two-photon near-infrared photopolymerisation (40); (c) SEM image of photonic spiral structures obtained by direct laser writing using SU8 with a 180° phase shift between adjacent spirals (41) (From the ref. (4)).

The particularity of SU8 is certainly its ability to perform direct three-dimensional (3D) lithography patterning. Several lithography-based methods for fabrication of 3D structures have been developed including: layer-by-layer multiexposure, inclined/rotated lithography, modulated exposure, holographic lithography (or interference lithography), stereolithography of resist multilayers, and laser scanning of single resist layers (4) (Fig. 2.2).

Clearly, the design of all these impressive constructs (shown in Fig. 2.2) was possible due to the exceptional physical and chemical properties of SU8.

2.1.3 Physical properties

The physical properties of SU8 are listed in Table 2.1. The richness of data shown in Table 2.1 clearly points to the fact that SU8 has been a very comprehensively investigated material. In addition to the listed properties, SU8 has a good stability at elevated temperatures and resistance to moisture and solvents. Thus, SU8 has unusually high glass transition and degradation temperatures (the latter being of $\sim 380^{\circ}\text{C}$) (8). Resistance to moisture and solvents means that the polymer should not swell, dissolve, or in no way degrade in solvents exposing environments (42). Moreover, SU8 has good impact and scratch resistance, as well as excellent adhesion properties typical for an epoxy (43).

Table 2.1: Summary of the most important properties of SU8

Property	Value	Conditions	Ref.
Density	997.8kg/m ³	raw SU8	(44)
	1190kg/m ³	raw SU8	(45)
	1218kg/m ³	fully cross-linked	(46)
Epoxide Equivalent Weight	(195 – 230)g/eq	raw SU8	(44)
Melting Point	82°C	raw SU8	(44)
Polymer shrinkage	7.5%	during cross-linking	(47)
Glass transition temperature	$\sim 50^{\circ}\text{C}$	unexposed resin	(8)
	$> 200^{\circ}\text{C}$	fully cross-linked	(8)
	194°C	fully cross-linked	(44)
Degradation temperature	$\sim 380^{\circ}\text{C}$	fully cross-linked	(8)
Coefficient of thermal expansion	(52.0 \pm 5.1)ppm/K	postbaked at 95°C	(48)
		hardbaked at 150°C	(49)

Thermal conductivity	(0.2-0.3)W/mK	hardbaked at 150°C	(49)
Dynamic viscosity	0.059 Pa s	40wt% solid SU8 + GBL	(50)
	1.5 Pa s	60wt% solid SU8 + GBL	
	15 Pa s	70wt% solid SU8 + GBL	
Refractive index	1.668	unexposed at $\lambda=365\text{nm}$	(34)
	1.650	unexposed at $\lambda=405\text{nm}$	(34)
	0.8	postbake 100°C, KOH, 520 μm thick; 0.1THz	(51)
	0.7	postbake 100°C, KOH, 520 μm thick; 1.6THz	(51)
Absorption coefficient	$\sim 2\text{cm}^{-1}$	postbake 100°C, KOH, 520 μm thick; 0.1THz	(51)
	$\sim 40\text{cm}^{-1}$	postbake 100°C, KOH, 520 μm thick; 1.6THz	
Volume resistivity	$(1.8-2.8)\times 10^{14}\Omega\text{m}$	hardbaked at 150°C	(49)
Surface resistivity	$(5.1-18)\times 10^{14}\Omega\text{m}$	hardbaked at 150°C	(49)
Relative dielectric constant	2.8	postbake 100°C, KOH, 520 μm thick; 0.1THz	(51)
	3	postbake 100°C, KOH, 520 μm thick; 1.6THz	(51)
	4	postbake 100°C; (20-40)GHz	(52)
	3.2-4.1	hardbaked at 150°C; 1GHz	(49)
	5.07	hardbaked at 150°C; 1MHz	(44)
Young's modulus	(1.25-3.89)GPa	(75 μm thick) postbaked at 95°C	(53)
	(1.6-2.6)GPa	postbake at 95°C (4 durations)	(54)
	(3.23-3.57)GPa	(200 μm thick) postbaked at (95-105)°C	(55)
	4.02GPa	postbaked at 95°C	(30)
	(3.2 \pm 0.2)GPa	30 μm thick layer	(46)
	2.0GPa	hardbaked at 150°C	(49)
	2.7GPa	hardbaked at 200°C	(54)
(4.95 \pm 0.42)GPa	hardbaked at 200°C	(56)	

Bi-axial modulus of elasticity	(5.8±0.89)GPa	postbaked at 95°C	(48)
Tensile Strength	51MPa	fully cross-linked	(44)
Film stress	(16-19)MPa	postbaked at 95°C	(48)
Maximal stress	34MPa	hardbaked at 200°C	(56)
Maximal strain	0.009	hardbaked at 200°C	(56)
Poisson coefficient	0.22	postbaked at 95°C	(45)
Friction coefficient	0.19	postbaked at 95°C	(30)
Elongation at break	(4.8-6.5)%	hardbaked at 150°C	(49)

2.1.4 Composition

The SU8 photoresist consists of three main components: 1) Bisphenol A Novolak epoxy oligomer, 2) appropriate organic solvent in order to dissolve solid SU8 resin, and 3) the photoinitiator (PI) to cross-link SU8. Usually, PI compounds used in the context of SU8 processing are from the triarylsulfonium salts family.

Bisphenol A Novolak epoxy oligomer (EPON™ Resin SU-8, also known as EPIKOTE™ 157) (44) is commercially available in the granular form and manufactured by Momentive Specialty Chemicals Inc. (previously by Shell Chemical and Hexion Specialty Chemicals Inc. (57).

The thickness of the processed SU8 layer depends on the viscosity of the SU8 formulation, which can be adjusted by changing the weight ratio of the solid SU8 and solvent. In particular, while using a wide range of the commercially available SU8 formulations, thin film coatings in the thickness range from 200 nm to 350 µm can be obtained in a single coating process (58), or up to 3 mm by multicoating processes (59).

The molecular structures of the SU8 monomer (*i.e.* the epoxy oligomer, Bisphenol A Novolak SU8) before and after cross-linking are shown in Figure 2.3 (a) and (b), respectively. The number '8' in the polymer's name (SU8) can be assigned to the number of epoxy groups in the oligomer (Fig. 2.3 (a)). The original definition of SU8 by its manufacturer, Momentive Specialty Chemicals Inc., clearly points to this fact: "EPON™ Resin SU-8 is a polymeric solid epoxy novolac resin possessing average epoxide group functionality around eight" (44). This high number of reactive epoxy functional sites per each monomer molecule allows a high

degree of cross-links after photoactivation (4). As a result, cross-linked SU8 has high stability and satisfactory industrially-important properties (see Table 2.1).

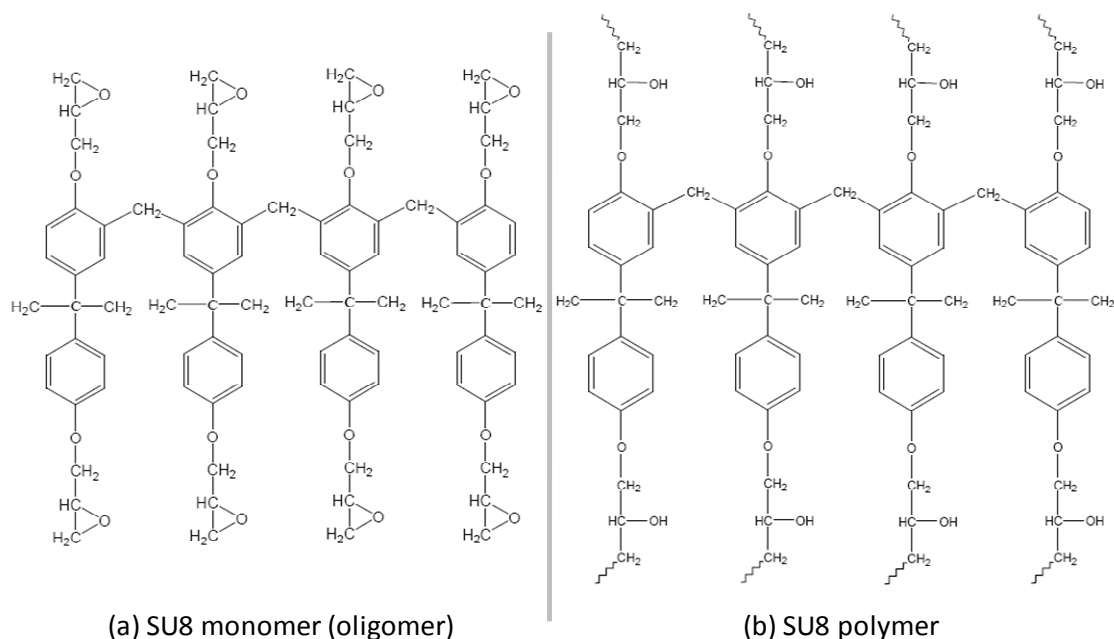


Figure 2.3: Molecular structures of the SU8 monomer (Bisphenol A Novolak SU8 epoxy oligomer) (a) and the monomer unit in the cross-linked SU8 polymer (b) (From the ref. (60)).

2.1.5 UV-induced cationic ring opening polymerisation

Although, SU8 can be cross-linked by different technological routes (see section 2.1.2 of this Chapter), the key mechanism is UV-induced cationic ring opening polymerisation and will be discussed in more details below.

In general, the process of photolithography is based on the transfer of a suitable pattern onto a photosensitive polymer by selective exposure to a radiation source, such as light. The selective illumination initiates photochemical processes in the photoresist, thus resulting in the predominantly chemical differentiation of the exposed areas. Therefore, in the subsequent development step, the exposed areas can also be physically differentiated. If polymer structures remaining after the development step match the areas exposed to irradiation, the obtained image is called negative-tone image. In the opposite case, a positive-tone image is obtained. Thus, the corresponding photosensitive polymers can be classified as negative- or positive-tone photoresists. The final result of the development is the pattern on the resist layer which corresponds to the image geometry of the mask utilized during illumination (4).

If the polymer contains certain types of molecular structures, like epoxy rings, then the polymerisation process proceeds by ring-opening polymerisation. In polymer chemistry, ring-opening polymerisation is a form of chain-growth (addition) polymerisation, in which the terminal end of a polymer acts as a reactive center, where further cyclic monomers join to form a larger polymer chain through ionic propagation. The treatment of some cyclic compounds with catalysts induces cleavage of the ring followed by polymerisation to yield high-molecular-weight polymers. When the reactive center of the propagating chain is a carbocation or carbanion, the polymerisation is called cationic or anionic ring-opening polymerisation, respectively. If cationic ring-opening polymerisation starts with UV-induced protonation of the monomer, then we speak about UV cationic ring-opening polymerisation, which is a type of photopolymerisation.

The term photopolymerisation refers to a process of a rapid transformation of liquid monomers into a solid polymer induced by UV light. Essential steps in photopolymerisation are: 1) absorption of light by a mixture of monomers and photoinitiators (PIs); 2) bond cleavage in the PI (generation of reactive species); 3) addition of reactive species to monomers (initiation of polymerisation); 4) chain growth (propagation of polymerisation), and finally 5) termination of the polymerisation process, which results in a cured polymer (Fig. 2.4) (14; 61).

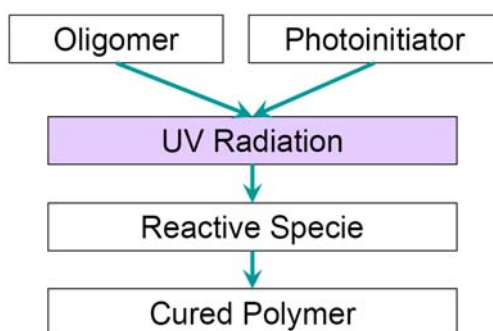


Figure 2.4: Schematic representation of the basic steps in the photopolymerisation process.

Cationic polymerisations are considered as “the most versatile of all addition-type polymerisations” (62), because nearly every type of known cationically polymerisable monomer can be polymerised with some cationic PIs. The most effective known cationic PIs are onium salts due to their strong absorption in the short-wavelength UV region (63).

In order to choose an appropriate PI among numerous onium salts, certain criteria have to be put forward. Crivello, who identified these salts as PIs, established the following criteria (61): 1) the PI should be completely stable by itself and toward spontaneous polymerisation when dissolved in reactive monomers; 2) when irradiated, the PI should undergo photolysis with high quantum efficiency and without the liberation of by-products that either inhibit polymerisation or degrade the quality of the final product; 3) the

synthesis of the PI should be simple and inexpensive, and 4) the PI should have as low toxicity as possible.

Simple synthesis, excellent photosensitivity and excellent stability are characteristics of the two classes of PIs (61): diaryliodonium ($\text{Ar}_2\text{I}^+\text{MtX}_n^-$) (22) and triarylsulphonium ($\text{Ar}_3\text{S}^+\text{MtX}_n^-$) (15; 16) salts (Fig. 2.5), where Ar stands for an aryl group (functional group or substituent derived from a simple aromatic ring), Mt stands for metal or metalloid, X is a halogen, and n is a number which has typical value of 4-6. Group MtX_n^- is a nonnucleophilic and photostable anion such as for example tetrafluoroborate (BF_4^-), hexafluoroantimonate (SbF_6^-) or hexafluorophosphate (PF_6^-) (14). These compounds are considered as nearly ideal PIs. In particular, they reveal a high degree of photosensitivity in combination with an excellent thermal stability. In addition, the processes of photolysis of these salts are not affected by radical inhibitors or the presence of air or oxygen (61).

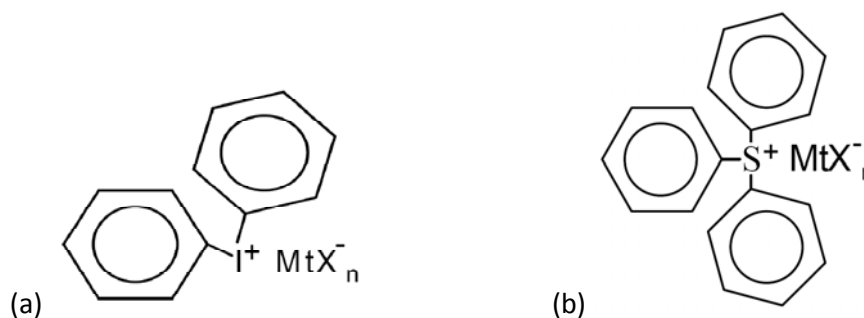


Figure 2.5: Generalised structure of some of the possible PIs for cationic polymerisation of SU8: (a) diaryliodonium salt and (b) triarylsulphonium salt.

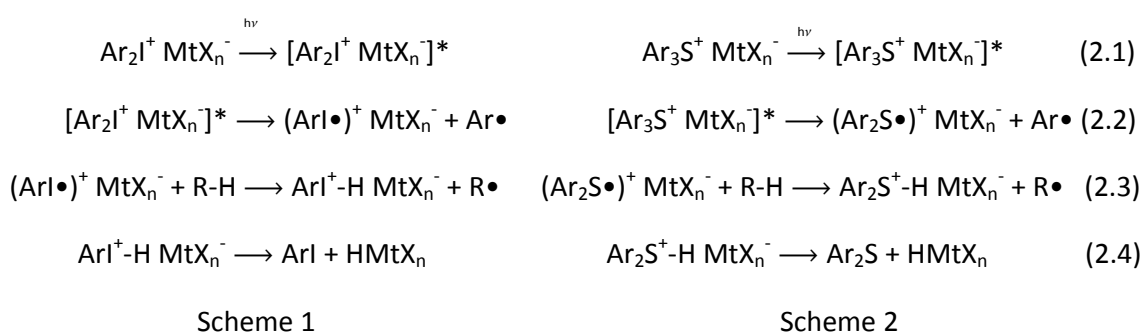
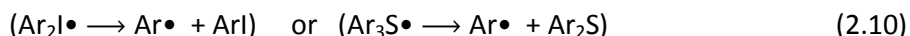
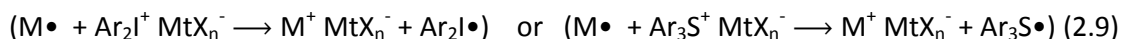


Figure 2.6: The major process by which diaryliodonium and triarylsulphonium salts undergo photolysis is depicted in schemes 1 and 2, respectively (adopted from the ref. (61)).

The mechanism of the UV-induced photolysis of diaryliodonium and triarylsulphonium salt PIs is complex and is depicted in an abbreviated form in schemes 1 and 2, respectively (Fig. 2.6). The mechanism can be explained by the example of one type of salts due to obvious analogy in their processes. Initially, photoexcitation of salt molecule forms highly reactive species (Eq. 2.1) which undergoes cleavages of the carbon-iodine (or

carbon-sulphur) bond to produce a radical /cation-radical pair (Eq. 2.2). The cation-radical abstracts hydrogen from its environment (which can be solvent, monomers, impurities or some other substance with a labile hydrogen) giving the species $\text{ArI}^+\text{-H MtX}_n^-$ ($\text{Ar}_2\text{S}^+\text{-H MtX}_n^-$) (Eq. 2.3), which quickly disintegrate to generate the aryl iodide (or sulphide) and the stable, long-lived, strong solvated protonic or Brønsted acid HMtX_n (Eq. 2.4). The strength of produced acids depends on the starting anion, such as BF_4^- , PF_6^- , AsF_6^- , and SbF_6^- , and these acids have Hammett acidity functions (H_0) ranging usually from -15 to \sim -30 (64). (H_0 values are used to express the acidity of very concentrated solutions of strong acids.) These strong Brønsted acids, HMtX_n , are the predominant initiators of cationic polymerisation, which starts with direct protonation of the monomer, M , (initiation step, Eq. 2.5) to form cationic species (M^+). The following step, propagation of polymerisation, takes place by the stepwise addition of monomers to the growing cationic chain end (propagation step, Eq. 2.6). On the other hand, aryl radicals, $\text{Ar}\bullet$, generated *via* the photolysis of the onium salts (Eq. 2.2) can also interact with the monomer. In fact, there are two possible interactions: (a) the aryl radical can be added to an unsaturated monomer (Eq. 2.7) or (b) the radical can abstract a hydrogen atom from the monomer (Eq. 2.8). Radical species, $\text{Ar-M}\bullet$ and $M\bullet$, created this way, can be oxidized by the diaryliodonium or triarylsulphonium salts (Eq. 2.9) to yield carbocations. The formed diaryliodine or triarylsulfin free radicals (Eq. 2.10) undergo subsequently irreversible fragmentation to form iodoaromatic or sulfoaromatic compounds and new aryl radicals (14; 61; 65).



A very important aspect of this polymerisation mechanism is a phenomenon of chemical amplification. Namely, a single photo-event initiates formation of various compounds and ionic and radical species, followed by a cascade of subsequent chemical reactions (7). Therefore, the photolysis is actually amplified with respect to the number of produced initiating species (65). Another significant feature of this polymerisation is the complex role of the monomer in the overall mechanism. A monomer usually provides only polymerizable functional groups, but in this mechanism the monomer additionally provides either a site of unsaturation (Eq. 2.7), which reacts further, or an abstractable proton (Eq. 2.8). This implies a large impact of the monomer on the overall efficiency of polymerisation (65).

Ledwith et al. (66; 67) first demonstrated that photochemically and thermally induced free-radical decompositions of onium salts take place through a very similar mechanism to the presented one proposed by Crivello (61; 65). Therefore, the onium salts can be used to thermally initiate cationic polymerisation (68; 69). However, this cannot be used for micro- and nano-fabrication patterning application but it is worth to mention it. Actually, the temperature of the initiation process can be tuned by additives and lower to even room temperature (70). The major difference between temperature- and light-initiated cationic polymerisations consists in the way of excitation of salt molecules (Eq. 2.1), that is by heat and light, respectively. The subsequent steps, *i.e.* initiation, propagation and eventual termination processes, are the same (61).

The molecular structure of the onium salts (photoinitiators), especially the structure of cation and anion portions of these salts, determines their functions and influences the photo-polymerisation process (Fig. 2.7). The light-absorbing fragment of onium salts is cation. Hence, the cationic portion determines the photochemical pathways and controls the UV absorption characteristics and the overall photosensitivity (quantum yield). The cationic portion also influences the thermal stability of the salt and the rate of acid generation (14; 61). Therefore tuning of the spectral response of the onium salts-based photoinitiators, that is absorption wavelength, absorption coefficient, quantum yield, photosensitivity and thermal stability can be achieved via an appropriate modification of the structure of the aromatic groups in the cationic portion (71).

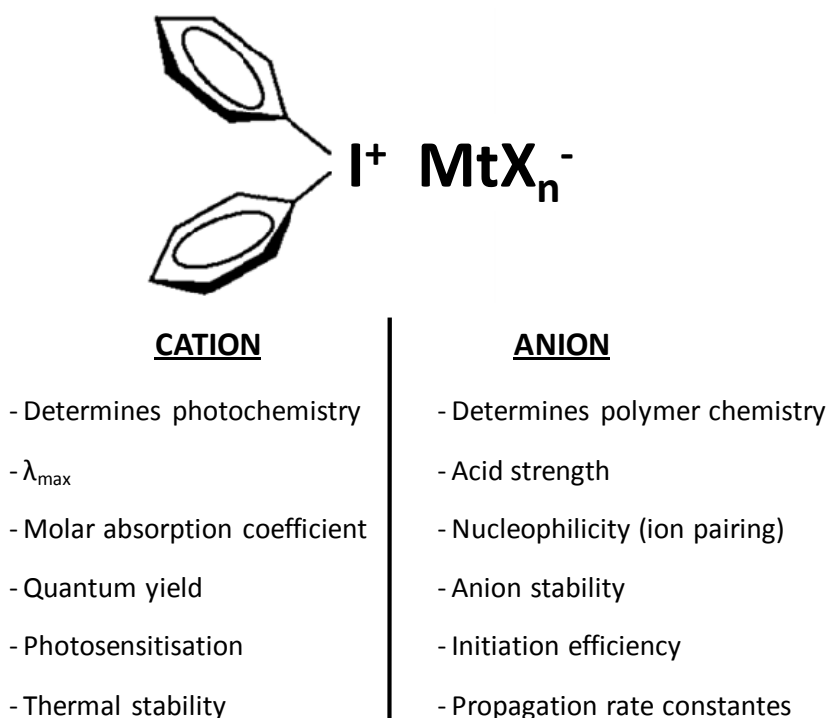
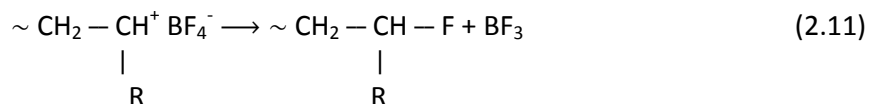


Figure 2.7: Schematic representation of the molecular structure of an onium-salt photoinitiator (adopted from the ref. (14)).

On the other hand, the polymer chemistry is determined by the anion. The structure of the anion determines the type and strength of the acid formed during photolysis and its corresponding initiation efficiency. The nature of the anion also determines the character of the propagating ion pair, which directly influences the rate of polymerisation and whether termination can occur by anion-splitting reactions such as shown in Eq. 2.11 (71):



In fact, the character of the anion has a major influence on the rate and extent of the polymerisation (its initiation, propagation and termination). For instance, if anions are strongly nucleophilic, such as I^- , Cl^- or Br^- , polymerisation fails because these anions are successfully competing with all cationically polymerizable monomers for the active cationic species. The anions of intermediate nucleophilicity, such as HSO_4^- , FSO_3^- or NO_3^- , show less interfering in the polymerisation process than previous ones. Yet, onium salts containing non-nucleophilic anions, like ClO_4^- , BF_4^- , AsF_6^- , PF_6^- , and SbF_6^- , are capable of polymerizing “virtually all known types of cationically polymerizable monomers” (61). A study of the photoinitiated bulk polymerisation induced by triphenylsulfonium salts containing SbF_6^- , AsF_6^- , PF_6^- and BF_4^- anions shows that the reactivity rates of these salts are: $\text{SbF}_6^- > \text{AsF}_6^- > \text{PF}_6^- > \text{BF}_4^-$ (Fig. 2.8 (a)) and that a very rapid polymerisation occurs in the case of the triphenylsulfonium SbF_6^- salt (61). In addition, the rates of polymerisation are highly sensitive to the light intensity, but they are limited at both high and low light intensities. In fact, the limiting factor at low intensities is “the competition of terminating impurities present in the system for the available cationic centres” (61). On the other hand, the rate of polymerisation at high intensities is limited by the absorptivity and the concentration of the photoinitiator. Further, acceleration of the polymerisation rate can be generally achieved by increasing the temperature of a ring-opening photo-polymerisation (14; 61).

A very important feature of photoinitiated cationic ring-opening polymerisations is “dark” curing. Namely, light is required in the photo-polymerisation process only in amounts sufficient to generate trace quantities of an acid while the polymerisation itself continues in the dark in the absence of terminating impurities (61). In fact, this polymerisation is a type of “living” polymerisations (that is processes without chain-breaking reactions) (71). The “living” character of this polymerisation can be seen in Figure 2.8 (b), which shows that the polymerisation continued in the absence of light, after the UV lamp was turned off (the data point marked by the arrow). In the same manner, cationic polymerisations of epoxide which are photoinitiated by triarylsulfonium salts containing the SbF_6^- , AsF_6^- , PF_6^- , BF_4^- anions also demonstrate a “living” behaviour manifested in the “post cure” observed in these systems. In fact, directly after UV exposure (normally at room temperature), an epoxy resin is incompletely polymerised. Sample heating for a certain period of time induces further polymerisation, ideally until complete conversion (14; 61). This property of “dark” curing is

usually considered as the sharpest distinction between photoinitiated cationic and radical polymerisations. In fact, the latter ones stop immediately at the end of illumination. The other difference between these two types of photo-polymerisations is the pronounced temperature dependence of the reaction rates for cationic-driven processes (71).

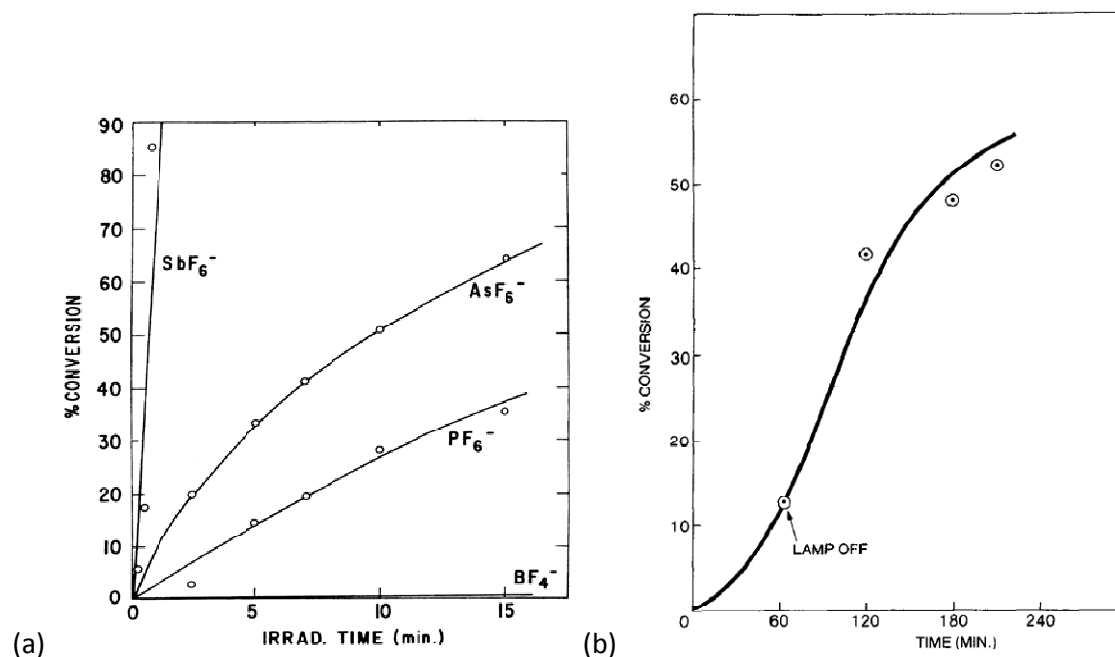


Figure 2.8: (a) Photoinitiated polymerisation of styrene oxide using 0.02-M $(\text{C}_6\text{H}_5)_3\text{S}^+ \text{MtX}_n^-$ as photoinitiators, where the anion, MtX_n^- , is indicated on the graph; (b) Photoinitiated polymerisation of tetrahydrofuran using 5×10^{-3} -M triphenyl sulfoniumhexafluorophosphate as photoinitiator (adopted from the ref. (61)).

One of the major advantages of photoinitiated cationic polymerisations is the lack of inhibition by oxygen. Thus, this polymerisation type is not affected by the presence of atmospheric oxygen or other radical scavengers. Nevertheless, bases exert a strong inhibiting effect. Moreover, water, alcohols, and other hydroxyl-containing compounds due to the relatively high nucleophilicity of the HO- group, behave as chain transfer agents having the effect of reducing the molecular weight. Therefore, high humidity which results in high localized concentration of water at a surface of an epoxy coating should be avoided, since it inhibits cationic curing of epoxides. Furthermore, the presence of water is an important factor for the initiators as well, because triarilsulfonium and diaryliodonium salts are sensitive to humidity. This is considered as one of the disadvantages of cationic photopolymerisation, besides of their slow rate of polymerisation (slower than the radical one) and the presence of strong Brönsted acids (which corrode metal substrates and cause difficulties in establishing control over cationic polymerizations) (71; 14; 61).

A **summary** of discussed factors which affect the efficiency and speed of cationic ring-opening UV polymerisation is given in Figure 2.9.

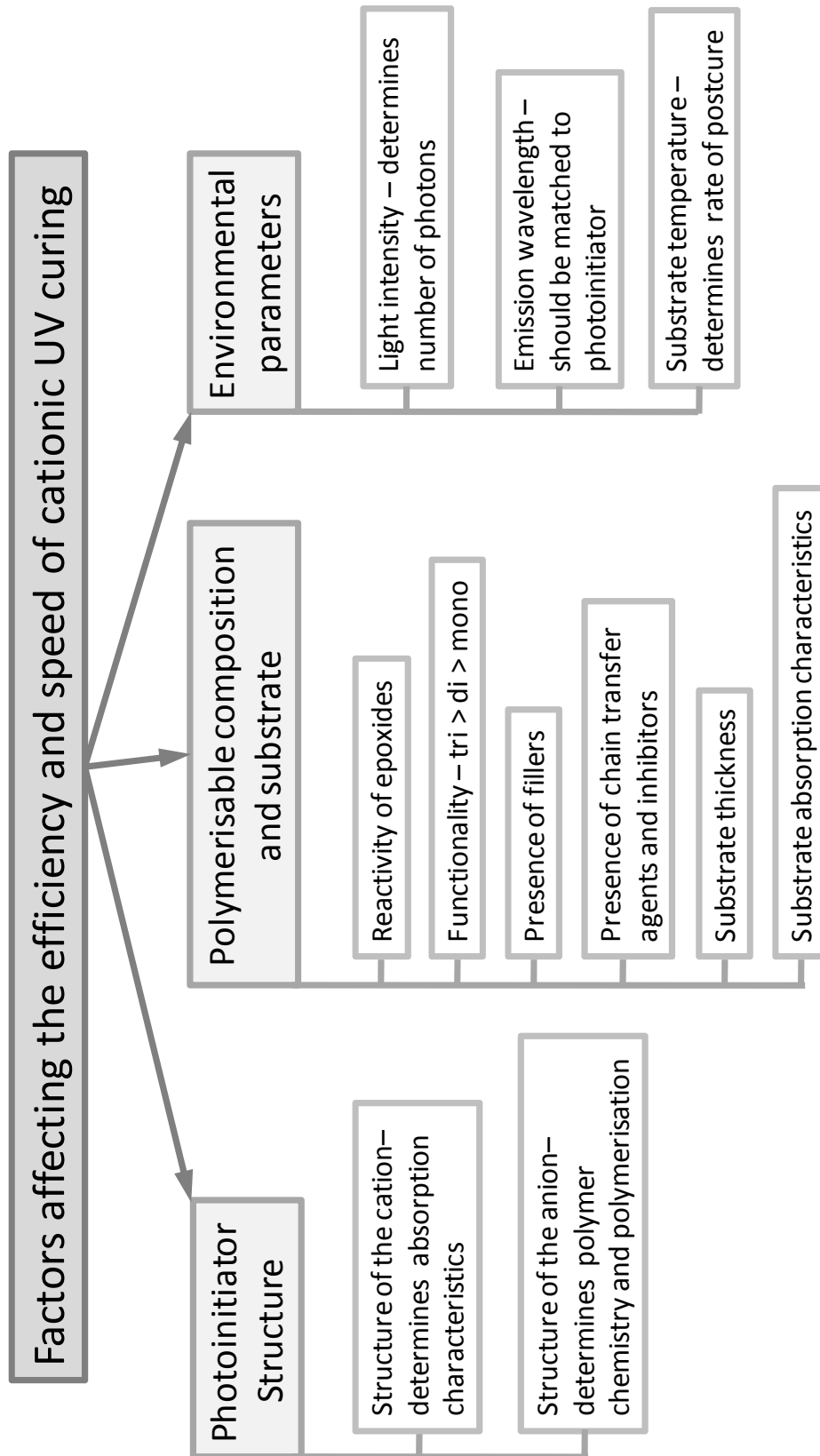


Figure 2.9: Factors which affect the efficiency and speed of cationic UV curing (Adopted from the ref. (72)).

2.1.6 Problems related with SU8

From the stand point of practical applications, high internal stress and cracks formation represent the major drawback of SU8. Additionally, quite a number of applications require easy removal of SU8 from the substrate. This reveals quite often to be difficult, even with the employment of 'sacrificial' inter-layers (5). On the other hand, a better adhesion towards a much larger variety of substrates still remains a necessity. From the industrial point of view, the application field of SU8 can still be expanded by adding new functionalities to SU8 formulations. Especially, one of the desired new SU8 functionalities would be its electrical conductivity with preserved processability (4). Other properties, like thermal conductivity and mechanical properties need also be improved for a further broadening of SU8 applications.

2.2 Fillers

Besides the matrix, composites always contain fillers, which are often considered as reinforcement, because they reinforce or enhance the properties of the matrix. Most often, fillers enhance the mechanical properties on the host matrix (43). However, the electrical and thermal characteristics may also be improved. Indeed, the simultaneous improvement of several characteristics of the matrix by given filler would be ideal. Quite often, fillers are object having at least one 'small' dimension, *e.g.* of the order of few nanometres to hundreds of micrometers (2). It is clear that a number of composite's properties, including the mechanical ones, depend on the size, shape and orientation of the filler as well as on its interaction with the matrix. According to shape, fillers are classified as particulate and fibrous (Fig. 2.10).

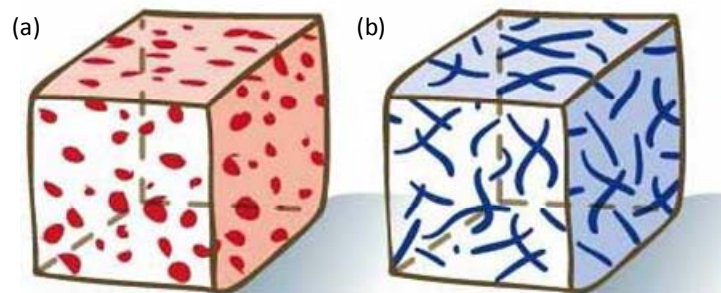


Figure 2.10: Schema of (a) particle- and (b) fibre-reinforced composites (from ref. (73)).

The particulate fillers are these having approximately equal dimensions in all directions, regardless the exact shape, which can be spherical, cubic or any other geometry. The particles' arrangements in the composite may have 'preferred' or 'random' orientations (Fig. 2.11). In the great majority of cases, however, 'random' orientations are encountered (2).

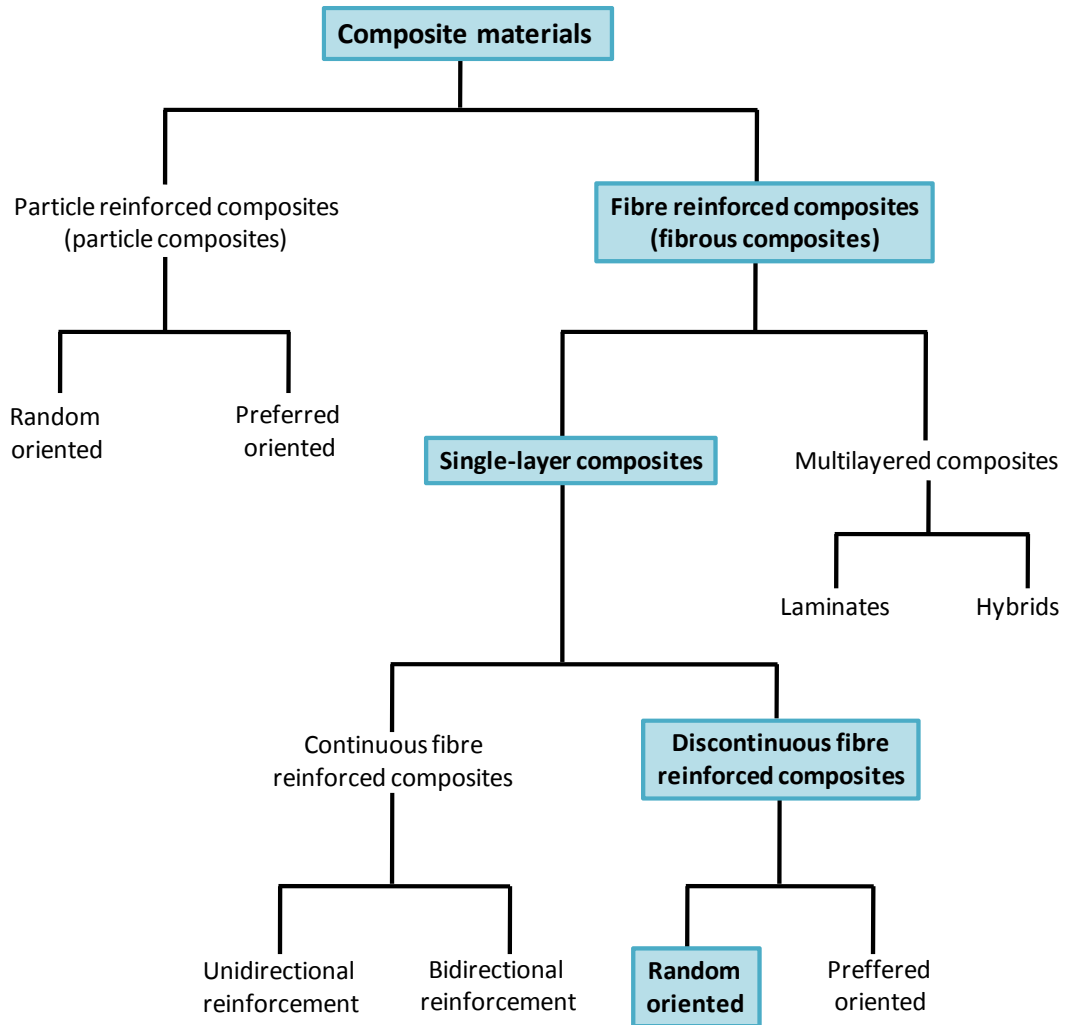


Figure 2.11: Classification of composite materials according to fillers (From the ref. (2)). Blue-green colour indicates types of composites which are compatible with CNTs-SU8 composites.

Fibrous fillers exhibit a high aspect-ratio, thus having a much greater length than their cross-sectional dimensions. The fibre-reinforced composite can be in form of single-layer or multilayered composites. The last ones are classified as laminates (*i.e.* sheets made by stacking layers in specified sequence) or hybrids (composites with mixed fibres or containing mixtures of fibrous and particulate fillers) (2). On the other hand, single-layer composites may contain continuous fibres in one (unidirectional) or two (bidirectional) preferred orientations (2). The fibres are considered as continuous if the length of the fibres corresponds to one of the dimensions of the composite layer. Except for being continuous, fibres can also be discontinuous or short and their orientation can be preferred or random. Actually, continuous fibres have much more influence than short ones on the overall composite's properties, especially mechanical, electrical and thermal properties (3). Clearly, the unidirectional alignment of continuous fibres is unavoidably associated with anisotropy, which might limit certain applications. In fact, the frequently required isotropy of the

composite system can be obtained either by equiaxed particles or by random orientation in the case of reinforcement with unequal dimensions (2).

In the context of the polymer composite chosen for this study (CNTs-SU8), most commonly used fillers are particles or short fibres. The fabrication of such composite usually proceeds by mixing the filler with a liquid resin. In the case of thermoplastic polymers the liquid resin is the molten polymer or the polymer dissolved in a solvent. In any case, the physical and chemical properties of the resin and fillers should be carefully adjusted in order to avoid floating or sinking of fillers (3).

Since the most significant improvements of the composite materials have been achieved *via* fibre reinforcement (2), for the purpose of this study, we also chose fibrous fillers.

2.3 CNTs

Since the beginning of the '90s, the scientific society was preoccupied by the 're-discovery' of "new" carbon allotrope, that is *all-carbon-atoms-based* molecular structures having cylindrical (hollow) symmetry with lengths of up to several micrometres and diameters in the nanometer range (74). In the '90s, these new carbon-based molecules, having walls consisting of one or more coaxial carbon layers, were named CNTs (3). The next part of this Chapter will focus on CNTs.

2.3.1 Basic morphologies of CNTs

From the structural point of view, CNTs can be considered as being made of rolled-up graphitic sheets (*i.e.* sheets of graphene). CNTs are classified according to the number of rolled-up graphene sheets which form concentric cylindrical carbon-layered walls. Thus, CNTs can be single-, double- or multi-walled.

A single-walled CNT (SWCNT) is the simplest basic form of CNTs, consisting of a single rolled-up graphitic sheet (Fig. 2.12 (a)). CNTs often bundle in the form of crystalline "ropes" (75), Fig. 2.12 (b), where the ropes or bundles are built of SWCNTs held together by van der Waals interactions. Example double-walled CNTs formed by rolling-up two graphitic sheets is shown in Fig. 2.12 (c).

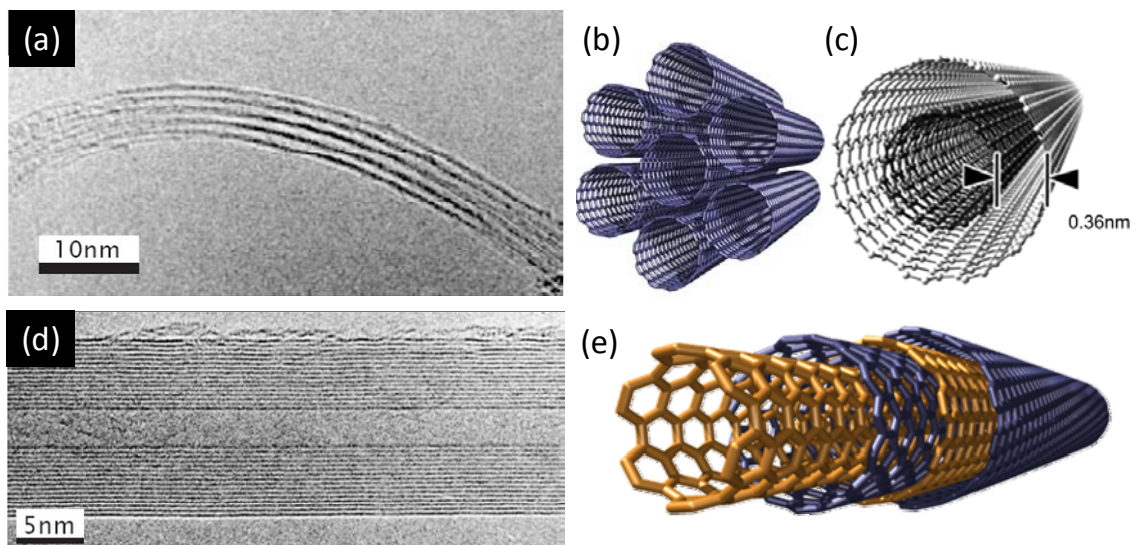


Figure 2.12: Basic morphologies of CNTs with corresponding schematic drawings. (a) The TEM image and a schematic drawing of: (b) a bundle or rope of SWCNTs and (c) a double-walled CNT. (d) The TEM image and (e) a schematic drawing of a MWCNT.

Multi-walled carbon nanotubes (MWCNTs), which were actually first discovered, consist of several rolled-up graphene sheets. The interlayer spacing in MWCNTs can range from 0.342 to 0.375 nm, depending on the diameter and number of shells comprising the tube (76). This interlayer spacing is larger than in graphite (0.335 nm), thus pointing to a relatively weak interaction between individual shells, which was also confirmed by studies of mechanical and electronic properties of CNTs.

2.3.2 Historical background

The modern CNTs revolution started in 1991 with the publication of Sumio Iijima (77), who published clear TEM images of multi-walled CNTs (Fig. 2.13 (a)). This seminal *Nature* paper, is often considered as an advent of CNTs. It is worth mentioning, however, that there were previous documented TEM observations of CNTs reported by Endo in 1976 (78) (Fig. 2.13 (b)), and also followed by Iijima in 1980 (79).

Thus, although most of CNTs-related publications start with the following phrase: “the discovery of CNTs by Iijima in 1991. . .”, Sumio Iijima is not necessarily accepted as the discoverer of CNTs by the entire scientific community. The question about the first observation of CNTs was posed in 1997 by the Boehm (80), a former editor of the journal “Carbon”, without receiving too much attention from the researchers active in the field, especially newcomers. The article of Monthieux and Kuznetsov published in 2006 (81) had bigger impact, but still not enough to make the scientific community aware of the past research. Therefore, in the following, we will briefly discuss the advent of the CNTs’ topic.

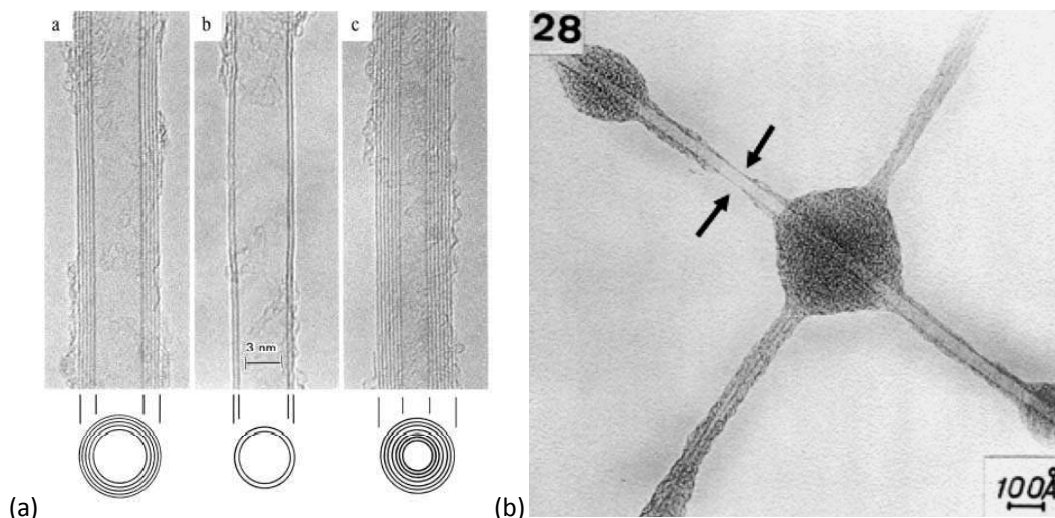


Figure 2.13: (a) The TEM image of S. Iijima often considered as the “discovery” of CNTs (From the ref. (77)). (b) TEM image from the PhD thesis by Endo pointing to a possible observation of SWCNT (similar TEM image was also published in (78)) (From the ref. (81)).

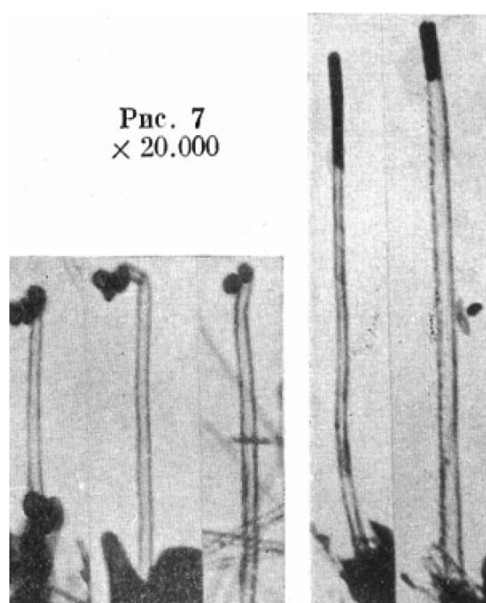


Figure 2.14: Examples of TEM images of CNTs published in the ref. (82).

Due to the fact that CNTs are nanometre-sized objects, they could not be observed before the advent of the transmission electron microscopy (TEM). In fact, the TEM systems become commercially available only in the end of the 1930s (the first TEM systems were commercialized by Siemens) (81). Concerning the first reported observations of CNTs, Kuznetsov recently emphasised: “The first TEM evidence for the tubular nature of some nano-sized carbon filaments is believed to have appeared in 1952 in the Journal of Physical Chemistry of Russia” (81). The referred TEM evidence is given in Figure 2.14, where hollow tubular structures can be seen, but without clear distinction of the walls due to the early stage of TEM characterisation. Kuznetsov also expressed himself regarding dimensions of

these carbon structures: “Despite the fact that there is no scale bar, the indicated magnification value allows one to calculate (from the original journal issue) that the diameters of the carbon tubes imaged are in the range of 50 nm, *i.e.*, definitely nano-sized.” (81). According to Kuznetsov, the fact that the article was published in Russian “... may explain why the related papers are not well known and cited. Due to the cold war, access to Russian scientific publications for Western scientists was not easy at that time, and the use of the Russian language was pretty discouraging anyway!” (81).

However, one can argue with that this Russian publication remained unknown to the rest of the scientific community. For example, in an American study from 1955 (83), the article of Radushkevich was cited among the other Russian works. This study, gave as well, a brief overview of Radushkevich’s work on elongated thread-like shapes of carbon formed by decomposition of carbon monoxide on an iron catalyst. This would mean that the American scientific community in the fifties was actually aware of the work from Russia despite the ongoing Cold War. Interestingly, the American group studied “the carbon deposits formed by the action of carbon monoxide on iron, cobalt and nickel” (83). The results were: “These deposits are in the form of filaments from 0.01 to 0.2 μm in diameter. These filaments of the deposits on iron are single solid strands. The carbon deposits on nickel seemed to consist almost entirely of either tubules or, less likely, of untwisted bifilaments. The deposits on cobalt exhibit both the form of solid filaments and of tubules or bifilaments.” (83). And the so called “bifilaments” are tubular structures. Moreover, “Most of these filaments contain dense nuclei of about the same diameter as the diameter of the filaments in which they lie” (83).

The Russian work from 1952 was not only known to the American scientists, but also to the Western European scientific community. For instance, in the article “The structure of graphite filaments” (84) published in 1958 in “Zeitschrift für Kristallographie”, the authors, Mats Hillert and Nils Lange, also quoted the article of Radushkevich among other Russian works. Their article was about the examination of graphite filaments, where “... Very straight threads have been observed with a diameter ranging from 100 Å to 0.15 mm.” (84). Interestingly, Hillert and Lange started their article with following statement (84): “*Filamentary growth of graphite was observed long ago^{1,2} and has recently been discovered again and examined by a great number of research workers³⁻¹⁵, usually as a result of decomposition of a carbon-rich gas (e.g. carbon monoxide, methane, cyanogen, benzene, cyclohexane, propane, butane, ethylene, acetylene) in the presence of some solid material (e.g. iron, cobalt, nickel, iron ore, silica, firebrick) at a temperature ranging from 400 to 2.000°C.*” The great number of examinations cited as references 3-15 originate from 1944 to 1958. This would actually mean that in 1991 the scientific community ‘re-discovered’ carbon hollow structures for the second time and under a different name, while reporting the results of experiments where the same catalysts and carbon-rich gases were used as in experiments *ca.* 50 years ago!

Interestingly, numerous statements in the article of Hillert and Lange published in 1958 look like comments from the today's CNTs publications: "It seems to be generally accepted that the solid material acts as a catalyst, absorbing carbon from the gas and depositing it as graphite. ... Electron micrographs have also shown that some thin threads are either hollow or consist of two remarkably parallel filaments. ... Furthermore, the end of each thread is always spherical. ... When material from a zone of lower temperature was examined in an electron microscope very thin threads were found, some of them irregularly bent and as thin as 100 Å, others exceedingly straight and at least 0.1 mm long although as thin as 800 Å. ... All the filaments were found to be hollow tubules, the diameter of the hole varying appreciably... *dark circles, often with a light centre, are frequently observed in the middle of irregularly bent filaments and they provide good evidence that these filaments are in fact hollow tubules with circular cross sections.* ... Result of electron diffraction... indicating that the thin graphite threads are also built up of lamellar units bent into cylinders." (84).

This raises the question, how it is possible that CNTs are for most of the scientists discovered in 1991, besides all known research on the hollow filamentous carbon containing concentric graphite sheets and having diameters in the nanometres range. One of the possible answers is that these filaments were: "investigated by material scientists, whose main goal was to understand the growth mechanisms so that they could prevent their formation in coal and steel industry processing" (81). In line with this, there is an interesting Canadian study by Watson and Kaufmann from 1946 (85). They studied cuprene, a well-known pipe-clogging product of pyrolysis in the acetylene industry, which was extracted from "... clogging deposits taken from acetylene lines. This is illustrated by a deposit taken from a reactor used in the process of hydrogenation of acetylene to ethylene." (85). The observed products were "... composed of hollow fibers characterized by both longitudinal and transverse structure ... showing a fine fiber of diameter 170 Å" (85). Was then this finding of fibres with diameter in nanometres and with longitudinal and transverse structures the *true discovery* of CNTs?

After all, it seems that the scientific community before the '90s was still not ready to think "nano". After the famous Feynman's lecture "There's Plenty of Room at the Bottom" in 1959, the overall research minds were already directed towards nanotechnology. The open-mindedness in the '90s can definitely be attributed to the appearance of STM and AFM in the '80s (86; 87), which finally fully opened the door to fruitful "nano" investigations to the scientific community already prepared by Feynman for the upcoming "new" dimension of the world.

Besides the intriguing and obviously irresolvable debate "who did discover CNTs", there is an even more intriguing, but still unanswered question raised recently in Nature Nanotechnology, that is: "Do single-walled carbon nanotubes occur naturally?" (88).

2.3.3 Synthesis of CNTs

There are several methods of CNTs synthesis. Three of them, *i.e.* arc-discharge, laser ablation and catalytic chemical vapour deposition (CCVD), are the mainstream of the CNTs production. Therefore, in the following, we will give a short overview of these three methods. The first two methods, arc-discharge (89) and laser ablation (75), are based on cooling of carbon plasma generated by the evaporation of solid carbon sources. The third, and by far the most used technique, CCVD (90), is based on the vapour-phase carbon source which is decomposed chemically.

2.3.3.1 Arc-discharge growth

Arc-discharge synthesis method of CNTs is the earliest one, although initially used for production of fullerenes (91). It is based on cooling of carbon plasma generated by an electric arc between two graphite rods placed in an inert atmosphere (helium or argon). Carbon evaporation is ignited by a high-intensity electric current (of *ca.* 100 A) (92) passing through the two rods, which are just gently touched to initiate the arc. Because of this high current density, the temperature in the arc can reach 3000°C (74) and thus, the electrodes evaporate and their length decreases. In order to keep the current between the electrodes constant, the distance between them has to be kept constant, and hence, the cathode is moved downwards during the reaction (Fig. 2.15). The evaporated carbon condenses upon cooling, forming the deposits on the chamber-walls and the cathode (77). The deposits contain CNTs, but also by-products, like multilayered graphitic particles, fullerenes and carbon soot. CNTs have to be separated from the impurities present in the high percent. This separation requires excessive purification, thus making the arc-discharge method inconvenient for large scale CNTs synthesis.

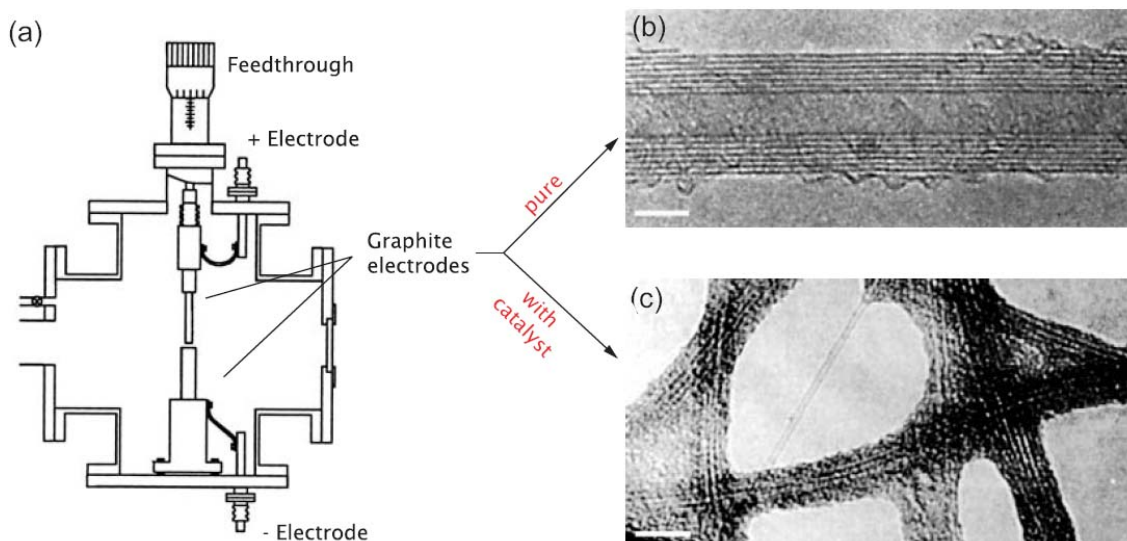


Figure 2.15: (a) The arc-discharge method. MWNTs are produced when using pure graphitic electrodes, whereas SWNT ropes are formed when using electrodes containing a small

amount of catalyst particles. (b) One of the first images of a MWNT (77). (c) One of the first reported images of SWNT ropes (93) (From the ref. (92)).

2.3.3.2 Laser-ablation method

Another way of producing high quality CNTs from carbon plasma is by the laser ablation method where intense laser pulses ablate a carbon target (75). The target is placed into a furnace heated to 1200°C and for SWCNTs growth it contains 0.5% of nickel and cobalt (74). During the laser ablation, a flow of inert gas (helium or argon) is passed through the chamber, carrying the ablated carbon towards a cold collector (Fig. 2.16 (a)). Upon cooling, the carbon atoms from the vapour quickly condense into large clusters. In this way produced SWCNTs are mostly in form of bundles (ropes) consisting of several SWCNTs closely packed into hexagonal crystals and held together by van der Waals interactions (Fig. 2.12 (a) and (b), Fig. 2.16 (b)), with a typical inter-tube distance of 0.33 nm (94).

This synthesis method is similar to arc-discharge compared to the applied high temperature required to bring the solid carbon source to a vapour phase (74). In general, these both methods produce high quality CNTs; however, in very small quantities and without the possibility of scaling-up to industrial production.

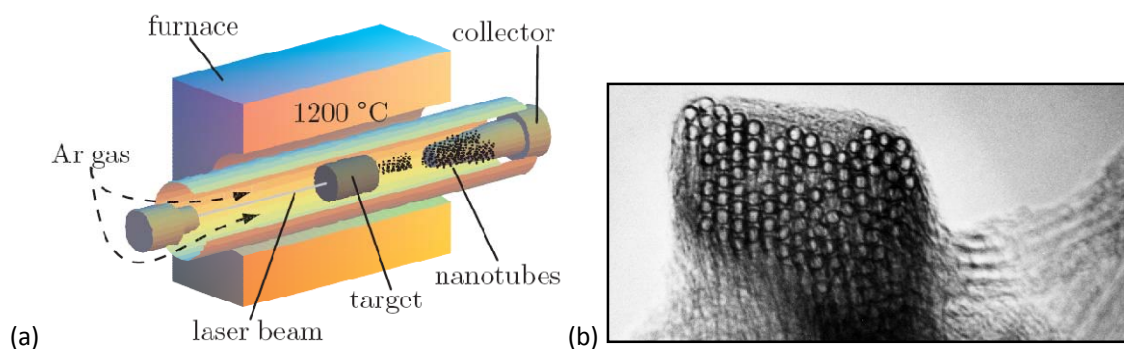


Figure 2.16: (a) Synthesis of CNTs by laser ablation of a graphitic target. SWCNT bundles, like the one on (b), are collected on the cooled collector (75) (From the ref. (74; 92)).

2.3.3.3 CVD growth

Over the last few decades, the CCVD (also called catalytic CVD) has become a well-established technique for synthesis of carbon fibres. This synthesis method essentially consists of two steps: a) the catalyst preparation and b) the carbon-catalyst reaction, *i.e.* the actual synthesis of CNTs. The second step, CNT growth, involves the flow of a hydrocarbon gas through a tube over a catalyst material in a heated furnace (Fig. 2.17) (95).

The CVD CNTs growth is controlled by: the carbon source, gas flow rate and ratio, catalyst, support and growth temperature (96; 97). A commonly used carbon source is a hydrocarbon gas, (C_nH_m), such as acetylene (C_2H_2) or methane (CH_4) (98). CNTs grow from the catalysts particles, such as particles of Fe, Co, Ni or their alloys, dispersed on a support

material e.g. silicon, alumina or zeolite. The support can be powder or in the form of flat solid film. In the first case, CVD synthesis can easily be scaled-up, but the control over the CNTs properties is rather difficult and requires further research. On the contrary, in the second case, the control over the diameter of both SWCNTs and MWCNTs can be achieved by careful catalyst preparation and precise setting of the growth conditions. Moreover, by patterning the catalyst, this method enables the control of the position of CNTs growth (99). Therefore, this method is more suitable for producing nano-structured constructs with integrated CNTs. The growth of CNTs in a desired direction by bridging prefabricated structures on substrates can be achieved by the application of an electric field (100) or by the fine control over the gas flow (Fig. 2.17 (b)) (101).

The main advantages of this method are: scalability up to an industrial production, controllable growth on flat support, existence of many variations of the method, among which plasma-enhanced CVD allows low temperature synthesis at only 120°C. This latter feature of the CVD technique enables one to grow CNTs on even plastic surfaces (102).

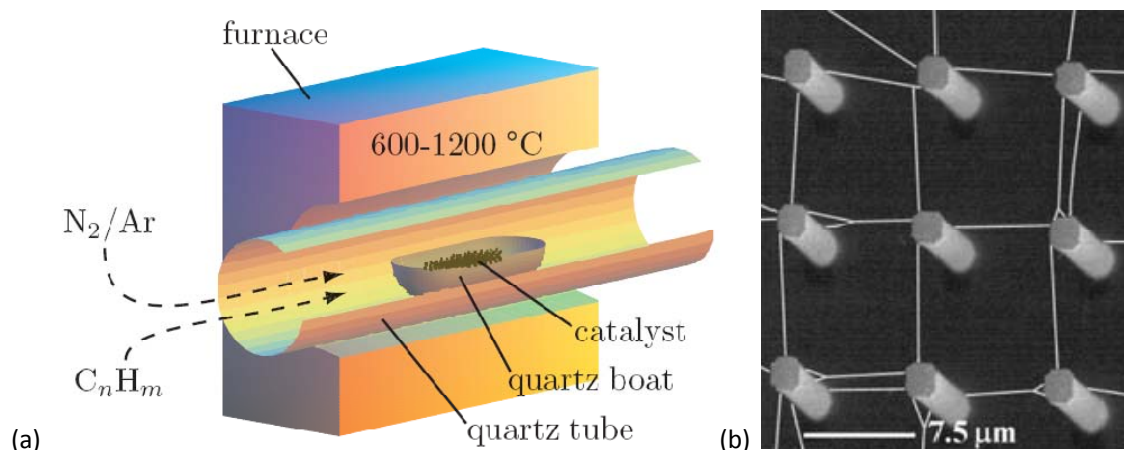


Figure 2.17: (a) The furnace for CVD based growth of carbon nanotubes over the catalyst particles placed in a quartz boat (From the ref. (74)). (b) gas flow alignment of growing nanotubes between prefabricated pillars (101) (From the ref. (92)).

The main disadvantages of CVD methods are: a) difficulties to control CNTs growth from the powder form of catalyst-support system what is important for the large scale CVD synthesis aiming industrial applications and b) the higher concentration of defects than in the case of arc-discharge or laser ablation growth methods, which can significantly diminish the mechanical and transport properties of CNTs (103).

In particular, the CVD technique was used for the CNTs growth study in this work. Therefore, it will be discussed in detail in Chapter 4, together with other experimental results.

2.3.4 Theory of catalytic growth of CNTs

Despite many uncertainties concerning CNTs growth mechanism, there are some general features related to all catalytic processes. In particular, in CCVD processes catalysts are always required, whereas in the case of arc-discharge and laser ablation, only SWNT production requires catalyst, while MWNTs can be grown without it. In this latter case, two pure graphite electrodes or graphite targets are sufficient for MWCNTs growth.

The catalysts used for CNTs growth are usually transitional metals, like Fe, Co or Ni. The catalysts are deposited on a graphite target (for arc discharge and laser ablation synthesis methods) or on a support, which can be powder or in form of a solid film (for CVD synthesis). In the following, we will give a brief overview of the global picture of the CNTs growth. In brief, when a catalyst is placed into a high temperature environment enriched with carbon in a vapour-phase, an unsaturated catalyst particle absorbs carbon, what is a highly exothermic process. The absorbed carbon subsequently starts to diffuse into the metal. However, the catalyst particles are asymmetrically adsorbing-emitting carbon and carbon diffusivity is not the same over the catalyst cross-section. Saturation of the catalyst particle with carbon, leads to endothermic carbon segregation on catalyst's surface. In order to form an energetically favourable atomic configuration (i.e. avoid dangling bonds on the surface of the carbon), the carbon atoms assemble in a sp^2 structure at a less reactive facet of the particle. The size of catalyst particles is a crucial parameter, since it can be correlated with the CNT's diameter.

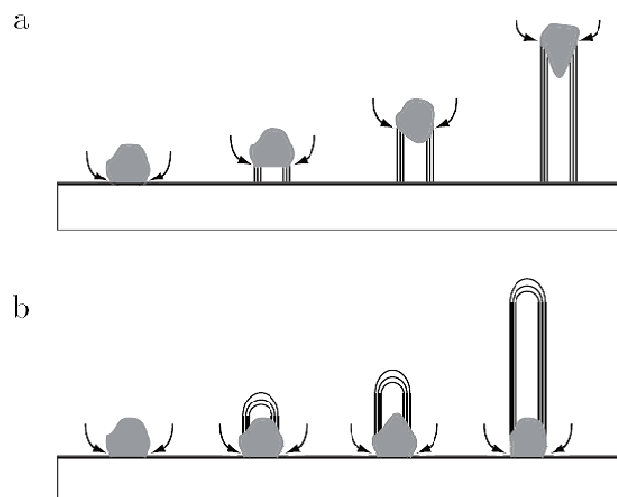


Figure 2.18: Schematic drawing of: (a) the tip and (b) the bottom growth models of CNTs. Depending on the adhesion force between the particle and the substrate, the catalyst can be pushed up by the growing CNT (a), tip growth, or the carbon diffusion continues from the bottom (b), bottom growth (From the ref. (74)).

A simple model, presented in Figure 2.18 describes the growth with a catalyst particle at the top or bottom of the CNT. In principle, both cases are the same, but in the

case of bottom growth (Fig. 2.18 (b)), the catalyst adhesion to the substrate surface is stronger than in the top growth case (Fig. 2.18 (a)). If the adhesion force is not high enough to attach the catalyst particle to the surface, the catalyst can be either lifted up or sucked into the tube, as is can be frequently seen in TEM images of CVD grown CNTs.

2.3.5 Properties of CNTs

2.3.5.1 Electronic properties and chirality of CNTs

Electronic properties of CNTs are primary determined by the CNTs chirality. In fact, each SWCNT can be described as a single sheet of graphite (graphene nano-ribbon), rolled-up into a cylinder (Fig. 2.19), with diameter between few Angstroms to tens of nanometres.

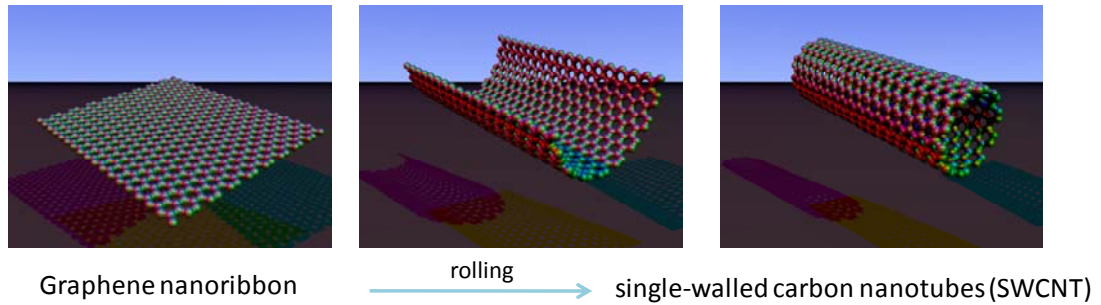


Figure 2.19: Schematic diagram of nanotube formation by “rolling-up” a graphene sheet.

A graphene sheet is shown in Figure 2.19 together with the unit vectors and of the hexagonal lattice. The “rolling-up” is described by a chiral vector \vec{C}_h , whose length corresponds to the tube’s circumference. The chiral vector is expressed as:

$$\vec{C}_h = n\vec{a}_1 + m\vec{a}_2 \equiv (n, m) \quad (3.1)$$

where integers n and m represent the chiral indices while \vec{a}_1 and \vec{a}_2 are those unit vectors which span the unit cell of the hexagonal lattice. The atomic structure can be classified according to the chiral vector or chiral angle ϑ , since both of them describes the “twist” in the CNT lattice. The chiral angles are in the 0 to 30° interval, where the limits are referred to “zigzag” $(n, 0)$ and to “armchair” (n, n) nanotubes, respectively.

The diameter d of the nanotube is given by the equation: $d = L/\pi$, where L is the length of the chiral vector or the circumference of the CNT:

$$L = |\vec{C}_h| = a\sqrt{n^2 + m^2 + nm} \quad (3.2)$$

where $a = 2.49 \text{ \AA}$ is the lattice constant of graphite. The nearest neighbour distance between carbon atoms in graphite is 1.42 \AA .

The chirality of CNTs has a significant influence on their properties. Electronic properties can be semiconducting or metallic, depending on the chirality and even a small change of diameter can drastically alter their conductivity from metallic to semiconducting (104). This interesting electrical property of CNTs is due to the peculiar electronic structure of the graphene and it can be deduced by taking into account the confinement of the electrons around the circumference of the CNT.

MWCNTs contain several coaxial cylinders, each cylinder being a SWCNT. Consequently, each carbon shell of MWCNT can have different electronic character and chirality. In general, MWCNTs are considered as metallic because at least one of the MWCNT's walls should be metallic. However, studies of MWCNTs revealed that electrical transport is dominated by outer-shell conduction (105).

2.3.5.2 Mechanical properties

Concerning mechanical properties, both theoretical (106) and experimental (107) studies have shown that CNTs can undergo enormous bending deformation and recover elastically (108; 109). One of the first theoretical studies on the elastic properties of CNTs was published by Lu (94). This study estimated the Young's modulus of CNTs to be of 0.97 TPa, being practically independent of the tube's chirality and diameter (in the range of 0.68–27 nm). The measurements of the Young's modulus values of CNTs have confirmed the theoretical expectations (107; 110). These values have been found similar to that of in-plane modulus of graphite. In fact, the mechanical properties of CNTs are closely related to those of graphite: strong sp^2 -hybridized in-plane σ -bonds of 1.42 Å, give them a remarkably high Young's modulus. On the other hand, π -bonds out of the graphite plane are responsible for the weak, van der Waals interlayer binding.

Furthermore, recent studies in our group showed that the CNTs growth method significantly influences CNTs' mechanical properties (111). Actually, all arc-discharged CNTs have Young's modulus above 600 GPa, whether they are MWCNTs (110) or SWCNTs (107). In contrast, CVD-grown CNTs have the diameter-dependent Young's modulus, with higher Young's modulus values for lower-diameter CNTs (112; 113). These measurements have also pointed out that CVD-synthesised CNTs may have high Young's modulus values only for CNTs which are defect-free, because structural defects are considerably reducing their mechanical properties (112; 113; 111).

2.3.5.2.1 Defects and deformations in CNTs

Depending on the synthesis method, but especially for CVD growth, CNTs usually depart from the ideal structure and contain numerous defects. The defect density also depends on the growth conditions and the most commonly observed types of defects are point- or planar ones. In fact, a defective structure can easily be created by simply replacing hexagons in graphitic structure with pentagons or heptagons, which can even close the CNT

if they are abundant. The most frequent point-defects are pentagon-heptagon defects (Stone-Wales transformations (114)), which appear in the sidewall of the CNT.

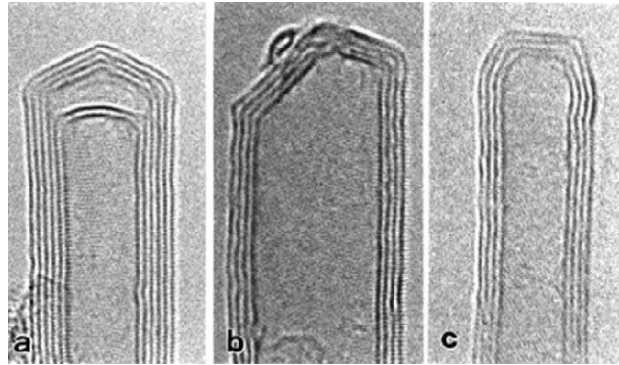


Figure 2.20: TEM micrographs of different MWNT caps published in the paper of Iijima (115).

The positions of the pentagons at the tips vary from one tube to another (Fig. 2.20). Moreover, wedges in the sidewall heptagons cause a negative inclination, thus resulting in a saddle-like structure of the tube (Fig. 2.21) (116).

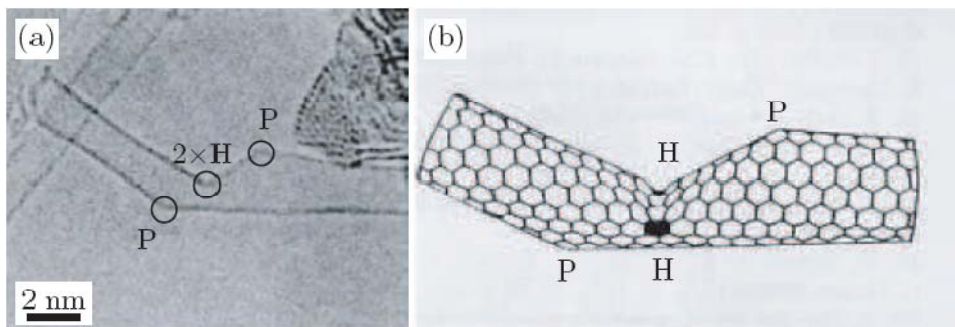


Figure 2.21: Pentagon and heptagon deformations in the hexagonal lattice indicated by letters P and H (115) (From the ref. (74)).

The bending of CNTs can be completely reversible up to angles in excess of 110° despite the formation of complex kink shapes (Fig. 2.22), as shown experimentally and theoretically by Iijima et al. (117).

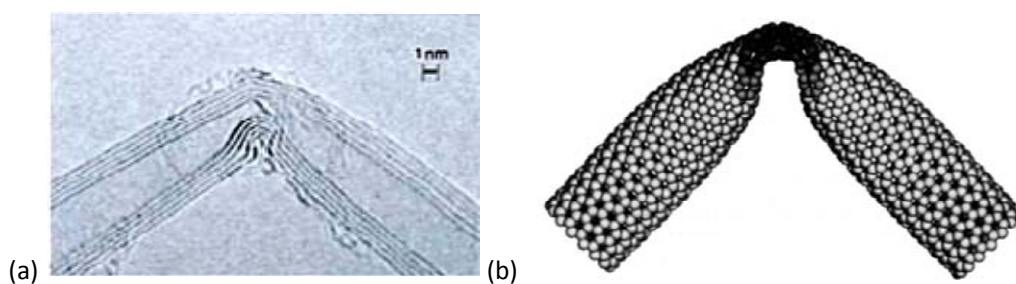


Figure 2.22: (a) The TEM micrograph (117) and (b) the molecular dynamics simulation of a buckled CNT (106).

Consequently, electrical and mechanical properties of CNTs heavily depend on defects and deformations caused by structural inhomogeneities and imperfections created during or after the growth process.

2.3.6 Potential applications

CNTs comprise a unique combination of properties, like small size, low density (similar to that of graphite), high stiffness, high strength and a broad range of electronic properties from metallic to semiconducting *p* or *n* doped (92). The rich interplay between the geometric and electronic structures of CNTs has already given rise to many interesting, new physical phenomena. Owing to such extraordinary properties of CNTs, they can be employed in many different fields of applications where high strength, low weight, high elasticity and high durability are required. In fact, CNTs discovery opened new avenues of research in physics, chemistry, and material, micro-nano-engineering and bio-medical sciences.

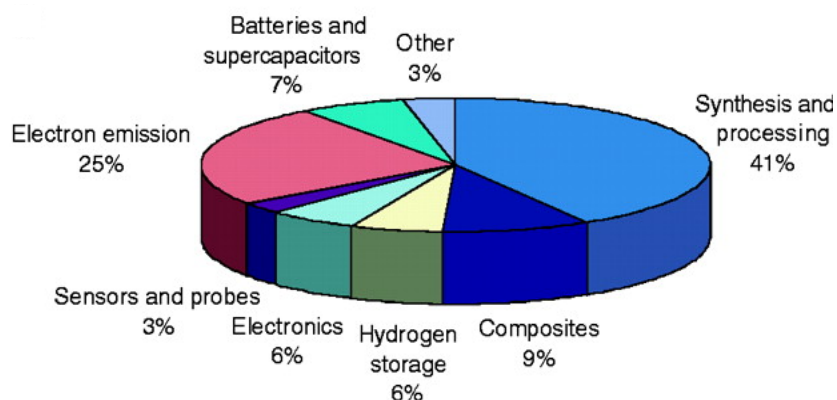


Figure 2.23: Patent filings and issuances for the CNTs field, divided according to the main area of the invention (From the ref. (118)).

The field of their potential proposed applications is enormous (Fig. 2.23), including: “conductive and high-strength composites; energy storage and energy conversion devices; sensors; field emission displays and radiation sources (Fig. 2.24); hydrogen storage media” (118). CNTs are widely considered as highly promising candidates for reinforcement in composite materials, where electrical conductivity, high strength and low weight are necessary.

Besides the already mentioned applications related to the industrial domain, CNTs can also be implemented as “small X-ray sources, ultra-sharp and resistant AFM tips with high aspect ratios, gas sensors, as components of future nanoscale electronics” (92) and “nanometer-sized semiconductor devices, probes, and interconnects” (118). Moreover, CNTs are suitable systems for studying fundamental physical phenomena on the nano-scale.

Anyhow, current and future advances in production and processing of CNTs, will enable their integration into many devices that we use in our everyday life (118).

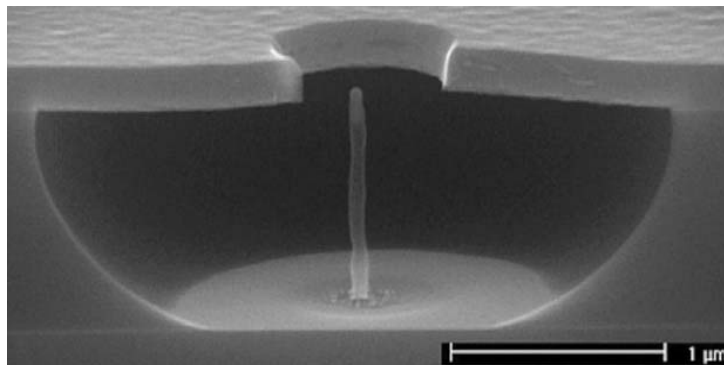


Figure 2.24: Single CNT grown inside a gated silicon cavity as a field electron emitter (119) (From the ref. (120)).

2.3.6.1 Problems related to CNTs

Concerning SWCNTs, one of the main problems is their purity, because their synthesis is always followed by impurities in form of fullerenes, amorous carbon and/or catalytic particles, what requires extensive purifications. Another drawback is that SWCNTs often bundle up in ropes during the production, where single tubes are held together by weak van der Waals interaction (75). The separation of SWCNTs from the bundles is very difficult. In fact, the separation of bundles often results in tubes breaking.

On the other hand, MWCNTs are not bundling, but they are associated to some other problems. The main one is their quality. MWCNTs produced by arc-discharge and laser ablation method are well graphitised and possess good mechanical properties (111), but their production cannot be scaled-up. However, CVD synthesised MWCNTs can be easily scaled-up, but their quality is often far beyond the quality of MWCNTs produced by the other two methods (111). This is the main reason why CVD-MWCNTs-based composites yield mechanical properties far below expectations. The other reason is insolubility of CNTs in most of the common solvents (although dissolution in limited number of cases has been obtained (121)) what prevents homogeneous dispersion of CNTs in the host matrix. The low solubility, along with intrinsic entanglement of CVD CNTs leads to their unavoidable aggregation. Since the behaviour of CNTs is different when they aggregate comparing to individual CNTs, lots of physical properties may be changed or degraded. Consequently, lots of efforts have been put into the dispersion of CNTs in various media (122). Unfortunately, there is no single solution, since each system is unique and has to be treated separately.

Finally, for potential industrial applications, CNTs should have outstanding, high-quality properties, even while produced on a large scale. Since the synthesis process affects the properties of CNTs, which in turn affects the properties of composite materials, our first goal was to optimize CVD CNTs synthesis to yield high-quality CNTs. Furthermore, we aimed

to optimize large quantity synthesis of CNTs with good control over their properties, particularly of their diameters and lengths, in order to facilitate their dispersion in the SU8 matrix, and hence obtain homogeneous composites with superior properties.

References

1. **D. Hull.** *An introduction to composite materials.* Cambridge : Cambridge University Press, 1981. Vol. Cambridge Solid State Science Series.
2. **F. L. Matthews and R. D. Rawlings.** *Composite materials: Engineering and science.* Cambridge : Woodhead publishing limited, 1994.
3. **D. D. L. Chung.** *Composite Materials: Science and Applications.* Second Edition. London : Springer-Verlag London Limited, 2010. Vol. Engineering Materials and Processes.
4. *SU-8: a photoresist for high-aspect-ratio and 3D submicron lithography.* **A. del Campo and C. Greiner.** 17, 2007, Journal of Micromechanics and Microengineering, p. R81.
5. *A comparative study of different thick photoresists for MEMS applications.* **E. Koukharenko, M. Kraft, G. J. Ensell and N. Hollinshead.** 16, 2005, Journal of Materials Science: Materials in Electronics, p. 741.
6. *Fabrication of microstructures with high aspect ratios and great structural heights by synchrotron radiation lithography, galvanofarming, and plastic moulding (LIGA process).* **E. W. Becker, W. Ehrfeld, P. Haggmann, A. Maner and D. Münchmeyer.** 1986, Microelectronic Engineering, Vol. 4, p. 35.
7. **G. Genolet.** *New photoplastic fabrication techniques and devices based on high aspect ratio photoresist.* thesis no. 2421. Lausanne : EPFL, 2001.
8. *Micromachining applications of a high resolution ultrathick photoresist.* **K.Y. Lee, N. La Bianca, S.A. Rishton, S. Zolgharnain, J.D. Gelorme, J. Shaw, and T.H.-P. Chang.** 6, 1995, Journal of Vacuum Science and Technology B, Vol. 13, p. 3012.
9. *UV-LIGA process for high aspect ratio structure using stress barrier and C-shaped etch hole.* **H. K. Chang and K. Y. Kim.** 84, 2000, Sensors Actuators A, p. 342.
10. *A novel method to fabricate complex three-dimensional microstructures.* **J.-Q. Liu, H.-W. Sun, L.-H. Li and D. Chen.** 12, 2006, Microsyst Technol, p. 786.
11. *Microfluidics for processing surfaces and miniaturizing biological assays.* **E. Delamarche, D. Juncker and H. Schmid.** 17, 2005, Adv. Mater., p. 2911.
12. **J. J. Licari, W. Crepeau and P. C. Crepeau.** *Electromagnetic Radiation Polymerization.* 3,205,157 U.S., 7 Sept 1965.
13. **S. I. Schlesinger.** *Epoxy Photopolymer Duplicating Stencil.* 3,826,650 U.S., 30 July 1974.
14. *The Discovery and Development of Onium Salt Cationic Photoinitiators.* **J. V. Crivello.** 1999, Journal of Polymer Science: Part A: Polymer Chemistry, Vol. 37, p. 4241.
15. **J. V. Crivello.** 828670 Belgium, 2 May 1974.
16. **J. V. Crivello.** *Method for Making Certain Halonium Salt Photoinitiators.* 3,981,897 US, 21 Sept 1976.
17. **J. V. Crivello and S. H. Schroeter.** *Photocurable Compositions and Methods.* 4,026,705 31 May 1977.
18. **J. V. Crivello.** *Cationically Polymerizable Compositions Containing Group Via Onium Salts.* 4,058,400 and 4,058,401 U.S., 15 Novem 1977.

19. *Ueber eine neue Klasse jodhaltiger, stickstofffreier organischer Basen.* **C. Hartmann and V. Meyer.** 1894, *Berichte der Deutschen Chemischen Gesellschaft*, Vol. 27, p. 426.
20. *Ueber die Jodonimbasen.* **C. Hartmann and V. Meyer.** 1894, *Berichte der Deutschen chemischen Gesellschaft*, Vol. 27, p. 502 and 1592.
21. **O. A. Ptitsyna, M. E. Pudeeva, N. A. Belkevich and O. A. Reutov.** 1965, *Doklady Physical chemistry: Proceedings of the Russian Academy of Sciences*, Vol. 163, p. 671.
22. **G. H. Smith.** 828 841 Belgium, 7 Nov 1975.
23. **G. H. Smith.** *Photopolymerizable compositions.* 4,394,403 U.S., 19 July 1983.
24. **E. R. Skarvinko.** *Photosensitive Patternable Coating Composition Containing Novolak Type Materials.* 4,237,216 US, 2 Dec 1980.
25. **J.D. Gelorme, R.J. Cox and S.A.R. Gutteriez.** *Photoresist composition and printed circuit boards and packages made therewith.* 4,882,245 U.S., 21 Nov 1989.
26. **L. M. Brown, J. D. Gelorme, J. P. Kuczynski and W. H. Lawrence.** *Method for patterning cationic curable photoresist.* 4,940,651 U.S., 10 July 1990.
27. **R. W. Angelo, J. D. Gelorme, J. P. Kuczynski, W. H. Lawrence, S. P. Pappas and L. L. Simpson.** *Photocurable epoxy composition with sulfonium salt photoinitiator .* 5,102,772 U.S., 7 April 1992.
28. *Epoxies: lithographic resists for thick film applications.* **N. La Bianca and J.D. Gelorme.** Ellenville Conf. : s.n., Nov. 1994, Proc. SPIE, Vol. 2423, p. 846.
29. *High aspect ratio optical resist chemistry for MEMs applications.* **N.C. La Bianca, J.D. Gelorme, K.Y. Lee, E. Sullivan and J. Shaw.** Chicago, USA : The Electrochem. Soc., 1995, Proceedings of the 4th International Symposium on Magnetic Materials, Processes, and Devices: applications to storage and microelectromechanical systems, Vol. 95-18, p. 386.
30. *EPON SU-8: a low-cost negative resist for MEMS.* **H. Lorenz, M. Despont, N. Fahrni, N. La Bianca, P. Vattiger and P. Renaud.** Barcelona, Spain : s.n., 1996, Proc. of the seventh Micromechanics Europe Workshop (MME '96), p. 32.
31. *High-aspect-ratio, ultrathick, negative-tone near-UV photoresist for MEMS applications.* **M. Despont, H. Lorenz, N. Fahrni, J. Brugger, P. Renaud and P. Vattiger.** Nagoya, Japan : s.n., 1997, Proc. of the 10th IEEE Int'l Workshop on Micro Electro Mechanical Systems, MEMS '97, p. 518.
32. **H. Lorenz.** *Nouvelles Technologies de Microstructuration de Type UV-LIGA et Fabrication de Composants Micromécaniques.* Lausanne : EPFL, 1998. Thesis no. 1770.
33. *Study on the postbaking process and the effects on UV lithography of high aspect ratio SU-8 microstructures.* **J. D. Williams and W. J. Wang.** 3, 2004, *J. Microlithogr. Microfabr. Microsyst.*, p. 563.
34. *A numerical and experimental study on gap compensation and wavelength selection in UV-lithography of ultra-high aspect ratio SU-8 microstructures.* **R. Yang and W. Wang.** 2, 2005, *Sensors and Actuators B: Chemical*, Vol. 110, p. 279.
35. *Use of SU-8 photoresist for very high aspect ratio x-ray lithography.* **A. L. Bogdanov and S. S. Peredkov.** 2000, *Microelectron. Eng.*, Vol. 53, p. 493.
36. *Comparison of high resolution negative electron beam resists.* **B. Bilenberg, M. Schøler, P. Shi, M. S. Schmidt, P. Bøggild, M. Fink, C. Schuster, F. Reuther, C. Gruetzner and A. Kristensen.** 4, 2006, *Journal of Vacuum Science and Technology B*, Vol. 24, p. 1776.
37. *Exploring the high sensitivity of SU-8 resist for high resolution electron beam patterning.* **A. Pépin, V. Studer, D. Decanini and Y. Chen.** 2004, *Microelectronic Engineering*, Vol. 73-74, p. 233.
38. *High resolution 100 kV electron beam lithography in SU-8.* **B. Bilenberg, S. Jacobsen, M.S. Schmidt, L.H.D. Skjolding, P. Shi, P. Bøggild, J.O. Tegenfeldt and A. Kristensen.** 2006, *Microelectronic Engineering*, Vol. 83, p. 1609.

39. *Proton beam writing: a progress review*. **J. A. V. Kan, A. A. Bettiol, K. Ansari, E. J. Teo, T. C. Sum and F. Watt.** 4, 2004, *Int. J. Nanotechnology*, Vol. 1, p. 464.
40. *Effect of low numerical-aperture femtosecond two-photon absorption on „SU-8... resist for ultrahigh-aspect-ratio microstereolithography*. **W. H. Teh, U. Dürig, U. Drechsler, C. G. Smith and H.-J. Güntherodt.** 2005, *Journal of Applied Physics*, Vol. 97, p. 054907.
41. *Three-Dimensional Spiral-Architecture Photonic Crystals Obtained By Direct Laser Writing*. **K. K. Seet, V. Mizeikis, S. Matsuo, S. Juodkakis and H. Misawa.** 5, 2005, *Advanced Materials*, Vol. 17, p. 541.
42. **P. K. Mallick.** *Fiber-Reinforced Composites: Materials, Manufacturing, and Design*. Second edition, revised and expanded. New York : Marcel Dekker, Inc., 1993. Vol. Mechanical Engineering.
43. **L. H. Sperling.** *Introduction to Physical Polymer Science*. Fourth Edition. Hoboken : John Wiley & Sons, Inc., 2006.
44. [Online] Hexion. [Cited: 7. 9. 2011.] <http://www.hexion.com/Products/TechnicalDataSheet.aspx?id=3603>.
45. *Fabrication and characterization of an SU-8 gripper actuated by a shape memory alloy thin film*. **I. Roch.** 2, 2003, *Journal of Micromechanics and Microengineering*, Vol. 13, p. 330.
46. *The characterization of thermal and elastic constants for an epoxy photoresist SU8 coating*. **R. Feng and R.J. Farris.** 2002, *Journal of Materials Science*, Vol. 37, p. 4793.
47. *Simple and low-cost fabrication of embedded microchannels by using a new thick-film photoplastic*. **L.J. Guérin, M. Bossel, M. Demierre, S. Calmes and Ph. Renaud.** Chicago, USA : s.n., June 1997, *Proceedings of the IEEE International Conference on Solid-State Sensors and Actuators (Transducers '97)*, p. 1419.
48. *Mechanical characterization of a new high-aspect-ratio near UV-photoresist*. **H. Lorenz, M. Laudon and P. Renaud.** 1998, *Microelectronic Engineering*, Vol. 41/42, p. 371.
49. [Online] [Cited: 7. 9. 2011.] <http://www.microchem.com/pdf/SU-8-table-of-properties.pdf>.
50. *SU-8: a low-cost negative resist for MEMS*. **H. Lorenz, M. Despont, M. Fahrni, N. La Bianca, P. Vettiger and P. Renaud.** 1997, *J. Micromech. Microeng.*, Vol. 7, p. 121.
51. *Terahertz time-domain spectroscopy of films fabricated from SU-8*. **S. Arscott, F. Garet, P. Mounaix, L. Duvallaret, J.-L. Coutaz and D. Lippens.** 3, 1999, *Electronics Letters*, Vol. 35, p. 243.
52. *High frequency transmission line using micromachined polymer dielectric*. **J. Thorpe, D. Steenson and R. Miles.** 1998, *Electronics Letters*, Vol. 34, p. 1237.
53. *Young's modulus and interlaminar fracture toughness of SU-8 film on silicon wafer*. **S. F. Hwang, J. H. Yu, B. J. Lai and H. K. Liu.** 2008, *Mechanics of Materials*, Vol. 40, p. 658.
54. *Influence of processing conditions on the thermal and mechanical properties of SU8 negative photoresist coatings*. **R. Feng and R.J. Farris.** 2003, *Journal of Micromechanics and Microengineering*, Vol. 13, p. 80.
55. *Stress engineering and mechanical properties of SU-8-layers for mechanical applications*. **J. Hammacher, A. Fuelle, J. Flaemig, J. Saupe, B. Loechel and J. Grimm.** 2008, *Microsyst. Technol.*, Vol. 14, p. 1515.
56. *Fabrication process of high aspect ratio elastic structures for piezoelectric motor applications*. **L. Dellmann, S. Roth, C. Beuret, G. Racine, H. Lorenz, M. Despont, P. Renaud, P. Vettiger and N. de Rooij.** Chicago, USA : s.n., 1997, *Proceedings of the IEEE International Conference on Solid-State Sensors and Actuators (Transducers '97)*, p. 641.
57. [Online] Momentive Specialty Chemicals Inc. [Cited: 5. 9. 2011.] <http://ww2.momentive.com/home.aspx>.
58. [Online] Gersteltec. [Cited: 5. 9. 2011.] <http://www.gersteltec.ch/su-8-Photoresists/>.

59. *High-aspect-ratio, ultrathick, negative-tone near-UV photoresist and its applications for MEMS.* **H. Lorenz, M. Despont, N. Fahrni, J. Brugger, P. Vettiger and P. Renaud.** 1, 1998, *Sensors and Actuators A: Physical*, Vol. 64, p. 33.
60. **S. Jiguet.** *Microfabrication d'objets composites fonctionnels en 3D et à haut facteur de forme, par procédés UV-liga et microstéréolithographie.* s.l. : EPFL, 2004. Thesis No 3096.
61. *Photoinitiated Cationic Polymerization.* **J. V. Crivello.** 1983, *Ann. Rev. Mater. Sci.*, Vol. 13, p. 173.
62. **J. P. Kennedy and E. Maréchal.** *Carbocationic Polymerization.* New York : Wiley, 1982. pp. 1-5.
63. *Photoinitiated Interfacial Cationic Polymerization.* **A. Hult, Scott A. MacDonald and C. G. Willson.** 10, 1985, *Macromolecules*, Vol. 18, p. 1804.
64. **G. A. Olah, G. K. S. Prakash and J. Sommer.** *Superacids.* New York : Wiley, 1985. pp. 7-8.
65. *Visible and Long-Wavelength Photoinitiated Cationic Polymerization.* **J. V. Crivello and M. Sangermano.** 3, 2000, *Journal of Polymer Science Part A: Polymer Chemistry*, Vol. 39, p. 343.
66. *Possibilities for promoting cationic polymerization by common sources of free radicals.* **A. Ledwith.** 1978, *Polymer*, Vol. 19, p. 1217.
67. *Photochemical and thermal cationic polymerizations promoted by free radical initiators.* **F. A. M. Abdoul-Rasoul, A. Ledwith and Y. Yagci.** 1978, *Polymer*, Vol. 19, p. 1219.
68. *Photothermally enabled lithography for refractive-index modulation in SU-8 photoresist.* **B. H. Ong, X. Yuan, S. Tao and S. C. Tjin.** 10, 2006, *Optics Letters*, Vol. 31, p. 1367.
69. *Thermal stability of SU-8 fabricated microstructures as a function of photo initiator and exposure doses.* **K. Lian, Z. Ling and C. Liu.** San Jose, CA. USA : s.n., 2003. *Photonics West 2003: Micromachining and Microfabrication, Proceedings of SPIE.* Vol. 4980, p. 208.
70. **J. V. Crivello.** *Thermally or Photochemically Induced Cationic Polymerization.* [ed.] James E. McGrath. *Ring-Opening Polymerization: Kinetics, Mechanisms, and Synthesis.* s.l. : American Chemical Society, 1985, Vol. ACS Symposium Series, 15, pp. 195-204.
71. **G. Odian.** *Principles of Polymerization.* Fourth Edition. Hoboken : Wiley-Interscience, A John Wiley & Sons, Inc., 2004.
72. **Y. Leterrier, M. Sangermano, H.-A. Klok, and E. Nouzille.** *Science and Technology of UV-induced Polymerization.* EPFL. 2008.
73. **J. P.-P. González.** *Thèse.* Toulouse : L'Université de Toulouse, 2008.
74. **C. Miko.** *Synthesis, characterization and macroscopic manipulation of carbon nanotubes.* Lausanne : EPFL, 2005. These No 3364.
75. *Crystalline Ropes of Metallic Carbon Nanotubes.* **A. Thess, R. Lee, P. Nikolaev, H. Dai, P. Petit, J. Robert, C. Xu, Y. H. Lee, S. G. Kim, A. G. Rinzler, Daniel T. Colbert, G. Scuseria, D. Tománek, J. E. Fischer and R. E. Smalley.** 1996, *Science*, Vol. 273, p. 483.
76. *Size Effects in Carbon Nanotubes.* **C.-H. Kiang, M. Endo, P. M. Ajayan, G. Dresselhaus and M. S. Dresselhaus.** 1998, *Physical Review Letters*, Vol. 81, p. 1869.
77. *Helical microtubules of graphitic carbon.* **S. Iijima.** 1991, *Nature*, Vol. 56, p. 354.
78. *Filamentous growth of carbon through benzene decomposition.* **A. Oberlin, M. Endo and T. Koyama.** 1976, *Journal of Crystal Growth*, Vol. 32, p. 335.
79. *High-resolution electron-microscopy of some carbonaceous materials.* **S. Iijima.** 1980, *Journal of Microscopy*, Vol. 119, p. 99.
80. *The first observation of carbon nanotubes.* **H. P. Boehm.** 1997, *Carbon*, Vol. 35, p. 581.
81. *Who should be given the credit for the discovery of carbon nanotubes?* **M. Monthieux and V. L. Kuznetsov.** 2006, *Carbon*, Vol. 44, p. 1621.

82. *O strukture ugleroda, obrazujućegosa pri termiceskom razlozenii okisi ugleroda na zeleznom kontakte.* **L. V. Radushkevich and V. M. Lukyanovich.** 1952, Zurn Fistic Chim, Vol. 26, p. 88.
83. *Structure of the carbon deposited from carbon monoxide on iron, cobalt and nickel.* **L. J. E. Hofer, E. Sterling and J. T. McCartney.** 1955, The Journ. of Phys. Chem., Vol. 59, p. 1153.
84. *The structure of graphite filaments.* **M. Hillert and N. Lange.** 1958, Zeitschrift für Kristallographie, Vol. III, p. 24.
85. *Electron Microscope Examination of the Microphysical Properties of the Polymer Cuprene.* **J. H. L. Watson and K. Kaufmann.** 1946, Journal of Applied Physics, Vol. 17, p. 996.
86. *Surface studies by scanning tunneling microscopy.* **G. Binnig, H. Rohrer, C. Gerber and E. Weibel.** 1982, Physical Review Letters, Vol. 49, p. 57.
87. *Atomic force microscope.* **G. Binnig, C. F. Quate and C. Gerber.** 1986, Physical Review Letters, Vol. 56, p. 930.
88. *Do single-walled carbon nanotubes occur naturally?* **K. J. MacKenzie, C. H. See, O. M. Dunens and A. T. Harris.** 2008, Nature Nanotechnology, Vol. 3, p. 310.
89. *Large scale synthesis of carbon nanotubes.* **T. W. Ebbesen and P. M. Ajayan.** 1992, Natur, Vol. 358, p. 220.
90. *Self-oriented regular arrays of carbon nanotubes and their field emission properties.* **S. Fan, M. G. Chapline, N. R. Franklin, T. W. Tomblor, A. M. Cassel and H. Dai.** 1999, Science, Vol. 283, p. 512.
91. *Solid C-60-a new form of carbon.* **W. Kratschmer, L. D. Lamb, K. Fostiropoulos and D. R. Huffman.** 1990, Nature, Vol. 347, p. 354.
92. **A. Kis.** *Mechanical Properties of Mesoscopic Objects.* Lausanne : EPFL, 2003. These No 2876.
93. *Cobalt-Catalyzed Growth of Carbon Nanotubes with Single-Atomic-Layer Walls.* **D. S. Bethune, C. H. Kiang, M. S. Devries, G. Gorman, R. Savoy, J. Vazquez and R. Beyers.** 1993, Nature, Vol. 363, p. 605.
94. *Elastic Properties of Carbon Nanotubes and Nanoropes.* **J. P. Lu.** 1997, Physical Review Letters, Vol. 79, p. 1297.
95. *The study of carbon nanotubules produced by catalytic method.* **V. Ivanov, J. B. Nagy, Ph. Lambin, A. Lucas, X. B. Zhang, X. M. Zhang, D. Bernaerts, G. Van Tendeloo, S. Amelinckx and J. Van Landuyt.** 1994, Chemical Physics Letters, Vol. 223, p. 329.
96. *Alumina and silica supported metal catalyst for the production of carbon nanotubes.* **N. Nagaraju, A. Fonseca, Z. Konya and J. B. Nagy.** 2002, Journal of Molecular Catalysis: A, Vol. 181, p. 57.
97. *Selective formation of carbon nanotubes over co-modified beta zeolite by CCVD.* **P. Ciambelli, D. Sannino, M. Sarno, A. Fonseca and J. B. Nagy.** 2005, Carbon, Vol. 43, p. 631.
98. *Optimization of catalytic production and purification of buckyutubes.* **A. Fonseca, K. Hernadi, J. B. Nagy, D. Bernaerts and A. A. Lucas.** 1996, Journal of Molecular Catalysis: A, Vol. 107, p. 159.
99. *Synthesis of Individual Single-Walled Carbon Nanotubes on Patterned Silicon Wafers.* **J. Kong, H. T. Soh, A. M. Cassell, C. F. Quate and H. J. Dai.** 1998, Nature, Vol. 395, p. 878.
100. *Electric-Field-Directed Growth of Aligned Single-Walled Carbon Nanotubes.* **Y. G. Zhang, A. L. Chang, J. Cao, Q. Wang, W. Kim, Y. M. Li, N. Morris, E. Yenilmez, J. Kong and H. J. Dai.** 2001, Applied Physics Letters, Vol. 79, p. 3155.
101. *An Enhanced CVD Approach to Extensive Nanotube Networks with Directionality.* **N. R. Franklin and H. Dai.** 2000, Advanced Materials, Vol. 12, p. 890.
102. *Controlled low-temperature growth of carbon nanofibres by plasma deposition.* **S. Hofmann, B. Kleinsorge, C. Ducati and J. Robertson.** 2003, New Jour. of Phys., Vol. 5, p. 153.
103. *Carbon nanotube electronics.* **P. Avouris.** 2002, Chemical Physics, Vol. 281, p. 429.

104. *Electronic structure of chiral graphene tubules.* **R. Saito, M. Fujita, G. Dresselhaus and M. S. Dresselhaus.** 1992, Applied Physics Letters, Vol. 60, p. 2204.
105. *Interference and interaction in multi-wall carbon nanotubes.* **C. Schonenberger, A. Bachtold, C. Strunk, J.-P. Salvetat and L. Forro.** 1999, Applied Physics A, Vol. 69, p. 283.
106. *Nanomechanics of carbon tubes: Instabilities beyond the linear response.* **B. I. Yakobson, C. J. Brabec and J. Bernholc.** 1996, Physical Review Letters, Vol. 76, p. 2511.
107. *Elastic and shear moduli of singlewalled carbon nanotube ropes.* **J.-P. Salvetat, G. A. D. Briggs, J.-M. Bonard, R. R. Bacsa, A. J. Kulik, T. Stockli, N. Burnham and L. Forro.** 1999, Physical Review Letters, Vol. 82, p. 944.
108. *Bending and buckling of carbon nanotubes under large strain.* **M. R. Falvo, G. J. Clary, R. M. Taylor, V. Chi, F. P. Brooks, Jr. S. Washburn and R. Superfine.** 1997, Nature, Vol. 389, p. 582.
109. *Exceptionally high young's modulus observed for individual carbon nanotubes.* **M. M. J. Treacy, T. W. Ebbesen and J. M. Gibson.** 1996, Nature, Vol. 381, p. 678.
110. *Elastic modulus of ordered and disordered multiwalled carbon nanotubes.* **J.-P. Salvetat, A. J. Kulik, J.-M. Bonard, G. A. D. Briggs, T. Stockli, K. Metenier, S. Bonnamy, F. Beguin, N. A. Burnham and L. Forro.** 1999, Advanced Materials, Vol. 11, p. 161.
111. **K. Lee.** *Surface-Bound Nanostructures: Mechanical and Metrological Studies.* Lausanne : EPFL, 2008. Thesis No 4042.
112. *Catalytically grown carbon nanotubes of small diameter have a high young's modulus.* **B. Lukic, J. W. Seo, R. R. Bacsa, S. Delpeux, F. Beguin, G. Bister, A. Fonseca, J. B. Nagy, A. Kis, S. Jeney, A. J. Kulik and L. Forro.** 2005, Nano Letters, Vol. 5, p. 2074.
113. *Elastic modulus of multi-walled carbon nanotubes produced by catalytic chemical vapour deposition.* **B. Lukic, J. W. Seo, E. Couteau, K. Lee, S. Gradecak, R. Berkecz, K. Hernadi, S. Delpeux, T. Cacciaguerra, F. B'eguine, A. Fonseca, J. B. Nagy, G. Csanyi, A. Kis, A. J. Kulik and L. Forro.** 2005, Applied Physics A, Vol. 80, p. 695.
114. *Theoretical-studies of icosahedral c60 and some related species.* **A. J. Stone and D. J. Wales.** 1986, Chemical Physics Letters, Vol. 128, p. 501.
115. *Carbon nanotubes.* **S. Iijima.** 11, 1994, MRS Bulletin, Vol. 19, p. 43.
116. *Carbon nanotubes.* **T. W. Ebbesen.** 1994, Annual Reviews of Material Science, Vol. 24, p. 235.
117. *Structural flexibility of carbon nanotubes.* **S. Iijima, C. Brabec, A. Maiti and J. Bernholc.** 1996, Journal of Chemical Physics, Vol. 104, p. 2089.
118. *Carbon Nanotubes--the Route Toward Applications.* **R. H. Baughman, A. A. Zakhidov and W. A. de Heer.** 2002, Science, Vol. 297, p. 787.
119. **Z. Cui.** *Nanofabrication: Principles, Capabilities and Limits.* New York : Springer Science+Business Media, 2008.
120. *Growth of nanotubes for electronics.* **J. Robertson.** 1-2, 2007, Materials today, Vol. 10, p. 36.
121. *Dissolution of small diameter single-wall carbon nanotubes in organic solvents.* **J. L. Bahr, I. T. Mickelson, M. J. Bronikowski, R. E. Smalley and J. M. Tour.** 2001, Chemical Communications, Vol. 2, p. 193.
122. *Functionalization of single-walled carbon nanotubes.* **A. Hirsch.** 2002, Angew. Chem. Int. Ed., Vol. 41, p. 1853.

Chapter 3

Experimental techniques

This Chapter presents as an overview of the experimental techniques and technological pathways used in this work to obtain CNTs-SU8 composites.

The first part of this Chapter describes the experimental techniques related to CNTs, including: the choice and preparation of catalyst supports and precursors, the processes of CNTs synthesis, and, finally, the CNTs post-synthesis treatment. The second part of this Chapter focuses on preparation pathways and characterisation of the three types of CNTs-SU8 composites. The third part of this Chapter deals with processing of CNTs-SU8 composites with particular stress on the photolithographic, inkjet printing and screen-printing processes.

3.1 CNTs

3.1.1 Supported catalyst precursor for CVD MWCNTs synthesis

3.1.1.1 Catalyst support

Preparation

The commercially available Calofort U calcite powder (Specialty Minerals Lifford) and mechanically treated Fluka 21060 calcite (Sigma-Aldrich Chemie GmbH) were used as catalyst support. Mechanical treatment was carried out in a planetary ball mill (Retsch Ball Mill Type PM 100; Schieritz & Hauenstein AG) with zirconium oxide balls (3mm \varnothing , Schieritz & Hauenstein AG) in distilled water (Aqua purificata Ph. Eur. Reactolab SA). More precisely, the zirconium oxide impregnated jar container having 250 ml volume was firstly filed with

270 g of zirconium oxide balls, then with 28.5 g of calcite powder and finally with 100 ml of distilled water. The treatment was performed at 400 rpm and run continuously for 12 h.

Characterization

X-ray Powder Diffraction (XRPD) is the most commonly used tool to determine the composition of powders, because each crystalline solid has its unique characteristic XRPD pattern. For obtaining crystallographic phase content we used XRPD (Kristalloflex 805, Siemens, using a copper electrode with $\lambda_{x1}=1.54060 \text{ \AA}$ and $\lambda_{x2}=1.54443 \text{ \AA}$). The XRD peak broadening allows us to determine the size of the primary crystallite using the Scherrer equation (Eq. 3.1) (1). The instrumental peak broadening was determined using a calcium carbonate powder with a large crystal size ($>1 \mu\text{m}$, Fluka).

$$d_{\text{XRD}} = \frac{K\lambda_x}{\beta_{x_p} \cos(\theta)} \quad (3.1)$$

where K is a numerical factor referred to as the crystallite-shape factor and frequently assumed to be equal to 1, λ_x is the X-ray wavelength, and β is the peak width at half intensity, calculated using $\beta = \sqrt{\beta_{\text{sample}}^2 - \beta_{\text{Fluka}}^2}$.

Transmission electron microscope (TEM). Philips CM 20 operated at 200 kV was used in conventional mode to measure the primary particle sizes of calcite powders (Calofort U and ground Fluka). In order to prepare samples for TEM imaging, calcite powders were firstly dispersed in the water by sonication. A drop of obtained suspension was put on a copper grid covered with holey carbon film.

Laser diffraction particle size analyzer (Malvern Mastersizer) uses the technique of laser diffraction based on the principle that particles passing through a laser beam will scatter light at an angle that is directly related to their size: large particles scatter at low angles, whereas small particles scatter at high angles. The secondary particle size distribution of the calcite powders was measured by dynamic light scattering (DLS) in water with using Malvern Mastersizer S, with the following parameters, material's density $\rho = 2.71 \text{ g/cm}^3$, material's refracting index $n = 1.596$ (2).

The specific surface areas for the precipitates, S_{BET} (m^2/g), were obtained by nitrogen absorption using Brunauer-Emmett-Teller (BET) approach (3) and using BET-measuring device, Gemini 2375, from Micromeritics.

Scanning electron microscopy (SEM) (high-resolution and low-kV SEM at small working distances FEI XL30-SFEG and high-resolution field emission SEM Zeiss NVision 40 CrossBeam) were used to assess surface morphology of calcite powders.

3.1.1.2 Catalyst precursor

Preparation

The catalyst was synthesized using the following procedure. Metal salts (cobalt(II)nitrate hexahydrate 99,999% metals basis, Aldrich and iron(III)nitrate nonahydrate 99.99+%, Sigma-Aldrich) were mixed in stoichiometric amounts corresponding to Fe to Co ratio of 2:1, dissolved in distilled water and subsequently added in a previously prepared suspension of CaCO₃ powder in distilled water. The total amount of metals corresponds to 5 wt% relative to the net mass of metals and calcium carbonate. The precipitation of Fe and Co salts was induced by instantaneously adding of weak base to the solution. As a base we used ammonia, ammonium hydrogen carbonate (99%, Aldrich) or triethylamine.

Drying of supported catalyst

We employed two drying processes of the supported catalyst: by heat treatment or by freeze drying. The suspension of CaCO₃ particles and Fe, Co salts is dried under vigorous stirring on a hot plate on temperature of 100°C (hereafter as dry on a hot plate). The second process, freeze drying, is based on the sublimation of the solvent. The suspension is frozen by dropping into liquid nitrogen. Once collected, it is subsequently placed in homemade freeze drying chamber. According to the phase diagram of water, sublimation of ice occurs by raising the temperature while the vapour pressure remains below 5 mbar.

Characterization

TEMs (Philips CM 20 and Philips CM 300, the latter used in high-resolution mode operated at 300 kV) were used to determine size and shape of catalyst precursor and its relation with support.

Energy dispersive X-ray spectroscopy (EDX) is an analytical method which was used for the chemical characterization of supported catalyst precursors.

3.1.2 CVD MWCNTs synthesis

3.1.2.1 Furnace

For CVD synthesis of MWCNTs we used a tube-type heating furnace containing 80 mm OD quartz tube and having a 750-mm long heating zone. The furnace was set in the so-called *fixed-bed* operating conditions, meaning:

- before synthesis, typically 3 g of supported catalyst were placed directly in the middle zone of the quartz tube (without quartz boat);

- the ends of the quartz tube were then connected to the gasses inlet and outlet, respectively;
- during the typical 2-hours-long synthesis, quartz tube remains in the horizontal position, as at the beginning of the synthesis. In the middle of the synthesis, after 1 h, the quartz tube was manually rotated by 180° in order to facilitate exposure of catalyst to the carbon source.

3.1.2.2 Synthesis conditions

After the gasses inlet and outlet were connected to the quartz tube's ends, the quartz tube (containing in its middle part supported catalyst) was heated from room temperature to 640°C. After 2 h, the heating was switched off and the furnace was left for about half of a day to cool down to the room temperature. Afterwards, the connections for gasses were removed from the ends of the quartz tube. Subsequently, the quartz tube was taken out of the furnace and turned aside in order to collect synthesis product in a beaker.

All CVD MWCNTs synthesis processes performed in this work were carried out in a flow of acetylene and nitrogen, with flow rates of 45 L/h and 50 L/h, respectively.

3.1.3 CNTs post-synthesis treatment

Purification: Raw MWCNTs are purified by 1 day stirring in non-oxidizing acid ($\approx 1M$ hydrochloric acid, HCl), filtered and washed with distilled water. CNTs dispersion in diluted HCl was accompanied with remarkable CO₂ gas release, what indicates that CaCO₃ did not decompose during the CNTs synthesis.

Drying: We employed two drying processes of purified CNTs: by heat treatment or by freeze drying. The wet CNTs were dried overnight by heating on 100°C. The second process, freeze drying, is based on the sublimation of the solvent. The wet CNT were dilute with water and shortly sonicated. The suspension was subsequently frozen by dropping into liquid nitrogen and placed in homemade freeze drying chamber. CNTs dried by heating were used for preparation of composites 1 (see below), while freeze dried CNTs were used for preparing composites 2 (see below).

Characterization of CNTs after drying: TEM (Philips CM 20) was used for MWCNTs characterization and for determination of their diameters.

Functionalization (used only for preparation of Composites 1F - see below): MWCNTs surface is functionalized with -COOH groups by 8 h stirring in diluted mixture of sulphuric and nitric acids (volume ratio 3:1).

Cutting (used only for preparation of composites 2C, see below, especially designed for inkjet printing applications, but tested also for photolithography): CNTs grinding experiments were carried out in a planetary ball mill apparatus (Retsch Ball Mill Type PM 100). In the case of planetary ball milling, which is usually used for mechanical alloying of materials in powder form in dry environment, compact layers of powders are often formed on the balls and the jar walls (4). Therefore, we choose to grind CNTs in the liquid environment. We choose low energy ball milling and a ball from zirconium oxide with a 3 mm radius to avoid the influence of increase of balls temperature which is increasing with ball diameter and rotational speed. For example, from the study of Kwon *et al.* can be derived that 3 mm iron balls with a rotational speed from 200 rpm to 500 rpm may have a temperature from about 30°C to 50°C while 5 mm steel balls under the same speeds may have approximately two times higher temperature (5). The capacity of the zirconium oxide impregnated jar container was 250 ml. We have processed standard batches consisting of 3 mm zirconium oxide balls, distilled water (Aqua purificata Ph. Eur. Reactolab SA) and CNTs in 40:20:1 mass ratio in 250 ml zirconium oxide-lined jars. Volume of liquid in the milling jar was kept constant, as well. The diameter of zirconium oxide balls (Schieritz & Hauenstein AG) were chosen to be 3 mm also in order to increase balls' surface and to maximize the number of contacts between balls and CNTs and enhance grinding efficiency. Milling times were varied between 1 to 6 h and the speeds between 200 to 600 rpm.

Characterization of CNTs after cutting: The effect of ball milling on the CNTs length was analysed by Scanning Electron Microscopy (SEM, Philips XL 30 FEG operated at 30 kV). The length distributions of CNTs upon grinding were derived from SEM micrographs. CNTs characterization was performed by Transmission Electron Microscopy (TEM, Philips CM20 operated at 200 kV), while the tube ends morphology of ball milled CNTs was studied by high resolution TEM (HR TEM, Philips CM300).

Raman spectroscopy: The quality of CNTs upon cutting was studied by Raman spectroscopy. It was performed using the 488 nm line of an Ar ion laser (Koheras GmbH) as an excitation source. The laser beam was focused onto the sample by a long working distance objective (20X Mitutoyo Plan Apo SL Infinity-Corrected). The same objective was used to collect the Raman backscattered light which was then coupled to an optical fibre connected to the input of a MicroHR spectrometer (HORIBA Jobin Yvon). A holographic notch filter (Kaiser Optical Systems) was placed between the fibre end and the spectrometer entrance slit to block out the Rayleigh scattered light. All of the spectra were collected at ambient temperature. The spectra were recorded using the SynerJY software (HORIBA Jobin Yvon) with the cosmic-spikes-removal routine enabled. Three consecutive acquisitions for each spectrum were performed in order to filter out the cosmic spikes. Several spectra at different positions were recorded for each sample in order to minimize the effects of structural inhomogeneities. The spectra were then normalized to the G-band ($\sim 1580 \text{ cm}^{-1}$) peak intensity and averaged.

3.2 CNTs-SU8 composites

3.2.1 Composites 1

Preparation

At room temperature, Epon™ Resin SU8 (manufactured by Hexion Specialty Chemicals) is in the form of solid chunks with sizes up to one centimetre. Dissolution of SU8 is often very slow due to the large size of SU8 solid pieces. Therefore, in order to facilitate dissolving of SU8, we have mechanically ground SU8 until powder. In order to obtain fine powder with more uniform particle size, the ground SU8 powder was sieved through colanders with 500 µm, 300 µm and finally with 150 µm mesh. In this way we had SU8 powder of size less than 150 µm.

In order to find solvents that can dissolve SU8, we have tested eight solvents: gamma-butyrolacton (GBL), propylene glycol methyl ether acetate (PGMEA), methyl-ethyl ketone (MEK), acetone, benzene, 1-methyl-2-pyrrolidone (1M2P), N,N-Dimethylacetamide (NNDMAA), and distilled water. From tested solvents, five were found to be suitable for SU8.

For the composites preparation, CNTs were first dispersed in solvents followed by 48h vigorous stirring. The quantity of MWCNTs in composites 1 was fixed at 5 wt% in respect to SU8. Afterwards, small quantities of fine SU8 powder were added regularly under vigorous stirring. After dissolving all SU8, the photoinitiator (PI) for the polymerisation from the family of triarylsulfonium salt (Dow Chemical) was added to the suspension of CNTs in SU8 and solvent, in order to obtain UV photosensitive composite materials. The schema of preparation of CNTs-SU8 composites 1 is given in Figure 3.1.

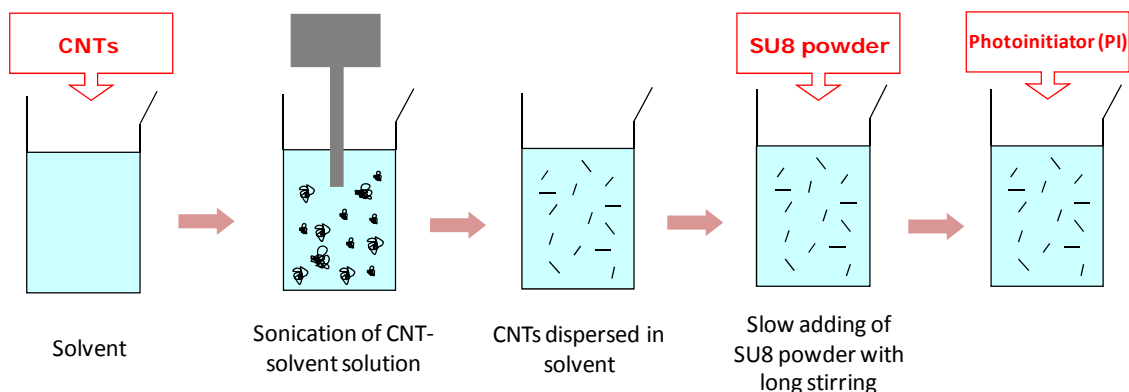


Figure 3.1: Schematic drawing of preparation of CNTs-SU8 composites 1.

All the Composites 1 were prepared by using the above-presented procedure. Two types of CNTs were implemented: (a) purified and dried by heating and (b) purified, functionalized and dried by heating. In the following, the first and the second group of

composites 1 will be referred to as composites 1N (non-functionalized CNTs) and composites 1F (functionalized CNTs), respectively.

3.2.1.1 Characterization of composites 1

(A) Samples preparation for indentation testing and microtome

The first step in sample preparation was pouring composite into suitable molds, followed by soft baking on a hot plate at 95°C for 24 h in order to evaporate the solvent. Polymerization was achieved by thermal cross-linking by heat treatment at 150°C. For the nanoindentation measurements, samples were finally polished to the final thickness of more than 100 µm - to avoid substrate effect in indentation. The non-reinforced SU8 sample (control) was prepared using the same procedure.

Samples characterization

Nanoindentation: Since SU8 is mostly used in the form of thin films in the field of microengineering, we focused on mechanical properties of the SU8 surface. The Young's modulus (E_Y) and hardness (H) were deduced from nanoindentation measurements using XP (NanoInstrument Inc.) in the conjunction with the specialized software, TestWorks®4. The technique is based on pushing an indenter tip into the tested material, where both elastic and plastic deformations occur. When the indenter is withdrawn from the material, the elastic deformation is recovered. The loading and unloading force on the sample can be plotted as a function of displacement into the sample's surface. This kind of plot, usually called load-displacement curve, allows the determination of E_Y and H of the material using the Oliver-Pharr theory (6). The XP indenter used in this measurement operates in the continuous stiffness measurement (CSM) mode. A Berkovich-type three-sided diamond pyramidal tip is used. The force and displacement resolutions are 50 nN and 0.02 nm, respectively. The maximal displacement was 2000 nm. The mechanical uniformity of the samples was tested by 25 indents for each material.

Microtomy: In order to characterize homogeneity of the composites, thin slice (40-80 nm) were prepared by room temperature ultra microtome (Diatome diamond knife ultra 45°). Microtome slice were placed on the TEM grid and afterwards studied by TEM (Philips CM20 operated at 200kV).

The structural characterization of the composites was performed on the fractured samples by **HR SEM**.

(B) Samples preparation for other characterizations

Composites were spin-coated on float glass wafer cleaned by oxygen plasma treatment. To evaporate solvent we perform soft baking on a hot plate at 95°C. Afterwards samples were exposed to UV light to induce polymerization, which was completed by a

post-exposure baking at 95°C. The photo-patterned structures were then developed and lifted-off by dipping in PGMEA solution. Finally, lifted samples were hard bake at 150°C.

Samples characterization

Impedance: Composites homogeneity was characterized by impedance spectroscopy using a precision impedance analyser (Agilent 4294A) operating in the frequency range from 40 Hz to 110 MHz. The samples had area about 2 cm².

Resistivity as a function of temperature: Resistivity was measured in a standard 4-point configuration using Keithley K2400 current sources and K2182 nanovoltmeters. The sample current was adjusted during the measurement in order to minimize Joule heating. Current reversal was used to counter thermoelectric or other parasitic effects. The resistivity measurements were carried out in a He bath cryostat in the 4.2-300 K range.

Thermoelectric power as a function of temperature: For the measurement of the Seebeck coefficient we glued two ends of the sample on SMD chip resistances, which were used as heaters, mounted on thick copper wires at a distance 1 mm from each other. AN E-type differential thermocouple was glued to the two heating elements in order to determine the temperature difference. Different currents were applied to the heaters, and two Keithley K2182 nanovoltmeters measured the thermal voltage on the sample and the differential thermocouple. Linearity was verified and the thermoelectric power of the Au-sample-Au thermocouple was determined from the slope of the thus obtained curve. It must be noted that at signal levels our samples produce, it was necessary to correct measured values for the absolute thermoelectric power of the measuring wires. The latter was determined by measuring the thermopower of a known standard, a high purity lead sample. Data evaluation was done using the statistical package R. The thermoelectric power measurements were carried out in a He bath cryostat in the 4.2-300 K range. The thermopower was measured in a closed cycle refrigerator with minimum temperature 12 K. Cooling rate was 0.5 K/min, controlled by a Lakeshore 331 controller.

3.2.2 Composites 2

Preparation

Preparation of CNTs-SU8 composites 2 is a simple 3-steps process which is given as schematically drawing in Figure 3.2. Firstly, CNTs and surfactant were added in SU8 solution. Subsequent sonication with the use of a high-energy sonication finger yielded well dispersed CNTs in the SU8-solvent-surfactant solution. At the end, as the 3rd step, PI was added into the previously obtained CNTs suspension to obtain the final formulation of the photosensitive composite.

In order to disperse CNTs in SU8 solution, several different surfactants having different concentrations were tested [MM1]. The best results were obtained for two of them, herein referred to as surfactant 1 and 2. This technology is now the subject of patent application. Therefore, more technological details concerning the procedure for dispersing CNTs can be obtained from the **Technology Transfer Office** of EPFL.

Moreover, we also tested two types of PIs, *i.e.* in the liquid and solid state. The PI containing mixed Triarylsulfonium hexafluoroantimonate salts in propylene carbonate, referred to as “old PI”, is the most often used PI for SU8 cross-linking. Therefore we also decided to use it for CNTs-SU8 composites. Since the overall curing process is mostly affected by the PI and its nature (see Chapter 2), we decided to test the photolithographic process of CNTs-SU8 composites with the recently developed PI, Tris-[4-(4-acetylphenylsulfanyl)-phenyl]-sulfonium-tris (trifluoromethanesulfonyl) methide, referred to as “new PI”, which has not been used for processing of SU8 resin until now. The particularity of this new PI is that it is available in solid form without any additional solvents and does not contain antimony, which is a toxic chemical element. This latter feature might be very important for some applications, in particular bio-medical ones.

Any modification of dispersion and any interaction of PI with other components in the composite may easily influence and even prevent polymerization. With the liquid “old PI” polymerization was possible with surfactant 1. With the solid “new PI”, polymerization was possible with both surfactants, 1 and 2.

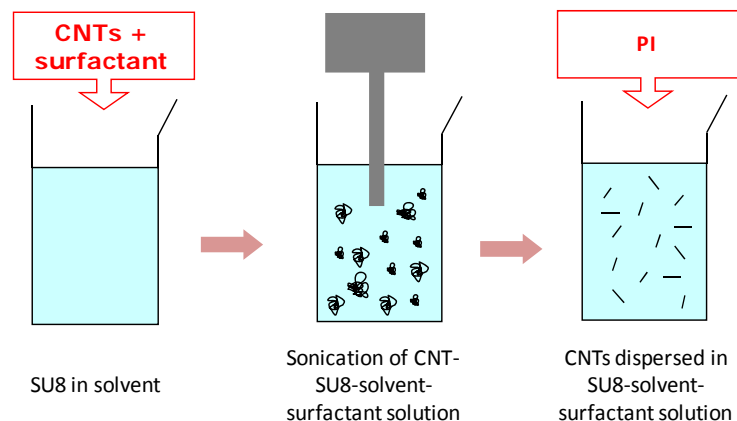


Figure 3.2: Schematic drawing of preparation of CNTs-SU8 composites 2.

Especially for the inkjet printing applications, composites 2 were prepared with cut CNTs and these composites are in this thesis denoted as composites 2C (meaning composites 2 with cut CNTs).

3.2.2.1 Characterization of composites 2

(A) Samples preparation for microtome and thermal conductivity

The first step in sample preparation was pouring composite into suitable moulds, followed by soft baking on a hot plate at 95°C over 24 h in order to evaporate solvent. Polymerization was achieved by thermally cross-linked by heat treatment at 150°C.

Microtomy: In order to characterize homogeneity of the composites, thin slice (40-80 nm) were prepared by room temperature ultra microtome (Diatome diamond knife ultra 45°). Microtome slice were placed on the TEM grid and afterwards studied by TEM (Philips CM20 operated at 200kV).

The structural characterization of the composites was performed on the fractured samples by **HR SEM**.

Thermal conductivity as a function of temperature: Figure 3.3 shows the experimental setup for measurements of thermal conductivity of small samples. The heater was connected to one end of the sample, whereas the differential thermocouple was positioned on the sample to determine the heat-flow-induced temperature gradient. The biggest challenge is the precise determination of the latter since although the power dissipated in the heater can be measured with precision, there are several parallel paths for the heat to be dissipated. To minimize the error, we connect a stainless steel slab between the sample and the heat sink, and measure the temperature gradient on it as well.

Assuming that the heat flow is same across the sample and the reference (stainless steel), we can determine the thermal conductivity of the sample, κ_{sample} , with the formula:

$$\kappa_{sample} = \kappa_{steel} \cdot \frac{\Delta T_{steel}}{\Delta T_{sample}} \cdot \frac{G_{steel}}{G_{sample}} \quad (3.2)$$

where G_{steel} and G_{sample} denote the respective geometrical factors. This method gives much more reliable results than the direct κ_{sample} calculation based on the heat dissipated in the resistor, which combines the measured temperature gradient with the sample's geometry:

$$\kappa_{sample} = \frac{\Delta Q}{\Delta t} \frac{1}{A} \frac{x}{\Delta T} \quad (3.3)$$

The reason is that the electrical connections to the resistor form a parallel heat conduction pathway, thus leading to a wrongly inflated thermal conductivity of the sample. This can lead to incorrect data, as illustrated by the two figures given in Figure 3.4.

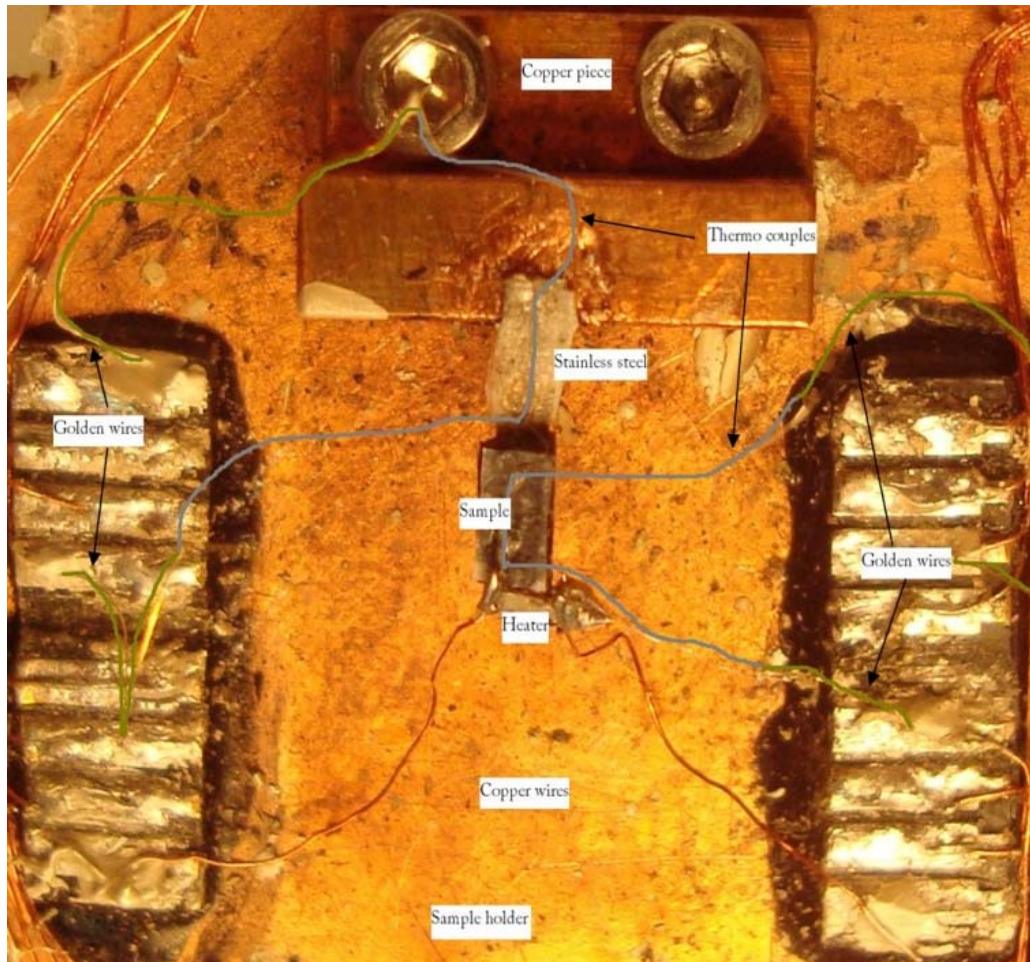


Figure 3.3: Photograph of the experimental setup for thermal conductivity measurements of small samples.

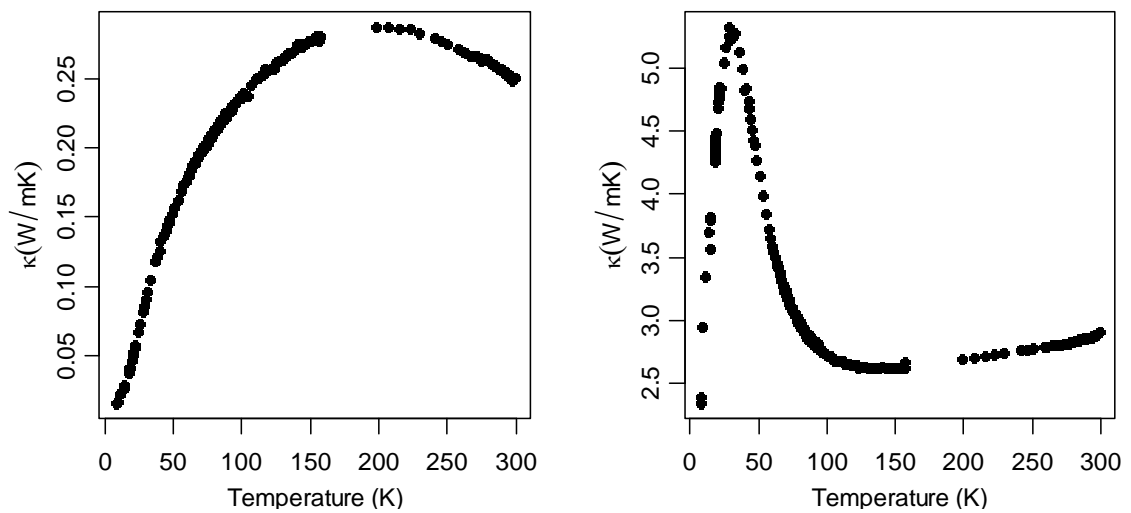


Figure 3.4: The left panel shows the thermal conductivity of a CNTs-SU8 composite with non-oriented tubes calculated by the differential method. The right panel shows the thermal conductivity obtained for the same dataset, using the direct calculation. The huge

apparent increase around 30 K is due to the increase of heat loss *via* the copper leads of the heater resistor.

(B) Samples preparation for other characterizations

Composites were deposited on glass slides by pulling the “doctor blade” over the substrate surface (Fig. 3.5 (a)). Glass slides were previously cleaned by sonication (sonication bath). Firstly, cleaning was performed in ethanol, then, in acetone, and finally in isopropanole, which was removed by a stream of nitrogen from the nitrogen gun. To evaporate the solvent, we performed soft baking on a hot plate at 95°C (Fig. 3.5 (b)). Afterwards samples were polymerized, either by heat treatment at about 150°C or by exposure to UV light, followed by subsequent post-exposure baking at 95°C in order to complete the UV light-initiated polymerization (Fig. 3.5 (c)). In the first case, obtained samples were thin films deposited on glass with typical dimensions 2×1 cm (Fig. 3.5 (d)). In the second case, the photo-patterned structures were developed and lifted-off by dipping in PGMEA solution. Finally, lifted samples were hard baked at 150°C.

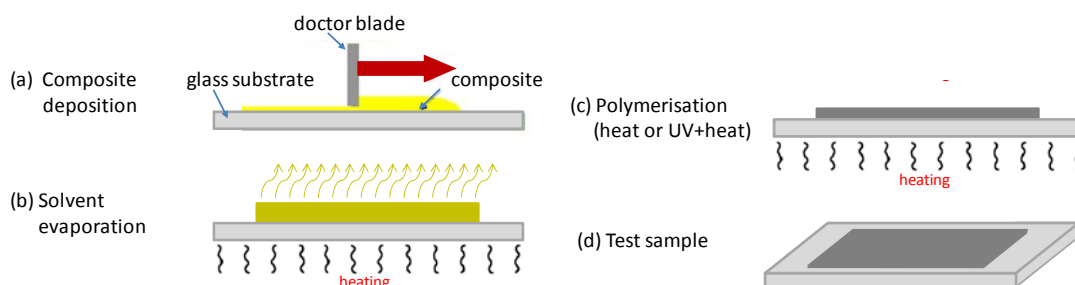


Figure 3.5: Schema of the sample preparation for characterization of composites 2.

Samples characterization

Nanoindentation: As already mentioned, SU8 is mostly used in the form of thin films in numerous domains of microengineering. Therefore, we focused on mechanical properties of the SU8 deposits on flat surfaces. The Young’s modulus was deduced from nanoindentation measurements carried out on the same apparatus and in the same way like explained above for nanoindentation of the composites 1.

Four Point Resistivity Measurements: In order to measure the electrical properties of CNTs-SU8 composites 2, we did 4-point resistivity measurement using the setup shown schematically in Figure 3.6. In this way, resistivity can be measured by passing a current through the outer probes and measuring induced voltage between the inner probes.

In order to observe if there is some change in the CNTs network rearrangement during the standard photolithography processing steps (see following), 4-point resistivity measurement was done before and after SU8 polymerization. We also performed 4-point measurement for the composites 2, which were prepared with and without PI. All these measurements were carried out at room temperature.

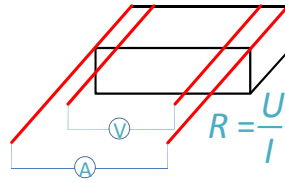


Figure 3.6: Scheme of the setup for four-point resistivity measurements.

Resistivity as a function of temperature: Resistivity was measured as previously explained for composites 1.

3.2.3 Composites 3

Preparation

For preparation of composites 3, CVD grown oriented CNTs were used in the as-grown form of “carpets” having ~250 μm height (the “carpet’s” height corresponds to the CNTs length). Impregnation of the “carpet” by SU8 was obtained using traditional drop-wise method at room temperature by adding SU8 (GM1040 from Gersteltec) containing 40 wt% of SU8 and 60 wt% of solvent. Subsequently, impregnated carpets were soft-baked at 95°C over at least 10h, followed by baking for 2h at 120°C to 150°C in order to cross link SU8.

Characterization

Structural homogeneity of samples, and distribution and alignment of CNTs in the composites 3 were characterised by SEM, HR SEM and TEM. The samples for TEM were prepared by room temperature ultra microtome (Diatome diamond knife ultra 45°).

Thermal conductivity as a function of temperature: The thermal conductivity was measured in the direction of the CNTs alignment and perpendicular on it. The measurement was performed as previously explained for the composites 2.

Resistivity as a function of temperature: Resistivity was measured in the direction of the CNTs alignment and perpendicular on it, in the same way as previously explained for composites 1.

3.3 Processing techniques

3.3.1 Photolithography

Photolithography process for patterning of composites 2 and 2C was carried out in Clean room at Centre for Micronanotechnology (CMI, EPFL, Lausanne) as follows:

- 1- substrate wafer (quartz, float and Pyrex) cleaning by oxygen plasma etching (Tepla 300)
- 2- spin-coating on manual coater for negative resists (Sawatec LMS200)

- 3- soft baking at 95°C on hot plate (Accu-Plate)
- 4- UV-exposure (Süss MA6/BA6, double side mask aligner and bond aligner)
- 5- post-exposure bake at 95°C on hot plate (Accu-Plate)
- 6- development first in PGMEA bath, followed by isopropanol (IPA) bath and drying (Plade Solvent, photolithography wet bench)

Stripping has additional processing steps. Before composite spin-coating, sacrificial layer (special product provided by Gersteltec) was deposited on (previously cleaned) wafer by spin coating (Süss RC8). After subsequent soft baking (Süss RC8), standard photolithographic steps (from 2 to 6) were carried out. In the last step, development, composite structures were lifted off from the supporting wafer, due to desolving of sacrificial layer. Free standing structures were carefully collected from the solution, deposited between two previously cleaned glass slides and then baked in order to dry them.

In order to optimize some processing steps (soft baking, UV-exposure and post-exposure bake) we needed to perform following measurements:

Thermogravimetric analysis (TGA): This technique measures the change in weight of a sample corresponding to the change of temperature or to the isothermal process. In our study we focussed on the thermal process which consisted of heating from room temperature to 95°C (what is the standard SB temperature for SU8 formulations with GBL as a solvent), isothermal process on 95°C for 30 minutes, followed by heating up to 600°C. All TGA measurements (Mettler Toledo TGA/SDTA 851e) were performed in air.

Differential scanning calorimetry (DSC): This method yields peaks related to endothermic and exothermic transitions and shows changes in heat capacity. The DSC method consists in supplying energy at a varying rate to the sample and the reference, but in such a way that their temperatures stay equal. The output of DSC measurements is the supplied energy as a function of temperature. The peaks enables finding of the glass transition temperature, T_g , which is taken as the temperature at which half of the increase in heat capacity has occurred. Moreover, the areas under the peaks can be directly related to the enthalpic changes quantitatively.

Ultraviolet and visible (UV-vis) absorption spectroscopy: This method measures the absorption as a function of the wavelength in the ultraviolet-visible spectral region.

3.3.2 Inkjet printing

Inkjet printing of composites 2C was carried out at LMIS1 lab (EPFL).

Inkjet Setup: The inkjet console consisted of a JetDrive III inkjet controller, a pneumatics console (CT-PT-01), and the JetServer software interface (Microfab Inc., Plano,

TX). All equipment was obtained from and integrated by Microfab's European distributor: Altatech Semiconductor (Montbonnot-Saint-Martin, France).

Inkjet Nozzle: The CNT-SU8 was printed with an 80 μm diameter microfab inkjet nozzle (MJ-AT-01-080, Microfab Inc.). The nozzle was heated to 70 $^{\circ}\text{C}$ to reduce the viscosity of the SU8 sufficiently for printing. A back pressure of 1.4 psi was applied using the pneumatics console to prevent the CNT-SU8 meniscus from wetting the entire surface of the nozzle. Before and after use, inkjet nozzles were cleaned in an ultrasonic bath while filtered acetone was aspirated through the nozzle. Before use, the inkjet nozzle was dried by passing a constant stream of filtered air through it from the pneumatics console.

Waveform: A biphasic trapezoidal waveform was used for the SU8 printing. The following time and voltage coordinates denote the 6 key vertices of the waveform [μs , V]: [0,0] [3,80] [12,80] [18,-70] [58,-70] [61,0]. Printing was stable at frequencies from 1 – 10 Hz, as well as 50, 100, and 200 Hz.

Patterning: Collections of single droplets and lines were printed by moving a substrate under the fixed inkjet head. The X and Y motions were provided by two motorized Thorlabs MTS50/M stages (ThorLabs GmbH, Germany). The stages were moved at a constant speed of 1 mm/sec, with droplet spacing being controlled by the print frequency. In order to print lines, the stage was heated to 100 $^{\circ}\text{C}$ to enhance solvent evaporation and prevent axial liquid transport along the line, which resulted in the formation of beads. Glass microscope slides were used as a printing substrate. All slides were rinsed with isopropanol and dried in an N₂ stream to ensure cleanliness. Overhead transparencies were cleaned under an N₂ stream and used as flexible plastic substrates (3M Inkjet printing transparency film CG3460, 3M Suisse SA, Rüschtikon, Switzerland). The inkjet printed SU8 patterns (droplets and lines) were imaged using a Nikon Eclipse L200 microscope under 5x, 10x, or 20x magnification (Nikon AG, Switzerland). Images were acquired using a Nikon Digital Sight DS-5M camera and Nikon Digital Sight DS-L1 viewing screen (Nikon AG, Switzerland).

Characterization

Contact Angle Measurements: Contact angle measurements were performed by micropipetting 1 to 5 μL volumes of the desired liquid sample onto a glass microscope slide. The edge of the droplet was imaged in diascopic illumination with a machine vision camera (Toshiba Teli CS8630Ci CCD camera, Tokyo Electronic Industry Co. Ltd., Japan) with a 5x lens. Using a frame grabber, images were saved as .bmp files for subsequent analysis. Over 12 measurements were made for each liquid, and the contact angles measured did not vary with the hand-pipetted volume. The contact angles were measured from the .bmp files using the DropSnake contact angle measurement plugin for ImageJ (7). The plugin uses a B-spline snake approach (active contours) in which the user defines the initial contour of the droplet. Through supervising student researchers, the measurement variability between

users was estimated at up to 3°. The measurement errors calculated by the individual researcher analyzing the contact angles in this work were consistently under this value.

Sheet resistance: For our one layer inkjet-printed structures, the sheet resistivity was determined by the 4-contact Van der Pauw method, since the samples could be considered as two-dimensional (i.e. much thinner than wide). The measurement was done on circular drops using a probe station with 4 metallic needles, at first touching the native surface, then polishing the sample surface to expose the bulk. About ten samples were measured in top-contact geometry for each CNTs concentration.

3.3.3 Screen printing

The screen printing process was carried out using a homemade setup and as well a commercial machine for standard fabrication (LPM lab at EPFL; the machine model: Aurel C900 Mod; the machine type: semi-automatic, with optical positioning and manual adjustment knobs). Standard screen printing was performed on an alumina substrate with composites 2 containing 3 wt%, 5 wt% and 10 wt% of CNTs in SU8 under different squeegee force and printing speed. In order to print on nonstandard substrates the homemade set-up was used. To be precise, rod coating of composite pastes through the stencil pattern was carried out on glass slides, on commercial Xerox paper (80 g/m²) or on absorbent fabric (standard cleaning tissue in chemistry labs). Printed composite layers were dried on 90°C, followed by SU8 cross linking (by UV exposure and baking at 120°C or by thermal treatment at 150°C).

References

1. **H. P. Klug and L. E. Alexander.** X-ray Diffraction Procedures. 2nd ed. New York: Wiley-Interscience, 1974. pp 687-707.
2. Particle Size Distribution Measurement from Millimeters to Nanometers and from Rods to Platelets. **P. Bowen.** 5, 2002, Journal of Dispersion Science and Technology, Vol. 23, p. 631.
3. *Adsorption of Gases in Multimolecular Layers.* **S. Brunauer, P. H. Emmett and E. Teller.** 1938, J. Am. Chem. Soc., Vol. 60, p. 309.
4. In situ thermal observation of explosive compound-formation reaction during mechanical alloying. **M. Atzmon.** 1990, Phys. Rev. Lett., Vol. 64, p. 487.
5. *Ball temperatures during mechanical alloying in planetary mills.* **Y. S. Kwon, K. B. Gerasimov and S. K. Yoon.** 2002, Journal of Alloys and Compounds, Vol. 346, p. 276.
6. *An improved technique for determining hardness and elastic modulus using load and displacement sensing indentation experiments.* **W. C. Oliver and G. M. Pharr.** 1992, Journal of Materials Research, Vol. 7, p. 1564.
7. *A Snake-Based Approach to Accurate Determination of Both Contact Points and Contact Angles.* **A.F. Stalder, G. Kulik, D. Sage, L. Barbieri and P. Hoffmann,.** 1-3, 2006, Colloids And Surfaces A: Physicochemical And Engineering Aspects, Vol. 286, p. 92.

Chapter 4

Optimization of properties of CVD-synthesised CNTs

4.1 Optimization and insight into the CVD synthesis of CNTs

Over the last two decades, CNTs have become a subject of extensive research because of their very attractive electrical, mechanical and thermal properties (1). However, even today, the detailed mechanism of their growth is not fully understood. Elucidating the growth of CNTs still remains the challenge and necessity for the scientific community and the industry. To increase industrial applications of CNTs, the mass production of high-quality CNTs (with the precise control of their diameter, chirality and length) is urgently needed. One of the techniques which are considered as suitable for such large scale production is CVD (see Chapter 2). The CVD synthesis method uses the decomposition of a carbon-containing gas over a supported catalyst. Large scale production of CVD CNTs for possible wider applications can be made from powders of supported catalysts, which consist of a high-surface-area material that serves as a support on which an active catalyst is deposited.

Since the CVD synthesis enables large-scale production of CNTs, CVD-synthesised CNTs are often considered to be the best candidates for reinforcement of polymers (2), with the aim to improve their electrical, thermal and mechanical properties. However, the properties of CNTs strongly depend on their quality. Moreover, better mechanical properties of CVD-synthesised CNTs are observed for CNTs with smaller diameter (3). In fact, CNTs produced by CVD with diameters below 11 nm reveal the elastic modulus close to the “ideal” value of 1TPa, which was found for CNTs synthesized using the arc-discharge method

(3). Therefore, one of the aims of this work was to tune the CVD CNTs synthesis towards high structural quality and enhancement of CNTs fraction with smaller diameter.

Over the last twenty years, many studies have been made on the different aspects of the CNTs growth. Theoretical studies of Bolton's group showed that the catalysts' metal cluster size determines the diameter and quality of tubes (4). The characteristics of CNTs critically depend also on the synthesis temperature (5). Moreover, the nature (composition) of metal clusters determines the chirality distribution of tubes (6) and the type of growth (either 'bottom' or 'tip'), throughout the diffusion rate of carbon and carbon-metal adhesion, respectively. Lots of studies were done in order to determine factors that define CNTs diameters. In particular, it was shown that CNTs' diameters depend on the catalyst size (7; 8) and/or on the flow rate of hydrocarbon (9). The CNT growth and quality are strongly influenced by the catalyst chemical state, morphology and catalyst-substrate interaction (10). The role of precursor gases on the catalyst behaviour and activity was studied as well (9; 7; 11). Due to development of the characterization techniques in recent years, especially electron microscopy, more studies have been made on catalyst dynamics during synthesis (12) and state of the catalyst during tube growth (13). Majority of these experimental studies were done on flat substrates as a support, facilitating the study on size and structure of catalyst precursors by means of surface experimental techniques.

Supported catalysts suitable for mass CVD synthesis are usually in powder form. It is generally considered that catalyst metal nanoparticles are generated on the support by in-situ reduction of the appropriate metal salts, which serve as the catalyst precursor. The preparation of such a precursor is usually from a solution containing transitional metal salts, base and support (typically alkaline or rare earth alkaline metal oxide) in a powder form or by sol-gel methods (14). In other words, the catalyst precursor is prepared through 'wet' chemical process by nucleation and precipitation from solution. Under such preparation conditions we may have very large variation in size and chemical composition of the catalyst precursor depending on small changes of process parameters. This fact is very important since size and composition of the precursor directly determine size (and composition in the case of bimetallic catalysts) of the final catalyst formed in situ. This means that to be able to control the quality and diameter of mass produced CVD tubes, we need to understand the process of precursor formation and how the support's nature influences this process. Most of the modern surface techniques cannot be applied to the study of the precursor for supported powder catalysts because of the support's particulate nature, required for large scale production, and the low content of metal (typically a few weight percent with respect to the support). That is one of the main reasons why there is a lack of studies on the real CVD catalyst precursor preparation with powder support.

Therefore, in this work, we studied the influence of support's nature on structure and size of the catalyst precursor. Additionally, we investigated how small changes in some parameters (temperature, basic environment, duration of the treatment and drying process)

influence the formation of the CVD catalyst precursors on the powder support. As a support, we used CaCO_3 , since it was previously shown in our group that this support enables simple, one-step purification process with non-oxidizing acid and thus, prevents CNTs from damage of and surface modifications in purification steps (14). Quite a number of studies have shown that bimetallic catalysts exhibit higher reactivity towards CNTs synthesis (15). Furthermore, a previous study in our group demonstrated that for iron-cobalt bimetal system, the iron to cobalt stoichiometric ratio of 2:1 showed the highest activity (16). Consequently, in this work, we studied: (i) the CaCO_3 catalyst support, (ii) the methods for preparation of the Fe-Co catalyst precursor, (iii) the obtained catalyst precursor size and morphology, and (iv) their correlation with the catalysts drying methods (*i.e.* freeze drying and drying on a hot plate). Moreover, we finally characterized the obtained CNTs to assess their diameter distributions and quality, as well as the correlation of CNTs diameters with catalyst precursor sizes. We observed significant variations of sizes and structures of the catalyst precursor and tried to understand the reasons of these phenomena.

4.1.1 Support

The main function of CaCO_3 is to serve as a support for the catalyst precursor, thus providing separation of the latter in the particulate form (instead of films on the flat substrate supports). The catalyst precursor is prepared through ‘wet’ chemical process by nucleation and precipitation from solution. Generally, it is preferred that these processes occur on the surface of the calcite support. However, the non-prepared calcite surface is not really suitable for docking iron or cobalt. In fact, for the CaCO_3 polycrystalline powder, the usually exposed facets are neutral, like (1 0 4), shown in Figure 4.1 (a). Clearly, these facets are not good docking surfaces. The best docking surfaces of calcite are the completely positively or negative charged surfaces (0 0 1), that are shown in Fig. 4.1 (b) and (c), respectively. Looking at the unit cell, there is also another such polar surface: (-1 0 2). Nevertheless, this surface is less preferred than (0 0 1) because of the tilted carbonate. Analogous situation occurs also for the polar facet (0 1 2). All the other calcite surfaces are less polar and not good for docking metals. Unfortunately, the preferred charged (0 0 1) surface for docking is not usually exposed, and thus, has to be “created”, *e.g.* by grinding.

Therefore, we ground Fluka calcite powder to “create” polar surfaces suitable for docking of metals. We also wanted to test if the creation of polar CaCO_3 surfaces plays a significant role in catalyst precursor precipitation onto calcite powders. To this end, we used additional calcite powder (Calofort U), without any mechanical modification of its surface. Thus, we used two calcite powders, with different surface properties: ground Fluka and Calofort U. To eliminate the influence of the specific surface area (S_{BET} – determined *via* the BET method), Fluka calcite, with an intrinsically low specific surface area ($S_{\text{BET}} < 1 \text{ m}^2/\text{g}$), was ground under such conditions that both calcite powders revealed comparable specific surface areas. Thus, the final S_{BET} values were of $\sim 18 \text{ m}^2/\text{g}$ for both calcite powders.

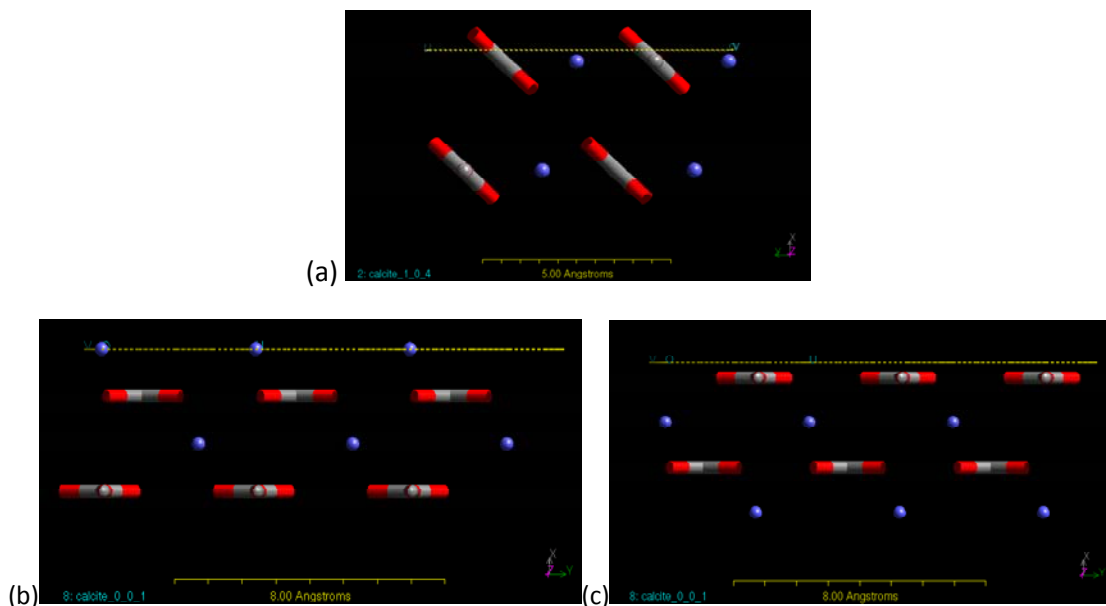


Figure 4.1: The usually exposed (1 0 4) surfaces of calcite are neutral (a). The completely positively Ca^{2+} - terminated (b), or completely negatively CO_3^{2-} -terminated (c), charged (0 0 1) surface of calcite. The yellow dotted lines on the top of each figure indicate surface, while Ca, C and O atoms are marked in blue, white and red, respectively.

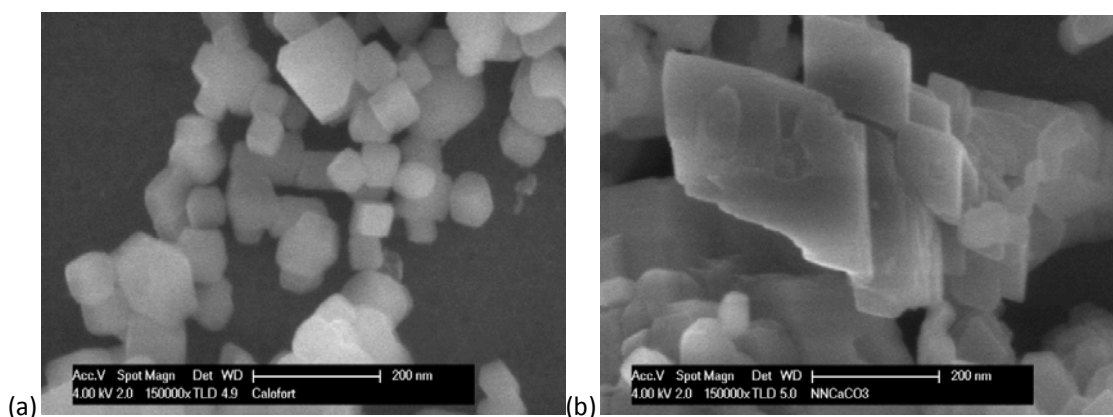


Figure 4.2: HR SEM micrographs of two calcite powders: Calofort U (a) and ground Fluka (b), pointing to the different surface morphologies: smooth for Calofort U (a), and with steps and kinks for ground Fluka (b).

The HR SEM micrographs of Calofort U calcite (Fig. 4.2 (a)) and ground Fluka calcite (Fig. 4.2 (b)) can give information about powders surface structure and shape. Calofort U with more regular shape and surface did not show defects observable with this technique. By grinding the Fluka calcite we introduce local surface distortion visible in HR SEM micrographs as defects, steps and kinks (Fig. 4.2 (b)). This distortion of the lattice and extended defects represent localized charge imbalances and highly reactive sites. In addition, probably therefore surface of ground Fluka in aqueous solution hydrate

($\text{CaCO}_3 \cdot n\text{H}_2\text{O}$) what makes it unstable under the first electron beam exposition, while Calofort U appears to be rather stable under the same conditions.

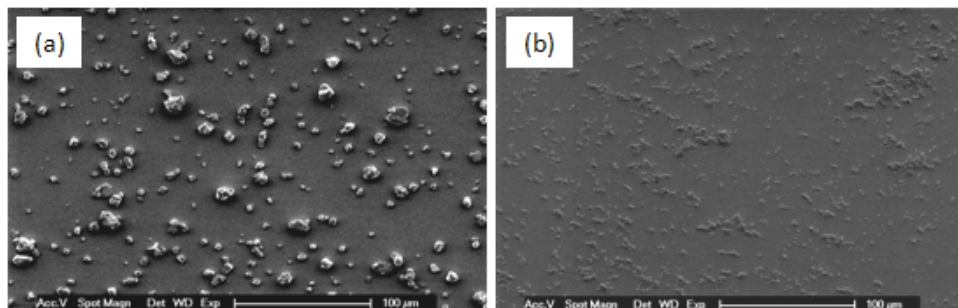


Figure 4.3: Scanning electron micrographs of the Fluka calcite: 'as received' (a) and after grinding in a planetary mill (b). The size reduction by grinding can be seen.

Figure 4.3 shows that the particle size has been efficiently reduced by grinding. The primary particle sizes of the calcite powders were derived from TEM micrographs. Example TEM micrographs are shown as inserts in Fig. 4.4. As can be seen in Figure 4.4(a), the ground Fluka CaCO_3 had average particle sizes around 50 nm, with a narrow size distribution. In contrast, as can be seen in Fig. 4.4 (b), Calofort U calcite had primary particle sizes slightly larger than Fluka powder, with a broader size distribution.

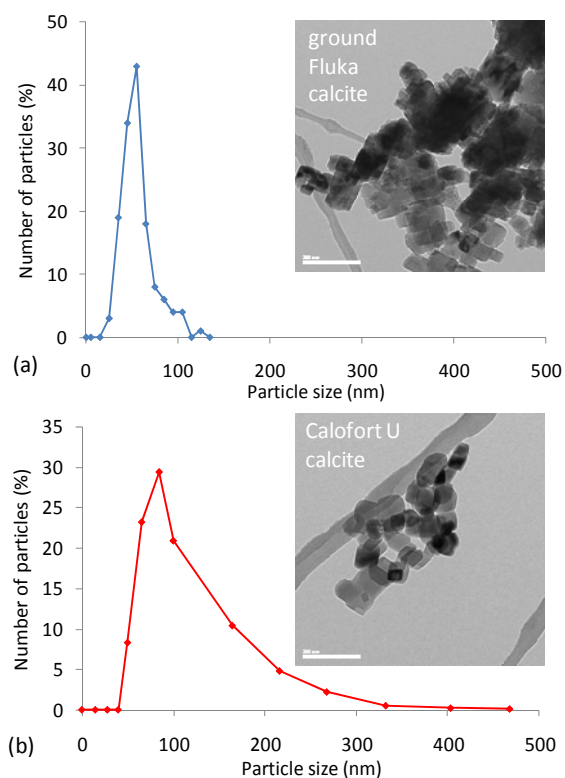


Figure 4.4: The primary particle size distribution of the calcite powders: ground Fluka CaCO_3 (a) and Calofort U (b), ((b) was reproduced from the MSDS of Calofort U calcite). The inserts show example TEM micrographs of the corresponding calcite powders.

The secondary particle size distribution of calcite powders was measured in aqueous suspension by DLS. The first measurement was done immediately after preparation. The particle size distribution of the calcite powder agglomerates (depicted by the red curves in Fig. 4.5) indicates that the Calofort U calcite has wider distribution (Fig. 4.5 (b)) than the ground Fluka calcite (Fig. 4.5 (a)). The second measurement, performed five minutes after the first one, showed that the size distribution changed for the Calofort U calcite, while it remained almost the same for the ground Fluka calcite (depicted by the blue curves in Fig. 4.5). Results show that the ground Fluka calcite powder in aqueous suspension is stable against further agglomeration, while the Calofort U calcite is unstable under the same conditions. Such differences might influence catalyst precipitation and the catalyst-precursor-preparation process longer than few minutes.

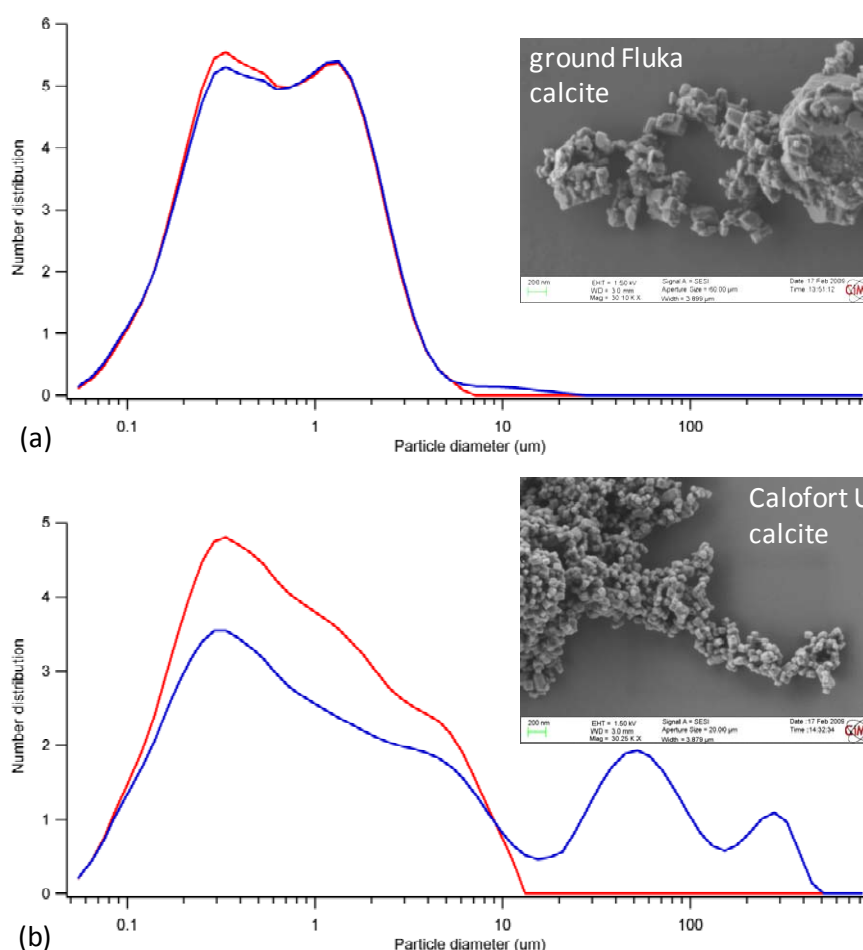


Figure 4.5: Secondary particle size distribution obtained by laser diffraction for the calcite powders: ground Fluka (a) and Calofort U (b). The inserts show HR SEM micrographs of the corresponding agglomerates. The size distributions measured immediately and five minutes after sample preparation are depicted by red and blue curves, respectively. Results suggest that the ground Fluka calcite is rather stable against further agglomerations (a). In contrast, Calofort U calcite reveals a strong tendency towards the further agglomeration (b).

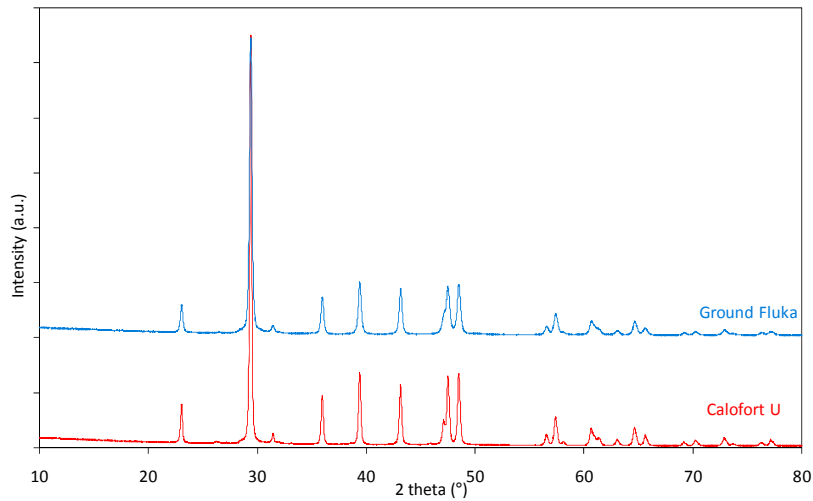


Figure 4.6: The XRD spectra of the calcite powders used as a support. The results for the ground Fluka and Calofort U, are depicted by blue (upper) and red (lower) curves, respectively.

	Crystallite size by Scherrer method [nm]	Crystallite size by Williamson-Hall method [nm]	Strain [%]
grund Fluka calcite	42.0	57.7	0.66
Calofort U calcite	62.9	69.8	0.24

Table 4.1: Crystallite size in (1 0 4) direction calculated by Scherrer method and volume - averaged crystallite sizes and strains obtain from the XRD data by Williamson-Hall method. The big difference in the strain values for two calcites points to big differences in their local deformations. These local deformations are particularly high for the ground Fluka calcite. Distortions present in the ground Fluka calcite are also indicated by a difference in volume-averaged crystallite size (the second column) and primary crystallite size in (1 0 4) direction (the first column).

Powder XRD was used to characterize the crystallographic structure, crystallite size (grain size), and preferred orientation in powdered solid samples (17). XRD data obtained for the calcite powders is shown in Figure 4.6 and point to the calcite structure for both powders. The Scherrer equation (Eq. 3.1) was used to determine the mean crystallite size of the primary crystallite of calcite in the characteristic (1 0 4) direction (see Fig. 4.1 (a)). The following mean crystallite sizes were found: 42.0 nm for the ground Fluka calcite and 62.9 nm for the Calofort U calcite (see Table 4.1). Volume-averaged crystallite sizes and strain, measured by the Williamson-Hall method (17) are respectively 57.7 nm and 0.66% for ground Fluka calcite, and 69.8 nm and 0.24% for Calofort U calcite. Since strain scales with the deformation, our results show that the ground Fluka calcite was significantly locally deformed by grinding. In contrast, marked distortions of the crystal lattice were not observed for the Calofort U calcite.

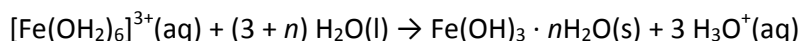
4.1.2 Supported catalyst precursor and synthesized CNTs

4.1.2.1 Fe and Co salts in calcite aqueous suspensions

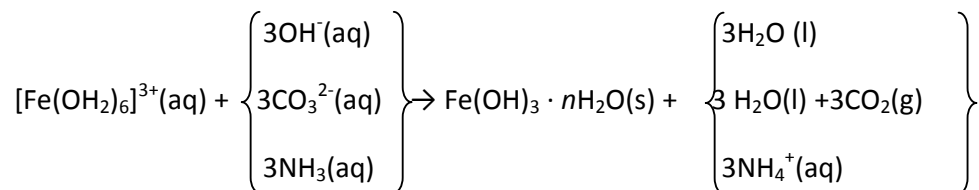
Chemistry of Fe and Co salts in aqueous solution is considered as extremely complex due to an enormous number of possible compounds which can form (18). Any additional component, like support and base, would complicate even more the already complex system by introducing additional uncertain reaction products. However, even under such complex conditions, it is necessary to precisely control the precipitates.

In this work, we mixed aqueous nitrates of Fe and Co with the calcite aqueous suspension and simultaneously added base in quantities required for: either neutral pH or pH 10, in the case when ammonia and ammonium hydrogen carbonate or triethylamine were used, respectively. Simultaneous adding of base is essential to avoid calcite dissolution, because the water solution of iron nitrate is acidic (19). The addition of base and metal salts to the calcite suspension did not result in the visible release of carbon dioxide due to possible calcite decomposition.

It is well known that with an increase of pH, the aqua-ions of metals that have basic or amphoteric oxides generally undergo polymerization and precipitation (20). The most common example of inorganic polymers are complex polymers formed by Fe(III) ions, which, in aqueous solutions, exists as octahedral hexaaqua ions $[\text{Fe}(\text{OH}_2)_6]^{3+}$ (18). These complexes appear as monomers, dimers and linear polymers, containing about 90 Fe atoms (20). In solution with $\text{pH} > 4$, at room temperature, this complexes precipitate as gelatinous hydrous oxides:



The precipitated polymers are often of colloidal dimensions (20). These amorphous polymers very slowly crystallize to form stable mineral forms. The study of interactions of calcite in various salt solutions showed that when aqueous solution of iron salt interacts with a carbonate, the calcite surface become less smooth due to the deposition of amorphous iron compounds (21). More general behaviour of Fe octahedral hexaaqua ions, $[\text{Fe}(\text{OH}_2)_6]^{3+}$, is the formation of rusty-brown hydroxide precipitate which is forming in the presence of base, carbonate and ammonia:



Situation is equally complex for the Co salt as for the presented Fe ones, due to their almost equal ionic radius. Co salts in calcite aqueous suspension may form various compounds (22), but in Cobalt (II) aqueous solutions predominantly formed species is the

pink octahedral hexaaqua cobalt (II) ion which precipitate in the form of hydroxide. In the excess of $\text{NH}_3(\text{aq})$, some hydroxide may dissolve because ammonia substitutes as a ligand forming yellow-brown octahedral $[\text{Co}(\text{NH}_3)_6]^{2+}(\text{aq})$ ion, which is unstable and easily becomes red-brown $[\text{Co}(\text{OH}_2)_6]^{3+}(\text{aq})$ (since air oxidises Co(II) to Co(III)). Study of adsorption of divalent metals on calcite showed that 100% of Co could not be absorbed onto the calcite surface under the studied conditions (pH from 7 to 10) and that maximal Co adsorption onto calcite surface was about $\sim 75\%$ at pH8.5 (22).

It appears extremely difficult to simultaneous precipitate both Fe and Co at the same pH value in the calcite aqueous suspension. The recent study of Dr. Stéphane Casimirus showed that the best results were obtained with triethyleamine as the base (unpublished data of the former member of our research team). Even in this study, however, a slight partial phase separation was noticed in the form of clear pink liquid traces, which indicated the presence of Co hydrated ions (Co complex with $6\text{H}_2\text{O}$ molecules in the solution). Rarely observable, opaque pink liquid indicated CoCO_3 precipitates onto the CaCO_3 surface, which was formed due to the $\text{Co}^{2+} - \text{Ca}^{2+}$ exchange. The other possible complexes of Co with $-\text{OH}$ and H_2O , usually recognisable by typical strong azure blue colour, were not observed.

4.1.2.2 Obtained precipitates, their characterisation and synthesized CNTs

Without support: The catalyst precursors were firstly synthesized without support in order to observe whether the presence of the latter would influence the formation, size and composition of CNTs. Figure 4.7 shows the catalyst precursor prepared by drying on a hot plate under the continuous stirring (a), and freeze dried catalyst precursor without support (b). The latter were amorphous, what was confirmed by lack of diffraction pattern (insert in Fig. 4.7 (b)).

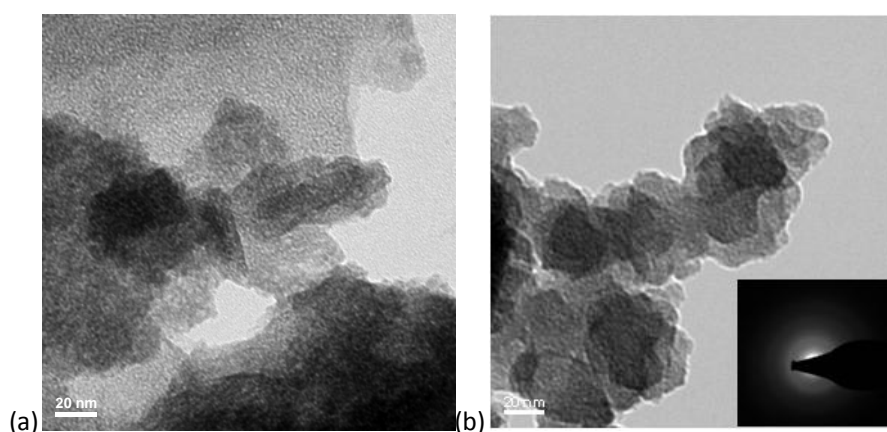


Figure 4.7: TEM micrographs of the catalyst precursor without support obtained by drying on a hot plate (a) or by freeze drying (b). The insert in (b) is the diffraction pattern of the sample in micrograph (b) which shows amorphous structure of freeze dried catalyst precursor.

With support: Seven support catalyst precursors, prepared with different supports, bases, metal salts and drying processes, are all listed in Table 4.2. In order to compare the

catalyst precursor with corresponding synthesised CNTs, the size and the stoichiometry of the catalyst precursor are indicated together with the percent of corresponding CNTs up to 11 nm and 15 nm.

Cat.	Calcite support	base	Fe salt	Co salt	Drying	Catalyst precursor size	Average diameter of CNTs (nm)	CNTs % with diameter up to	
								11 nm	15 nm
1	Calofort U	ammonia	nitrate	acetate	hot plate	few nm - few 100s nm	12.8	47	73
2	Calofort U	NH ₄ HCO ₃	nitrate	nitrate	freeze drying	~50 nm to ~1 μm	15.2	31	70
3	ground Fluka	ammonia	nitrate	acetate	hot plate	few 10s nm - few 100s nm	13.9	35	65
4	ground Fluka	ammonia	nitrate	acetate	freeze drying	few 10s nm - few 100s nm	13.7	24	56
5	ground Fluka	NH ₄ HCO ₃	nitrate	nitrate	4h 50°C+ freeze drying	few 10s nm - few 100s nm	13.3	40	68
6	ground Fluka	NH ₄ HCO ₃	nitrate	nitrate	freeze drying	few nm - few 10s nm	11.5	52	75
7	ground Fluka	3 ethylamine	nitrate	nitrate	freeze drying	≥1 μm	13.3	35	68

Table 4.2: The table of supports, bases, metal salts and the drying methods of seven studied supported catalyst. The catalyst precursor sizes vary from nanometres to microns, while corresponding CNTs have average diameters from 11.5 nm to 13.9 nm (measured for *ca.* 1300 CNTs per sample). Clearly, the size of the catalyst precursor does not determine the diameter of corresponding CVD synthesised CNTs. The highest fraction of CNTs with small diameters (up to 11 nm) was obtained for the catalyst 6, but very similar value was also obtained for the catalyst 1.

Catalyst 1

Calofort U calcite was used as support for the precursor precipitation from Fe nitrate and Co acetate induced by ammonia. Sample was dried on a hot plate under the continuous stirring. The obtained catalyst precursor appears as non-amorphous with particle sizes, which vary from few nanometres up to few hundreds of nanometres (Fig. 4.8 (a)). Most of the support's surface was not covered with the catalyst precursor. The CNTs produced by this supported catalyst precursor can be seen in Figure 4.8 (b). Catalyst can be seen in Figure

4.8 (c), as well as amorphous carbon which was covering surface of some CNTs in the form of additional layer on their surface.

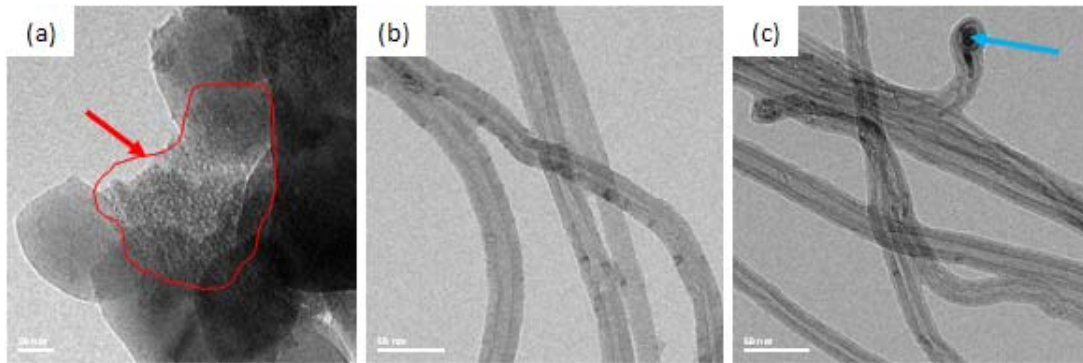


Figure 4.8: TEM micrographs of the catalyst 1 precursor (marked in red) (a), corresponding CNTs (b) and their catalyst, marked by blue arrows (c). Scale bars are: 20 nm (a) and 50 nm (b), (c).

Catalyst 2

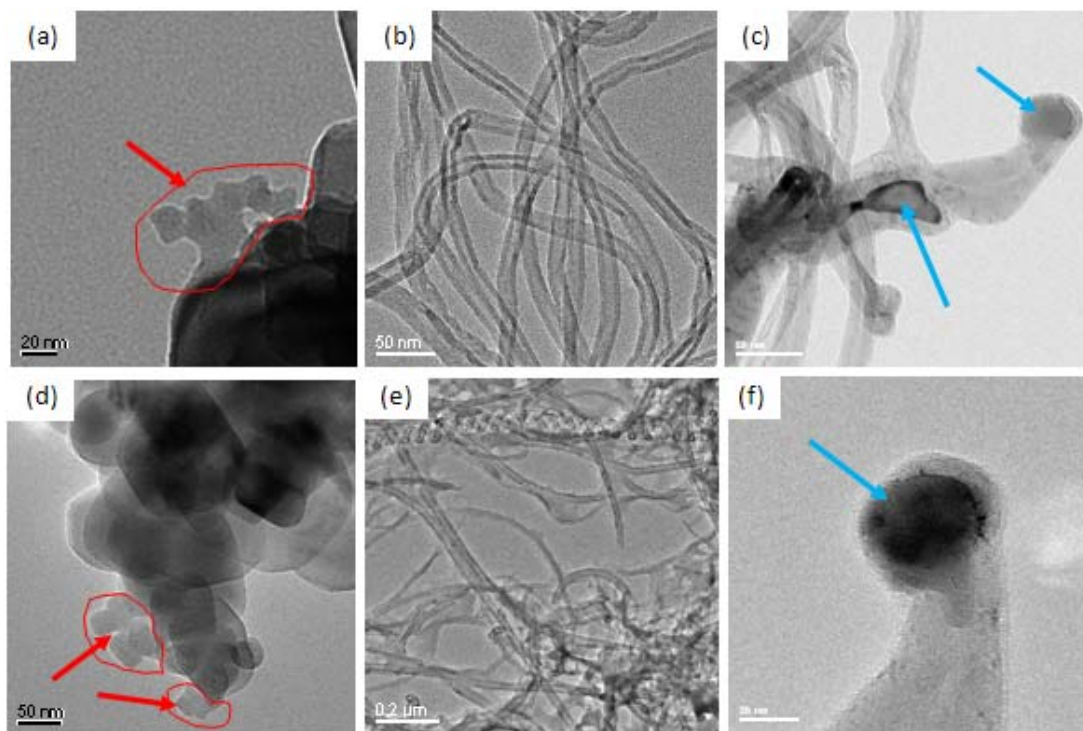


Figure 4.9: TEM micrographs of: the catalyst 2 precursor (marked in red) in (a) and (d), corresponding CNTs (b) and (e), and their catalyst (marked by blue arrows) (c) and (f). Some of the CNTs looked well structured (b), but we also noticed and curved and bamboo tubes (e) and amorphous carbon as well (e). The catalyst particles of irregular shape and up to hundred nanometres in size could be seen, (c) and (f). Scale bars are: 20 nm (a), (f); 50 nm (b), (c), (d); 0.2 μm (e).

For the catalyst 2, the Calofort U calcite was used as a support for the precursor precipitation from Fe and Co nitrates induced by ammonium hydrogen carbonate, followed by subsequent freeze drying. The obtained catalyst precursor showed the lack of diffraction patterns in TEM micrographs (Fig. 4.9 (a) and (d)), thus pointing to its amorphous nature. The precursor appears as lumps with sizes ranging from hundred nanometres (Fig. 4.9 (a) and (d)) up to micrometers. These lumps were always attached to the support surface by a very small contact area, suggesting unsuitableness of the calcite surface for docking of Fe-Co compounds. Some supports were found without any catalyst precursor on their surfaces. The CNTs produced by this supported catalyst precursor were often quite well-structured (Fig. 4.9 (b)), but, occasionally, the bamboo – like forms and deformed CNTs were also noticed, together with amorphous carbon (Fig. 4.9 (e)). Among the catalysts, examined after the synthesis, catalyst particles with irregular (f) and regular (c) shape and up to hundred nanometres large could be noticed.

Catalyst 3

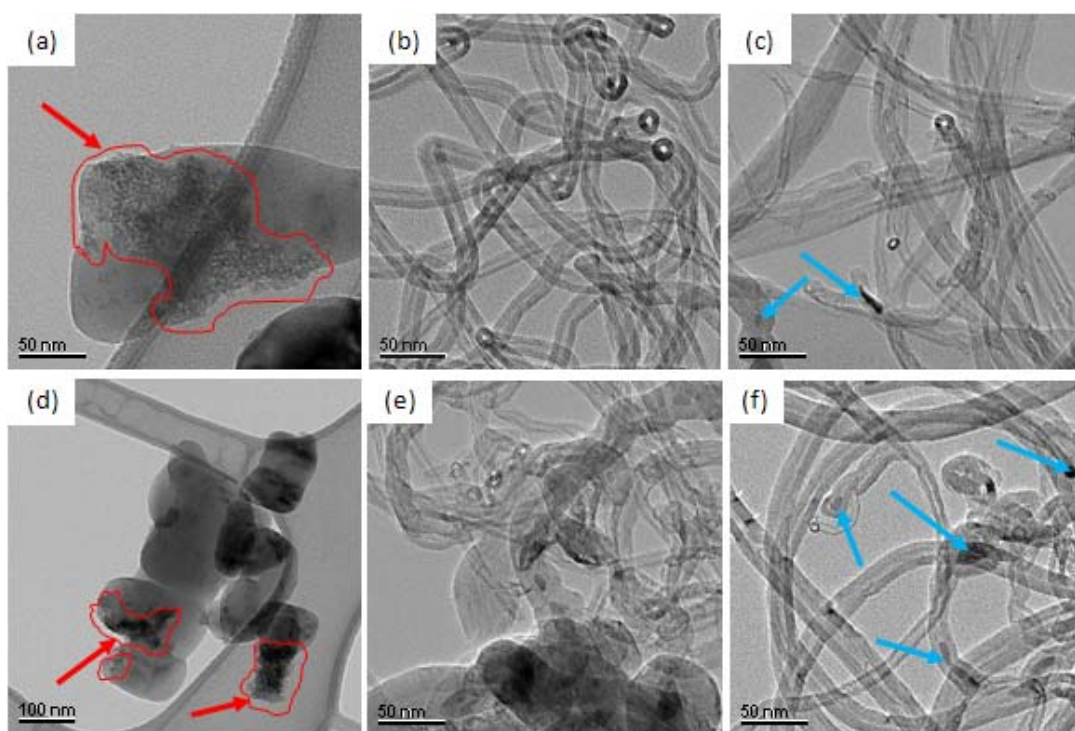


Figure 4.10: TEM micrographs of the catalyst 3 precursor (marked by red), (a) and (d), corresponding CNTs, (b) and (e), and their catalyst, marked by blue arrows, (c) and (f). The synthesised CNTs were often quite well structured (b), sometimes also big and deformed (e). The catalytic particles were with different shapes and sizes (c) and (f).

The ground Fluka calcite was the catalyst precursor support prepared with Fe nitrate, Co acetate and ammonia, followed by drying on a hot plate, under the continuous stirring. Similarly to the catalyst 1 precursor, this catalyst precursor on the support surface showed a grain-like structure and visible diffraction contrast with size varying from few nanometres

up to few hundreds of nanometres (Fig. 4.10 (a) and (d)). Still, the support's surface without the catalyst precursor could often be noticed. The CNTs produced by this supported catalyst precursor were often quite well-structured (Fig. 4.10 (b)), occasionally, however, also big and structurally deformed (Fig. 4.10 (e)). We also observed large variations of the catalyst particle sizes (Fig. 4.10 (c) and (f)).

Catalyst 4

Ground Fluka calcite was used as support for the catalyst precursor prepared by mixing Fe nitrate, Co acetate and ammonia with calcite suspensions, followed by subsequent freeze drying. The obtained catalyst precursor on the support surface was difficult to notice due to the poor diffraction contrast (Fig. 4.11 (a) and (d)). The catalyst particle sizes were in the range from few tens to hundreds of nanometres (Fig. 4.11 (a) and (d)). The CNTs produced by this supported catalyst precursor were sometimes well-structured (Fig. 4.11 (b)) and sometimes structurally deformed (Fig. 4.11 (e)). CNTs often contained more than one catalytic particle (Fig. 4.11 (c) and (d)).

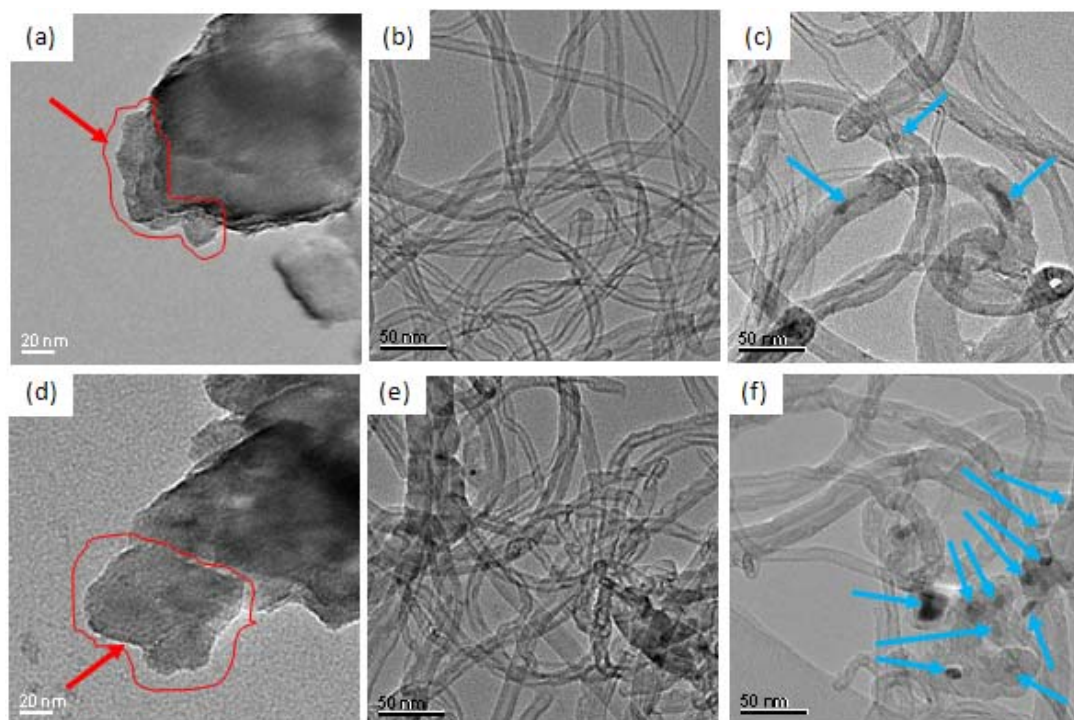


Figure 4.11: TEM micrographs of the catalyst 4 precursor (marked in red) (a) and (d), corresponding CNTs, (b) and (e), and their catalyst, marked by blue arrows, (c) and (f). Besides well structured CNTs (b), some deformed CNTs could be seen as well (e). CNTs were often containing more than one catalyst along the CNTs' length (c) or on the CNTs bottom (f). Scale bars are: 20 nm (a), (d); 50 nm all others.

Catalyst 5

The precursor of catalyst 5 was prepared by mixing Fe and Co nitrates with ammonium hydrogen carbonate with the ground Fluka calcite suspension, followed by continuous stirring at 50°C for 4 h and subsequent freeze drying. The obtained catalyst precursor often showed the grains typical for samples exposed to long-lasting heating (Fig. 4.12 (a)) but also amorphous nature, like freeze dried samples, (Fig. 4.12 (d)). The CNTs (Fig. 4.12 (e)) were produced in parallel to the by-products which appeared in the form of pallets and whiskers (Fig. 4.12 (e)). Catalyst was not observed on the top of the CNTs, but rather along the tube's length (c) and (f).

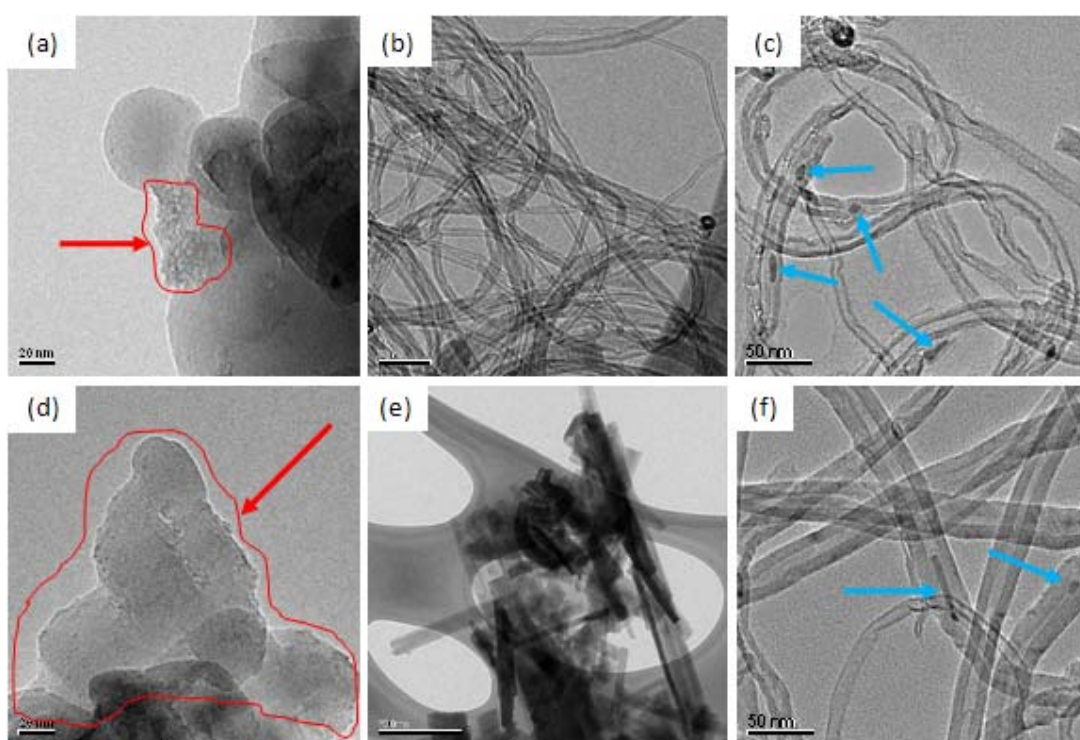


Figure 4.12: TEM micrographs of the catalyst 5 precursor (marked in red), (a) and (d), corresponding CNTs, (b) and (e), and their catalyst, marked by blue arrows, (c) and (f). Besides CNTs (b), we observed the synthesis by-products in the form of pallets and whiskers (e). Catalytic particles were always observed along the CNTs (c) and (f). Scale bars are: 20 nm (a), (d); 50 nm (b), (c), (f); 200 nm (e).

Catalyst 6

The catalyst 6 precursor was prepared by mixing Fe and Co nitrates with ammonium hydrogen carbonate in the suspension of the ground Fluka calcite. Mixture was freeze-dried for few minutes after the preparation. As a result, the support was uniformly covered with the catalyst precursor particles having sizes in the range of 2-10 nm (Fig. 4.13 (a)). The lumps having sizes of 50-100 nm were very rarely observed (Fig. 4.13 (d)). Numerous CNTs produced using this catalyst precursor, were well structured (Fig. 4.13 (b)), but some were

quite deformed and showed the diameter deviation. This was especially visible for CNTs with smaller diameters. Furthermore, CNTs with small diameters often formed big entanglements. In addition, some tubes were covered with an amorphous layer or imbedded in amorphous carbon (Fig. 4.13 (e)). Considering size of the catalyst precursor (Fig. 4.13 (a) and (d)), the catalyst size was rather large (Fig. 4.13 (c) and (f)).

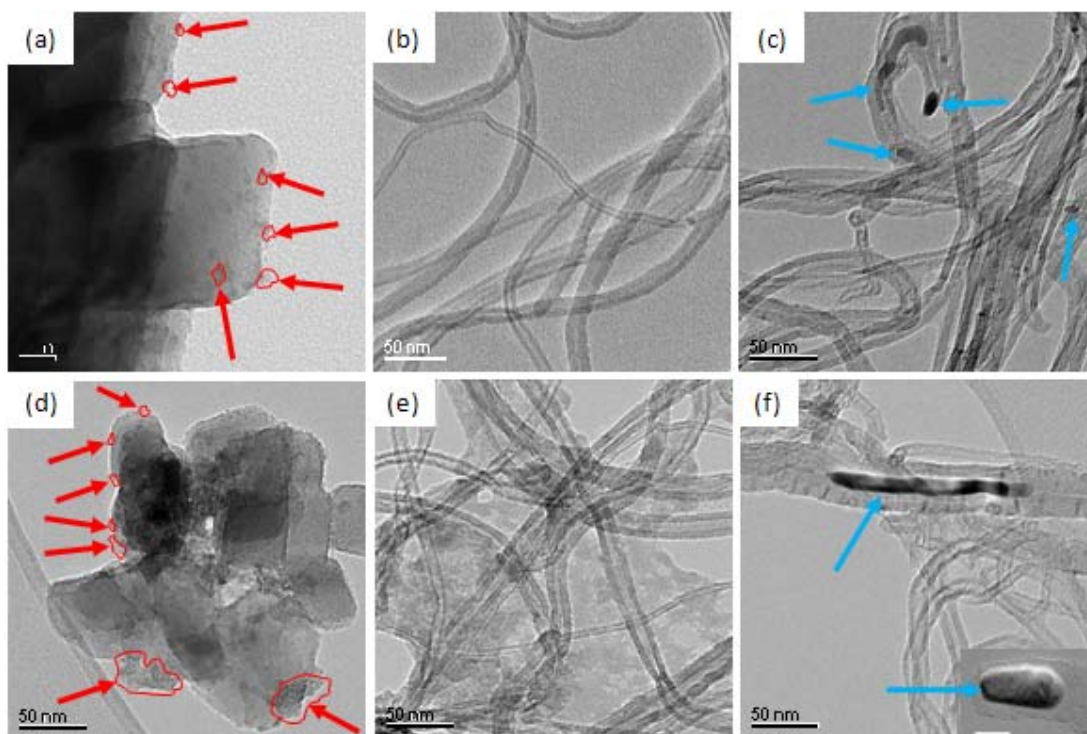


Figure 4.13: TEM micrographs of the catalyst 6 precursor (marked in red), (a) and (d), corresponding CNTs, (b) and (e), and their catalyst, marked by blue arrows, (c) and (f). Small particles of catalyst precursor, typically few nanometres, were uniformly covering support's surface (a); (d) is the only noticed example of precursor larger than few nanometres. Besides CNTs (b), we observed the synthesis by-products in the form of amorphous carbon (e). Catalytic particles were mostly observed along the CNTs (c) and (f), occasionally on the CNTs' tops (c). Insert in (f) shows HR TEM micrograph of catalyst 6 inside the top of CNT even after standard HCl purification, drying and 6 h grinding at 400 rpm in planetary ball mill followed by drying and sonication. Scale bars are: 10 nm for insert in (f); 20 nm (a); 50 nm (b), (c), (d), (e) and (f).

Catalyst 7

The Ground Fluka was the support for the catalyst 7 precursor. The catalyst 7 was prepared from Fe and Co nitrates and triethyleamine, followed by freeze-drying of the mixture for few minutes. In fact, the only difference between the catalysts 6 and 7 was in the base used to induce precipitation of Fe and Co compounds. Surprisingly, the resulting catalyst 7 precursor formed amorphous lumps having microns sizes (Fig. 4.14 (a)).

Moreover, the catalyst support was either immersed in that lumps (Fig. 4.14 (a)) or having no contacts with the catalyst precursor (Fig. 4.14 (d)).

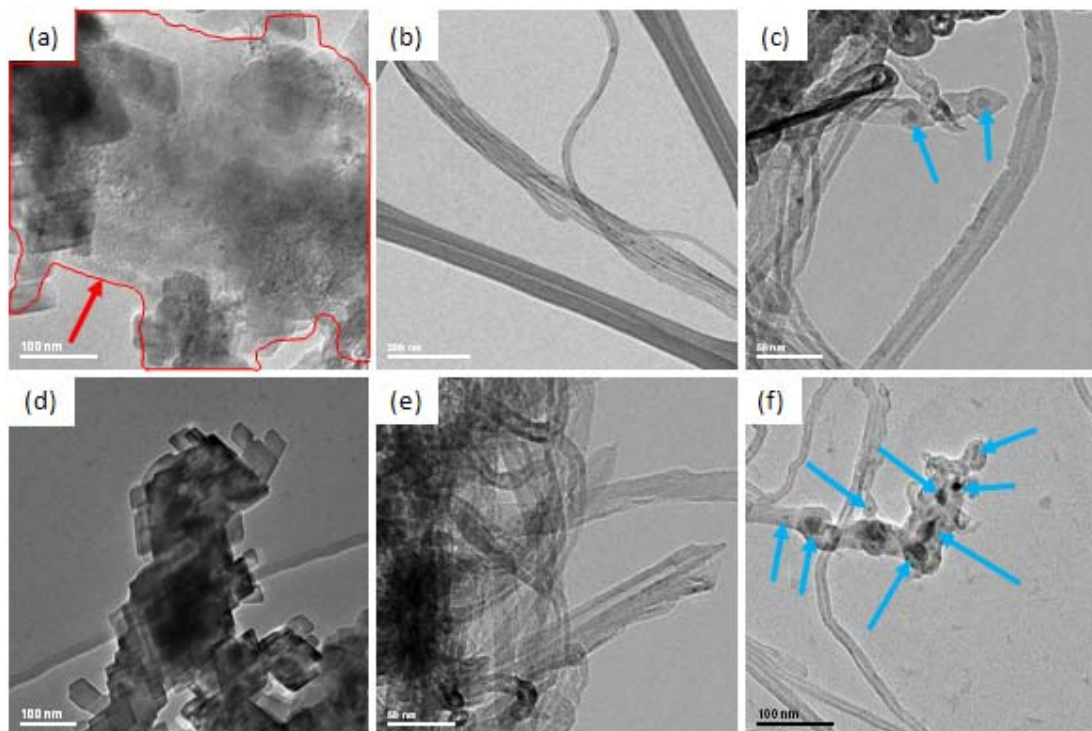


Figure 4.14: TEM micrographs of the catalyst 7 precursor (marked in red), (a) and (d), corresponding CNTs, (b) and (e), and their catalyst, marked by blue arrows, (c) and (f). The parts of support agglomerates are often completely immersed in amorphous lumps of catalyst precursor having microns sizes (a) ((a) shows just a part of one typical catalyst precursor lump), while some support agglomerates are not at all in contact with the catalyst support (d). Besides CNTs, usually very straight (b) and (e), we did not observe any synthesis by-products. Catalytic particles were always observed on the bottom of the CNTs (c) and (f). Scale bars are: 50 nm (c), (e); 100 nm (a), (d), (f); 200 nm (b).

Judging from the TEM observations of CNTs produced from all seven presented catalyst precursors, the best CNTs were synthesized with the catalyst 7, when the applied base was triethyleamine, and the metal precipitation was maximal. The majority of CNTs produced from the catalyst 7 were rather straight as compared with typical CVD CNTs (Fig. 4.14 (b) and (e)). Surprisingly, the catalyst size was up to tens of nanometres (Fig. 4.14 (c) and (f)), what was significantly different than the precursor size (in microns).

Nucleation and precipitation of Fe-Co compounds

Nucleation and precipitation of Fe and Co species may occur on the calcite surface or in the solution. In particular, the surface of the ground Fluka calcite (Fig. 4.2 (b)) revealed irregularities (defects, steps and kinks), that exposed metal atoms with low coordination numbers. These highly exposed, coordinatively unsaturated sites, appear to be particularly

reactive (20). Significant local distortions of the lattice also imply the localized charge imbalances. Furthermore, grinding could easily create usually unexposed calcite surfaces among which could be charged surfaces, like (0 0 1) (Fig. 4.1). As a result, the different sites on the surface may provide different conditions for precipitation process. Therefore, the ground Fluka calcite (Fig. 4.2 (b)), with the surface structure significantly different from Calofort U calcite (Fig. 4.2 (a)), provided convenient conditions for observing the substrate influence. As expected, the TEM examination of the catalyst precursors revealed that the contact area between the support and precursor was maximized in the case of the ground Fluka calcite (Fig. 4.13 (a)) and minimized for the Calofort U calcite (Fig. 4.9 (a)).

Processes of nucleation from pre-existing seeds, nuclei growth, aggregation and precipitation are classically governed by the energy reduction. Moreover, heterogeneous nucleation is energetically more favourable than the homogeneous one. If support surfaces contain surface defects favourable for docking, than precipitation of Fe and Co complexes on these sites require less energy than their aggregation in the solution. In this case, the energetically favoured process will be precipitation of metal complexes on the support's surface. In other words, if the difference of surface free energy of support and precipitant is smaller than the difference of surface free energy of solvent and precipitant, precipitation will be on the supports surface because this reaction would be determined by surface free energy reduction, or minimization of interfacial energy with solvent in this case. On the other side, seed growth stage throughout nuclei aggregation requires overcoming a considerable lower energy barrier than independent generation of free-standing metal cluster in the solution (23). This goes along with qualitative explanation on the basis of equilibrium thermodynamics by entropic solvent effects. The release of water molecules from the hydration layer of ions, caused by cluster formation, result in an increase of solution's entropy.

Especially in the case of the catalyst 6, the surface of support's particles was covered with catalyst precursor clusters (Fig. 4.13 (a)), what suggests immediate precipitation before calcite agglomerates emerge. Pre-existing seeds are low molecular weight species precipitated onto the support's surface. Nucleation and precipitation onto support are followed by nuclei growth stage. But, instantaneous freeze drying allows just beginning of clusters growth without further enlargement and that is the reason for observed small cluster size (Fig. 4.13 (a)). In the case of ground Fluka dried on a hot plate (Catalyst 3) smaller cluster species could still be detected, although bigger cluster appeared due to nuclei growth stage (Fig. 4.10 (a) and (d)). This suggests that during drying on a hot plate nucleation takes place through cluster aggregation on the precipitated nuclei.

In the case of Calofort U calcite as a support the nucleation and precipitation process is different. For the freeze-dried sample, the catalyst precursor is of irregular shape, large size has a tendency to minimize the surface contact area with support along with interfacial energy (Fig. 4.9 (a)). The size and the shape of precipitant, which matches with precursor

formed without support (Fig 4.7 (b)), suggest homogeneous nucleation. That would imply pre-existing seeds growth to clusters, the clusters form aggregates and nucleation takes place via aggregation of clusters. This process requires lower energy barrier than clusters' precipitation onto crystalline surface of Calofort U calcite with normally exposed neutral surfaces unfavourable for docking. Aggregates can still precipitate onto rare defects present even on so crystalline solid (20). This is going along with the observation that most of the Calofort U calcite particles are without any precipitant (Fig. 4.9 (d)). This is not the case for Calofort U calcite dried on a hot plate where size and shape of precursor resemble the case of ground Fluka calcite under the same drying conditions, what was not expected. To be precise, larger particles are energetically favoured over smaller particles due to the lower fractional surface energy (24), but their formation is governed by clusters mobility which depends of surface structure and temperature. If the surface structure would be predominant cause, the substrate with relatively rough surface, like ground Fluka calcite, would likely stabilize metal nanoparticles and prevents their coalescence. Particles would be then protected from fusing together into bulk metal by surface defects and precursor particle size would be preserved. Since this is not observed, the major effect on precursor size and shape in the case of drying on a hot plate has temperature and not support's surface structure. Presence of catalyst precursor cluster on most of the support's particle suggests that instability against agglomeration, characteristic for Calofort U calcite (Fig. 4.9 (a)), does not affect precursor formation.

The difference in sizes of the catalyst precursors observed while using the ground Fluka (for freeze- and hot-plate-dried preparations) requires more refined study. It was necessary to separate influence of temperature on precursor formation from full process of drying on a hot plate, which includes the changing of concentration from diluted to oversaturated solution. This is important since the degree of hydration and polymerization of Fe (III) depends on the concentration of the dissolved metal salts and decrease of the relative amount of water (25). At this point, TEM micrographs of the precursor of the catalyst 5 indicate that the precursor structure changed towards the structure observed for drying on a hot plate (Fig. 4.12 (a)). Size of the precursor became much larger comparing to the precursor of catalyst 6 (without heating) due to particle coarsening, since their mobility increased with temperature.

Stoichiometry of precipitated Fe-Co precursors

Comparison of the precursors with and without support showed that chemical structure of catalyst precursor is significantly affected by support's presence.

The drying method of catalyst precursors with and without support appears to be important as well. In fact, all freeze dried samples of catalyst precursors with and without support show the same shape and lack of diffraction contrast (and pattern) suggesting amorphous or gel-like nature of catalyst precursor. This is compatible with previously mentioned expected formation of metal hydrous polymers. With such a structure we would

expect that precipitation have nonuniform distribution of metals stoichiometric ratio, since it consists of polymer chains. In order to verify this, the energy dispersive X-ray spectroscopy (EDX) of catalyst precursors with and without support was performed in the TEM microscope operating in scanning mode (STEM). Samples without support and with Calofort U calcite as a support show the same precursor composition, either around Fe_7Co_2 or around FeCo_2 . However, for precursor on ground Fluka calcite as a support, Fe:Co stoichiometric ratio differs from 0 to 4.

Samples dried on a hot plate show the same shape. The structures observed by TEM looks the same, but EDX data reveals that catalyst precursor composition on both supports is the same, around approximately Fe_2Co , while without support metal stoichiometric ratio vary and consist from approximately Fe_7Co_2 , Fe_2Co , FeCo and FeCo_8 .

Inhomogeneity of the chemical composition of the obtained catalyst precursors can be explained in the following way. As mentioned in section 4.1.3.1, Fe and Co do not precipitate in calcite aqueous solutions at exactly the same pH values. Therefore, it might be expected that Fe and Co do not form the stoichiometric Fe_2Co compound, even though their salts were initially introduced in 2:1 ratio. Additional problem in forming Fe_2Co present the fact that Fe-Co phase diagram (26) do not show possibility of formation of Fe_2Co compound in the range of conditions used in our experiments (see Chapter 3). Moreover, Ustinovshikov *et al.* (27) studied Fe-Co compounds and showed strong tendency towards phase separation in their alloys. In fact, Fe and Co ratio of 2:1 was chosen for this study only because one previous study (16) of CVD CNTs synthesis on these metals showed that the largest CNTs yield can be obtained if Fe and Co are introduced in the support suspension in ratio 2:1. Unfortunately, this study examined only the chemical composition of the catalyst precursor in the absence of the catalyst support (16). Thus, these findings cannot be associated with the formation and chemical composition of the catalyst precursor formed in the presence of calcite support.

Why would Fe-Co bimetallic catalyst be better than monometallic Fe or Co?

The overall catalytic behaviour Fe and Co with respect to CNTs growth seems to be quite similar. These both metallic catalysts reveal only slightly different carbon-metal bond strengths and dissociation energies for CNTs from catalyst particles to the capped CNTs' ends (6). Yet, their combination yields a much higher catalytic activity and more efficient CNTs synthesis as compared to individual metal catalysts (16). Here, we propose an insight into this phenomenon, which is based on the composition nonhomogeneity of the biphasic catalyst. In fact, we suggest an analogous approach to the so-called multiphasic (28) or multicomponent (29) catalysts, which contain multiple phases. In such systems, the different phases "... cooperate, thus enhancing the catalytic performance with respect to each component phase...." (29). The different phases might have complementary functions and activities as reference to various reaction steps (29). In the same manner, our in-situ formed Fe-Co catalyst might locally form Fe- and Co-rich nano-clusters. These clusters may

have slightly different functions, due to the small but possibly not negligible differences in carbon-metal bond strength, support-metal interactions, dissociation energies, diffusion and precipitation of carbon. As a result, one metal can be more preferential for sorption and diffusion of carbon, while the other enables carbon precipitation on the catalyst surface and tubes formation. In this way, the biphasic system, consisting of bimetallic catalyst, would have higher efficiency than the monometallic catalysts.

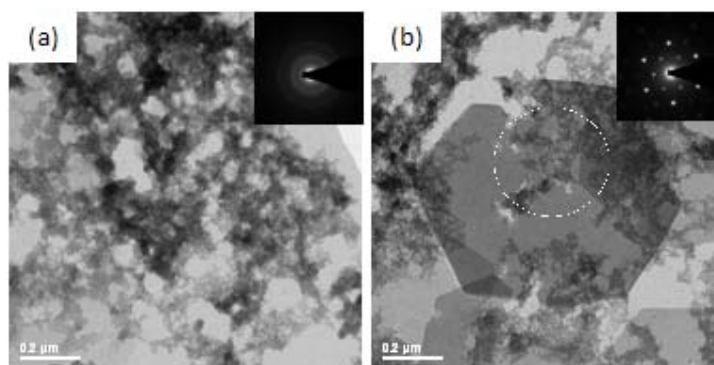


Figure 4.15: TEM micrographs of: (a) Fe polymers and the corresponding diffraction pattern pointing to their amorphous nature (insert); (b) crystalline Co compound surrounded with Fe polymers and the diffraction pattern from the marked area (insert) (b).

In particular, Kanzow and Ding pointed out on the condition for CNT formation, “... the effective average kinetic energy E_{kin} stored per carbon atom on the carbon-metal interface in one degree of freedom must be greater than the work of adhesion per carbon atom W_{Ad} in the graphitic sheet” (30). On the other hand, the adhesion energies of the pure metals are temperature dependent (they increase with the temperature increase). Moreover, the difference between the adhesion energies of Fe and Co increases with the decrease of carbon fraction in iron group metal carbides, and also with the decrease of temperature. For example, when the carbon atomic fraction is of 0.50 at 1000°C, the adhesion energy of Fe is almost zero, while it is $\sim 0.7 \text{ J/m}^2$ for Co (30). If the carbon atomic fraction is of 0.75 at the same temperature, the Fe and Co adhesion energies are around 0.1 J/m^2 and 0.4 J/m^2 , respectively. Judging from the linear dependence of the adhesion energy on temperature, at synthesis temperature of our study, 640°C, this difference in Fe and Co adhesion energies is even more pronounced. Consequently, the effective average kinetic energy E_{kin} stored per carbon atom on the carbon-metal interface in one degree of freedom would be much greater than the work of adhesion per carbon atom W_{Ad} in the graphitic sheet in the case of Fe as comparing to Co. That means that CNTs would growth easier from the Fe clusters than from the Co ones. To test this assumption we performed the following experiments. Fe and Co nitrates (aqueous) were mixed at room temperature and freeze-dried. TEM micrographs showed formation of amorphous Fe polymers (Fig. 4.15 (a)) and crystalline Co compound (Fig. 4.15 (b)).

On the other hand, the catalyst precursor with the maximum simultaneous Fe and Co precipitation (obtained with triethyleamine as a base) showed pink traces. This pointed to the presence of Co hydroxide and thus, partial phase separation of metals. Consequently, such supported catalyst precursor was the ideal candidate to study expected differences in Fe and Co catalytic activity. We performed rapid, 30-second synthesis processes on such supported catalyst precursor. As a result, we observed preserved crystals of Co precursor while CNTs were already growing from Fe catalyst (Fig. 4.16(a), which shows Co precursor similar to that shown in Fig. 4.15 (b)). Figure 4.16 also shows a rare example of observation of the graining process of Co precursor on its edges, which is then followed by Co catalyst formation and subsequent CNTs growth (Fig. 4.16 (c)).

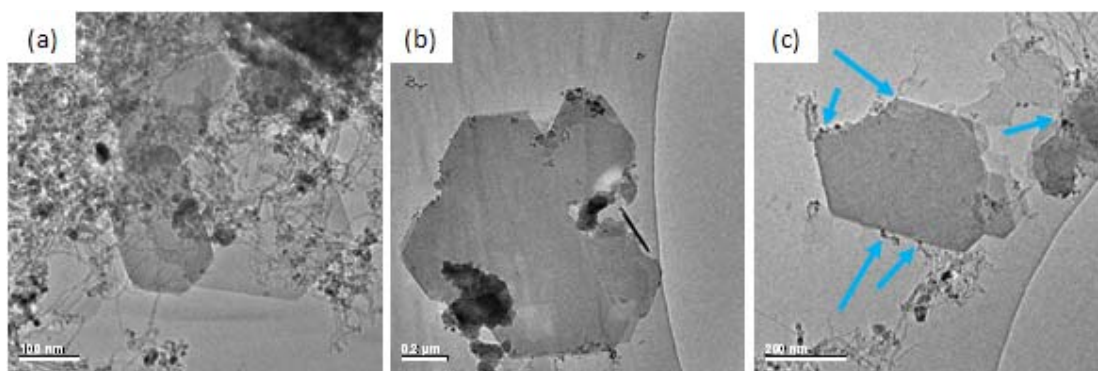


Figure 4.16: TEM micrographs of CNTs obtained after 30 seconds of the synthesis process. (a) The unchanged Co precursor (like before the CNT synthesis and similar to that shown in Fig. 4.15 (b)). In contrast, the growth of CNTs was already initiated from Fe catalyst. (b) The edges of Co precursor appear intact, with no traces of CNTs growth, even after 30 sec of the synthesis process. (c) In the upper left edge, marked by blue arrows, catalyst formation and activation of CNTs growth can be seen.

Overall, these experiments confirmed different functions of Fe and Co precursors, thus pointing to the fact that if they form bimetal catalysts, their nano-clusters behave differently with regard to the CNTs growth. This is similar, in fact, to multiphase catalysts where different phases might have complementary functions. Consequently, bimetallic catalysts can have higher catalytic activity than their monometallic counterparts.

CVD CNTs growth

In Figures 4.8 to 4.14 we have already shown the catalyst particles after the CNTs synthesis on seven different catalyst precursors. TEM micrographs revealed that majority of the catalyst particles were either on the top of the CNT or in their middle zone. Surprisingly, we did not find straightforward correlations between the precursor grain sizes and the final catalyst grain sizes. For example, the smallest catalyst precursor (few nanometres to few tens of nanometres) was prepared for the catalyst 6, while the particle size of the catalyst located inside the CNT was even of 150 nm. On the other hand, the catalyst 7 precursor was in the form of micron-size lumps, whereas the catalysts particles found inside CNTs had

sizes around ten nanometres. This unexpected lack of direct correlations between the sizes of precursors and catalysts point to a more complex CNTs growth mechanism than just a simple statement that the smaller catalyst precursors yield smaller catalysts, and consequently, narrower tubes. To get a better insight into this phenomenon, we thoroughly studied the catalyst 7. As mentioned before, we reported the biggest discrepancy between the precursor and catalysts sizes for this catalyst. Thus, we additionally performed the synthesis of CNTs on the catalyst 7, with the process duration times of 6 min, 4 min, 1 min, 41 sec, 14 sec and 8 sec, with the aim to gather information on the catalyst formation mechanism. However, this approach appeared to be a quite challenging task due to the very high CNTs growth rate. In fact, after only 8 sec of synthesis, the burst of CNTs growth could be observed (Fig. 4.17). Notwithstanding, it was still possible to find some areas with a lower CNTs density, where the CNT growing root could be observed (Fig. 4.18).

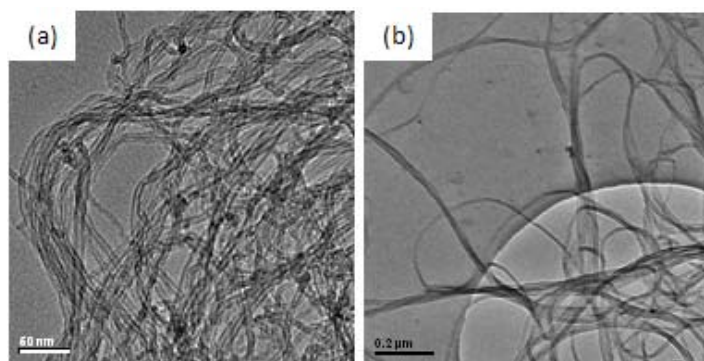


Figure 4.17: TEM micrographs of CNTs after 8 sec (a) and after 1 minute (b) of synthesis on the catalyst 7. Scale bars are: 50 nm (a) and 0.2 μm (b).

Figure 4.18 (a) shows that some of the catalyst particles, although small, were not consumed for the CNTs growth, but were covered by amorphous carbon. Concerning relation between the catalyst sizes and CNTs diameters, interesting phenomenon was noticed in Figure 4.18 (b), where the huge discrepancy between the catalyst size and to the CNT. Interestingly, both types of the CNT growth mechanisms i.e. “bottom” (Fig. 4.18 (d)) and “tip” (Fig. 4.18 (e)), were simultaneously observed. Surprisingly, in both cases, the catalyst particles were separated from the support. Sometimes we could also observe isolated catalyst grains grouped together and separated by carbon or more encapsulated by carbon, while CNTs were growing from some of them (Fig. 4.18 (d)).

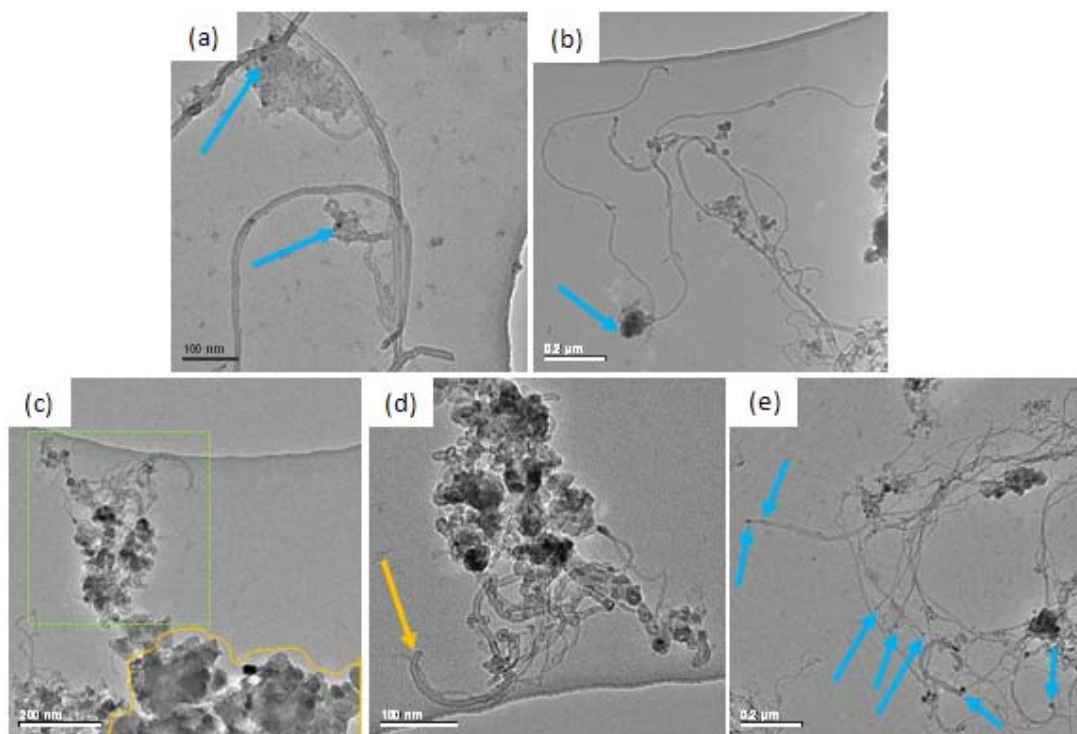


Figure 4.18: TEM micrographs of: (a) the catalyst 7 particles (marked by blue arrows) embedded into amorphous carbon; (b) catalyst particle having much larger size than the diameter of the corresponding CNT; (c) agglomerate of calcite powder (inside the area marked by yellow line) without catalyst and separate of it are catalyst particles and CNTs; (d) enlarged part of (c) (marked by green rectangle), where bottom growth of CNTs can be observed; yellow arrow indicate tip of the growing CNT; (e) tip growth of CNTs, where blue arrows indicate catalyst particle on the tip of CNTs. Scale bars are: 100 nm (a), (d); 200 nm (c); 0.2 μm (b), (e).

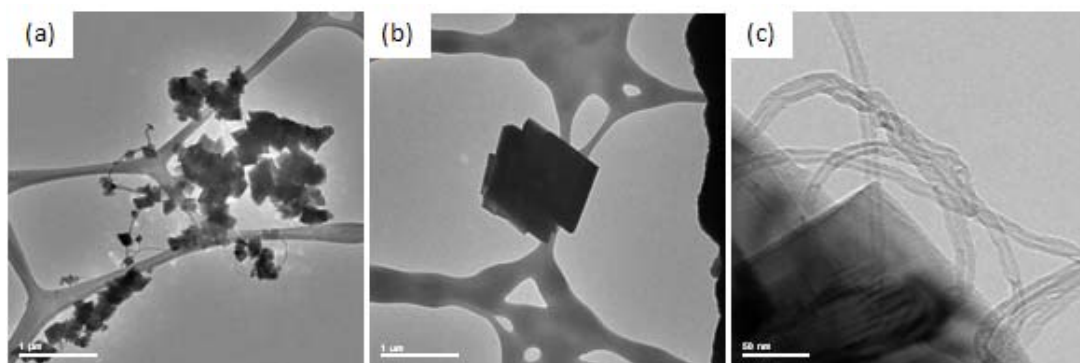


Figure 4.19: TEM micrographs of CaCO_3 support after 2 h synthesis at 640°C on the catalyst 7. Scale bars are: 50 nm (c); 1 μm (a), (b).

While comparing the TEM images of the catalyst 7 precursor (Fig. 4.14 (a)), occurring in the form of micrometer-sized amorphous lumps, partially covering calcite agglomerates, with the TEM images of CNTs grown on this catalyst (Figure 4.18), one can conclude that

during the CNTs growth process the amorphous precursor mass starts to form grains which melt and form nucleation sites for the CNTs growth. The above-mentioned grains were often observed without any connection to the support (Fig. 4.18 (b) and (d)). On the other hand, very often, there was no connection between the support and the catalyst (Fig. 4.18 (c)). The same happened also after a standard 2 h synthesis at 640°C, when we observed the completely preserved calcite (Fig. 4.19). As mentioned in Chapter 3, the dispersion of CNTs in diluted HCl (during purification) was accompanied by a marked release of CO₂. This indicated that CaCO₃ did not decompose during the CNTs synthesis.

In conclusion, there are two main mechanisms which proceed during the growth of CNTs:

- (1) the CNTs growth proceeds from the previously formed precursor grains (if the catalyst precursor is dried by heating and its grains are formed prior to the CNTs growing process);
- (2) firstly, the CNTs growth proceeds through the stage of *in-situ* catalyst grain formation, which is then followed by the direct CNTs growth from these grains (if the catalyst precursor did not pass heat treatment (lyophilisation only), and it was in amorphous phase prior it has been introduced into furnace).

Diameter distribution of obtained CVD CNTs

The CNTs' diameter is a very important parameter of the CVD-grown CNTs. In fact, it was recently shown in our group (3) that the elastic modulus of CVD CNTs strongly depends on their diameter (see Chapter 5). Moreover, it has been found that CVD CNTs have the elastic moduli below 100 GPa for the diameters above 15 nm, while tubes with diameter *ca.* 11 nm have, in average, the elastic moduli of ~600 GPa. Clearly, the highest possible elastic modulus of CNTs is prerequisite for applications of this material in reinforcement of polymer composites. Therefore, for each of seven CNT samples, diameters of around 1300 CNTs from 100-200 randomly taken TEM micrographs were measured. The average diameters and the percent of CNTs having diameter below 11 nm and below 15 nm are given in Table 4.1. One can see that CNTs with the largest fraction of small diameters are the ones grown on the catalyst 6. Actually, from all the CNTs synthesized on this catalyst, 52% had diameters up to 11 nm, while ~75% had diameters below 15 nm.

Therefore, we can conclude that fine tuning of the catalyst support, base used for the precursor formation/precipitation, and the precursor drying process, all together, can provide good control over the diameter of large scale CVD synthesised CNTs.

Furthermore, the above-discussed results point to the lack of correlations between the diameter of CNTs and the sizes of the catalyst precursor. One exception from this statement, to the certain extent, were CNTs grown on the catalyst 6, for which some correlation between the catalyst precursor size and CNT diameter was found.

Concerning the quality of the synthesized CNTs, the best CNTs were grown on the uniformly amorphous precursor of the catalyst 7. Interestingly, in this case, the average diameter of CNTs was 13.3 nm, which could not be correlated with the micrometer-range sizes of the catalyst precursors.

4.2 CVD – towards high-quality CNTs, graphene...

In the above-presented study (section 4.1), the calcite from Fluka was ground to create charged surfaces on the calcite support powder, thus enabling docking of the catalyst precursor. Moreover, the grinding process reduced the grain sizes of this powder to be comparable with those of Calofort U calcite. The grinding of the calcite powder from Fluka revealed a big impact on the catalyst precursor formation and composition, as well as on the CNTs growth. Thus, we explored the possibility of working with the calcite powder having its primary particle sizes even smaller than the original Calofort U calcite. It is also worth noting that the Calofort U calcite powder was actually more crystalline than the one from Fluka.

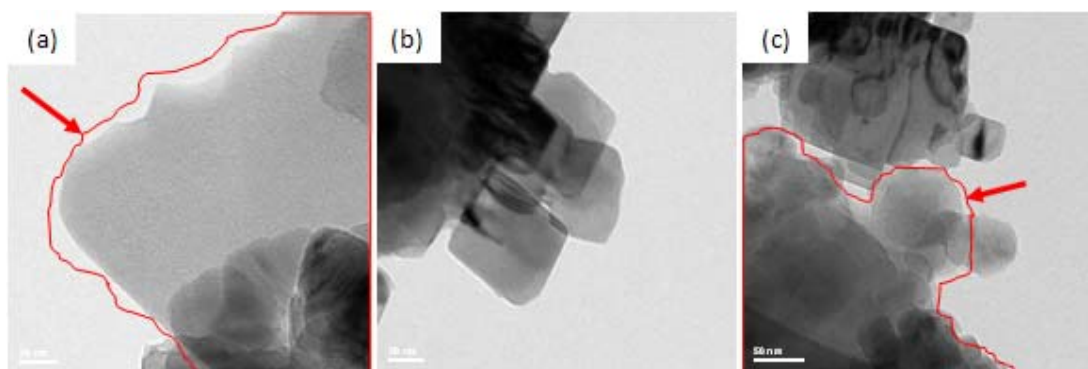


Figure 4.20: TEM micrographs of the supported catalyst precursor prepared by mixing Fe and Co nitrates and ammonium hydrogen carbonate with the ground Calofort U calcite suspension. Scale bars are: 20 nm (a), (b), and 50 nm (c).

The catalyst precursor was prepared in the same way as the catalyst 6 (see section 4.1), with the only difference in that, instead of the Fluka calcite, we ground the Calofort U calcite. It is also worth mentioning that the precursor of the catalyst 6 had typically few nanometres in size and it was uniformly covering the support's surface (Fig. 4.13 (a)). Due to the same support treatment, preparation procedure, chemicals and drying process, one could expect the same or similar final properties. Surprisingly, the obtained catalyst precursor had the form of amorphous lumps of up to few hundred microns size (Fig. 4.20), thus much more resembling the precursor of the catalyst 7 (Fig. 4.14 (a)), which yielded CNTs of the best quality.

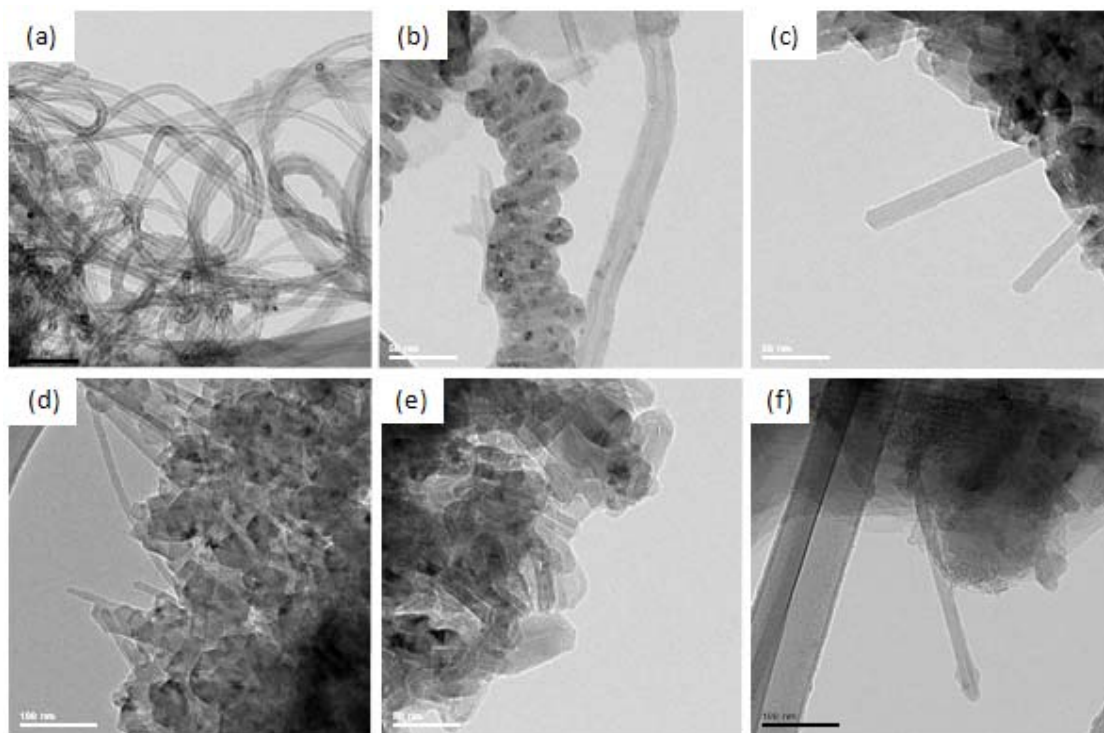


Figure 4.21: TEM micrographs of the synthesis products obtained by using the catalyst whose precursor is shown in Figure 4.20. (a) CNTs, (b) tubular graphitic structures, (c) rods, (d) whiskers, (e) onions, and (f) completely straight CNT and amorphous carbon. Scale bars are: 50 nm (b), (c), (e), and 100 nm (a), (d), (f).

The obtained catalyst precursor was used in a standard 2-h long CNTs synthesis. Figure 4.22 (a) shows the produced CNTs, which were quite often well-structured and rather rarely deformed. The TEM examination of this sample (by Dr. Duncan Alexander, CIME/EPFL, unpublished data) revealed also other carbon structures as by-products of the synthesis (Fig. 4.22 (b) to (f)). In particular, as can be seen in Figure 4.22, besides CNTs, highly curved tubular graphitic structures (b), rods (c), whiskers (d), onions (e), amorphous carbon and especially interesting very straight CNTs were found (f).

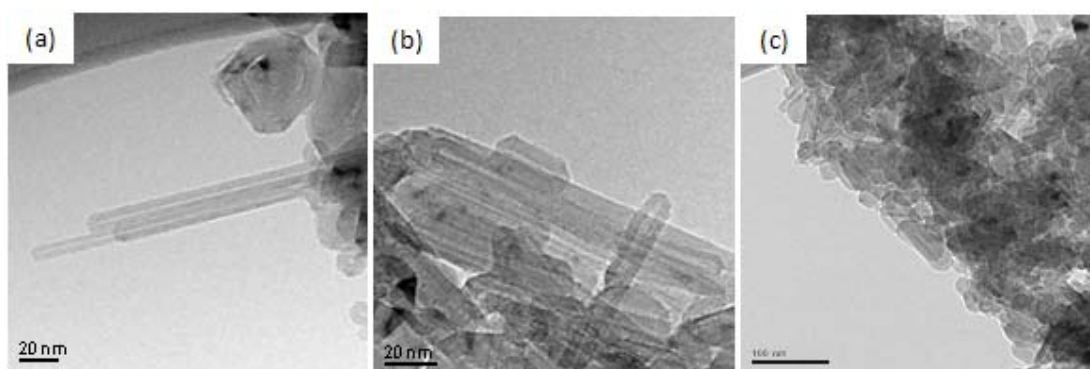


Figure 4.22: TEM micrographs of the well-graphitized, perfectly straight and unusually long CVD CNTs (a) and shorter ones (b, c). It can be seen that all CNTs do not contain any catalyst

particles trapped inside the tubes (either at tubes edges or along the tube). Scale bars are: 20 nm (a), (b), and 100 nm (c).

The closer observations of very straight CVD CNTs revealed that all straight tubes were completely empty inside, without any catalyst particles inside the tubes, either at their edges or attached to the tube walls (Fig. 4.22). HR TEM detailed study of these CNTs revealed that their structure over the whole CNT's length corresponds to the high-quality CNTs synthesized by the arc-discharge method. We observed well graphitized edges (Fig. 4.23 (a) and (b)), as well as the main body of the CNTs (Fig. 4.23 (c) and (d)). Thus, we observed high-quality, perfectly straight CVD CNTs, which looked like the CNTs prepared by the arc-discharge method and which did not contain any catalyst particles. Analogously to the arc-discharge synthesis, various by-products of synthesis were observed, like onions (Fig. 4.23 (e)). Furthermore, the sample areas, which in standard TEM images looked like amorphous or graphitized carbon, upon the observation with HR TEM, showed well-graphitized structures (Fig. 4.23 (f)).

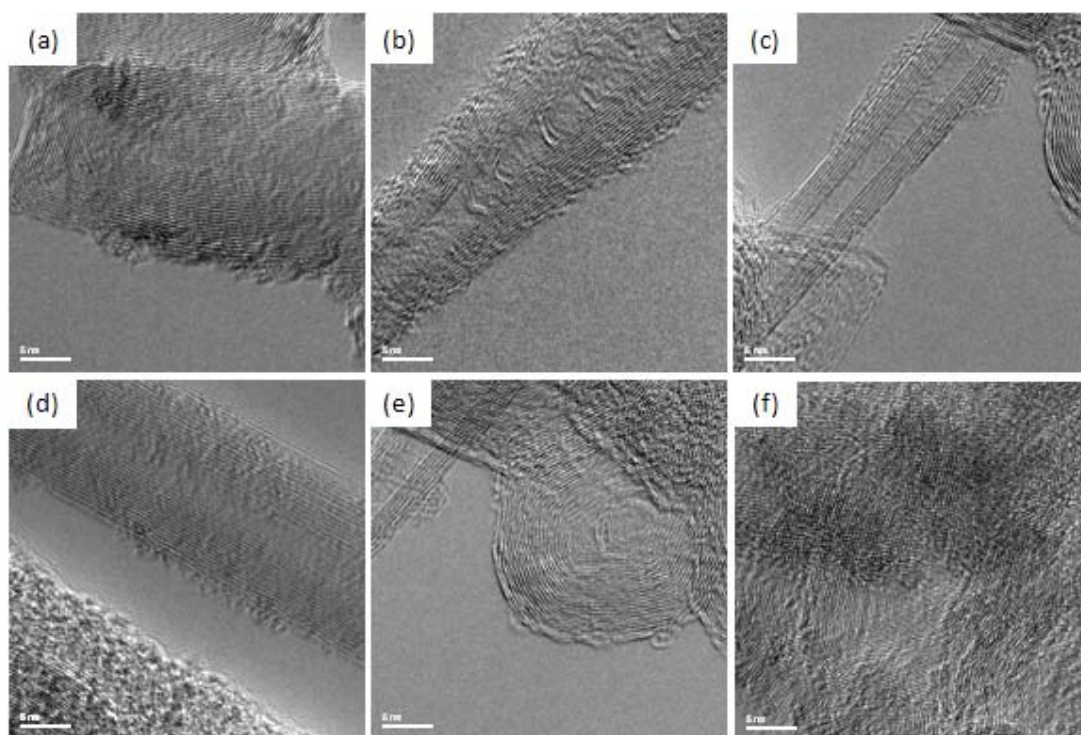


Figure 4.23: HR TEM micrographs of: (a, b) edges and (c, d) the main body of well-graphitized perfectly straight CVD CNTs which look like obtained by the arc-discharge method; (e) onions and (f) well graphitized carbon structures. All scale bars are 5 nm.

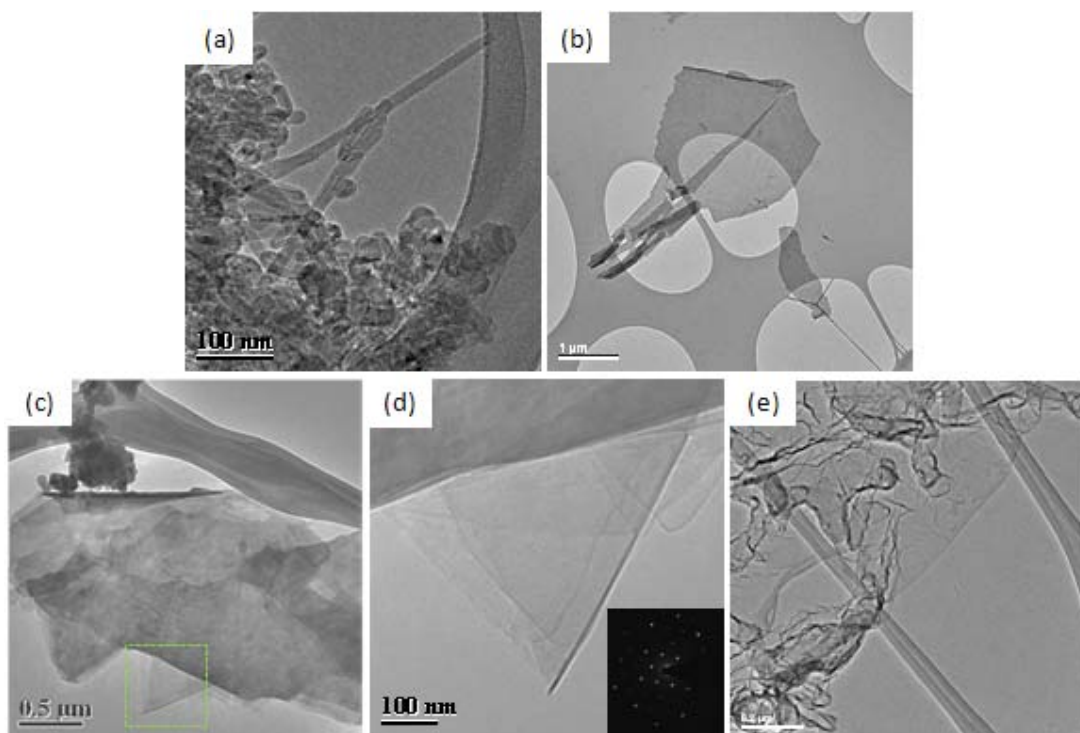


Figure 4.24: TEM micrographs of the product of CVD synthesis on the calcite powder without transition metal catalysts: CNTs (a), few layers of graphene either free standing (b) or bound to the calcite (c); (d) is enlarged insert from (c) (marked by green rectangle in (c)) and insert in (d) shows the diffraction pattern from area in (d), which confirm crystalline structure of few layers graphene. Graphene was usually in the form of free standing flakes (e). Scale bars are: 100 nm (a), (d); 0.2 μm (e); 0.5 μm (c); 1 μm (b).

Upon reported observation, it was evident that the graphitization could occur also without catalyst particles. Therefore we prepared Calofort U calcite like in previous cases, by grinding and subsequent freeze-drying, which was then followed by the synthesis in standard conditions. However, this time, no transition metal catalyst precursors added. In brief, the obtained powder was placed into the quartz tube and heated up to 640°C with the flux of nitrogen. Synthesis was performed over 2 h at 640°C with acetylene, followed by natural cooling of the system. Obtained products were afterwards collected from the quartz tube and examined by TEM. We rarely saw CNTs (Fig. 4.24 (a)), but we very often observed few layers of graphene. These layers were either free standing (Fig. 4.24 (b)) or, surprisingly, bound to the calcite surface with the very small contact area (Fig. 4.24 (c)). Graphene was usually observed growing over the bigger surfaces as free standing flakes (Fig. 4.24 (e)).

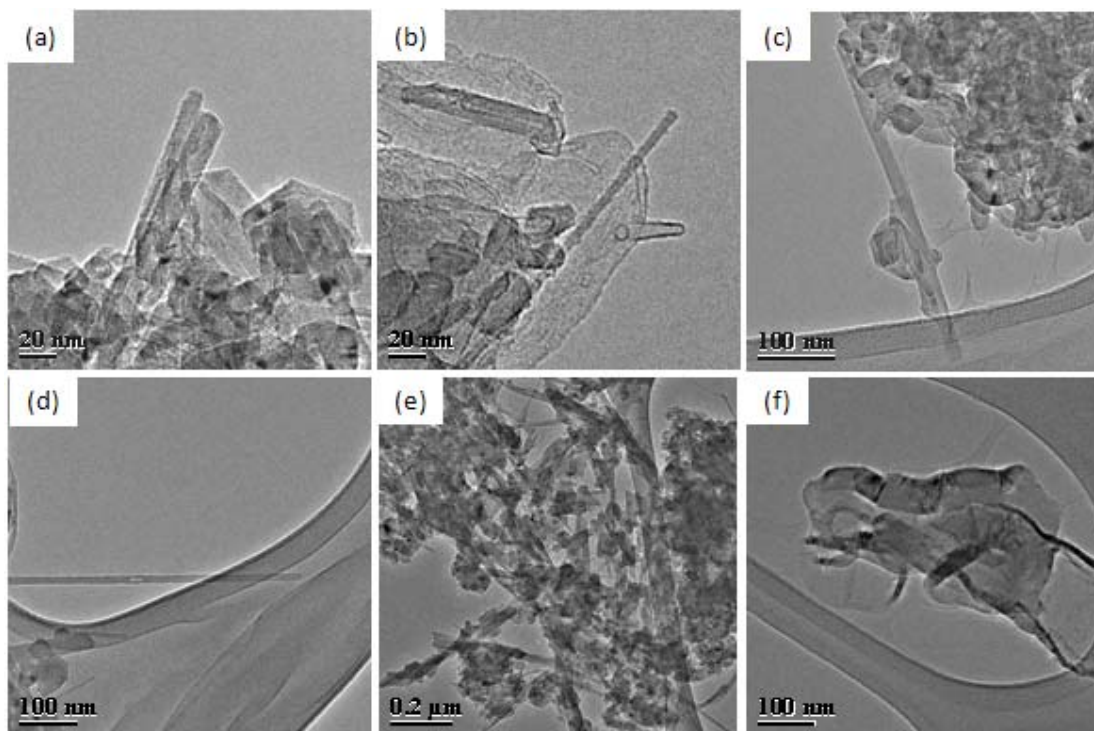


Figure 4.25: TEM micrographs of products of CVD synthesis on the calcite powder mixed with ammonium hydrogen carbonate, in the absence of transition metal catalysts: CNTs (a, b), amorphous carbon (b), rods (c, d), whiskers (f) and few layer graphene (f). Scale bars are: 20 nm (a), (b); 100 nm (c), (d), (f), and 0.2 μm (e).

Similar experiment with the ground Calofort U calcite was performed while mixing this calcite powder with the base, ammonium hydrogen carbonate. This attempt was done to study the role of the base, since it was present in the first prepared sample with the metal salts and yielded tubes without trapped catalyst particles. The synthesis yielded, although rather rarely, besides CNTs, also short CNTs (Fig. 4.2.5 (a) and (b)), amorphous carbon (Fig. 4.25 (b)), rods (Fig. 4.25 (c) and (d)), whiskers (Fig. 4.25 (e)) and very rarely few layers graphene (Fig. 4.2f (f)).

Besides numerous recent reported metal-free CNT synthesis (31; 32), CNTs formation without any catalyst and closed from the both sides was noticed in counter-flow oxygen enriched methane diffusion flames during the study of soot generation from hydrocarbon flames (33). On the other hand, Rümeli *et al.* reported formation of few graphitic layers over the nanocrystals of various oxides (34). Interestingly, they explained their results by a mechanism of formation of primary soot particles in hydrocarbon flames. These primary soot particles originate from the polycyclic aromatic hydrocarbons, which serve as nuclei for soot formation (34). In general, these polycyclic aromatic hydrocarbons are easily formed from small hydrocarbon species under the standard CNTs synthesis conditions in which formation of bigger hydrocarbon molecules is much more energetically favourable.

Among numerous hydrocarbon molecules used for CNTs production, acetylene is especially studied as a source of carbon atoms for the CNTs synthesis processes. In fact, it was found already in the 50's that the acetylene may undergo two different mechanisms: its ionization will lead to the polymerization process, while electronic excitation leads to cyclisation (35). The first cyclotrimerization of acetylene to benzene was reported already in 1866, but the process needed to find alternative due to its high temperature and the presence of different hydrocarbon species, including mixed products of the cyclisation reaction (36). In principle, in exactly the same way, our high-quality CNTs and graphene could be synthesized. The obvious question arises: why we did not produced such structures in the case of metal-catalysed CVD synthesis? In the presence of metal, the cyclisation reactions are catalysed by the metal in the same manner like that reported by Reppe (36). In fact, Reppe's synthesis was found as an alternative for the earlier high temperature (less than 400°C) cyclisation without metal which was followed by various reaction by-products (36). The lack of the catalytic active metal surface lead to poly-cyclisation or/and polymerisation in the gas phase enriched in highly concentrated reactive carbon species. Clearly, this might explain the CNTs formation which we observed. However, the graphene growth mechanism might be different.

Some insight can come from the observation that the produced structures of single- and few-layered graphene were often found to be attached (by a small surface area) to the ground calcite support. Nowadays, the growth of graphene is achieved using the following approach based on searching for: (i) a surface (substrate), which could provide graphene growth onto that surface, and (ii) a technological process of removal of the produced monolayer from the growing substrate. In this work, we have proposed a completely different approach. Instead of a substrate having the whole surface suitable for absorption of carbon species, we have suggested using modified substrates, with rarely present active sites. Then, the growth of carbon-based structures would be only initiated on the limited area suitable for the absorption of carbon atoms, while the growth itself could proceed in the lateral direction. In such way, graphene can grow radially from the seed on the surface of the substrate. Consequently, graphene-substrate contact area can be dramatically reduced comparing to the direct growth on the whole metal surfaces.

In conclusion, we noticed that under the certain experimental conditions, CVD synthesis yielded well-graphitized, perfectly straight CNTs, which resembled CNTs obtained by the arc-discharge method. Further study of this phenomenon and its better understanding might open the possibility for large scale synthesis of arc-discharge-like CVD CNTs, thus overcoming the challenging problem of scalability of high-quality CNTs. Moreover, we synthesized single- and few-layered graphene by the CVD method in the absence of transition metal catalysts or specially prepared highly crystalline metal surfaces. Purification process did not require oxidizing acids and thus, graphene surface could be preserved without altering its properties. The reported graphene synthesis method is very simple, scalable and inexpensive.

4.3 Optimization of the lengths of CVD CNTs

Numerous applications require short CNTs with a determined length and open ends. This is because some properties of CNTs are strongly affected by their length, for instance the electron transport properties. In particular, Onoa *et al.* emphasised (37): "... transport through short (<300 nm) CNT is free of acoustic phonon scattering and thus favours ballistic transport, which is highly desirable for memory and logic devices...". Thus, the fabrication of uniformly short CNTs might enable high-performance CNTs based electronics. Indeed, one of the most promising applications of short CNTs with open ends is in achieving an enhanced field emission (38; 39; 40). Moreover, the open ends CNTs enable processes necessary for certain applications. If necessary, these ends can be afterwards closed by high temperature annealing (41). For instance, short CNTs with open ends facilitate molecular gas diffusion and thus, they are favourable for hydrogen absorption (*e.g.* for hydrogen storage) (42). As a support for platinum catalyst in fuel cells, short CNTs were much more suitable than the long ones (43). CNTs shortening by cutting also facilitate the selective chemical functionalization of the ends with targeted groups (44), often necessary for altering CNTs' dispersion properties. Moreover, short CNTs with open ends showed much better properties than long ones, when used as electrode material in Li-ion batteries (43). For some type of applications length of CNTs play an important role (see section 6.2).

There are various methods to produce CNTs (see Chapter 2). However, for large scale synthesis, the CVD method is the most commonly used. In that case, catalyst support is often in powder form what limits the control of catalyst size (see section 4.1) and its uniformity of exposure to the carbon-containing gas. Consequently, the growth rate is not the same for all CNTs, resulting in the lack of the precisely controlled length of CNTs grown from catalyst on powder support. In fact, in that case the CNTs length can range from a few microns to millimetres, but cannot be tuned to be for instance 200 nm.

Although there were reports on direct synthesis of short CNTs (43; 45), shortening of initially long growth CNTs is still considered to be an easier process than the controlled growth of short CNTs, probably owing to the numerous methods developed for cutting CNTs. The most frequently used methods are: sonication-induced scission, chemical treatment and different milling methods.

Cutting of CNTs by sonication-induced scission is a simple and easy to use method (46; 47). However, the considerable disadvantage of cutting CNTs by ultrasound is a decrease of their quality. Actually, the study of mechanical damage of CNTs by ultrasound showed that this treatment considerably increased disorder of carbon structures (48).

Another method frequently used for larger scale cutting is chemical treatment, which is usually carried out in oxidizing acids (41; 49), which are cutting CNTs by attacking the point-defects on their surface. In fact, the first CNTs cutting method reported by Smalley's group (41) was a combination of sonication induced scission and chemical

treatment in oxidizing acids. However, as a result of chemical oxidation, it was found that the ends and often the sidewalls of treated CNTs were covered with oxygen containing groups (50). This is not suitable for most applications, which require a preserved nature of CNTs surface.

Mechanical milling is another possibility, often used to process powders. From various milling methods of CNTs cutting, the vibration ball milling method was most studied for large scale CNT cutting (51; 52). The major disadvantage of this method is related to the process lengths (up to 200 h). Moreover, there is no unique conclusion concerning the time evolution of CNTs average length as a function of the process parameters. The two-roller milling method was also used, but in order to pass through the roll miller, CNTs needed to be imbedded in the polymer, which had to be chemically removed afterwards (53). Planetary ball milling was used for cutting of cup-stacked CNTs resulting in a uniform decrease of CNTs lengths with increasing milling time (54). Moreover, this method was also used for cutting of CVD CNTs, but the authors presented only results of a short CNTs application, without the characterisation of cut CNTs (42).

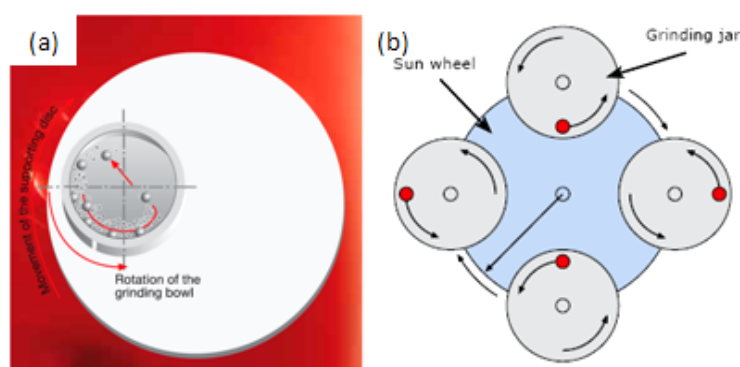


Figure 4.26: Schematic drawing of: (a) working principle of a planetary ball milling apparatus (From the ref. (55)); (b) the rotational movement of the grinding jar and the sun wheel (From the ref. (56)).

To summarize, one can conclude that there is a lack of detailed studies concerning cutting methods of CNTs. Therefore, in this study, we tried to check which parameters for a chosen cutting method should be tuned to obtain desired average CNTs lengths. To this end, we studied milling conditions and their outcomes for the planetary ball milling. The working principle of this cutting method is schematically shown in Fig. 4.26. According to one of the producers of planetary ball milling machines (Fritsch), this method can be described as follows (57): “...The material is crushed and disintegrated in a grinding bowl by grinding balls. The grinding balls and the material in the grinding bowl are acted upon by the centrifugal forces due to the rotation of the grinding bowl about its own axis and due to the rotating supporting disc. The grinding bowl and the supporting disc rotate in opposite directions, so that the centrifugal forces alternately act in the same and opposite directions. This results in, as a frictional effect, the grinding balls running along the inner wall of the

grinding bowl, and impact effect, the balls impacting against the opposite wall of the grinding bowl. ... ”

Till present, the application of this cutting method for CNTs has not been very extensively reported. This is probably due to the fact that planetary ball milling is a complex stochastic process depending on a number of technological parameters. In order to acquire a better understanding of this complex process, we aimed to find the correlation between average length of the cut CNTs and the ball milling process parameters. We studied the influence of the rotational speed (rpm) and the process duration on the length distribution of CNTs.

4.3.1 Results and discussions

Starting material

The starting material was CVD CNTs (Fig. 4.27) with known diameter distribution previously optimized to contain 75% of CNTs with a diameter up to 15 nm (see section 4.1 and the ref. [MM18]). The length of CNTs before grinding was around 10 μm .

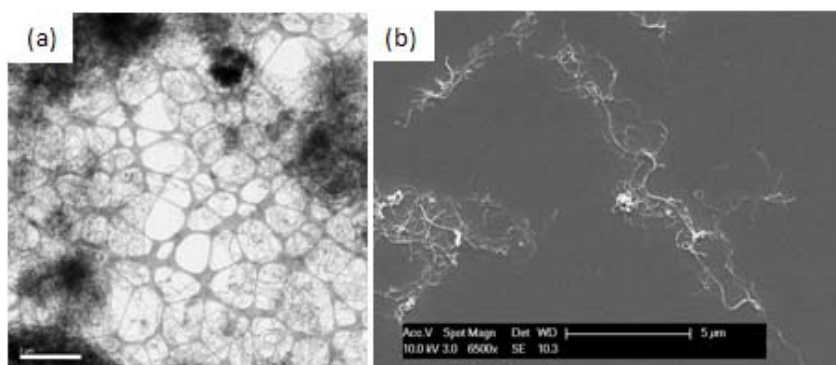


Figure 4.27: (a) The low-magnification TEM micrograph and (b) SEM micrograph of CVD CNTs which were used as a starting material for ball milling study. Scale bars are: 2 μm (a) and 5 μm (b).

Results of Raman spectroscopy

Upon employing different grinding conditions, we studied the quality of the final products by Raman spectroscopy (Fig. 4.28). The spectra of all CNT samples investigated in this study display a similar Raman fingerprint, as shown in Figure 4.28. The three well-known Raman bands - the tangential G band (at $\sim 1580 \text{ cm}^{-1}$), the defect induced D band (at $\sim 1350 \text{ cm}^{-1}$), and its overtone, the 2D or G' band (at $\sim 2690 \text{ cm}^{-1}$) – were clearly observed. The G band in the spectra of CNTs corresponds to the in-plane optical phonon mode of graphite and graphite-like materials (58). The D band is associated with the in-plane breathing of the hexagonal carbon rings (59) and signifies the presence of defects, such as vacancies, heptagon–pentagon pairs, and carbonaceous impurities with sp^3 bonding (60;

61). The 2D peak originates from a two-phonon second order scattering process (62) and indicates the presence of long-range order (61). A well-defined 2D peak is absent in amorphous carbon materials (59).

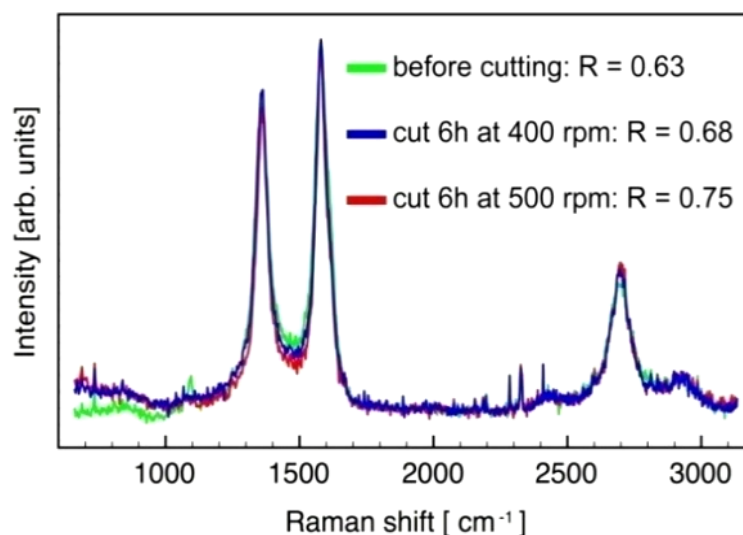


Figure 4.28: Raman spectra of different CNTs samples investigated in this study.

Raman spectroscopy is often used to compare the quality of different CNTs samples. This is usually done by calculating the D band to G band peak intensity ratios (I_D/I_G) for the investigated samples, where a high ratio indicates a sample of lower quality. Recent experiments have shown (61; 63; 64; 65) that in order to perform such a quality comparison the relative intensity of the 2D peak should also be considered. In fact, Larouche and Stansfield (66) have argued that the I_D/I_G ratio alone is not sufficient to adequately characterize the quality of graphitic materials, since it does not take into account the possible curvature and connection of the crystalline layers. They derived a new Raman index in order to properly assess the quality of these materials. This index can be expressed as the ratio of the integrated areas (A) of the 2D and D bands: $R = A(2D)/A(D)$, where a high R indicates higher crystalline quality (66).

Figure 4.28 shows that there are only very small differences in the Raman spectra of CNTs before and after cutting. We can confirm this by comparing the integrated area ratios for the spectra of these samples. The ratios were obtained by fitting single Lorentzians to the D and 2D peaks. The relatively small differences between these ratios for CNTs before cutting ($R = 0.63$) and CNTs after cutting ($R = 0.68$ for 6h at 400 rpm and $R = 0.75$ for 6h at 500 rpm) indicate that the quality of the CNT samples did not decrease during cutting. Surprisingly, the spectra show even a trend of increasing R as the degree of cutting intensifies. This might suggest that the quality of cut samples could be even higher than for pristine CNTs. The possible explanation of this trend could be associated to the removal of the trace amount of amorphous carbon during ball milling and / or to the decrease of initial defects due cutting 'through the defects'.

Length distributions and their analysis

Upon grinding, obtained CNTs lengths were measured from SEM micrographs (see Figure 4.29 for example SEM micrographs). We performed the statistical analysis of the length distributions for the obtained samples (see Appendix 1). As a result, we noticed that the location parameter, which is the mean of the logarithm of the lengths, linearly decreases with 'RPM*grinding time' until the product reached value of 2400, what can be seen in Fig. 4.30. For 'RPM*grinding time' value larger than 2400, like for instance for 3000, the observed dependence was not valid. This would suggest existence of upper limit for the conditions for CNTs cutting by ball milling. Previous studies of ball milling cutting of CNTs showed that after a certain time of cutting, a further increase of milling duration either did not change CNTs average length (51) or the relation between the milling time and the CNTs length became undefined (42). A study of Zhang *et al.* (38) showed that CNTs length decreased as a function of time until a certain period after which a disorder and a defect density of CNTs were increased and amorphous carbon appeared. These all studies also indicate the existence of an upper limit for the product 'RPM*grinding time'. Such behaviour was also observed for other CNTs cutting methods, like for sonication-induced scission (47).

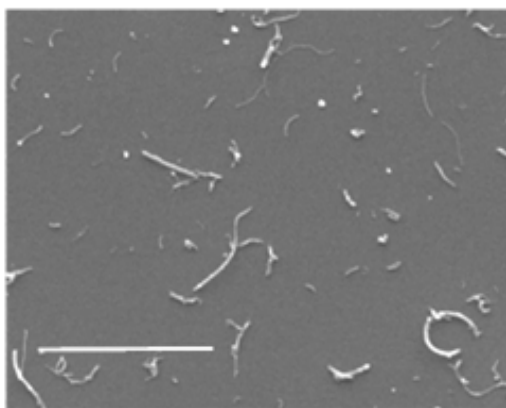


Figure 4.29: Example SEM micrograph used to measure the CNTs length after cutting (see the ref. [MM15]). Scale bar is 2 μm .

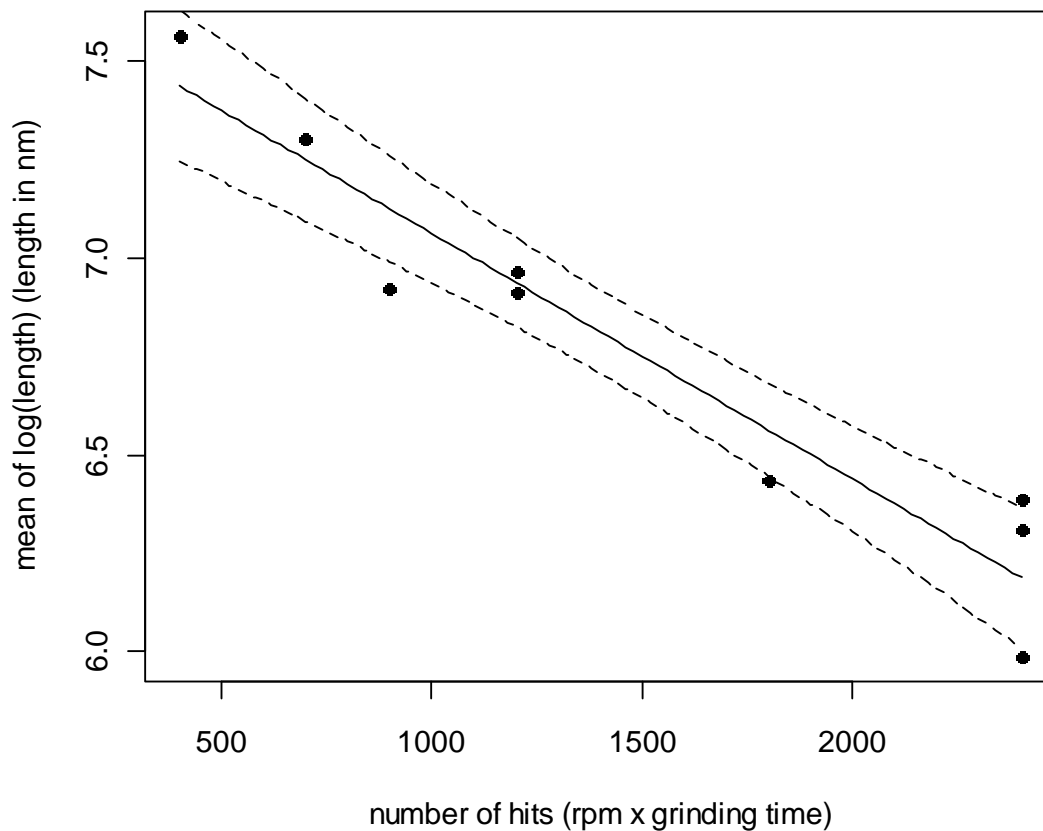


Figure 4.30: The linear dependence of the location parameter (mean of the $\log(\text{length})$) as a function of the product 'RPM*grinding time'. The dotted lines delimit the 95% confidence interval for the fitted line (see the ref. [MM15]).

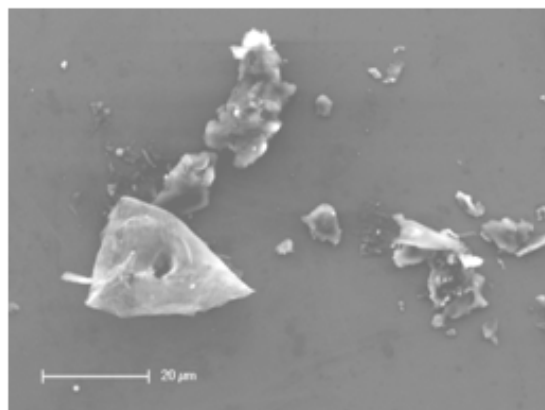


Figure 4.31: SEM micrograph of pieces of zirconium oxide balls found in the sample of CNTs milled for 6 h at 500 rpm. Scale bar is 20 μm .

However, in our study the upper 'RPM*grinding time' limit of 2400 cannot be attributed to the carbon amorphisation what was confirmed by the Raman study (Fig. 4.28). On the other hand, under this grinding condition with 'RPM*grinding time' of 3000, serious damage and mechanical degradation of zirconium oxide milling balls was observed. In fact,

pieces of zirconium oxide with sizes up to tens of micrometers were found in the samples ground for 6 h at 500 rpm (Fig. 4.31). Such large mechanical degradation of milling balls changed the effective contact surface of the balls. As a result, the grinding process became less efficient than with the balls having intact surfaces. Thus, the product 'RPM*grinding time' of 3000 was found unsuitable, due to the deterioration of the milling balls.

CNTs used for all presented results were (as mentioned in *Starting material*) CVD MWCNTs with average diameter 11.5 nm (75% of these CNTs had diameters below 15 nm) (see section 4.1 and the ref. [MM13]). Since we previously concluded that any hit of the ball cuts under all studied milling conditions, one could argue that this conclusion is valid only for the specific CNTs which were used here. In fact, it is known that CNTs diameter is related to the mechanical properties of CVD synthesized CNTs, particularly to the elastic modulus (3). Therefore, different energies would be required for braking CVD CNTs with different diameter. In order to check if our conclusion was affected by the CNTs' diameter, we used CNTs also produced by CVD method, but with average diameter 22 nm (for the details of diameter distribution and synthesis conditions see reference (2)). For the CVD CNTs with diameter of 11.5 nm and 22 nm, the corresponding elastic moduli are ~600 GPa and ~20 GPa, respectively (3). If CNTs cutting depended on the mechanical properties of CNTs used, the location parameter should be significantly different if we grind these two types of CNTs under the same grinding conditions. In order to check this possibility we ground CNTs with average diameter of 22 nm on the "edge" grinding conditions where the difference in obtained results should be the most noticeable. This conditions corresponds to grinding on 500 rpm over 6h, what is 'RPM*grinding time' value of 3000. The obtained location parameter for CNTs with average diameter of 22nm was 7.0, what is not significantly different then value of 6.8 for CNTs with average diameter of 11 nm ground under the same grinding conditions. As a result, our previous conclusions were independent of the diameter of CVD CNTs and thus, of their mechanical properties.

Cutting mechanism

All previous studies of CNTs cutting by ball milling (67; 68; 51; 52) were explaining CNTs cutting with essentially the same mechanism. Pierard *et al.* (51) stated that CNTs cutting occurs at places of structural defects such as curvatures and that breaking by compression occurs at "partly discontinuous" junctions of straight tube's segments. Moreover, CNTs held in matrix after dehydration break because they cannot absorb elastically the mechanical constraints like the tubes whose end is moving freely (51). Later Kónya *et al.* performed detailed study of end morphology of ball milled CNTs and they observed closed and open tube's ends which were either symmetric or asymmetric, what they supported by following argumentations (67). Kukovec *et al.*, from the same research group, in the later study (52), explained the appearance of the closed CNTs ends by the following reasoning: CNTs ends which were opened in the beginning of milling, were afterwards multiple times hit by the balls what initiated end closure. The recent study (68)

of Tucho *et al.* goes along with the study of the Hungarian group (67; 52). Before accepting or rejecting these opinions, it would be useful to firstly discuss some of the important aspects of this problem.

Actually, there is an interesting argument in the study of Kónya *et al.* (67) that the pressure generated during the ball milling process often reaches 2-6 GPa (where the two references given in this article just stated these pressure values without any explanation), but that these pressures are still not enough to break the CNTs by direct impact because the measured compressive strength of MWCNTs was beyond 5.3 GPa. Therefore, the authors concluded that CNTs are breaking in the points of kinks. We tried to go beyond this conclusion and to elaborate it further.

The first important point is contact area of ball impact. Considering ball impact by the Hertzian contact of a sphere and jar's wall or another sphere (69), for the ZrO₂ balls of 3 mm in diameter and the speeds used in this study, the contact area can be estimated to be even hundreds of μm^2 . Since initial CNTs length was about 10 μm and it was shorter with the milling duration, as a consequence, there can be lots of CNTs whose whole length could be covered by the area of single ball impact. If the impact energy, or the pressure generated during the impact of the ball would be high enough to break a CNTs, than whole CNTs' length in an impact cross-section would be smashed. This would rapidly create large quantities of amorphous carbon easily detectably by Raman measurement or by electron microscopy if amorphisation is substantial. Such behaviour was already observed by Tucho *et al.* They ball milled CVD MWCNTs for 1.3 h at a speed of 720 rpm with steel balls (10 mm in diameter) and CNTs were entirely changed into amorphous material, while at 520 rpm for different times, CNTs were transformed into nanoparticles and their tubular properties were almost gone (68). As a conclusion we think that the ball impact energy is not high enough to break the CNTs directly as long as carbon amorphisation is not observed.

Secondly, we took into consideration CNTs failure stress in order to relate CNTs breaking with the pressures generated during the ball milling process. Instead of searching the results of measurement of mechanical properties performed on other types of CNTs, we use data measured on CNTs produced in our labs and thus, compatible with starting material of this study. The average failure stress, measured in our group (70), for the CVD MWCNTs with diameter of 11 nm was ~ 140 GPa. Since our starting material are CVD MWCNTs with average diameter of 11.5 nm, the measured value of failure stress can be taken as a reasonable value for the CNTs used in this study. Since such high pressures are not developed during the ball milling process, we can consequently conclude that the ball impact cannot "directly" cut the CNTs.

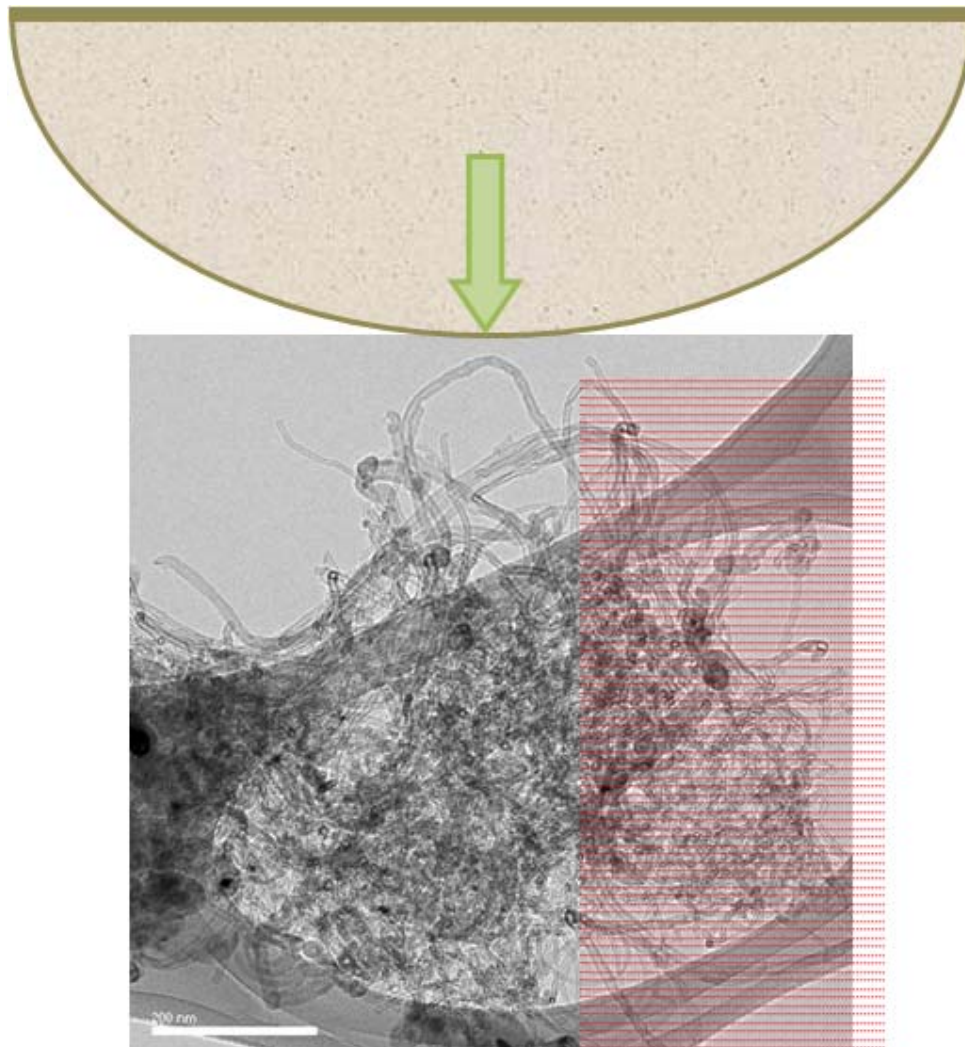


Figure 4.32: Schematic drawing of milling ball (brown) which is impacting CNTs aggregate. The red dotted lines indicate sliced layers of CNTs aggregate with the thickness roughly corresponding to the CNTs diameter. Scale bar on TEM micrograph is 200 nm.

As the last point, we considered more carefully “what is ground”. Simple consideration that the milling ball is impacting a few CNTs certainly cannot be accepted, because CVD CNTs are strongly entangled and aggregated. In Figure 4.27 (a), which shows typical image of CVD CNTs prior to cutting, we can see CNT aggregates of irregular shape with few micrometers wide spatial dimensions. Apparently, *the milling ball is impacting aggregates* and not few nicely separated CNTs. In this case, the impact can be seen like schematically presented in Figure 4.32.

Namely, the ball contact area is directly touching only surface layer of CNTs aggregate and this layer have roughly thickness of the order of diameter of CNTs. From this first layer, pressure generated by the ball milling impact is carried forward to the next layer which is beneath the first one. Only this time, the connections between the two adjacent layers are point contacts between the tubes’ segments from these two layers. Therefore,

the load transfer from each layer to the following one is carried by the tube-tube point contacts. Thus, all stress is concentrated at significantly smaller contact area of these points, comparing to the contact area of the first layer of aggregate (for which we assumed that approximately corresponds to the cross-section of the ball impact with the solid surface). It seems logical to assume that the tubes are cutting each other at these points of contact and that balls are actually cutting tubes “indirectly” over load transfer through significantly reduced area.

The proposed cutting mechanism by tube-tube cutting initiated by the ball impact can proceed in different ways. More precisely there are two possibilities of CNT-CNT cutting as schematically depicted in Figure 4.33: [a] one tube cut the other (which is suspended in CNTs network) and the segments of these two tubes are under the angle α ($0^\circ < \alpha \leq 90^\circ$) in the point of their crossing, and [b] two tubes (t_2 and t_3) are crossing over the segment of third tube (t_1) which get cut. In the second case the sum of the angles between tubes, α and β (like indicated in Figure 4.33 (b)) is less than 180° .

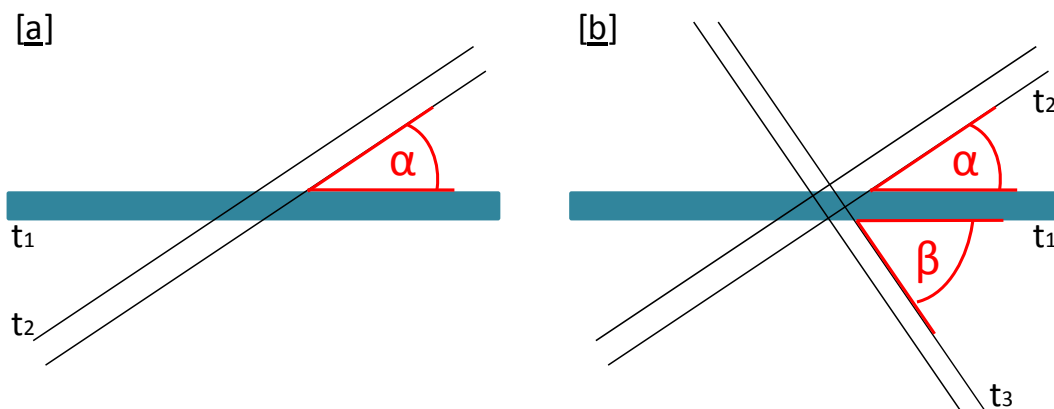


Figure 4.33: Schematic drawing of the proposed CNTs cutting mechanism where tube 1 (t_1), subjected to cutting, can be cut by: [a] the other tube (t_2) under the angle α in the crossing point, or [b] the other two tubes, t_2 and t_3 , forming the angles α and β , respectively.

Study of the edges of cut CNTs by HR TEM clearly confirmed our proposed theory of the CNTs cutting mechanism. Figure 4.34 shows HR TEM micrographs of cut CNTs edges as an example for the case that cutting proceeds by the mechanism [a], one tube cut the other under the angle α ; the micrographs are sorted out that the first shows an example of $\alpha \approx 90^\circ$ (Fig. 4.34 (a)), followed by the decrease of the angle (Fig. 4.34 (b)). The rarely observed examples of CNTs cut by the same mechanism [a], but with even lower values of angle α ($\sim 30^\circ$ and less), can be seen in Figure 4.34 (c). From that figure is obvious that values of $\alpha \rightarrow 0^\circ$ are supporting appearance of gliding and hence, they are unfavourable for “clear” and good cut without tube’s damage.

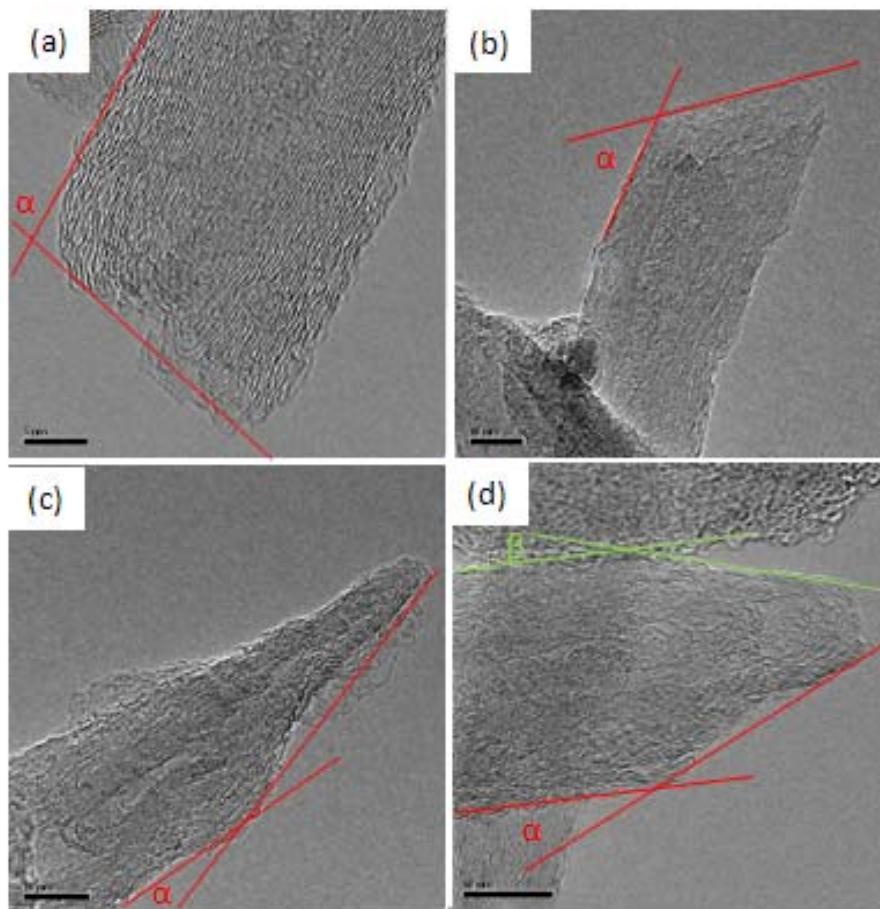


Figure 4.34: HR TEM micrographs of cut CNTs edges as an example for the case that cutting proceeds by the mechanism [a] where one tube cut the other under the angle α , starting with $\alpha \approx 90^\circ$ (a) followed by the decrease of the angle (b) and (c). (d) An example of CNTs cutting by the mechanism [b]. Angles ' α ' and ' β ' are marked by red and green, respectively. Scale bars are: 5 nm (a); 10 nm (b), (c), (d).

The curvature on the edges of cut CNTs obviously suggests the cutting mechanism in which CNTs cut each other (Fig. 4.34 (c) and (d)). Many tube ends are not cut straight, but rather seem to have been impressed by objects of similar curvature as the CNTs. Thus, our proposed cutting mechanism, that the tubes that are caught in between colliding balls or ball and wall of the milling jar, cut each other, naturally leads to the observed damage pattern, without invoking very complicated defect formation mechanism.

Furthermore, if the proposed cutting mechanism is correct, it should be possible to find the CNTs which were cutting some other tubes, but simultaneously they remained uncut. In such case, it would be expected that these tubes would have remaining fingerprints of cutting in the form of side-wall dents with profile corresponding to the other tube subjected to cutting. Indeed, such tubes were observed as it can be seen in Figure 4.35, where red arrows point out to the dents on the surface of the unsuccessfully cut tubes which were probably cutting the other tubes.

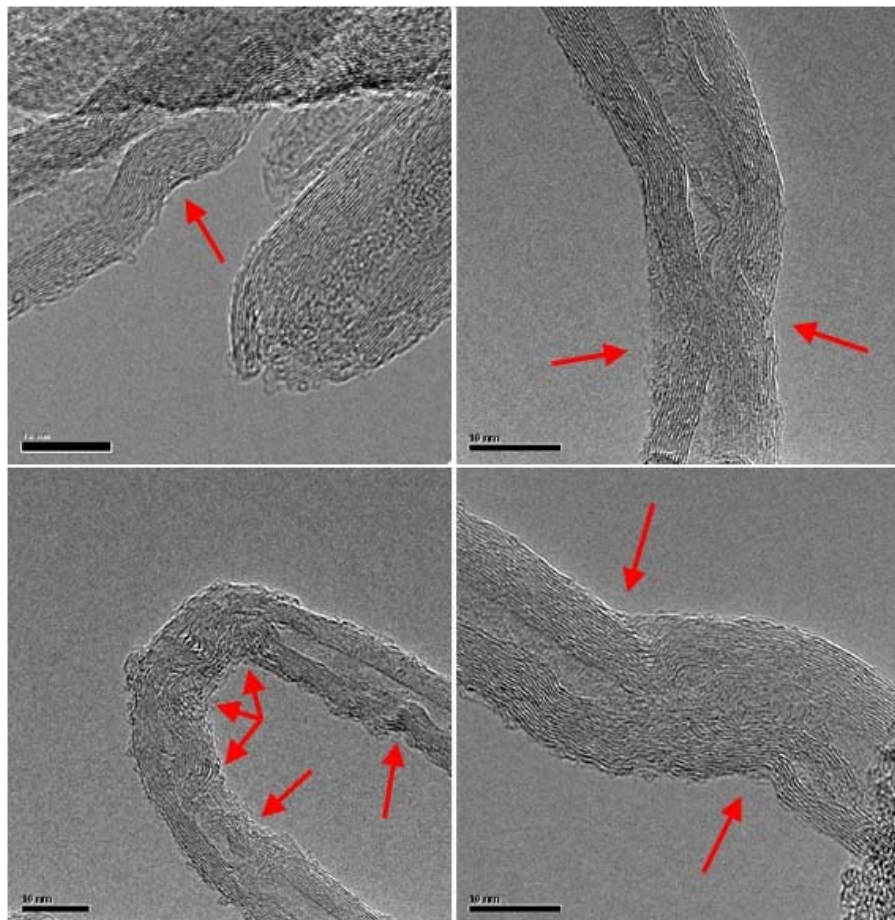


Figure 4.35: HR TEM micrographs of CNTs after the ball milling. The red arrows point out to the dents on the surface of the uncut tubes which were probably cutting the other tubes. Scale bars are 10 nm.

4.3.2 Conclusions

We studied which parameters influence the average length of ground CNTs for the cutting process by planetary ball milling. Average length of CNTs ground by planetary ball milling is not a function of energy and CNTs mechanical properties, but only is a function of the number of hits defined as the product of the grinding time and rpm. In conclusion, the required CNT's length can be achieved by simple choosing the value of the product 'RPM*grinding time' for the planetary ball milling process according to the dependence presented in Figure 4.30. The only limitation found for this process was the rpm value of 400, above which degradation of the employed milling balls took place.

References

1. **M. S. Dresselhaus, G. Dresselhaus and Ph. Avouris (Eds.).** *Carbon Nanotubes Synthesis, Structure, Properties, and Applications*. s.l. : Springer, Topics in Applied Physics , 2001. Vol. 80.
2. *Multiwalled Carbon Nanotubes Produced by a Continuous CVD Method and Their Use in Melt Mixed Composites with Polycarbonate.* **P. Pötschke, D. Fischer, F. Simon, L. Häußler, A. Magrez and L. Forró.** 2007, *Macromol. Symp.*, Vol. 254, p. 392.
3. *Diameter-Dependent Elastic Modulus Supports the Metastable-Catalyst Growth of Carbon Nanotubes.* **K. Lee, B. Lukic, A. Magrez, J.W. Seo, G.A.D. Briggs, A.J. Kulik and L. Forró.** 2007, *Nano Letters*, Vol. 7, p. 1598.
4. *Molecular dynamics study of the catalyst particle size dependence on carbon nanotube growth.* **F. Ding, A. Rosén, and K. Bolton.** 6, 2004, *J. Chem. Phys.*, Vol. 121, p. 2775.
5. *Reduced Carbon Solubility in Fe Nanoclusters and Implications for the Growth of Single-Walled Carbon Nanotubes.* **A. R. Harutyunyan, N. Awasthi, A. Jiang, W. Setyawan, E. Mora, T. Tokune, K. Bolton and S. Curtarolo.** 2008, *Phys. Rev. Lett.*, Vol. 100, p. 195502.
6. *The Importance of Strong Carbon-Metal Adhesion for Catalytic Nucleation of Single-Walled Carbon Nanotubes.* **F. Ding, P. Larsson, J. A. Larsson, R. Ahuja, H. Duan, A. Rosn and K. Bolton.** 2, 2008, *Nano Lett.*, Vol. 8, p. 463.
7. *Diameter-Controled Synthesis of Carbon Nanotubes.* **C. L. Cheung, A. Kurtz, H. Park, and C. M. Lieber.** 2002, *J. Phys. Chem. B*, Vol. 106, p. 2429.
8. *Nanoengineered Catalyst Particles as a Key for Tailor-Made Carbon Nanotubes.* **F. Schäffel, C. Kramberger, M. H. Rummeli, D. Grimm, E. Mohn, T. Gemming, T. Pichler, B. Rellinghaus, B. Büchner and L. Schultz.** 2007, *Chem. Mater.*, Vol. 19, p. 5006.
9. *Synthesis of single- and multi-wall carbon nanotubes over supported catalyst.* **A. Fonseca, K. Harnadi, P. Piedigrosso, J.-F. Colomer, K. Mukhopadhyay, R. Doome, S. Lazarescu, L. P. Biro, Ph. Lambin, P. A. Thiry, D. Bernaerts and J. B. Nagy.** 1998, *Applied Physics A*, Vol. 67, p. 11.
10. *The Influence of Catalyst Chemical State and Morphology on Carbon Nanotube Growth.* **T. de los Arcos, M. G. Garnier, J. W. Seo, P. Oelhafen, V. Thommen and D. Mathys.** 2004, *J. Phys. Chem. B*, Vol. 108, p. 7728.
11. *The role of precursor gases on the surface restructuring of catalyst films during carbon nanotube growth.* **S. Pisana, M. Cantoro, A. Parvez, S. Hofmann, A. C. Ferrari and J. Robertson.** 2007, *Physica E*, Vol. 37, p. 1.
12. *In situ Observations of Catalyst Dynamics during Surface-Bound Carbon Nanotube Nucleation.* **S. Hofmann, R. Sharma, C. Ducati, G. Du, C. Mattevi, C. Cepek, M. Cantoro, S. Pisana, A. Parvez, F. Cervantes-Sodi, A. C. Ferrari, R. Dunin-Borkowski, S. Lizzit, L. Petaccia, A. Goldoni and J. Robertson.** 3, 2007, *Nano Lett.*, Vol. 7, p. 602.
13. *State of Transition Metal Catalysts During Carbon Nanotube Growth.* **S. Hofmann, R. Blume, C. T. Wirth, M. Cantoro, R. Sharma, C. Ducati, M. Hävecker, S. Zafeiratos, P. Schnoerch, A. Oestereich, D. Teschner, M. Aldrecht, A. Knop-Gericke, R. Schlögl and J. Robertson.** 2009, *J. Phys. Chem. C*, Vol. 113, p. 1648.
14. *CVD synthesis of high-purity multiwalled carbon nanotubes using CaCO₃ catalyst support for large-scale production.* **E. Couteau, K. Hernadi, J.W. Seo, L. Thien Nga, Cs. Mikó, R. Gaál and L. Forró.** 2003, *Chem. Phys. Lett.*, Vol. 9, p. 378.
15. *Catalytic growth of single-walled nanotubes by laser vaporization.* **T. Guo, P. Nikolaev, A. Thess, D.T. Colbert and R.E. Smalley.** 1995, *Chemical Physics Letters*, Vol. 243, p. 49.
16. *Growth of Carbon Nanotubes with Alkaline Earth Carbonate as Support.* **A. Magrez, J. W. Seo, C. Mikó, K. Hernádi and L. Forró.** 2005, *J. Phys. Chem. B*, Vol. 109, p. 10087.

17. **H. P. Klug and L. E. Alexander.** X-ray Diffraction Procedures. 2nd ed. New York : Wiley-Interscience, 1974. pp 687-707.
18. *Hydrolysis of inorganic iron(III) salts.* **C. M. Flynn Jr.** 1, 1984, Chem. Rev., Vol. 84, p. 31.
19. *CaCO₃ supported Co-Fe catalysts for carbon nanotube synthesis in fluidised bed reactors.* **C. H. See and A. T. Harris.** 3, 2008, AIChE Journal, Vol. 54, p. 657.
20. **D. F. Shriver and P. W. Atkins.** *Inorganic Chemistry.* Third edition. s.l. : Oxford University Press, 1999.
21. *Interactions of CaCO₃ Minerals in Electrolyte Solutions.* **P. Kaushansky.** 1982, Ind. Eng. Chem. Prod. Res. Dev., Vol. 21, p. 182.
22. *Sorption of divalent metals on calcite.* **J. M. Zachara, C. E. Cowan and C. T. Resch.** 1991, Geochimica et Cosmochimica Acta, Vol. 55, p. 1549.
23. *Exchange-Coupled Bimagnetic Cobalt/Iron Oxide Branched Nanocrystal Heterostructures.* **M. Casavola, A. Falqui, M. A. Garcia, M. Garcia-Hernandez, C. Giannini, R. Cingolani and P. D. Cozzoli.** 1, 2009, Nano Lett., Vol. 9, p. 366.
24. *Role of Water in Super Growth of Single-Walled Carbon Nanotube Carpets.* **P. B. Amama, C. L. Pint, L. McJilton, S. M. Kim, E. A. Stach, P. T. Murray, R. H. Hauge and B. Maruyama.** 1, 2009, Nano Lett., Vol. 9, p. 44.
25. *Printing gel-like catalysts for the directed growth of multiwall nanotubes.* **H. Kind, J. Bonard, L. Forro, K. Kern, K. Harnadi, L. Nilsson and L. Schlapbach.** 2000, Langmuir, Vol. 16, p. 6877.
26. *Co-Fe (Cobalt-Iron).* **H. Okamoto.** 4, 2008, Journal of Phase Equilibria and Diffusion, Vol. 29, p. 383.
27. *Ordering and phase separation in alloys of the Fe–Co system.* **Y. Ustinovshikov and B. Pushkarev.** 1-2, 2006, Journal of Alloys and Compounds, Vol. 424, p. 145.
28. *Uniform Heterogeneous Catalysts: The Role of Solid-state Chemistry in their Development and Design.* **J. M. Thomas.** 1988, Angew. Chem. Int. Ed. Eng., Vol. 12, p. 1673.
29. *Selective oxidation of isobutene to methacrolein on multiphasic molybdate-based catalysts.* **S. R. G. Carrazan, C. Martin, V. Rives and R. Vidal.** 1995, Applied Catalysis A: General, Vol. 135, p. 95.
30. *Formation mechanism of single-wall carbon nanotubes on liquide-metal particles.* **H. Kanzow and A. Ding.** 15, 1999, Physical Review B, Vol. 60, p. 11180.
31. *Nanoscale Zirconia as a Nonmetallic Catalyst for Graphitization of Carbon and Growth of Single- and Multiwall Carbon Nanotubes.* **S. A. Steiner III, T. F. Baumann, B. C. Bayer, R. Blume, M. A. Worsley, W. J. MoberlyChan, E. L. Shaw, R. Schlögl, A. J. Hart, S. Hofmann and B. L. Wardle.** 34, 2009, Journal of American Chemical Society, Vol. 131, p. 12144.
32. *Mesoporous silicates as nanoreactors for synthesis of carbon nanotubes.* **M. Urban, Z. Konya, D. Mehn, J. Zhub and I. Kiricsi.** 2002, PhysChemComm, Vol. 5, p. 138.
33. *Formation of carbon nanotubes in counter-flow, oxy-methane diffusion flames without catalyst.* **W. Merchan-Merchan, A. Saveliev, L. A. Kennedy and A. Fridman.** 2002, Chemical Physics Letters, Vol. 354, p. 20.
34. *On the Graphitization Nature of Oxides for the Formation of Carbon Nanostructures.* **M. H. Rummeli, C. Kramberger, A. Grüneis, P. Ayala, T. Gemming, B. Büchner and T. Pichler.** 17, 2007, Chemistry of Materials, Vol. 19, p. 4105.
35. *The Radiation Chemistry of Acetylene: 1. Rare Gas Sensitization. II. Wall Effect in Benzene Formation.* **L. M. Dorfman and A. C. Wahl.** 1956, Radiation Research, Vol. 10, p. 680.
36. **N. Agenet, O. Buisine, F. Slowinski, V. Gandon, C. Aubert and M. Malacria.** *Cotrimerizations of Acetylenic Compounds.* s.l. : John Wiley & Sons, Inc., 2004.

37. *Bulk production of singly dispersed carbon nanotubes with prescribed lengths.* **G. B. Onoa, T. B. O'Reilly, M. E. Walsh and H. I. Smith.** 2005, *Nanotechnology*, Vol. 16, p. 2799.
38. *Improve the field emission uniformity of carbon nanotubes treated by ball-milling process.* **Z. Zhang, Z. Sun and Y. Chen.** 2007, *Applied Surface Science*, Vol. 253, p. 3292.
39. *Field Emission Properties of Short Crystalline Carbon Nanotubes Cut by Sonication on Substrate.* **S.-H. Jeong and K.-H. Lee.** 8B, 2004, *Japanese Journal of Applied Physics*, Vol. 43, p. L1106.
40. *Improved field emission stability of thin multiwalled carbon nanotube emitters.* **G. Chen, D. H. Shin, S. Kim, S. Roth and C. J. Lee.** 2010, *Nanotechnology*, Vol. 21, p. 015704.
41. *Fullerene Pipes.* **J. Liu, A. G. Rinzler, H. Dai, J. H. Hafner, R. K. Bradley, P. J. Boul, A. Lu, T. Iverson, K. Shelimov, C. B. Hoffman, F. R. Macias, Y. S. Shon, T. R. Lee, D. T. Colbert and R. E. Smalley.** 1998, *Science*, Vol. 280, p. 1253.
42. *Preparation of short carbon nanotubes by mechanical ball milling and their hydrogen adsorption behaviour.* **F. Liu, X. Zhang, J. Cheng, J. Tu, F. Kong, W. Huang and C. Chen.** 2003, *Carbon*, Vol. 41, p. 2527.
43. *Preparation and electrochemical performance of ultra-short carbon nanotubes.* **X. X. Wang, J. N. Wang and L. F. Su.** 2009, *Journal of Power Sources*, Vol. 186, p. 194.
44. *Lithographically Cut Single-Walled Carbon Nanotubes: Controlling Length Distribution and Introducing End-Group Functionality.* **S. R. Lustig, E. D. Boyes, R. H. French, T. D. Gierke, M. A. Harmer, P. B. Hietpas, A. Jagota, R. S. McLean, G. P. Mitchell, G. B. Onoa and K. D. Sams.** 8, 2003, *Nano Letters*, Vol. 3, p. 1007.
45. *Synthesis of Length-Controlled Aerosol Carbon Nanotubes and Their Dispersion Stability in Aqueous Solution.* **Y. K. Moon, J. Lee, J. K. Lee, T. K. Kim and S. H. Kim.** 2005, *Langmuir*, Vol. 25, p. 1739.
46. *The Mechanism of Cavitation-Induced Scission of Single-Walled Carbon Nanotubes.* **F. Henrich, R. Krupke, K. Arnold, J. A. R. Stutz, S. Lebedkin, T. Koch, T. Schimmel and M. M. Kappes.** 2007, *J. Phys. Chem. B*, Vol. 111, p. 1932.
47. *Strength of Nanotubes, Filaments, and Nanowires From Sonication-Induced Scission.* **Y. Y. Huang, T. P. J. Knowles and E. M. Terentjev.** 2009, *Adv. Mater.*, Vol. 21, p. 3945.
48. *Mechanical Damage of Carbon Nanotubes by Ultrasound.* **K. L. Lu, R. M. Lago, Y. K. Chen, M. L. H. Green, P. J. F. Harris and S. C. Tsang.** 6, 1996, *Carbon*, Vol. 34, p. 814.
49. *Controlled Oxidative Cutting of Single-Walled Carbon Nanotubes.* **K. J. Ziegler, Z. Gu, H. Peng, E. L. Flor, R. H. Hauge and R. E. Smalley.** 2005, *Journal of American Chemical Society*, Vol. 127, p. 1541.
50. *Oxygen-Containing Functional Groups on Single-Wall Carbon Nanotubes: NEXAFS and Vibrational Spectroscopic Studies.* **A. Kuznetsova, I. Popova, J. T. Yates, Jr., M. J. Bronikowski, C. B. Huffman, J. Liu, R. E. Smalley, H. H. Hwu and J. G. Chen.** 43, 2001, *Journal of American Chemical Society*, Vol. 123, p. 10699.
51. *Production of short carbon nanotubes with open tips by ball milling.* **N. Pierard, A. Fonseca, Z. Konya, I. Willems, G. Van Tendeloo and J. B. Nagy.** 2001, *Chemical Physics Letters*, Vol. 335, p. 1.
52. *Long-time low-impact ball milling of multi-wall carbon nanotubes.* **A. Kukovecz, T. Kanyo, Z. Konya and I. Kiricsi.** 2005, *Carbon*, Vol. 43, p. 994.
53. *Cutting of carbon nanotubes by a two-roller mill.* **L. Chen, X. Pang, Q. Zhang and Z. Yu.** 2006, *Materials Letters*, Vol. 60, p. 241.
54. *Effect of ball milling on morphology of cup-stacked carbon nanotubes.* **Y. A. Kim, T. Hayashi, Y. Fukai, M. Endo, T. Yanagisawa and M. S. Dresselhaus.** 2002, *Chemical Physics Letters*, Vol. 355, p. 279.
55. [Online] 02. 10. 2011. <http://www.ncnr.nist.gov/userlab/pdf/E133fritschpulverisette.pdf>.

56. [Online] [Cited: 02. 10. 2011.] http://www.retsch.com/dltmp/www/115997-0eae732a479e/brochure_planetary_ball_mills_en.pdf.
57. [Online] 02. 10. 2011. http://www.fritsch.de/uploads/media/ba_074000_0487_e_01.pdf.
58. *Raman spectroscopy of carbon nanotubes*. **M. S. Dresselhaus, G. Dresselhaus, R. Saito and A. Jorio**. 2005, Phys. Rep., Vol. 409, p. 47.
59. *Interpretation of Raman spectra of disordered and amorphous carbon*. **A. C. Ferrari and J. Robertson**. 2000, Phys. Rev. B., Vol. 61, p. 14095.
60. *Characterizing carbon nanotube samples with resonance Raman scattering*. **A. Jorio, M. A. Pimenta, A. G. Souza Filho, R. Saito, G. Dresselhaus and M. S. Dresselhaus**. 2003, New J. Phys., Vol. 5, p. 139.1.
61. *Purity assessment of multiwalled carbon nanotubes by Raman spectroscopy*. **R. A. DiLeo, B. J. Landi and R. P. Raffaele**. 2007, J. Appl. Phys., Vol. 101, p. 064307.
62. *Double resonance Raman spectroscopy of single-wall carbon nanotubes*. **R. Saito, A. Grüneis, Ge G. Samsonidze, V. W. Brar, G. Dresselhaus, M. S. Dresselhaus, A. Jorio, L. G. Cançado, C. Fantini, M. A. Pimenta and A. G. Souza Filho**. 2003, New J. Phys., Vol. 5, p. 157.1.
63. *Surface Characterizations of Carbon Multiwall Nanotubes: Comparison between Surface Active Sites and Raman Spectroscopy*. **C. Vix-Guterl, M. Couzi, J. Dentzer, M. Trinqucoste and P. Delhaes**. 2004, J. Phys. Chem. B, Vol. 108, p. 19361.
64. *A comparison between Raman spectroscopy and surface characterizations of multiwall carbon nanotubes*. **P. Delhaes, M. Couzi, M. Trinqucoste, J. Dentzer, H. Hamidou and C. Vix-Guterl**. 2006, Carbon, Vol. 44, p. 3005.
65. *Calibration of reaction parameters for the improvement of thermal stability and crystalline quality of multi-walled carbon nanotubes*. **S. Santangelo, G. Messina, G. Faggio, M. Lanza, A. Pistone and C. Milone**. 2010, J. Mater. Sci., Vol. 45, p. 783.
66. *Classifying nanostructured carbons using graphitic indices derived from Raman spectra*. **N. Larouche and B. L. Stansfield**. 2010, Carbon, Vol. 48, p. 620.
67. *End morphology of ball milled carbon nanotubes*. **Z. Konya, J. Zhu, K. Niesz, D. Mehn and I. Kiricsi**. 2004, Carbon, Vol. 42, p. 2001.
68. *The effects of ball milling intensity on morphology of multiwall carbon nanotubes*. **W. M. Tucho, H. Mauroy, J. C. Walmsley, S. Deledda, R. Holmestad and B. C. Hauback**. 2010, Scripta Materialia, Vol. 63, p. 637.
69. **W. C. Young and R. G. Budynas**. *Roark's formulas for stress and strain*. 7th ed. New York : McGraw-Hill, 2002.
70. **M. Duchamp**. *Growth and Optical, Electrical and Mechanical Characterization of Zinc Oxide Nanowires*. Lausanne : EPFL, 2010. Thesis No 4623.

Chapter 5

CNTs-SU8 composites and their properties

CNTs are considered to be the most suitable reinforcing fibres in polymer-based composites, where they lead to dramatic improvement of electrical, thermal and mechanical properties (1). However, the design of polymer and CNTs-based composites remains a big challenge. It is well known that CNTs have a strong tendency to aggregate and their homogeneous dispersion in the great majority of media is extremely difficult. The major reason for this is the strong hydrophobic character of CNTs. In colloidal suspensions CNTs, large, fiber-like and hydrophobic macromolecules are thermodynamically unstable and require stabilization (2). Indeed, CNTs are difficult to dissolve or disperse in most organic or inorganic solvents because of their stable, long structure consisting exclusively of carbon atoms. Inter-tube interactions within the CNTs are dominated by van der Waals interactions of high cohesive energy (3). Therefore, CNTs have a tendency to aggregate due to extremely high surface energy, which is, *e.g.* of 123 mJ/m^2 at 37°C for multi walled CNTs (4). Clearly, such strong aggregation of CNTs results in their low solubility and low dispersability. This may affect the mechanical and electronic properties of the composites, and thus, represents a serious difficulty in designing CNTs-based composites.

All CVD produced CNTs have defects, what leads to local fluctuations of charge density that may cause interaction of different segments of one CNT or between different CNTs. Since the overall shape (macroconformation) of CNT depends on inter- and intramolecular interactions, which can be short- and long-range, the CNTs defects can significantly influence final CNT's shape often yielding significantly entangled and curved structures (Fig. 5.1 (a)).

There are several possible routes towards the surface modification of hydrophobic molecules to suppress aggregation. The most important are: chemical modification of the molecule's surface (Fig. 5.1 (b) A) (5; 6) and adsorption of surfactants (Fig. 5.1 (b) B) (7; 8; 9). However, both methods involve some disadvantages. Surface modification of CNTs means covalent bonding of functional groups to CNTs surface. Such covalent modification of CNTs often leads to impairing of their mechanical and electrical properties (10), and to a change in the electronic structure (5). The methods based on surfactants are either restricted to low concentrations of CNTs (7) or they can induce additional problems, due to the chemical interactions with some of the components in a complex chemical systems, like for example photosensitive composites.

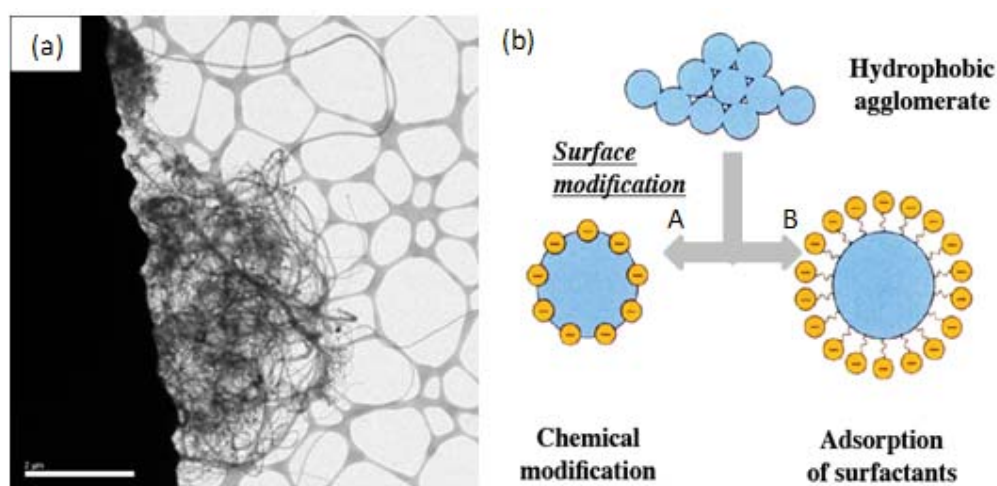


Figure 5.1: (a) TEM micrograph of CVD CNTs (scale bar is 2 μm). (b) Two possible routes to avoid aggregation of strongly hydrophobic macromolecules in colloidal suspensions: by chemical modification of surface (A) and by adsorption of surfactants (b) (from the ref. (2)).

At this point, we need to focus on a very important detail. In particular, in the field of composites, it is often claimed that simultaneous “good dispersion” of the filler and the “low filler percolation threshold” are prerequisite for obtaining good electrical conductivity. These statements might lead to some misinterpretations. In fact, “good dispersion” means that the fillers are so far away of each other that they do not “feel each other” or in other words, there are no any interactions among them, meaning distribution without agglomeration and aggregation. In contrast, having “percolation threshold” means that the fillers are touching each other (aggregation). Therefore having a good dispersion means no percolation threshold, and thus, no electrical conductivity. What might be then behind this ‘misunderstanding’?

Clearly, to obtain composites with good electrical conductivity, the CNT fillers aggregation must be controlled. Probably the best approach is to have them firstly very well dispersed. But, when a suspension with well dispersed objects is exposed to a change of certain parameters, like temperature, volume or pressure, the objects will undergo

aggregation. Then, the main point is to establish the actual mechanism of aggregation occurring between the fillers particles or their clusters that is: the Eden model, ballistic and diffusion-limited aggregation (DLA) (11). The basic forms of these aggregation types are shown in Figure 5.2. The Eden model aggregation type apparently cannot provide percolation with low concentration, while the other types can, with differences in the necessary fillers fractions.

In principle, aggregation can provide touching of CNTs in such a way that they provide conductive path for the current. Therefore, if one aims to make electrically conductive composites from the suspensions, the way to do it is by destabilizing the initially good dispersion by altering it towards aggregation. This should result in formation of numerous electrical contacts, which are necessary for achieving percolation. In the case of our composites, destabilisation of the dispersion can be due to the change in temperature (followed by volume change), or by the induced 2D or 1D confinement, by making thin layers or by passing the suspension through the cables and nozzle of an inkjet system, respectively. Consequently, while preparing CNTs-SU8 composites, we firstly need to well disperse CNTs in the solution containing all the components, *i.e.* SU8, the solvent of SU8, the PI, and the solvent for the PI. The above-mentioned destabilization of such a well-dispersed CNTs suspension should result in the desired aggregation type, thus, leading to the formation of percolating CNTs network.

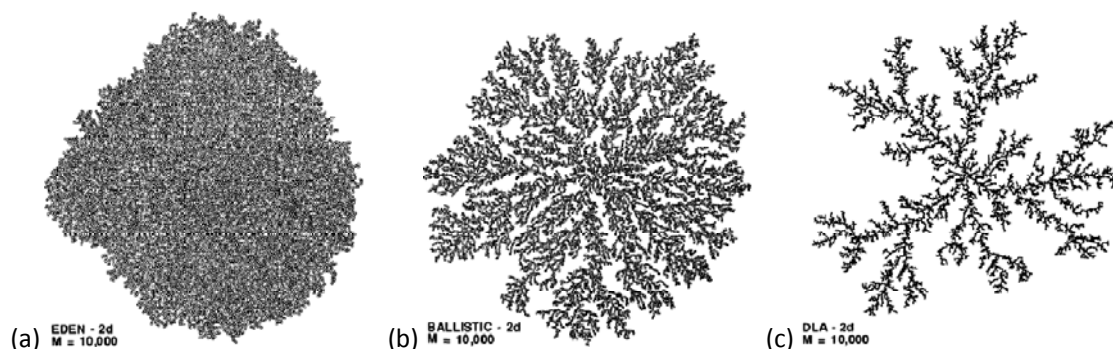


Figure 5.2: Aggregation types: (a) the Eden model, (b) ballistic and (c) diffusion limited (from the ref. (11)). All images are given for the 2D aggregations, what corresponds to our system, because composite samples were prepared in the form of thin films.

It needs to be pointed out that conditions for percolation threshold for enhanced electrical, thermal and mechanical properties are not necessarily the same. In fact, the electrical conductivity can be obtained by aggregation of fillers in a randomly oriented network (like in Fig. 5.2 (c)) with good intertube contacts. On the other hand, perfect filler alignment is favourable for thermal conductivity, but is not prerequisite for achieving good electrical and mechanical properties. In order to enhance mechanical properties one would need a network of interconnected fillers and good CNTs-matrix interface. Since we aimed to achieve enhancement of all three above-mentioned properties, we needed to optimally balance the aggregation type of CNTs. Therefore, to transfer the advantageous properties of

CNTs on the final composite and achieve simultaneous enhancement of thermal and electrical conductivity and improvement of mechanical properties, we needed to assemble CNTs in networks. In such inter-connected network systems, CNTs were contacting each other by overlapping and crossing. Final films of composite containing CNTs and SU8 is both physically interlocked (CNTs) and chemically cross-linked (SU8) non-regular network.

5.1 CNTs-SU8 composites 1

5.1.1 Dispersion of CNTs in SU8

In order to suppress CNTs aggregation we firstly tried chemical modification of the CNTs' surface by covalent functionalisation with carboxyl groups (-COOH). We also studied the influence of solvents used for composite preparation on the formation of CNTs networks within the composite materials, because it is well known that in a good solvent CNTs would be elongated (stretched) and in a bad one squeezed in a coil-shaped structure.

The solubility of SU8 was tested in 8 solvents (Table 5.1). SU8 was insoluble in NN-dimethylacetamide and water. The solution prepared by dissolving SU8 at 50°C in 1-methyl-2-pyrrolidone was not stable and therefore not suitable to prepare homogeneous composites. Complete dissolution of SU8 was achieved with five other solvents: GBL, PGMEA, MEK, acetone and benzene (Table 5.1). Subsequently, they were employed to prepare SU8-CNTs composites with 5 w% of CNTs. After CNTs dispersion in the solvent, SU8 and PI were added followed by vigorous stirring (see Chapter 3).

Solvent	SU8 solubility	Solution Stability
GBL	yes	yes
PGMEA	yes	yes
MEK	yes	yes
acetone	yes	yes
benzene	yes	yes
1M2P	yes above 50°C	becomes murky upon cooling
N,N-DMAA	no	
distilled water	no	

Table 5.1: SU8 solubility test in different solvents.

5.1.2 Nanoindentation

The mechanical uniformity of the composites was tested by nanoindentation. This technique is the usual way to characterise films by providing information about the mechanical response (see Chapter 3) at the surface and in the vicinity of surface, what is often important for the materials in the form of films.

For structurally homogeneous samples the load-displacement curves for 25 indents were overlapping, while for the inhomogeneous ones a noticeable scattering was recorded. The scattering in the data points depended on the solvent and not on the functionalization of the CNTs. For example, the composites prepared with MEK as a solvent for both types of CNTs, the load-displacement curves superpose (Fig. 5.3) indicating the homogeneous structure of the samples. For composites prepared with other solvents, load-displacement curves have shown scattering. This suggests a strong influence of the solvent on the structural and mechanical uniformity of the composites.

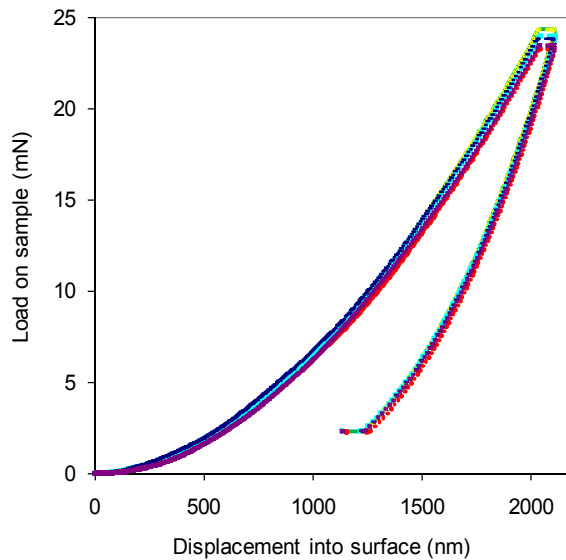


Figure 5.3: Load-displacement curves for samples prepared with MEK with not functionalized CNTs. For the visibility only five representative curves are shown (out of 25 curves recorded), since all curves were overlapping.

Nanoindentation allows the measurement of the Young-modulus as a function of penetration, thus allows assessment of the uniformity. Figure 5.4 shows E_Y versus penetration depth into the surface deduced from the load-displacement curves. Usually, the steep variations below 200 nm are considered as artifacts of surface imperfections and they are omitted. In most of the cases a decrease of E_Y with the indentation depth was observed.

Our working hypothesis is that the strong depth dependence of the mechanical response is due to solvent remaining trapped in the composite. It is known that solvent can remain even in the non-reinforced SU8 matrix upon polymerization (12). The mechanism is the following:

the solvent leaves the surface of the composite rapidly, and allows a quick polymerization of SU8 at the surface. This dense network would block the evaporation of the solvent molecules from the bulk, trapping them inside the material. This is the case for all solvents, and the behaviour of the trapped solvent determines the properties of the polymer, leading to a gradient of the Young's modulus in the cross section of the sample, like it was observed by nanoindentation (Fig. 5.4). The quantity of the remaining solvent depends on many parameters like the thickness of the SU8 layer, heating rate, process temperatures, the solvent type and the volume percentage of the polymer with respect to the solvent.

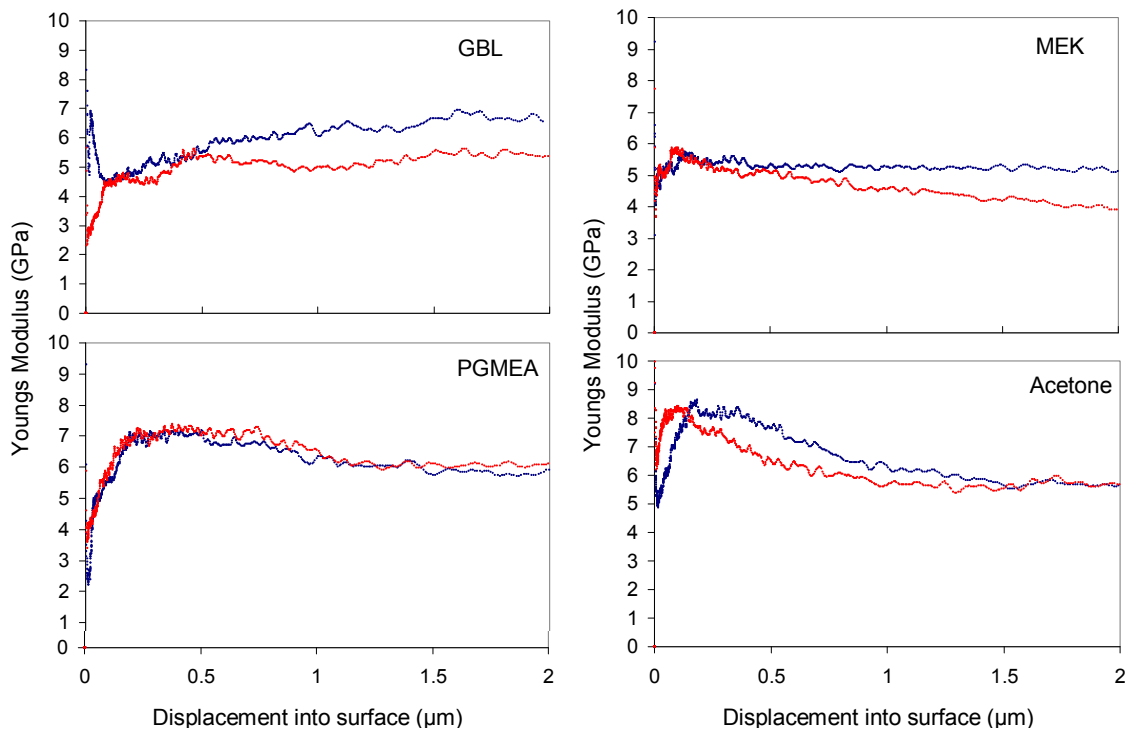


Figure 5.4: General trend of the variation of E_Y as a function of the displacement into the surface of the MWCNTs/SU8 composites prepared for various solvents denoted in the figures. Blue and red curves are representative for composites prepared with non-functionalized and functionalized MWCNTs, respectively.

One can see that only for the samples prepared with GBL E_Y increases with the penetration depth. It is known from the literature that SU8 cross-linking process is very different with and without the presence of GBL. Zhang et al. (13) have found that GBL copolymerizes with SU8 to bridge two neighbouring epoxy groups leading to longer aliphatic segments in the network and better mechanical response. Complete conversion of SU8 was achieved when the content of GBL with respect to the SU8 was 33 wt%. Below this percentage the non-polymerized molecules of SU8 weaken the material. The critical concentration is 15 wt % of GBL, which gives only $63 \pm 6\%$ of SU8 conversion (13; 14). Taking this into account one can explain the increase of E_Y with an increase of distance from the surface of the samples prepared with GBL. In the case the final weight fraction of GBL is

more than 33 wt%, the SU8 conversion is still 100% but the fraction of GBL surpassing 33 wt% acts as a plasticizer. This would lead to a decrease in E_Y with a penetration depth. We did not observe such a behaviour which means that there is no excess unpolimerised GBL in the SU8 network after SU8 cross-linking.

The other three solvents (PGMEA, MEK and acetone) do not copolymerise, they only remain in the structure and weaken it. Consequently, for these samples E_Y decreases with penetration depth (Fig. 5.4).

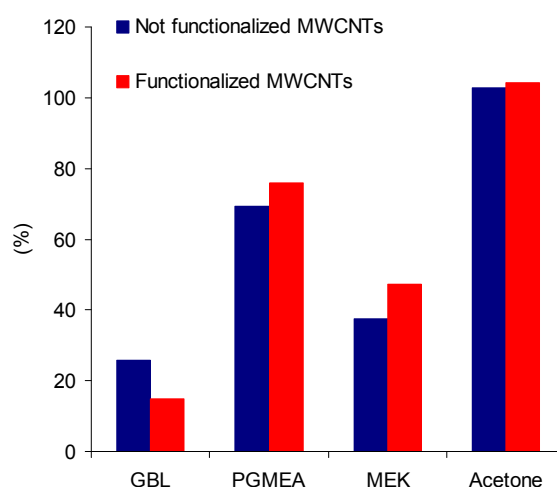


Figure 5.5 Enhancement of E_Y by MWCNTs reinforcement with respect to the non-reinforced epoxy. Values for non-functionalized and functionalized MWCNTs are denoted on the plot.

The relative increase of E_Y in MWCNTs/SU8 composites normalized to the non-reinforced epoxy ($E_Y^0 = 3.7$ GPa) is presented in Figure 5.5. Values for E_Y are taken at 200 nm depth to avoid influence of surface imperfections. The highest relative increase of 100% is achieved for samples prepared with acetone as solvent. Taking into account the high Young's modulus of ~ 500 GPa (15) of our CVD grown CNTs this is a modest increase of the mechanical response. However, the intrinsic properties of CNTs cannot be translated onto composites properties, because composite 1 have random CNTs network, which cannot carry the load. Furthermore, for a good reinforcement one needs an efficient load transfer from the matrix to the CNTs and the formation of an interlocked network of epoxy and CNTs. In principle, -COOH functionalized CNTs can chemically bind to the epoxy rings of the SU8 molecules what might by though leading to good load-transfer. If this were the case, we should have observed difference between the results for composites reinforced with functionalized or native CNTs. This was not the case; the results are essentially the same, except when using GBL as solvent, where the performance of the functionalized CNTs is clearly worse. The reason is probably the following: the presence of hydroxyl end groups leads to a softer polymer network in the cationic curing process, because the mechanism of

polymerization changes from a typical active chain-end mechanism to an activated monomer mechanism (16).

5.1.3 Microscopy

In order to test the dispersion of CNTs in the SU8 matrix, samples of composites 1 were cut by microtome and characterized by electron microscopy. SEM images of the composites surface, presented in Figure 5.6, clearly show large aggregates of CNTs in SU8 matrix (dark areas) alternating with bright areas of SU8 rich areas. The size of these bright areas was about $5\text{-}10\ \mu\text{m}^2$ clearly indicating phase separation at the surface of composites 1, which all showed the same structure.

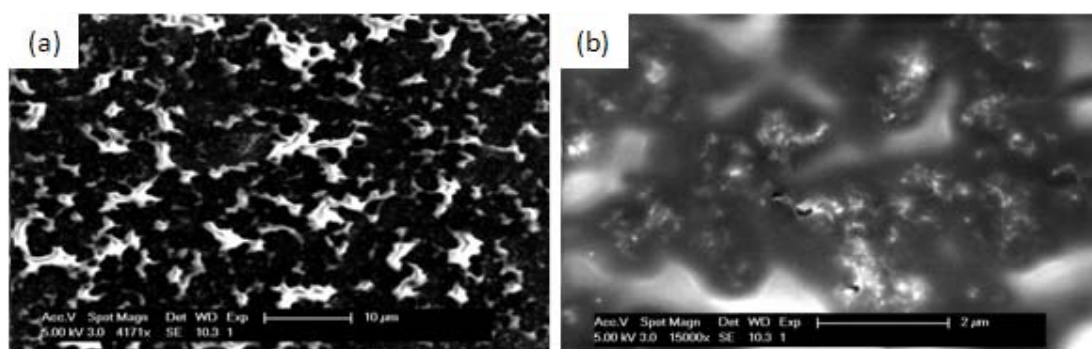


Figure 5.6: SEM micrographs of composites surface with two different magnifications. SU8 is an insulator and therefore, it appears as bright areas in SEM micrographs. Scale bars are: $2\ \mu\text{m}$ (b); $10\ \mu\text{m}$ (a).

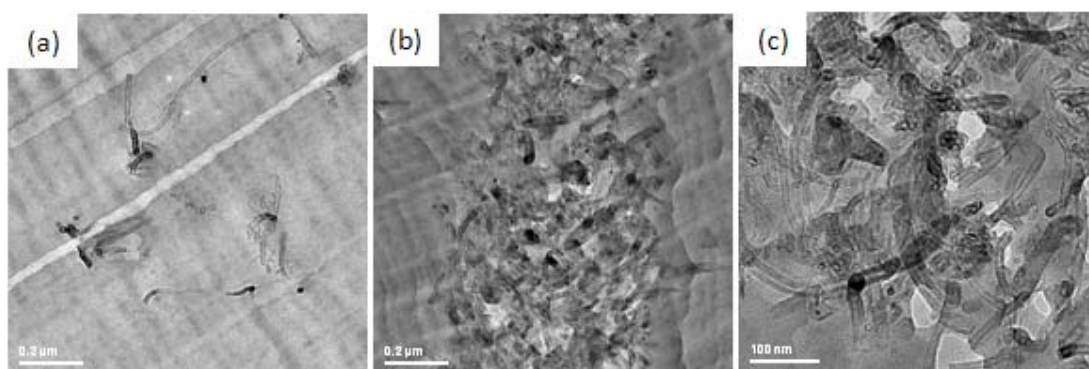


Figure 5.7: Representative TEM micrographs of microtome sections of composite 1 samples, which surprisingly all looked the same with the SU8 rich areas (a) and CNTs rich areas (b, c). Scoping lines visible in (a) and (b) are artefacts of microtome cutting. Voids in (c) can be artefacts of microtome cutting or areas inside the CNTs aggregates where SU8 could not penetrate. Scale bars are: $100\ \text{nm}$ (c); $0.2\ \mu\text{m}$ (a), (b).

TEM studies of the composites samples, prepared by microtome (Figure 5.7), reveal that the bulk material is the same as the surface for all composites 1. Regions rich in SU8

(Fig. 5.6 (a)) or in aggregates of CNTs (Fig. 5.6 (b) and (c)) were often seen in all composites 1.

5.1.4 Impedance spectroscopy

We further characterized the composites by means of impedance spectroscopy, measurements of the frequency dependent conductivity. Results were interpreted the following way. Below the percolation threshold, one can define CNTs rich areas, having a resistance Ra . They are surrounded by areas of almost pure polymer which represent low conductivity gaps expressed by a resistance (Rc) in parallel with a capacitance (C). Consequently, the real part (Z') of frequency (ω) dependent the complex impedance of the composite has the form:

$$Z' = \left(Ra + \frac{Rc}{1 + \omega^2 Rc^2 C^2} \right)$$

Above the percolation threshold, well dispersed CNTs are in contact and form conduction paths through the polymer matrix. In this case, Z' is frequency-independent having a simple form:

$$Z' = (Ra + Rc)$$

This means that the frequency dependence of Z' can be used as a tool to determine the distribution of CNTs within the composite.

In Figure 5.8 (a), Z' is plotted as a function of the frequency for composites 1N. Z' is clearly frequency dependent. In addition, Z' values are very close for all five composites produced as well as for unloaded SU8 (in particular for frequency higher than 100 kHz). Therefore the frequency dependence of Z' for SU8 composites loaded with 5w% of CNTs is ascribed to a poor CNTs distribution within the polymer matrix. An influence of the solvents used to disperse pristine CNTs as well as to dissolve the SU8 cannot be clearly drawn.

When CNTs surface is functionalized with -COOH groups, Z' is frequency independent (Fig. 5.8 (b)) suggesting the creation of Ohmic materials which possess well connected network of CNTs. In addition, it has to be noted that the Z' values are 2 or 3 order of magnitude lower in the case of -COOH functionalized CNTs than for non-functionalized CNTs what also reflects the improved dispersion in the first case. In fact, the carboxyl groups on the CNT surface can participate in the opening reaction of the epoxy rings, resulting in the formation of an ester bond and an -OH group (17). Consequently, CNTs could be covalently bonded to SU8 molecules what could reduce CNTs aggregation during the composite's processing.

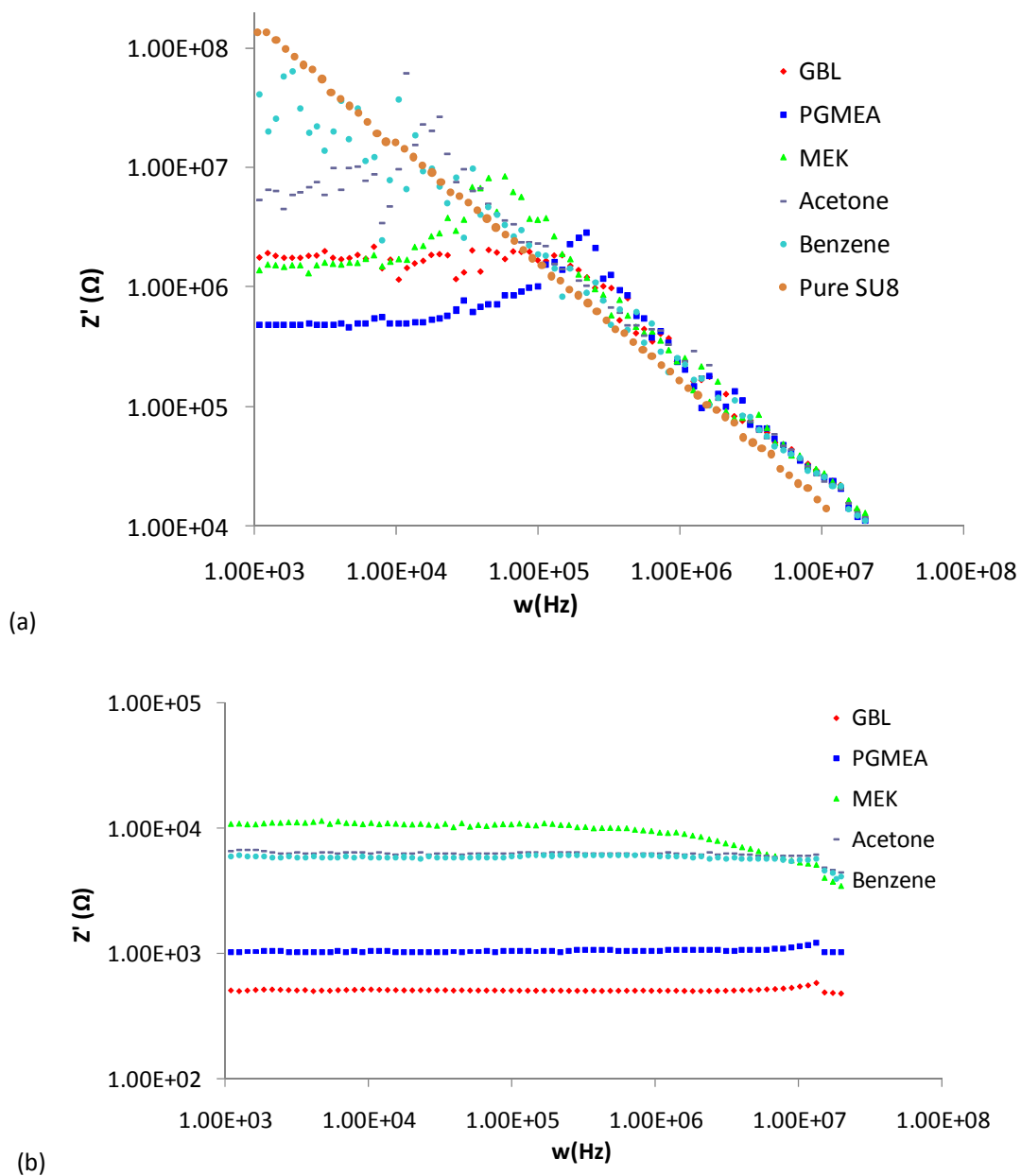


Figure 5.8: Evolution of the real part (Z') of the complex impedance as a function of frequency for composites 1N (a) and composites 1F (b). As a reference, measurement for unloaded SU8 is given in (a) and marked in legend as “Pure SU8”.

Furthermore, it has to be noted that Z' values obtained for composite 1F prepared with PGMEA are much lower than for composites 1F MEK, acetone and benzene as solvents and Z' for composite 1F with PGMEA is very close to that prepared with GBL (see red and dark blue curves in Fig 5.8 (b)). The most common SU8 solvent is GBL but some applications require a suitable alternative for GBL. Consequently, PGMEA could be the most suitable alternative of GBL for preparing composites with $-\text{COOH}$ functionalized CNTs.

5.1.5 Resistivity as a function of temperature

We measured resistivity as a function of the temperature for the composites 1N (Fig. 5.9 (a)) and 1F (Fig. 5.9 (b)) prepared with five different solvents.

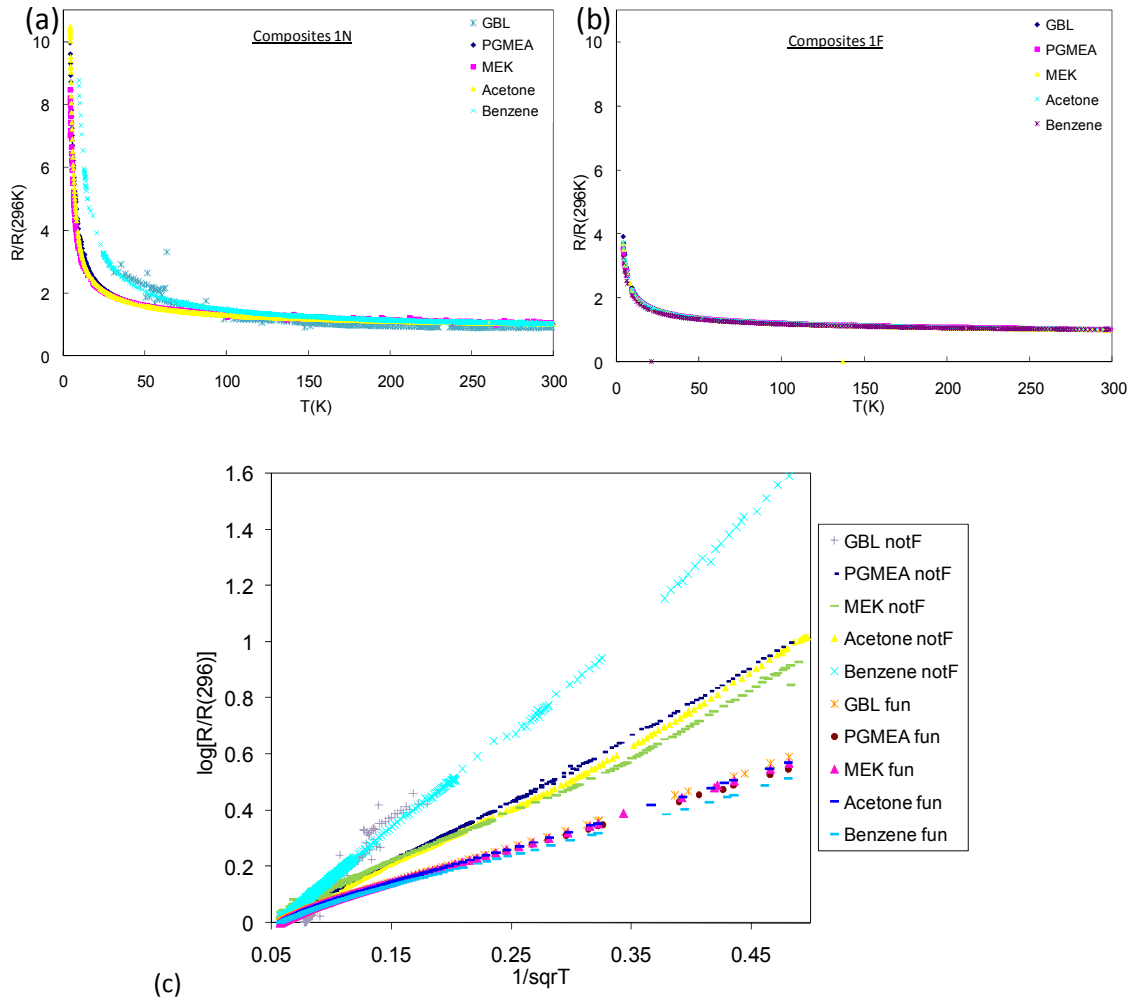


Figure 5.9: Resistivity as a function of the temperature for composites 1N (a) and composites 1F (b). (c) Resistivity of the composites 1N and 1F, normalized to the room temperature conductivity in $\log(R/R(292))$ vs. $1/\sqrt{T}$ representation. The straight line fits can be explained in the framework of Coulomb interaction limited variable range hopping model. The legend indicates the solvent and CNTs type (non-functionalized and functionalized CNTs are indicated by “notF” and “fun”, respectively) used for composites 1 preparation.

Resistivity of the CNTs-SU8 composites 1 normalized to the room temperature value show essentially no dependence on the solvent (Fig. 5.9 (a) and (b)). The same data in $\log(R)$ vs. $1/\sqrt{T}$ representation are straight (Fig. 5.9 (c)). This indicates hopping conduction (18). The essential part of this is that electrons hop from one conducting entity to another one which is separated by insulating polymer. In such a model, the slope of the curves is proportional to the barrier height. The fact that the slope is smaller for the functionalized CNTs (Fig. 5.9

(c) indicates better inter-tube contacts. Generally for composites 1, we can conclude that the resistivity is dominated by hopping mechanism between the well-conducting entities.

5.1.6 Thermoelectric power as a function of temperature

The thermopower was measured for the CNTs-SU8 composites 1 prepared by five different solvents, except for composites 1N prepared with benzene and GBL, we were unable to determine their thermoelectric power due to the high resistivity. However, all measured curves of thermopower vs. temperature showed the same behaviour, all were strikingly linear. The Figure 5.10 shows an example of these results. The overall shape of the curves is very similar to the measurements on pure CNTs (not embedded in the polymer). The values of $S(T)$ are all comparatively low and close to that of good metals. Such metallic thermoelectric power is surprising considering that the resistivity is largely nonmetallic.

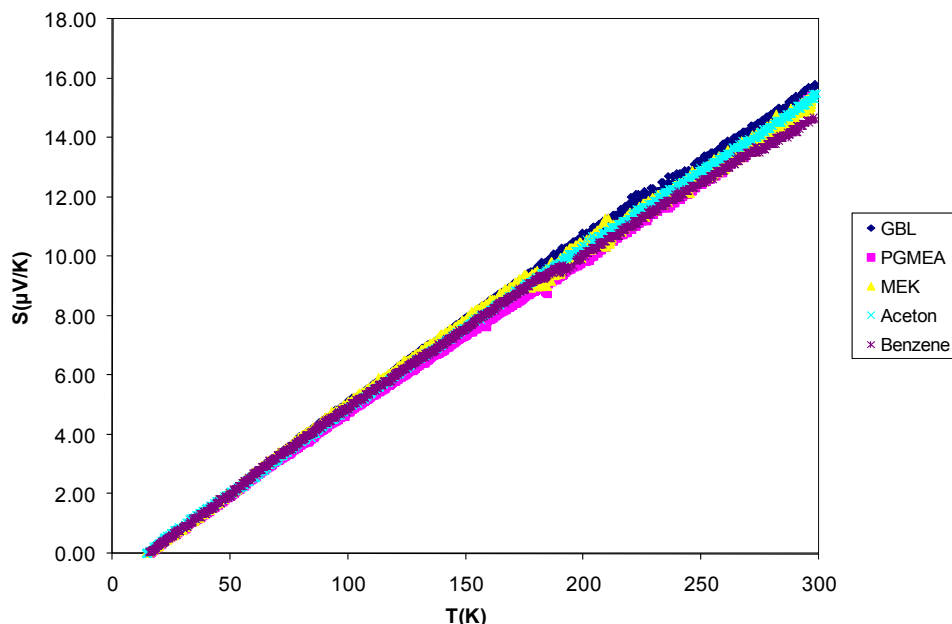


Figure 5.10: Temperature dependence of thermoelectric power composites 1F prepared with five different solvents (indicated in the legend).

According to the model for conducting polymers (19), the thermoelectric power should be more metal-like than the resistivity. When several materials are connected in series, such as bundles of CNTs in a polymer matrix, the defects and disordered regions between them form electrical barriers. The resistivity is dominated by electric field gradient across the material, as the electrons need to hop between different bundles. This leads to a non-metallic dependence of $\rho(T)$. On the contrary, thermoelectric power is measured in a zero-current configuration. Therefore it is governed by the temperature difference rather than by the presence of electrical barriers, consistently with the metallic behaviour we observed. This picture suggests that in these samples there is no percolation among

individual CNTs, but rather that the CNTs form agglomerates which are touching or which are separated by the polymer, what goes along with the results of microscopy and measurement of resistivity as a function of the temperature.

Interestingly, the nonlinearity often observed in the thermopower of free-standing buckypaper and even in polymer-CNTs composites, and interpreted as a phonon-drag peak (19) is absent. The thermopower is positive, except at very low temperature, where it crosses zero at 15 K. In order to extract the Fermi-energy, the obtained curves can be fitted with the straight line of the form:

$$S(T) = -\pi k^2 T / 2eE_F$$

which allows the determination of the Fermi energy, yielding $E_F = 0.7$ eV.

5.2 CNTs-SU8 composites 2

Besides presented composites with five different solvent and 5 wt% of CNTs, we prepared the same formulations but with 1 wt% of CNTs to follow the aggregation type and to observe if there were differences in solvent-related aggregation mechanisms. Surprisingly, all samples revealed aggregations having the same morphologies and sizes, thus being independent of the solvent (Fig. 5.11 (a)). Therefore, the actual mechanism of aggregation and clustering was governed by the intrinsic properties of CNTs. In particular, as produced CVD-made CNTs are known to form strongly aggregated structures, like those shown in Figure 5.11 (b) which depicts CNTs before dispersion into the SU8 resist. Therefore, we put forward the idea that the improvement could be achieved by freeze-drying of CNTs (see Chapter 3) in order to minimize strong CNTs aggregations even before CNTs were inserted into the resist. The obtained CNTs powders using freeze drying were finer and more voluminous, providing good starting material for the CNTs dispersion.

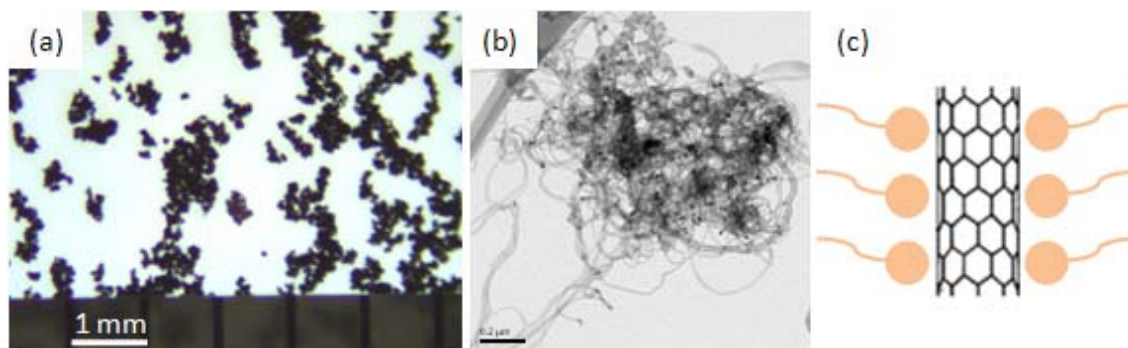


Figure 5.11: (a) Optical image of composite 1N prepared with acetone and 1 wt% of CNTs. (b) TEM micrograph of purified CVD MWCNTs after heat drying (scale bar is 0.2 μm). (c) Schematic drawing of CNT with non-covalently bonded surfactant molecules given in orange.

5.2.1 Dispersion of CNTs in SU8

As we mentioned, CNTs are hydrophobic and thus, their solutions are thermodynamically unstable and require stabilization by surface modification, like all hydrophobic molecules. Since surface functionalization of CNTs did not result in good dispersion in the SU8 network, we tried surfactants. Surfactants are molecules with two parts (head and tail) having distinctly different properties (hydrophilic, hydrophobic, liophilic etc.). This enables uniform orientation (with only head or tail) of surfactant molecules towards surface of the dispersed objects (Fig. 5.11 (c)). There are thousands of surfactants available and most of them are of unknown composition due to the protection of the producer. Therefore, it was very difficult to find the appropriate surfactant. We were searching for surfactants which are suitable for dispersion of organic molecules in organic medium, then the search was further refined to those which are suitable for dispersion of carbon black and for use in epoxy (as a medium of dispersion).

We tried different surfactants in different concentrations. Two of them showed good results, hereafter denoted as surfactant 1 and 2 (see Chapter 3). We also had to try 2 PIs - liquid and solid (see Chapter 3). Any modification of components or their ratios leads to destabilization of the dispersion. The interaction of the surfactant and PI can easily prevent polymerization. Indeed, with liquid old PI polymerization is possible only with 1 surfactant. With a solid new PI polymerization is possible with 2 surfactants.

5.2.2 Microscopy

Distribution of CNTs inside the SU8 network for the composites 2 was characterized by electron microscopy. The result showed that CNTs are not entangled into the big lumps like after the synthesis and like in composites 1. HR SEM micrographs of fractured surface of composite 2 with surfactant 1 showed well dispersed CNTs even for the sample containing 3 wt% of CNTs in SU8 (Fig. 5.12).

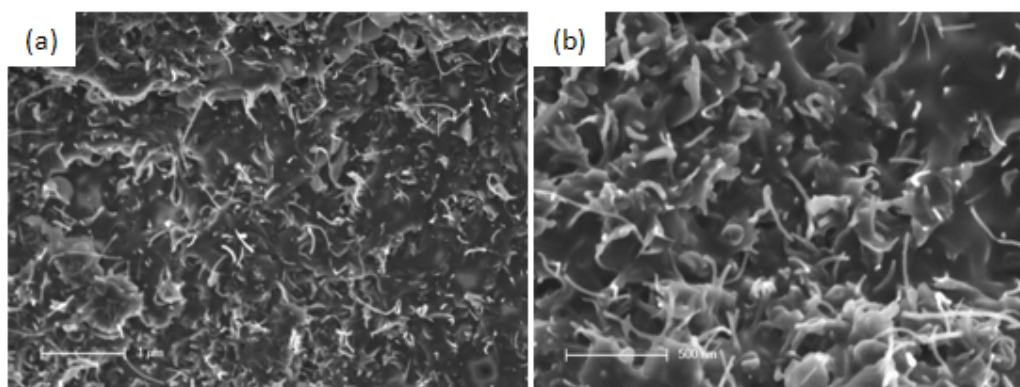


Figure 5.12: HR SEM micrographs (with different magnification) of composites 2 with surfactant 1 with 3 wt% of CNTs in SU8. Scale bars are: 500 nm (b); 1 μ m (a).

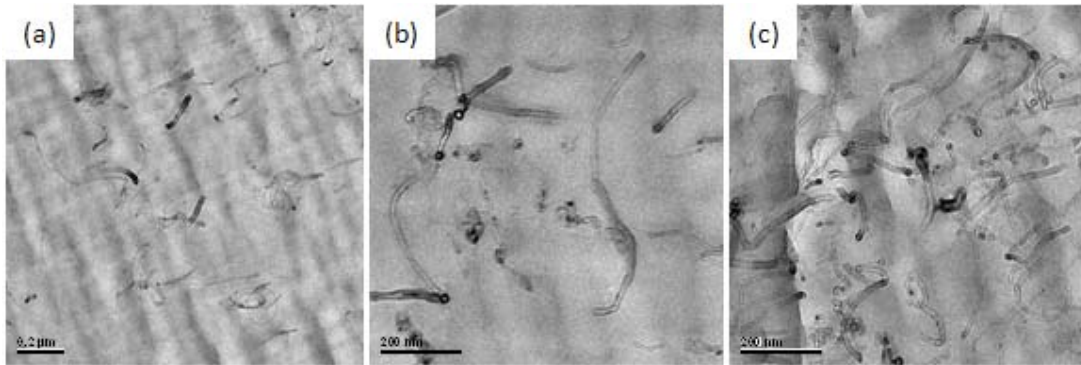


Figure 5.13: TEM of microtome cut composites 2 with surfactant 1 containing (a) 0.2 wt%, (b) 0.5 wt% and (c) 1.4 wt% of CNTs in SU8. Scale bars are 200 nm.

TEM micrographs of the microtome cuts of composites 2 with different CNTs concentrations also showed well dispersed CNTs (Fig. 5.13).

5.2.3 Thermal conductivity as a function of temperature

We measured the thermal conductivity of composites 2 as a function of CNTs' concentration and temperature. Figure 5.14 shows results of thermal conductivity measurement as a function of temperature in the temperature range from 4.2K to 300K.

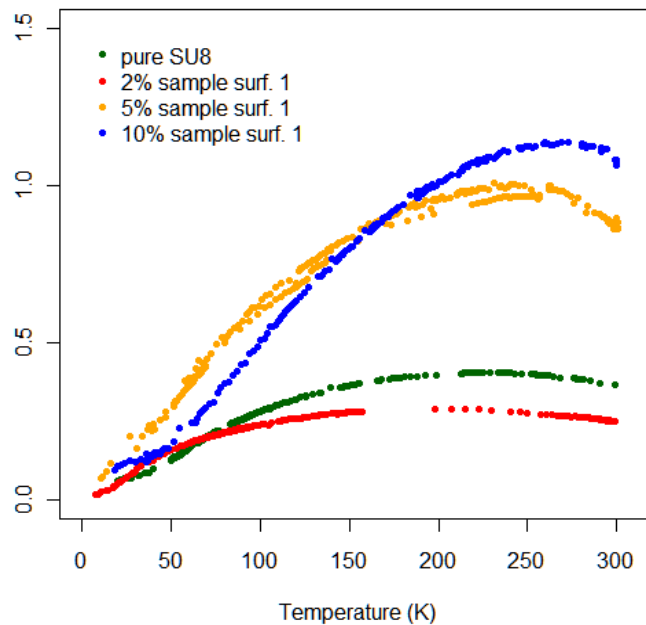


Figure 5.14: Thermal conductivity of CNTs-SU8 composites 2 as a function of temperature.

We can see that composite 2 with 2wt% of CNTs in SU8 have the same or even lower thermal conductivity than the unloaded SU8. With increase of CNTs content, the epoxy conversion is decreasing and thus, in composites 2 with 2 wt% of CNTs in SU8, it is possible that there is still no well-connected network of CNTs, while the SU8 network is already

heavily degraded by the presence of CNTs. Actually, studies of Sangermano et al. (20) showed that, with an increase of CNTs content, the epoxy conversion decreases; 0.1 wt% of CNTs reduced the epoxy conversion by 16%. Clearly, further increase of CNTs content might induce dramatic changes in the overall epoxy conversion. The composite with the highest CNTs content which we studied for applications in the photolithographic processing was of 1.6 wt%, which is 16 times more than in the study of Sangermano (20).

However, the composites with 5 and 10wt% of CNTs in SU8 showed the increase of thermal conductivity. By making composite with randomly oriented CNTs the thermal conductivity was increased up to 3 times. The thermal conductivity at room temperature (what is usually the most important information for the applications) grows from 0.3 W/mK for the unloaded SU8 (at zero CNTs concentration) to 1.1 W/mK at 10 wt% of CNTs in SU8 (Figure 5.15).

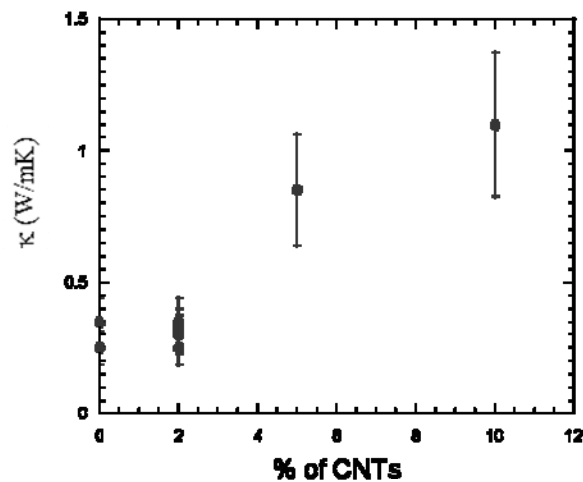


Figure 5.15: Thermal conductivity at room temperature of CNTs-SU8 composites 2 as a function of CNTs concentration.

5.2.4 Nanoindentation

As mentioned in section 5.1.2, nanoindentation is the common technique to characterize films. Therefore, we used it to determine hardness and Young's modulus (see Chapter 3). Composites 2 were prepared with CNT concentrations ranging from 0.1 wt% to 5 wt%. Obtained values for hardness and modulus are given in Figure 5.16. We can see that 3 fold increase in hardness was achieved with only 0.8 wt% of CNTs, while the Young's modulus increases from 4 GPa for unloaded SU8 to 6.2 GPa for the same composite.

Mechanical properties of the composites are usually estimated by using the simplified rule of mixtures. According to it, the maximal value of the Young's modulus of the composite which can be obtained is (21):

$$E_{\text{comp}} = E_{\text{CNT}}V_{\text{CNT}} + E_{\text{matrix}}(1 - V_{\text{CNT}}) \quad (5.1)$$

where E_{comp} , E_{CNT} , and E_{matrix} are, the Young's modulus of the composite, the modulus of pure CNTs, and the modulus of the non-reinforced SU8 (see Chapter 2), respectively, and V_{CNT} is the volume fraction of CNTs (in the case of CNTs used in this study calculation showed no significant difference between the weight and volume fractions).

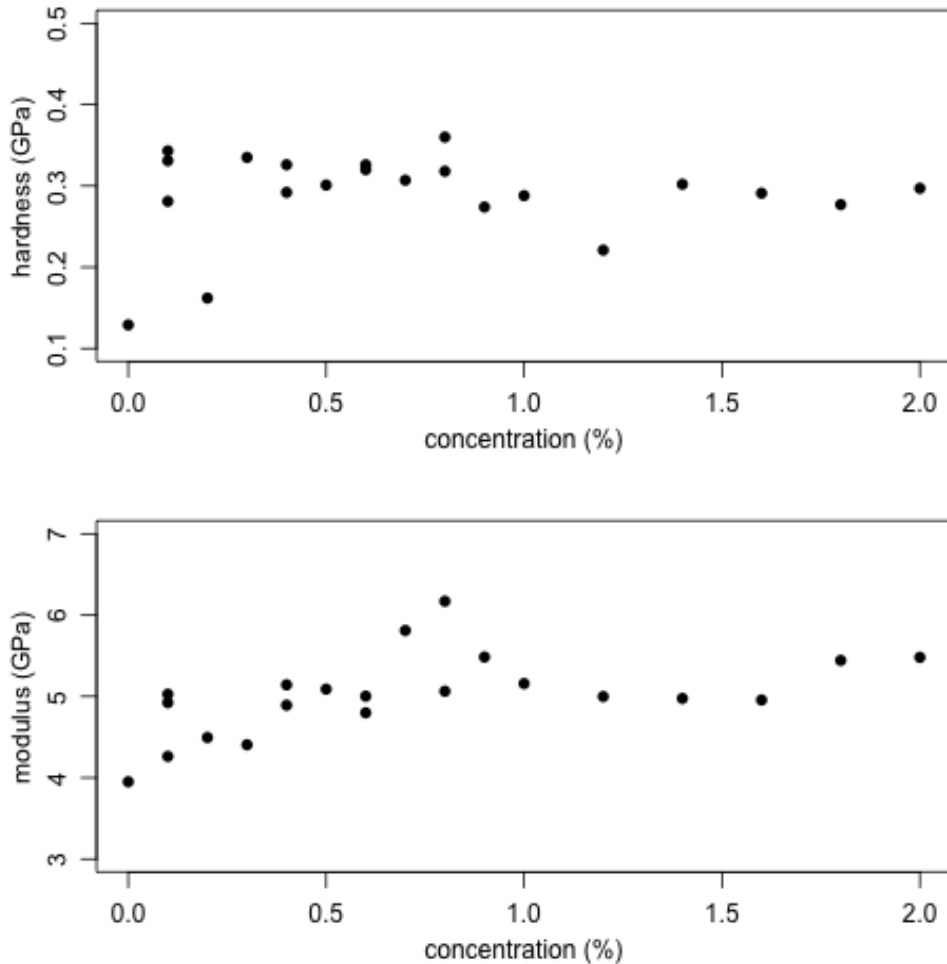


Figure 5.16: Hardness (upper panel) and modulus (lower panel) of CNTs-SU8 composites 2 (prepared with surfactant 1) as a function of CNTs concentration.

Due to the big difference between the modulus of polymer matrix and the CNTs (which can be a few orders of magnitude bigger), it is very important to estimate CNTs modulus correctly. Usually, CNTs reinforced composites show final modulus much below the values estimated by the mixture formula (5.1) and the main reason for the big discrepancy is the assumption that the modulus of CNTs is about 1TPa. In fact, most of the CNTs used for polymer reinforcement are produced by the CVD synthesis method. The modulus of CVD CNTs is proven to be strongly diameter dependent (Fig. 5.17). The average diameter of CNTs used for preparation of these composites is 13 nm and thus, from the graph in Figure 5.22 we can estimate that their modulus is around 300 GPa. Concerning unloaded SU8, there are very big differences among the reported modulus values (see Chapter 2). Moreover, when

the filler is introduced into the SU8 network the total polymer conversion is lower than for the unloaded SU8, meaning that the elastic modulus of SU8 decreases with the increase of the CNTs concentration. Taking into account the values of Young's modulus of the constituents, the SU8 matrix as we measured 3.95 GPa and the CNTs filler 300 GPa, by applying formula (5.1) for the 0.1 wt%, 0.2 wt%, 0.5 wt% and 0.8 wt% of CNTs calculated composite modulus are 4.2 GPa, 4.5 GPa, 5.4 GPa and 6.3 GPa what pretty much corresponds to the experimentally obtained values (Figure 5.16). For 0.9 wt% and higher CNTs concentrations, theory did not match the experimental results. The reason can be higher CNTs fraction that means larger excluded volume and beginning of overlapping concentration, what leads invariably to aggregation of CNTs.

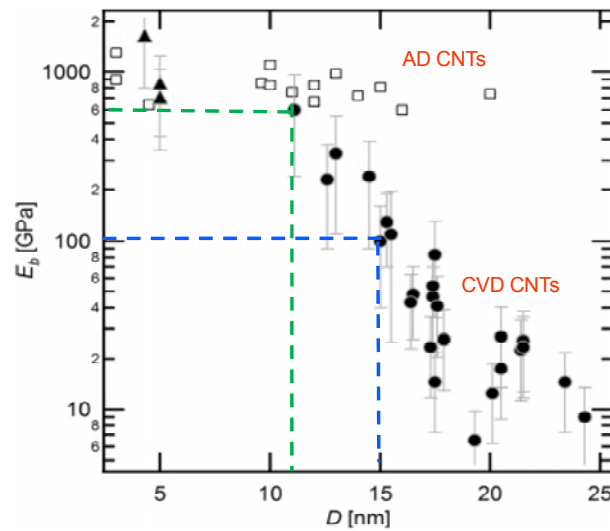


Figure 5.17: Elastic modulus of CVD CNTs shown by filled black circles (From the ref. (15)). The values of the Young's modulus of CVD CNTs having diameters of 11 nm and 15 nm are indicated by green and blue dotted lines, respectively.

5.2.5 Four Point Resistivity Measurements

Electrical percolation curves (dashed lines are guide for the eyes) for the composites with and without PI show significant differences (Fig. 5.18). The presence of PI enables lower resistance due to the SU8 crosslinking which brings tubes closer and fixes them into their position. In other words, with PI intertube contacts are better (CNTs and SU8 form interlocked network). It was very difficult to determine the value of percolation threshold, because the composite 2 with the lowest CNTs concentration was already electrically conductive. This also shows good dispersion of CNTs in composites 2. Percolation was estimated where resistance decreased by 4 orders of magnitude with respect to pure SU8. Thresholds determined by this criterion are around 0.4 wt% of CNTs in SU8 (for composites 2 without PI) and around 0.1 wt% (for composites 2 with PI). Moreover, we achieved more than 10 orders of magnitude decrease of the initial SU8 polymer matrix resistance with CNTs' load of 3 wt%.

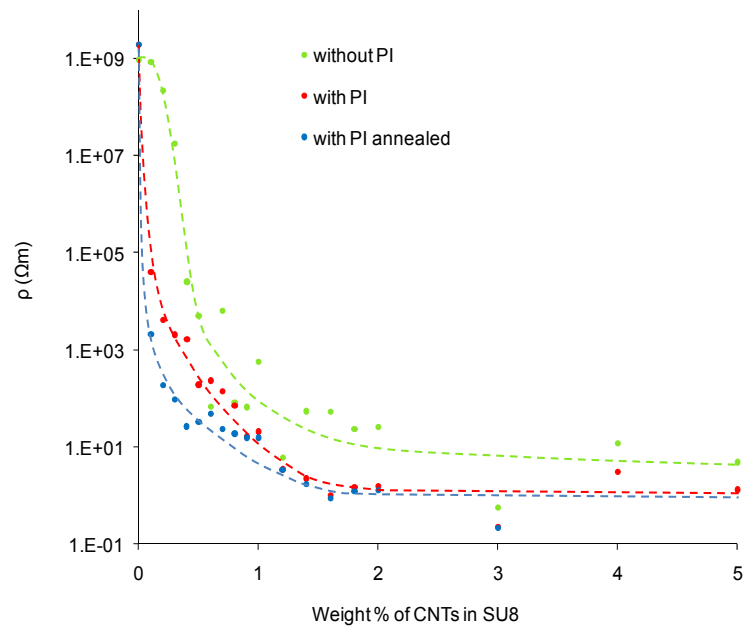


Figure 5.18: Electrical resistance of the composite (prepared with surfactant 1) as a function of CNTs concentration.

Electrical properties for the composite 2 prepared with surfactant 2 are given in Figure 5.19.

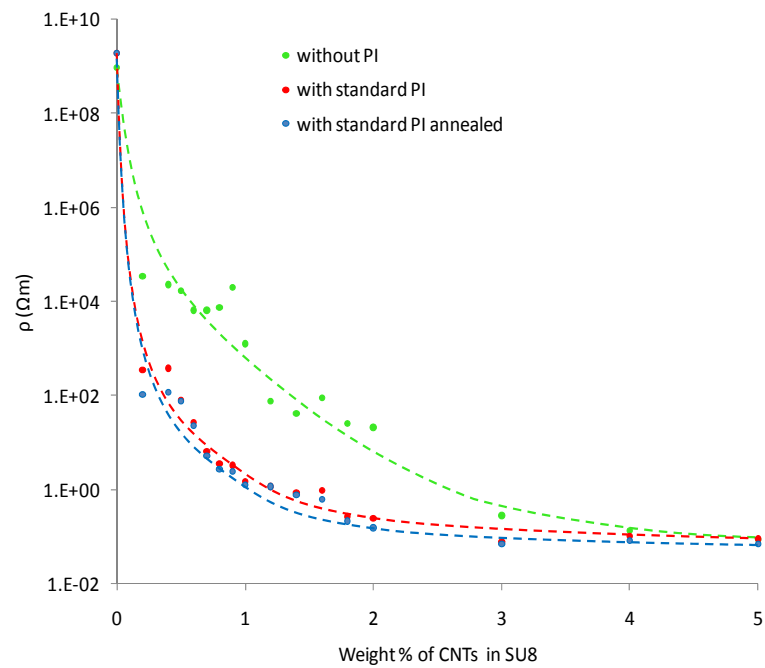


Figure 5.19: Electrical resistance of composite (prepared with surfactant 2) as a function of CNTs concentration.

Furthermore, we compared results for two series of composites at appropriate processing steps (Fig. 5.20) and have found no major difference between electrical properties of composites 2 prepared with surfactant 1 and 2. Hence, we can conclude that surfactants used in this study do not affect the electrical properties of composites 2. We achieved electrical percolation with around 0.1 wt% of CNTs in composites 2 with PI. Difference in electrical percolation curves for the composites prepared with and without PI indicates a better dispersion of CNTs and better inter-tube contact when SU8 was cross-linked.

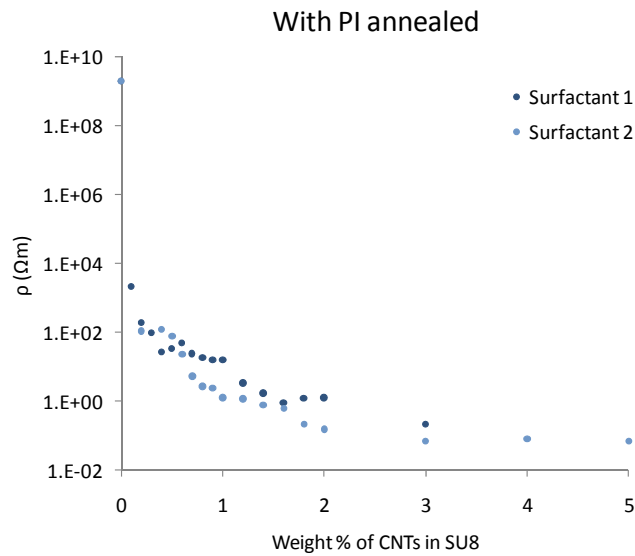


Figure 5.20: An example of comparison of electrical resistance of composites 2 (prepared with surfactant 1 and 2) after the last processing step as a function of CNTs concentration. Apparently, there is no significant difference among the corresponding electrical resistance of composites 2 prepared with two surfactants (measured values for 4 wt% and 5 wt% of CNTs in SU8 are completely overlapping).

5.2.6 Resistivity as a function of temperature

We measured resistivity as a function of temperature for the composites 2 prepared with surfactant 1. Figure 5.21 shows resistivity of a sample containing 3 wt% of CNTs in SU8, normalized to the room temperature value. The same data in $\log(R)$ vs. $1/VT$ representation is straight (insert in Fig. 5.21). This indicates hopping conduction, like for composites 1 (see section 5.1.5).

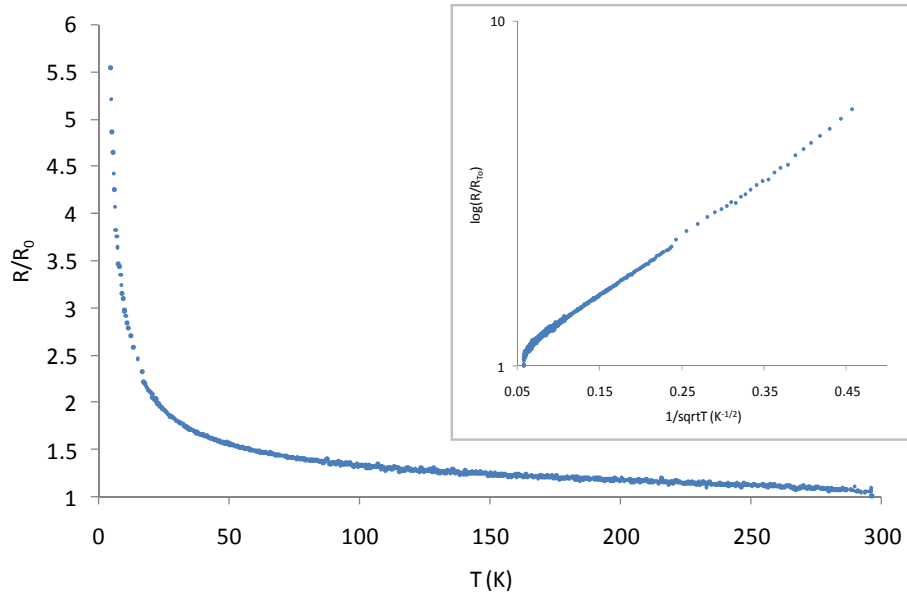


Figure 5.21: Resistivity of composite 2 containing 3 wt% of CNTs in SU8 (normalized to the room temperature resistivity value, R_0) as a function of temperature. Insert shows the same result in $\log(R/R_0)$ vs. $1/\sqrt{T}$ representation. The straight line fits can be explained in the framework of hopping model.

5.3 CNTs-SU8 composites 3

Impregnation of CNT carpets was obtained by capillary-driven wetting using the traditional method of dropwise adding low viscosity SU8 (standard 1040 formulation without dilution) at room temperature to an oriented CNT mat grown on a substrate (21) (see Chapter 3). The aim of the experiment was to analyze whether the electrical and thermal conductivity of composites 3 depends on the orientation of the CNTs inside the composite. Therefore the measurements were performed both along the CNT direction and perpendicular to it. In a composite 3, both electrical and thermal conductivity should be greater along the CNTs direction, since they are electrical conductors. That alone explains the difference in electrical conductivity, but can be applied to thermal conductivity as well, if we suppose that most of the heat is transported by the electrons or phonons of the CNTs.

5.3.1 Microscopy

Important factors for obtaining material with superior properties are: (i) good carpet wetting in the whole volume without presence of voids or inclusions and (ii) preserved CNTs alignment in the final composite. To assess good wetting over the whole carpet volume and over the whole CNTs length, we have studied CNTs-SU8 composites 3 by SEM. SEM micrographs (Fig. 5.22 (a)) have shown that we obtained uniform carpet impregnation in all regions from CNTs' top to the bottom. We did not observe voids or inclusions. On the same

micrograph, alignment of CNTs in composite seems preserved. In order to verify whether the CNTs alignment in carpet's inner structure is well-maintained, we have performed TEM observation on ultramicrotome section of composite 3. The results confirmed alignment of CNTs in composite 3 (Fig. 5.22 (b) and (c)). Alignment of CNTs in final composite 3 is essential for using CNTs as "direct thermal conductor" from heat source to the sink, what was our aim. Therefore, we additionally checked CNTs alignment by HR SEM, what revealed that some CNTs are curved and deformed (Fig. 5.23).

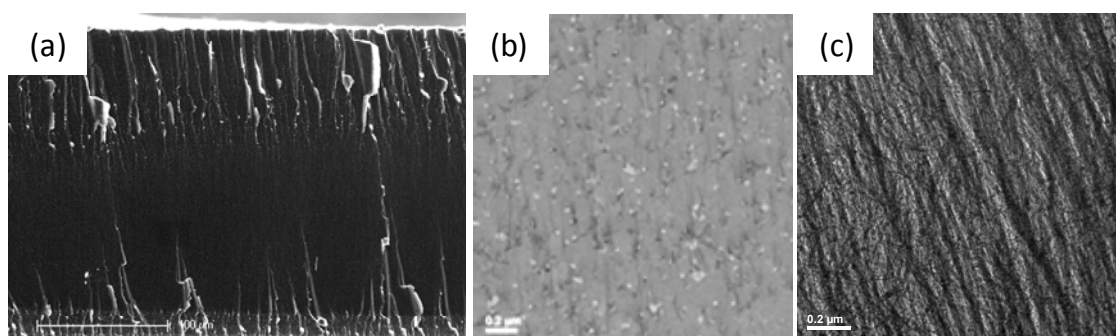


Figure 5.22: a) SEM micrograph of impregnated carpet's cross section confirming uniformity of carpet's impregnation with SU8 from top to the bottom (SU8 appears as white on the SEM micrograph since it is an insulator); b) TEM micrograph of $\sim 40 \mu\text{m}$ thick microtome composite's sample showing preserved MWCNTs alignment in the carpet upon impregnation with SU8. Scale bars are: $0.2 \mu\text{m}$ (b), (c); $100 \mu\text{m}$ (a).

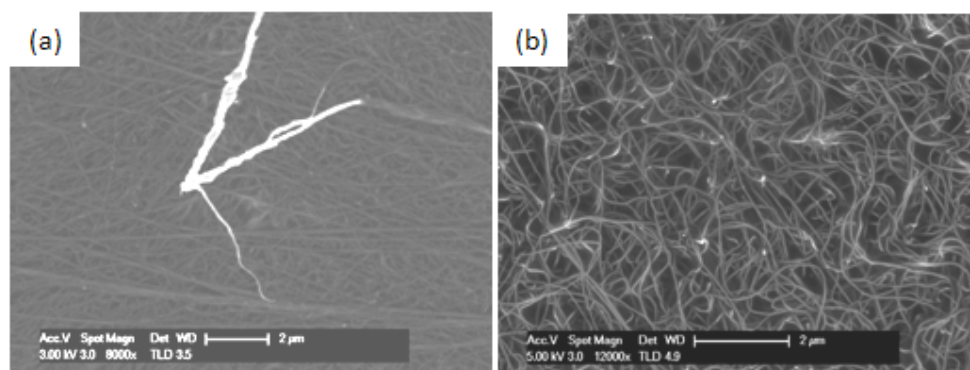


Figure 5.23: HR SEM micrographs of impregnated carpet showing lots of aligned CNTs (a) and parts without preserved tubes alignment (b). Both images were taken on the outer surface of the impregnated carpet and not in its cross-section like given in Figure 5.2 (b) and (c). Scale bars are $2 \mu\text{m}$.

5.3.2 Thermal conductivity as a function of temperature

The thermal conductivity (κ) of the nanotube carpet has been determined between 4K and 300 K. The sample space was kept under dynamic vacuum to reduce parallel heat conduction by residual gas. The result is shown in Figure 5.24.

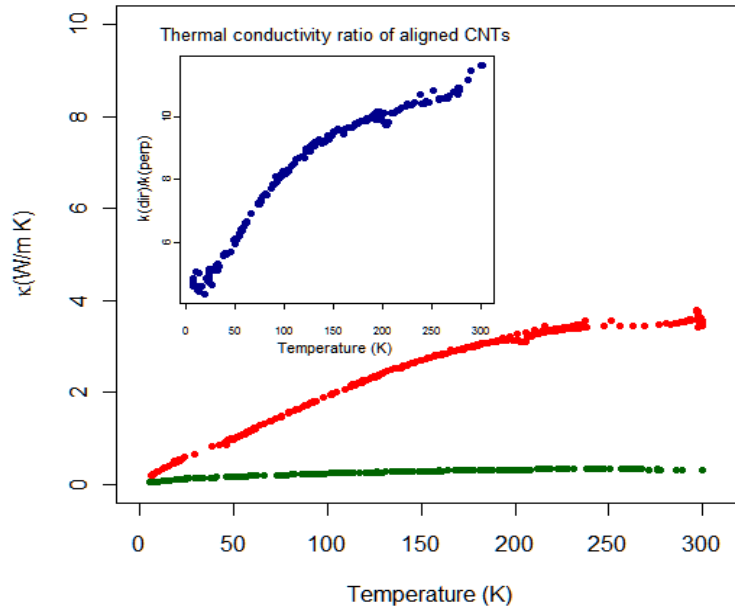


Figure 5.24: Thermal conductivity of aligned CNT carpet/SU8 composite sample along (red dots) and perpendicular (green dots) to the direction of the CNTs. The inset shows the anisotropy of the thermal conductivity (the ratio of previous two thermal conductivities).

The anisotropy of κ is more than 10 at room temperature, with the perpendicular conductivity barely higher than that of the pure epoxy. The value of the parallel heat conductivity is about 4 W/mK. Although not as high as the results published for aligned, high crystallinity carbon nanotubes (22), there are several reasons not to expect such outstanding results. Firstly, the fraction of the CNTs in the composite is estimated to be only about 5 wt%, the rest is low-thermal-conductivity epoxy resin. Secondly, there are no continuous tubes running from one end of the sample to the other. This means that no matter whether electrons or phonons are the dominant contributors to the thermal conductivity, hopping from one tube to the next limits transport.

5.3.3 Resistivity as a function of temperature

We have also measured the electrical conductivity and its anisotropy as a function of temperature. Figure 5.36 shows the result. The resistivity has similar temperature dependence, in both directions it varies as $R = R_0 \exp\left((T_0 / T)^{-1/2}\right)$, a behavior often observed in granular metals, carbon aerogels, activated carbon fibers or assemblies of graphitic particles, where this kind of temperature dependence was attributed to Coulomb-interaction limited hopping conduction (18). The very same behavior as in the case of the other two types of composites studied.

The anisotropy of the electrical conductivity at room temperature is smaller than that of the thermal conductivity. This suggests that the dominant contribution to the heat conduction comes from phonons, not from electrons, as is the case for simple metals.

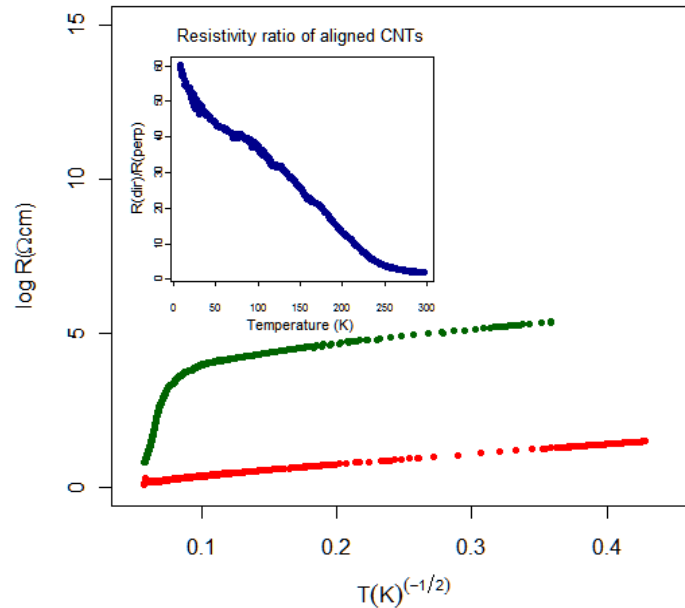


Figure 5.36: Resistivity of aligned CNTs in the direction of the alignment (red dots) and perpendicular to the alignment (green dots) as a function of temperature. Insert shows the ratio of previous two resistivities.

5.4 Conclusions

I have used different mechanical, electrical and thermal measurements, as well as electron microscopy to study CNT/SU8 composites prepared by different methods.

Nanoindentation of CNTs-SU8 composites 1 (native or functionalised CNTs mixed with SU8 epoxy) showed modest increase of mechanical properties (enhancement of E_V by 100%) with respect to unloaded SU8, due to the random CNTs network and poor dispersion which cannot carry the load. Impedance measurement showed presence of percolating CNTs network in composites 1F. However, microscopy and measurement of resistivity and thermopower as a function of temperature revealed presence of CNTs aggregates separated by SU8 rich areas. Therefore, electrical conduction was limited by inter-tube hopping.

I tried to improve CNT dispersion by using surfactants. Microscopy of these samples showed well dispersed CNTs for different CNTs concentrations, what was confirmed by four-point resistivity measurements which have shown percolation already around 0.1 wt% of CNTs in SU8. Threefold increase of thermal conductivity, with respect to the unloaded SU8, was achieved for composites 2 with 10 wt% of CNTs in SU8. Threefold increase of hardness, with respect to the unloaded SU8, was achieved for composites 2 with only 0.8 wt% of CNTs in SU8. However, measurement of resistivity as a function of temperature still indicated hopping mechanism meaning that CNTs were still separated by the polymer or in this case, by the surfactant molecules.

For the composites 3, consisting of oriented CNT carpets impregnated with SU8 we obtained an increase of the room temperature thermal conductivity almost 13 times by alignment of CNTs inside the composite, which was achieved by simple impregnation of CNTs carpets. Due to the high anisotropy of CNTs-SU8 composites, we can tailor material's functionality in the required dimension.

References

1. **P. J. F. Harris.** *Carbon Nanotubes and Related Structures: New Materials for the Twenty-First Century.* Cambridge : Cambridge University Press, 1999.
2. **H.-G. Elias.** *An Introduction to Polymer science.* Weinheim : VCH, 1997.
3. *Carbon nanotubes, buckyballs, ropes, and a universal graphitic potential.* **L. A. Girifalco, M. Hodak and R. S. Lee,** 19, 2000, Physical Review B, Vol. 62, p. 13104.
4. *Characterizing the surface properties of carbon nanotubes by inverse gas chromatography.* **X. Zhang, D. Yang, P. Xu and C. Wang,** 2007, J. Mater. Sci., Vol. 42, p. 7069.
5. *Solution Properties of Single-Walled Carbon Nanotubes.* **J. Chen, M. A. Hamon, H. Hu, Y. Chen, A. M. Rao, P. C. Eklund and R. C. Haddon,** 1998, Science , Vol. 282, p. 95.
6. *Reversible sidewall functionalization of buckytubes.* **P.J Boul, J Liu, E.T Mickelson, C.B Huffman, L.M Ericson, I.W Chiang, K.A Smith, D.T Colbert, R.H Hauge, J.L Margrave and R.E Smalley,** 1999, Chemical Physics Letters, Vol. 310, p. 367.
7. *Macroscopic Fibers and Ribbons of Oriented Carbon Nanotubes.* **B. Vigolo, A. Penicaud, C. Coulon, C. Sauder, R. Pailler, C. Journet, P. Bernier and P. Poulin,** 2000, Science, Vol. 290, p. 1331.
8. *Solubilization of Carbon Nanotubes by Nafion toward the Preparation of Amperometric Biosensors.* **J. Wang, M. Musameh and Y. Lin,** 2003, J. Am. Chem. Soc., Vol. 125, p. 2408.
9. *Individually Suspended Single-Walled Carbon Nanotubes in Various Surfactants.* **V. C. Moore, M. S. Strano, E. H. Haroz, R. H. Hauge, R. E. Smalley, J. Schmidt and Y. Talmon,** 2003, NanoLetters 3, (2003) 1379, Vol. 3, p. 1379.
10. *Effect of chemical functionalization on the mechanical properties of carbon nanotubes.* **A. Garg and S. B. Sinnott.** 1998, Chemical Physics Letter, Vol. 295, p. 273.
11. *Models for colloidal aggregation.* **P. Meakin.** 1988, Ann. Rev. Phys. Chern., Vol. 39, p. 237.
12. *Qualitative and quantitative characterization of outgassing from SU-8.* **J. Melai, C. Salm, R. Wolters and J. Schmitz,** 2009, Microelectronic Engineering, Vol. 86, p. 761.
13. *Network properties and acid degradability of epoxy-based SU-8 resists containing reactive gamma-butyrolactone.* **J. Zhang, M. B. Chan-Park and C. M. Li,** 2008, Sensors and Actuators B: Chemical, Vol. 131, p. 609.
14. *Analysis of Network Structure of UV-Cured Acrylates by ¹H NMR Relaxation, ¹³C NMR Spectroscopy, and Dynamic Mechanical Experiments.* **V.M. Litvinov and A.A. Dias.** 2001, Macromolecules, Vol. 34, p. 4051.
15. **K. Lee.** *Surface-Bound Nanostructures: Mechanical and Metrological Studies.* Lausanne : EPFL, 2008. Thesis No 4042.
16. **G. Odian.** *Principles of Polymerization.* Fourth Edition. Hoboken : Wiley-Interscience, A John Wiley & Sons, Inc., 2004.

17. *Surface Modification of Multiwalled Carbon Nanotubes: Toward the Tailoring of the Interface in Polymer Composites.* **A. Eitan, K. Jiang, D. Dukes, R. Andrews and L. S. Schadler,** 16, 2003, *Chemistry of Materials*, Vol. 15, p. 3198.
18. *Coulomb-gap magnetotransport in granular and porous carbon structures.* **A.W.P. Fung, Z. H. Wang, M. S. Dresselhaus, G. Dresselhaus, R. W. Pekala and M. Endo,** 1994, *Physical Review B*, Vol. 49, p. 17325.
19. *Electronic transport in carbon nanotube ropes and mats.* **A.B. Kaiser, Y.W. Park, G.T. Kim, E.S. Choi, G. Düsberg and S. Roth,** 1999, *Synthetic Metals*, Vol. 103, p. 2547.
20. *Antistatic Epoxy Coatings With Carbon Nanotubes Obtained by Cationic Photopolymerization.* **M. Sangermano, S. Pegel, P. Pötschke and B. Voit.** 5, 2008, *Macromolecular Rapid Communications*, Vol. 29, p. 396.
21. *Fabrication and Nanocompression Testing of Aligned Carbon-Nanotube–Polymer Nanocomposites.* **E. J. García, A. John Hart, B. L. Wardle and A. H. Slocum.** 2007, *Adva. Mater.*, Vol. 19, p. 2151.
22. *Electrical and thermal transport properties of magnetically aligned single wall carbon nanotube films.* **J. Hone, M.C. Llaguno, N.M. Nemes, A.T. Johnson, J.E. Fisher, D.A.Walters, M.J. Casavant, J. Schmidt and R.E. Smalley,** 2000, *Appl. Phys. Lett.*, Vol. 77, p. 666.

Chapter 6

CNTs-SU8 composites processing

The SU8 resist can be processed with a number of patterning and processing techniques (1), what makes it very attractive for industrial applications and scientific research. In this work we focussed on three specific processes which are considered as the most important ones from the industrial perspective. These processes are: inkjet printing, photolithography and screen printing.

The overall goal was to optimize the listed processing techniques towards obtaining CNTs-SU8 composite films that would possess advantageous properties, thus leading to well-defined, electrically conductive patterns, flexibility, tuneable transparency, processability with good adhesion on various substrates, as well as revealing substantial chemical resistance and stability in various environments.

6.1 Photolithography

Photolithography is one of the most important and most frequently used techniques for the patterning of microsystems. In photolithographic processes patterns (designs) are copied from templates (masks) into thin UV-light sensitive polymeric films (photoresists). Photoresists come in two tones: positive and negative. The negative tone photoresist yields final structures that match areas exposed to irradiation (2). Taking into account that SU8 is a negative tone photoresist, in the following, we will focus on the photolithographic processes of such resins. The processing steps that represent the standard SU8 lithographic procedure are schematically illustrated in Figure 6.1. A detailed description of each step is given in

Appendix 2. Moreover, potential technical difficulties and shortcomings of these technological steps, especially in the context of CNTs-loaded SU8, as well as possible ways to overcome them, will also be discussed in detail in Appendix 2.

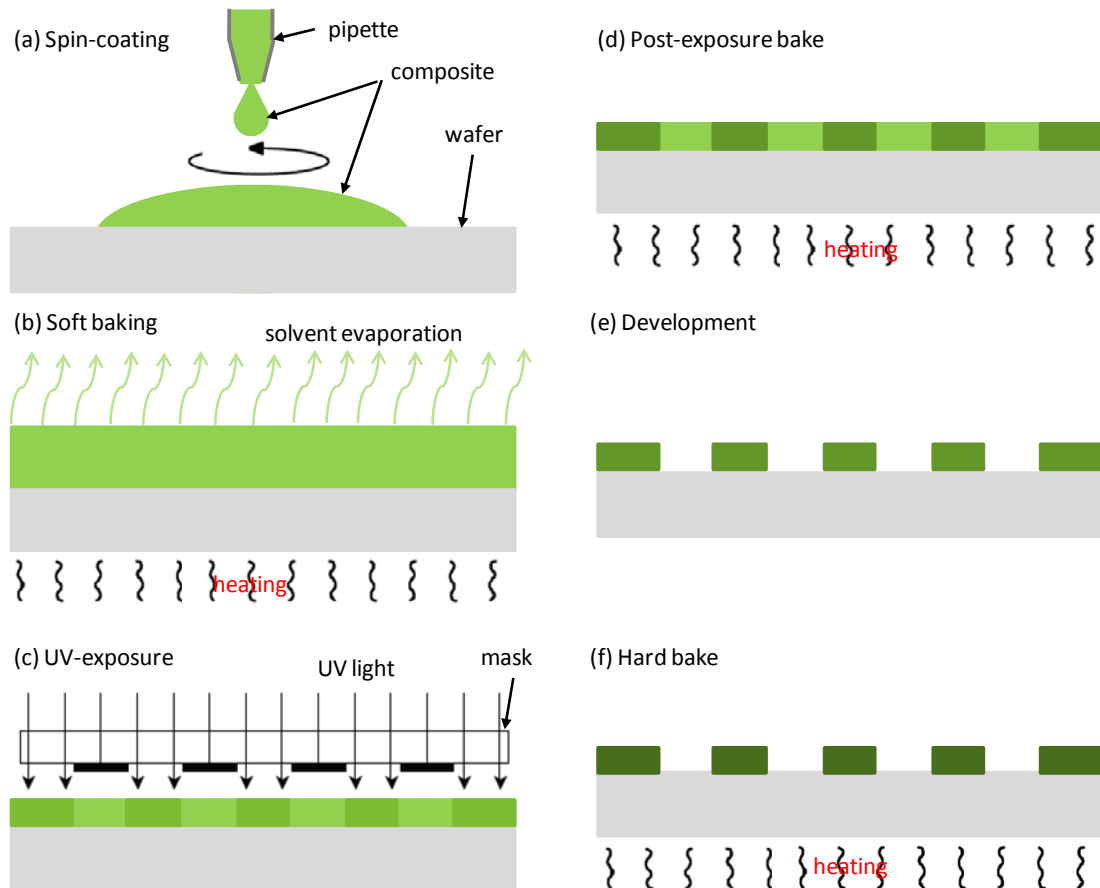


Figure 6.1: The scheme of basic photolithographic steps for processing of a negative tone photoresist, like, *e.g.* the SU8 epoxy resin and CNTs-SU8 composites.

In the spin-coating step (Fig. 6.1 (a)), a certain predetermined amount of relatively viscous liquid solution of photoresist is firstly deposited at the centre of the wafer. Subsequent spinning of the wafer induces radial spreading of the photoresist and coating of the surface of the wafer with the resist layer. Some difficulties may accompany the spin-coating step and one of them is the appearance of beads formed by a build-up of the photoresist on the wafer's edges on the front or back (or both) side of the wafer. Moreover, the planarization, which is the key issue for photolithography process, may easily be disrupted, for instance by the edge beading. Additional problem may present the aggregation of CNTs due to their exposure to the gradient of velocity and shear stress, what leads to the unwanted inhomogeneous composite film. Careful optimization of coating parameters (see Appendix 2) was done in order to minimize CNTs aggregation, planarization problem and edge beading.

After the spin-coating step, the substrate and the deposited resist layer are baked on a hot plate in order to remove the solvent in so called “soft baking” (SB) step (Fig. 6.1 (b)). The solvent removal in the SB step is usually followed by the volume shrinkage of the resin layer. This induces stress in the photoresist film and aggregation of the filler. The appropriate duration of the SB step (sufficient for the solvent removal), is determined by the thickness of the resist layer, which is in turn determined by the parameters of the previous processing step, *i.e.* spin-coating. The over- and under-baking have to be avoided, and thus, the SB duration has to be carefully chosen. In this work, the SB duration was optimized according to the thermogravimetric analysis (TGA) (see Appendix 2).

The structuration (patterning) of composites is provided by their exposure to UV light through a mask with a pattern (Fig. 6.1 (c)). The exposure initiates cross-linking of SU8. The exposure wavelength has to be carefully chosen to simultaneously correspond to the emission of the light source, the absorption of the PI and the transparency of the light source. The last was tested by UV-vis spectroscopy (see Appendix 2).

The previous UV-exposure step just defines the starting points of a chemical reaction that is actually driven by temperature in the subsequent step of post-exposure baking (PEB) (2) (3), (Fig. 6.1 (d)). Optimization of the PEB was done according to the results of TGA and DSC measurements (see Appendix 2).

The cross-linked SU8 is stable against dissolutions in the subsequent development step (Fig. 6.1 (e)), which have to be performed in such way that avoids structure’s cracking, collapse or detachment (see Appendix 2).

The hard baking (Fig. 6.1 (f)) is optional and it can be important for specific applications (see Appendix 2).

6.1.1 Results of CNTs-SU8 composite photolithography

Application of presented processing procedure yielded the most successful photo-patterning of composite films of different thicknesses when composites were containing the new PI and surfactant 1 (Fig. 6.2). The presence of CNTs in different concentrations did not disable photo-patterning, as it can be seen in the images in Figure 6.3.

However, as it has previously been mentioned, some problems may occur during the photolithographic processing of the CNTs-SU8 composites. For the composites prepared in this work, one of these frequently occurring problems, *i.e.* the lack of adhesion between the substrate and the composite film was not observed, even on Pyrex substrates known to be a ‘difficult’ substrate for SU-8 epoxy resin.

Another possible problem, *i.e.* formation of voids was noticed on the surface of the composites film deposits with 1.2 wt% and 1.6 wt% of CNTs in SU8 (Fig. 6.3 (c) and (d)).

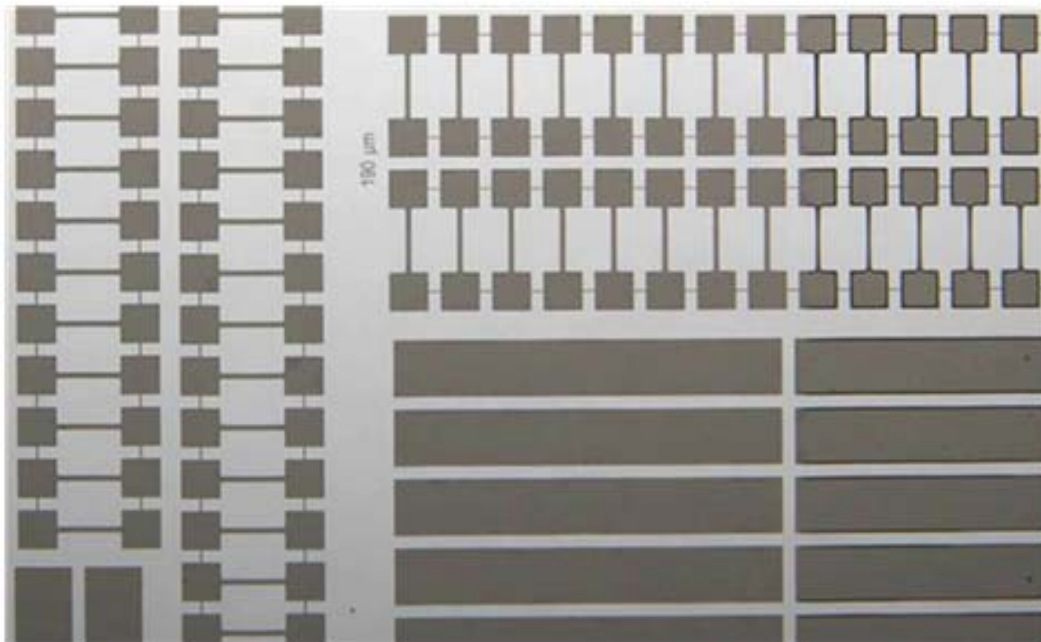


Figure 6.2: An example of photo-patterned structures of CNTs-SU8 composite containing 0.4 wt% of CNTs in SU8.

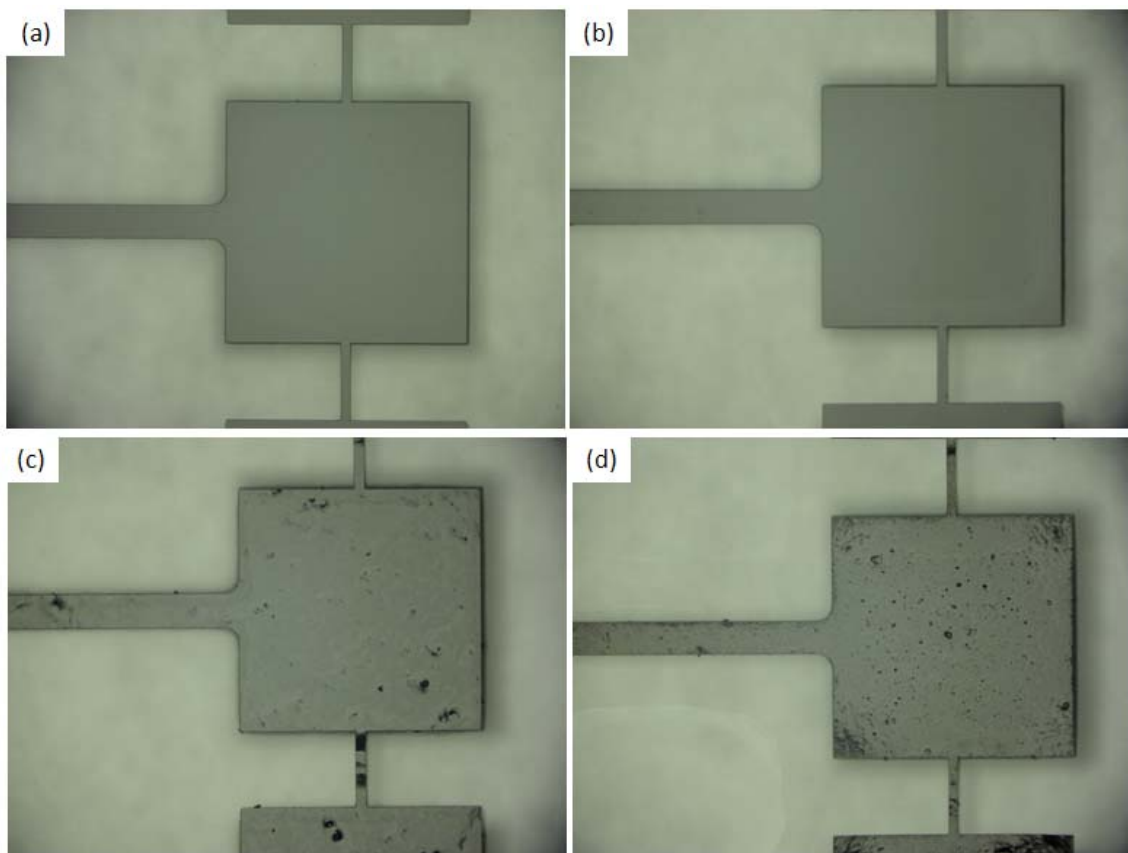


Figure 6.3: Photo-patterned structures of composites containing: (a) 0.4 wt%, (b) 0.8 wt%, (c) 1.2 wt% and (d) 1.6 wt% of CNTs in SU8.

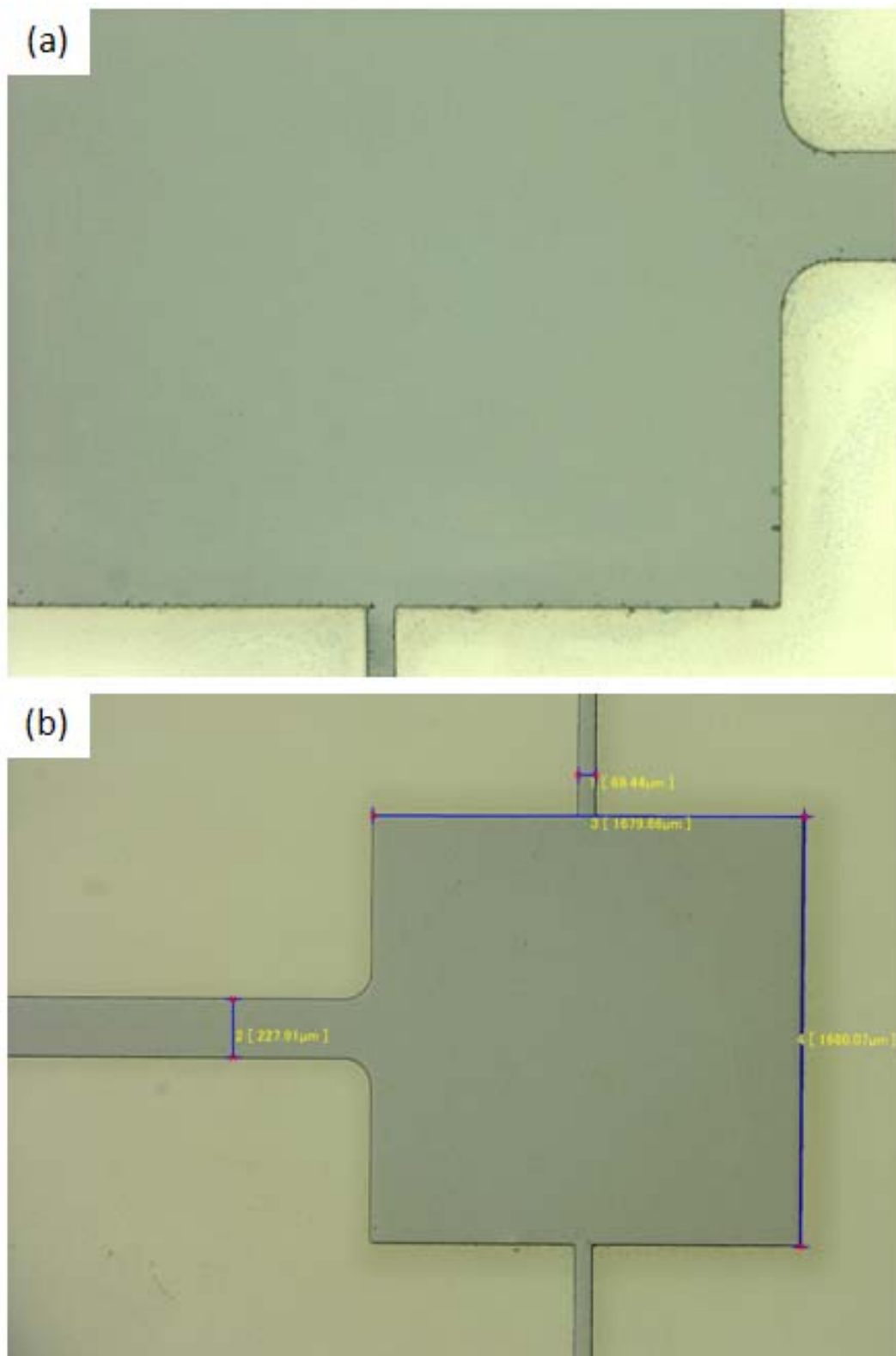


Figure 6.4: (a) Magnified edges of the composite deposit with 0.8 wt% of CNTs in SU8 show occasional edges imperfections; (b) dimensions of pattern of composite with 0.4 wt% of CNTs in SU8.

During curing, one of the major concerns is the internal stress, which can impair the final quality of the film's surface. This can be seen in the form of micro-cracks, which were occasionally noticed on the edges of the patterns, as shown in Figure 6.4 (a). This Figure depicts the magnified edges of the structure deposited using the composite containing 0.8 wt% of CNTs. Another problem relates to the deviation from the designed pattern dimensions, like in the structure shown in Figure 6.4 (b), with the final dimensions of: 69.44 μm , 227.91 μm , 1679.66 μm and 1680.07 μm , instead of expected ones: 70 μm , 230 μm , 1680 μm and 1680 μm , respectively. This deviation of dimensions can be negligible for some microengineering applications, but it also might jeopardize the dimensional stability in some other applications, like, *e.g.* in nano/micro-fluidics.

In the case when the surface of the composite film deposit is not perfectly planar, light diffraction may cause problems (4), like, *e.g.*, broadening of lateral dimensions of structures or traces of the resist (or composites in our case) outside the pattern edges. The example images of such shape distortions for the structures prepared on the same wafer (all structures were processed in the same way), with different distances from the centre of the wafer, are shown in Figure 6.5.

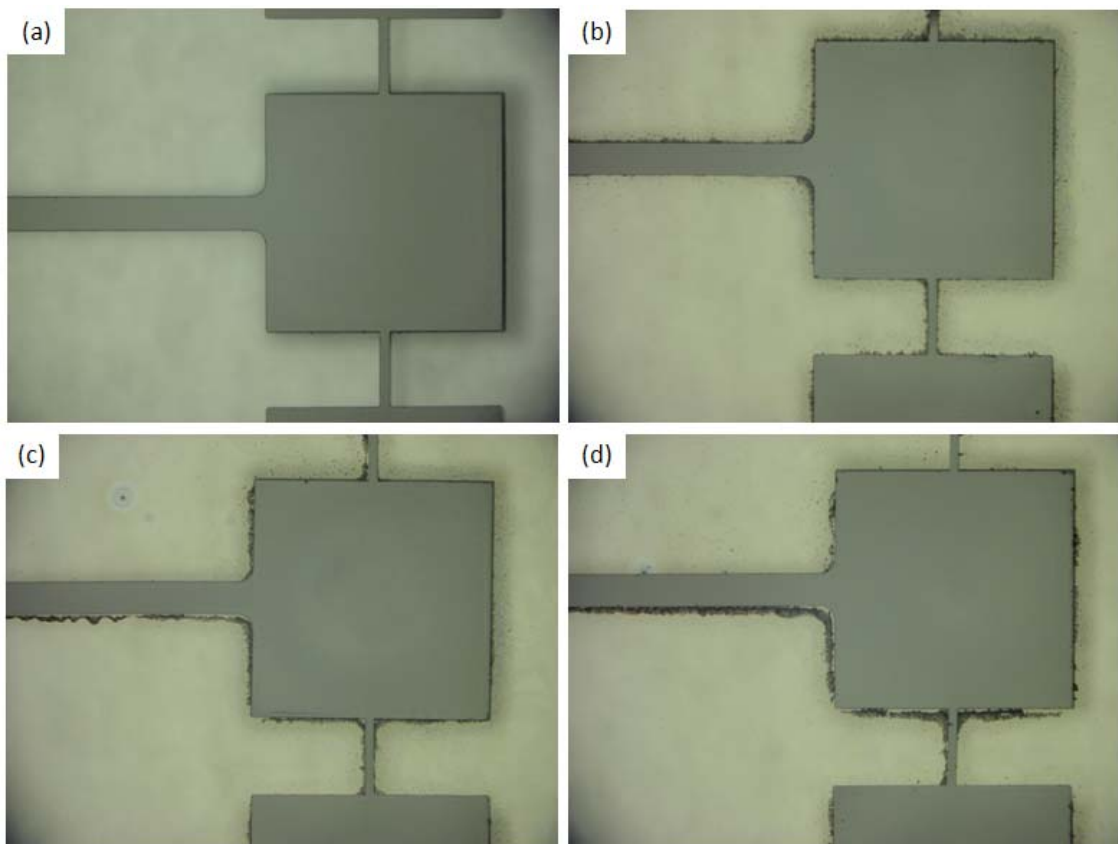


Figure 6.5: Images of the CNT-SU8 thin film structures deposited on the same wafer, but at different distances from its centre. The images of: (a) the structure deposited within the inner circle with the diameter of one half of the wafer's diameter; (b), (c) and (d) the structures

deposited outside of the inner circle towards the wafer's edge (the closest to the edge is image (d)). The deviation from the surface planarity causes light diffraction in the photolithographic process. This results in broadening of lateral dimensions of the composite outside the pattern edges. These effects are more pronounced with an increase of the distance from the centre of the wafer (from (a) to (d)).

Studies of Sangermano et al. (5) showed that, with an increase of CNTs content, the epoxy conversion decreases; in fact 0.1 wt% of CNTs reduced the epoxy conversion for 16%. Clearly, any further increase of CNTs content might induce dramatic changes in the overall epoxy conversion. The composite with the highest CNTs content which we studied for applications in the photolithographic processing was of 1.6 wt%, which is 16 times more than in the study of Sangermano (5). To a great extent, for thick deposits, an uncompleted SU8 conversion would certainly be visible in the form of a strong deviation from planarity of the surface. Indeed, this was observed for a portion of composite deposits with 1.6 wt% of CNTs, as shown in Figure 6.6.

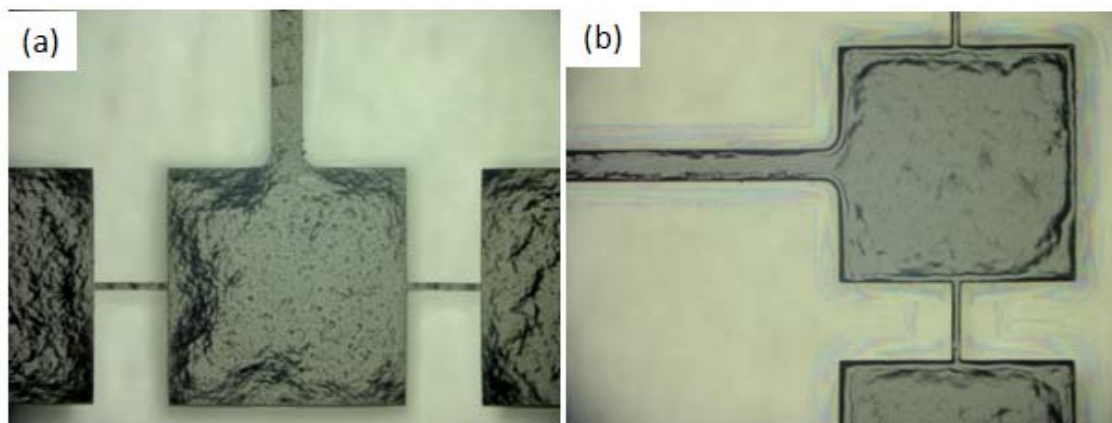


Figure 6.6: Images of the CNTs-SU8 thick film structures having 1.6 wt% of CNTs in SU8. Uncross-linked SU8 was removed in the development step, leaving a non-planar film surface.

6.1.1.1 Results of cut CNTs-SU8 composite photolithography

The photolithographic processing was also studied for composites prepared with cut CNTs (composites 2C, see Chapter 3). The main difference between composites prepared with cut CNTs and the ones with standard long CNTs is the strong probability of clustering of cut CNTs. Such aggregative behaviour could be expected due to the reduced size of CNTs and their higher mobility, which usually aids diffusivity. In this manner, the shear-induced aggregation would be facilitated. Moreover, objects with smaller size have higher surface area and higher surface free energy, and therefore, strongly tend to aggregate (3; 6). Indeed, the final structures of composite 2C showed very strong aggregations of cut CNTs where aggregates size exceed even few hundreds of micrometers, like it can be seen in example in Figure 6.7.

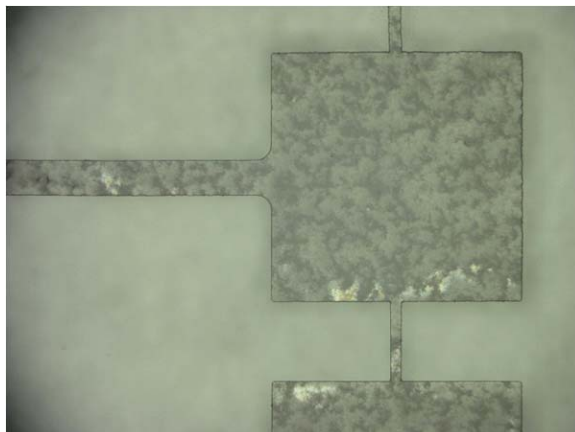


Figure 6.7: Example of the strong aggregation of the cut CNTs in the thin film deposits of CNTs-SU8 composite 2C containing 0.8 wt% of cut CNTs.

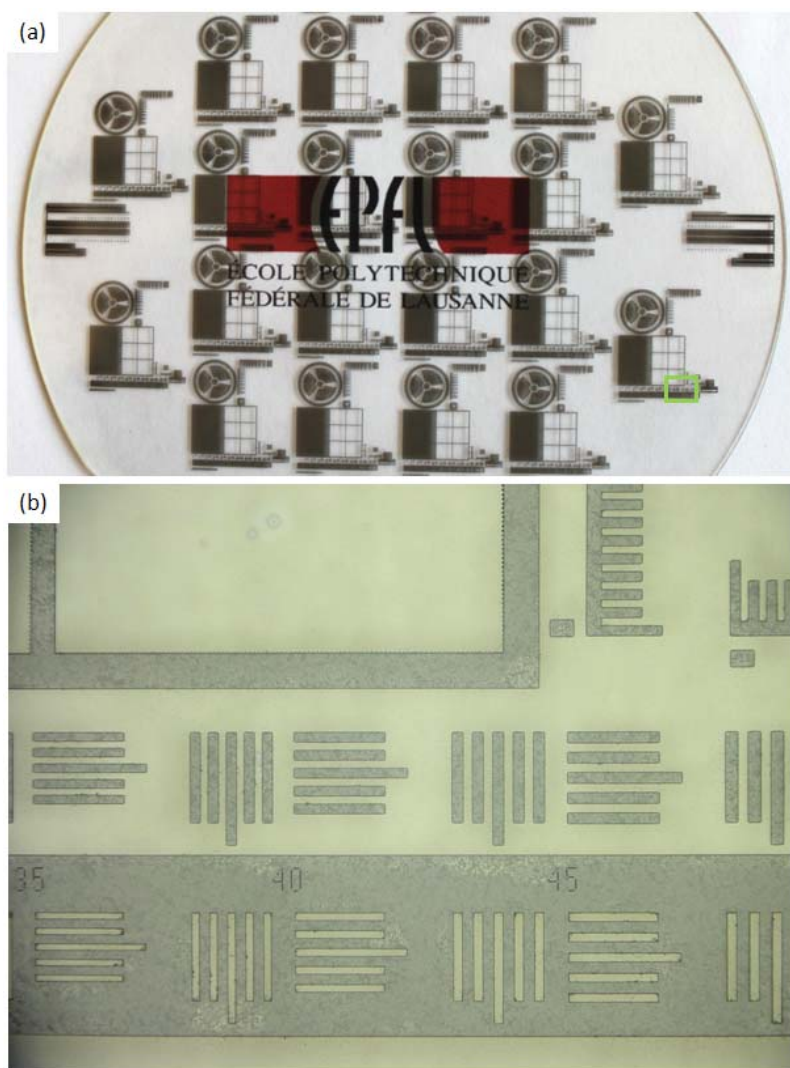


Figure 6.8: Structures of the CNTs-SU8 composite 2C containing 0.4 wt% of cut CNTs, where the lower image shows the magnified part of the upper one (marked by the green rectangle).

Numbers visible in the lower image (35, 40 and 45) indicate the line/space width in micrometers of the vertical and horizontal lines and spaces in the direction of the number.

Composites 2C were also photo-patternable with the use of the above-presented processing procedure and yielded structured films (Fig. 6.8 (a)). In spite of the strong aggregation of the cut CNTs, these composites yielded quite good resolution, typical for SU8-based thin film deposits (Fig. 6.8 (b)).

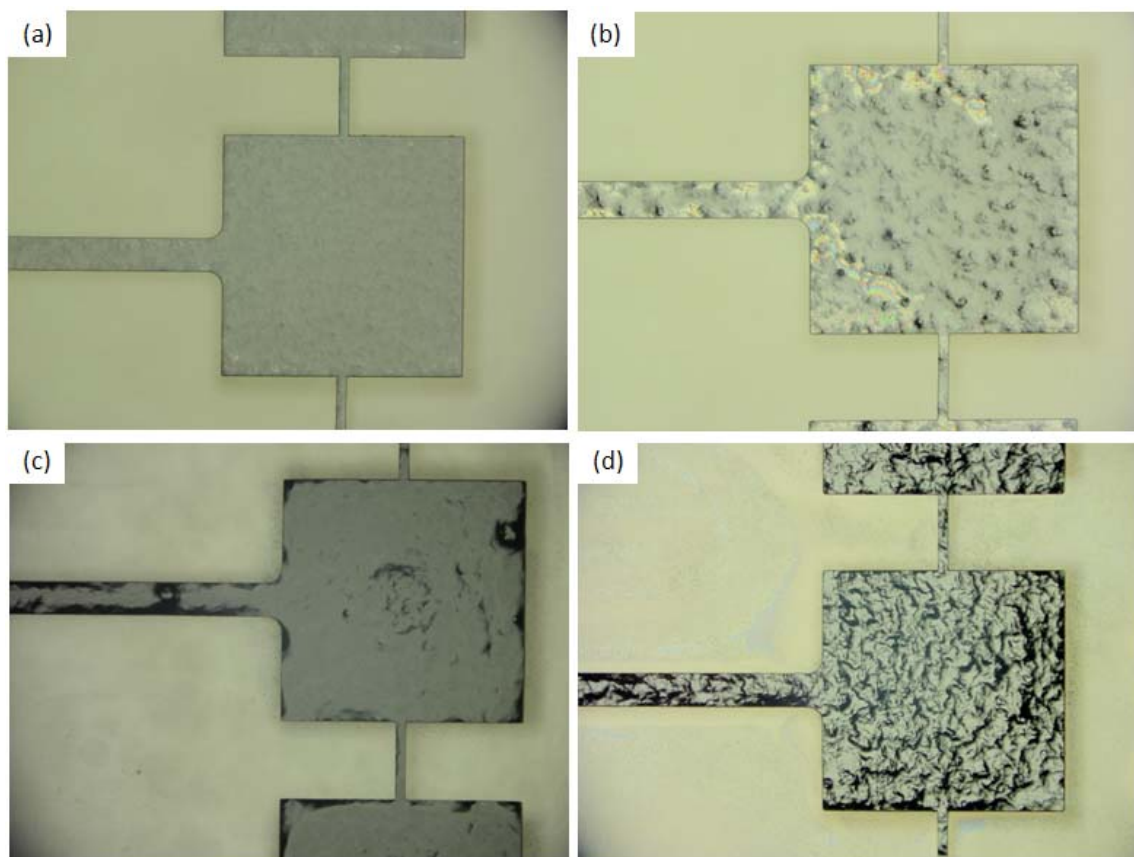


Figure 6.9: Photo-patterned structures based on CNTs-SU8 composites 2C containing: (a) 0.4 wt%, (b) 0.8 wt%, (c) 1.2 wt% and (d) 1.6 wt% of cut CNTs in SU8.

In the case of composites 2C, the presence of cut CNTs in different concentrations did not prevent photo-patterning what can be seen in the images in Figure 6.9. However, the surface roughness of obtained structures was significant already for composite films with the cut CNTs content of 0.8 wt%. This can be clearly seen in Figure 6.9 (b), (c) and (d). The same images show also the formation of voids, as a natural consequence of the high surface roughness.

As already mentioned, for composites 2, the adhesion problem did not appear. In contrast, composites 2C surprisingly often showed poor adhesion, even on quartz substrates. De-bonding of the edges of the structures was mostly observed for composites containing 0.4 wt% (Fig. 6.10 (a)) and 0.8 wt% of cut CNTs, while a more marked effect of

peeling at the ends of the structures was observed for composites with 0.4 wt% of cut CNTs (Fig. 6.10 (b)). The origin of such behaviour is probably due to the mechanical stress accumulation in the deposits of CNTs-SU8 composites containing cut CNTs.

Concerning transparency of the films, composites 2C showed higher transparency than composites 2, which were prepared with the same concentration of CNTs (Fig. 6.11).

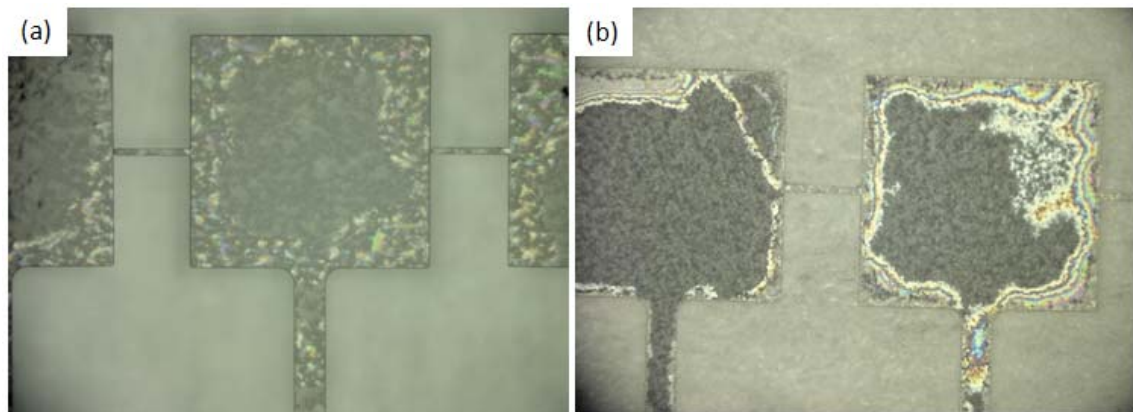


Figure 6.10: De-bonding of the edges (a) and peeling of the structures (b) of thin film deposit of CNTs-SU8 composites 2C containing 0.4 wt% of cut CNTs.

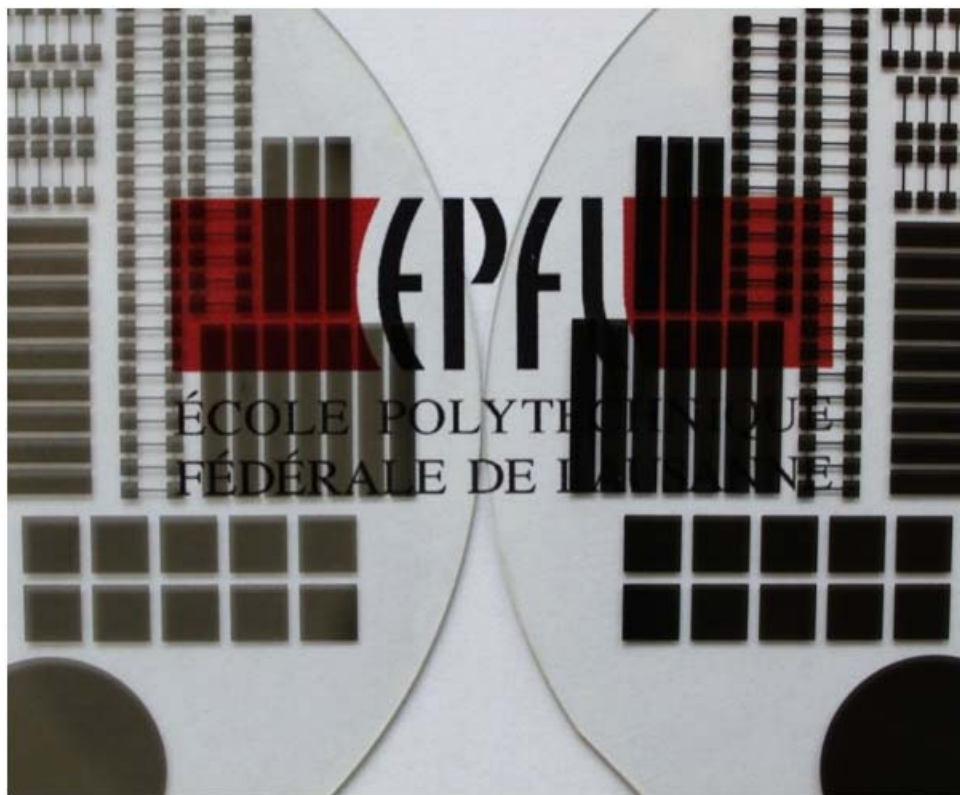


Figure 6.11: Structures formed from CNTs-SU8 composites having the same content of 0.4 wt% of CNTs, shown on the left and the right side of the image, for the cut CNTs and long CNTs, respectively. A higher transparency of the composite film on the left side can be seen.

6.1.1.2 Stripping

There are a lot of ways to lift-off SU8 deposits (7). In this work, the problem of the SU8 deposits lift-off (stripping) was solved by using a method of sacrificial layer. In general, this stripping method consists of depositing a sacrificial layer on the wafer before the deposition of the resist. After all standard UV-lithography processing steps previously listed, the wafer with the structured resist is dipped in the solution which can dissolve the material of sacrificial layer, but which, at the same time, does not react with the cross-linked resist. To this end, we made use of special products, usually employed for SU8 processing, as a sacrificial layer and its developer (provided by Gersteltec (1)). As a result, composite structures were successfully lifted-off from the substrates (quartz, float glass and Pyrex) (Fig. 6.12). However, stripping could be achieved only with the use of a mild sonication (in the ultrasonic bath), which accelerated the developer diffusion. Interestingly, lifted-off free standing composite structures showed substantial flexibility (Fig. 6.13).



Figure 6.12: Rectangular and dog-bone structures lifted-off from the wafer after photo-patterning.

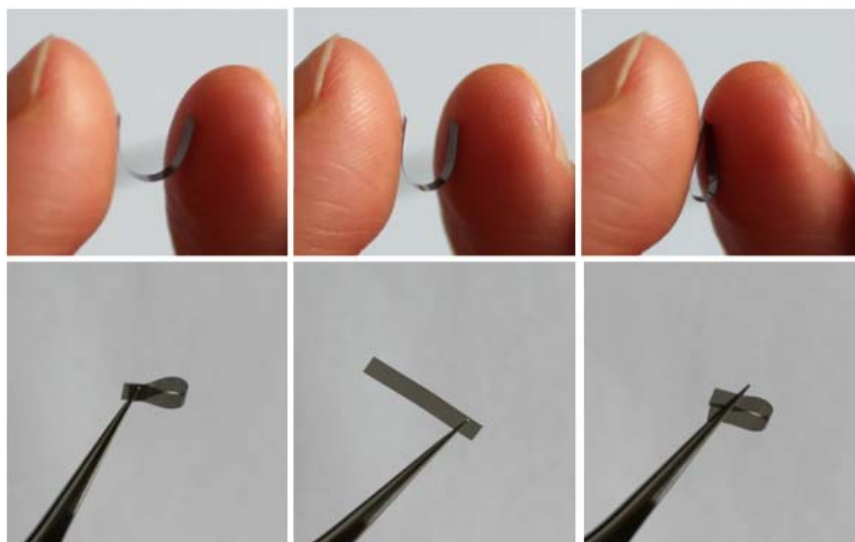


Figure 6.13: Flexibility of the CNTs-SU8 composites structures prepared by photolithography and lifted-off from the substrates.

6.1.2 Conclusions

As explained by Nouzille (8; 3), the development of an efficient, radiation-cured ink relies on numerous factors, which include the type of the printing facility, curing equipment and physical properties of the photosensitive ink. When the photosensitive ink is a composite material, the corresponding formulations comprise at least three components: epoxy (SU8), photo-initiator (PI), and filler (CNTs). In general, epoxy contributes to the majority of final properties of the cured film, while PI activates the polymerisation reaction and influences the surface curing, through cure and total degree of polymerisation. On the other hand, fillers provide with useful (required) complementary properties. In the case of UV-curing, the fillers greatly influence the ability of UV radiation to penetrate the ink film. Therefore, from the formulation standpoint, the major factors determining printability are: the material chemistry and presence of filler, that is, in our case, of CNTs. In fact, the optimisation of photosensitive formulations and their photolithographic processing is quite difficult due to the complex influence of various parameters. The optimisation of photosensitive formulation consists mostly of finding the best compromise between the cure speed, printability, adhesion and physical properties (8; 3). In this thesis, we report on the successful optimisation of thermo- and UV-curable CNTs-SU8 composite formulations, where the best photo-curable properties showed composites containing new PI, surfactant 1 and standard long CNTs.

In this work, by applying the *state-of-the-art* photolithographic processing, photo-patterned films of CNTs-SU8 composites 2 suitable for various applications were obtained. These films offer a plethora of tuneable features, including transparency, flexibility, electrical conductivity and variable mechanical properties.

6.2 Inkjet printing of CNTs-SU8 composites

In inkjet printing process, a sudden reduction of the chamber volume triggers the ejection of a fixed quantity of ink thorough a nozzle connected to this chamber. The ejected drop falls on the substrate, where it dries due solvent evaporation (9). In order to print patterned structures (drops or lines) by inkjet technique, firstly the appropriate ink formulations have to be prepared (see Appendix 3). To this end, in this work, we especially elaborated composites 2C (see Chapter 3). To achieve stable conditions for drop formation, applied voltage and the pulse shape have to be adjusted. Moreover, wetting of the nozzle surface have to be avoided (see Appendix 3). Ink-jetting of stable drops (Fig. 6.14 (a)) was followed by contact angle measurement (see Appendix 3) and printing of drops (Fig. 6.14 (b)) and lines (Fig. 6.14 (c)).

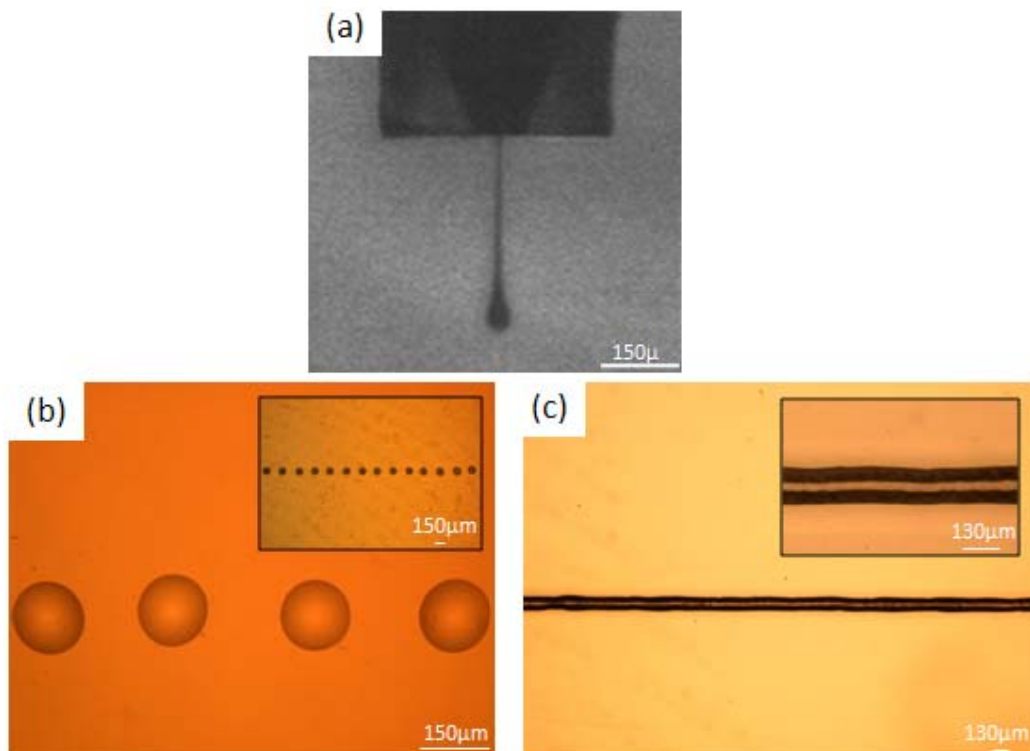


Figure 6.14: (a) Stroboscopic image of stable drop formation without wetting of nozzle faceplate. (b) Microscope image of CNT-SU8 droplets printed on a glass substrate. The droplet diameter is roughly 150 μm and the distance between the centres of the droplets is 400 μm (zoom out and zoom in images); (c) Optical microscope image of a CNT-SU8 ink-jet printed stripe on glass surface. The droplet spacing was set to 200 μm, which resulted in a continuous 130-μm wide stripe (The lighter line in the middle of the zoom out and zoom in images is the reflected light from the crest of the stripe) (see the ref. [MM13]).

6.2.1 Inkjet printing of CNTs-SU8 composites 2C inks onto flexible polyester substrates

Obtaining stable and precise patterns of desired structures is not the only requirement for successful inkjet printing. One of the key requirements for inkjet-printed structures is also a strong adhesion to the substrate. This latter feature is often difficult to achieve without substrate's surface modification by chemical treatments. Additional difficulty arises when flexible polymeric substrates are to be used. These are the most difficult ones for adhesion because the low surface energy of the polymers makes the wetting less favourable. When ink is printed onto a non-adsorbing surface, it will tend to bead up rather than form a uniform layer. In printing on polymer flat sheets (transparencies), adhesion can be obtained by the use of a swelling the polymer layer, adding a transparent but porous layer or *via* surface roughening (10). For instance, upon printing colloidal platinum suspension onto polyester transparencies, layers peeled off from

various coated and uncoated transparencies. In order to obtain good adhesion and stable not peeled off printed layers, transparencies had to be etched in sodium hydroxide (10). Another possibility is to tune the particles' surface properties by adding appropriate surfactants. This poses a problem because surfactant removal often involves extensive washing and/or special chemical treatments. This might induce separation of the printed structure from the substrate (11). On the other hand, if the surfactant is not removed from printed structures, their conductivity might be impaired. Additional adhesion promoters destabilize particle dispersion in the ink solution and may also significantly decrease desired electrical conductivity (11). Therefore, we inkjet-printed our CNTs-SU8 composite inks onto polyester transparencies without the use of additional adhesion promoters. Since CNTs-SU8 composites were inkjet-printed onto a mechanically flexible substrate, in our case polyester transparencies, printed structures had to be flexible as well. The bending of the substrate implies the need for toughness in the material of inkjet-printed patterns (10). It is observed that the film of CNTs-SU8 composite ink remained strongly attached to the surface of polyester transparencies. The adhesion between the wire and the substrate was excellent, and no delamination occurred even at repeatable, high mechanical deformations (Fig. 6.16).

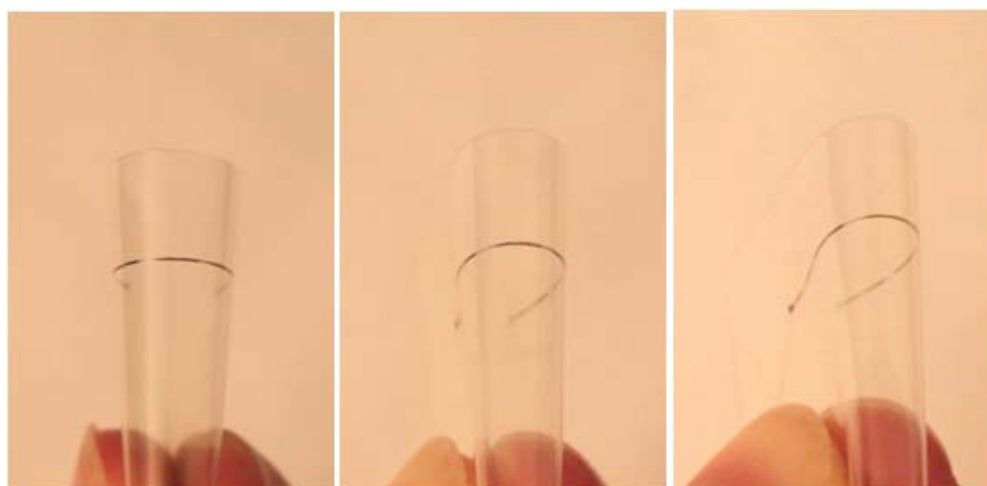


Figure 6.16: Photographs of inkjet-printed SU8-CNT wire on flexible polyester transparencies (see the ref. [MM13]).

6.2.2 Resistivity measurements

To adjust proper conditions for inkjet printing of CNTs-SU8 composites and good adhesion to various substrates, printed structures need to be electrically characterized. In the case of composite polymer materials containing elongated objects, like CNTs, a very important aspect is related to inter-chain interactions. These inter-chain interactions affect the printability, final morphology and transport properties of printed films (12). The degree of inter-chain interactions in CNTs-loaded inkjet inks can be significantly influenced by the presence of defects on CNTs' surface, by CNTs concentration and CNTs interactions with the

substrate and other components of composite. Additional problem is related to the well-known extreme difficulty achieving uniformly dispersed high fractions of CNTs in organic solvents. In such systems, due to aggregations, CNTs tend to form non-conductive mixtures.

Numerous research groups inkjet-printed solutions containing CNTs with aim to obtain electrically conductive structures. The results concerning the lowest obtained resistances are listed in the following.

Carboxyl functionalized SWCNTs (4–5 nm diameter and 0.5–1.5 μm long) mixed with PEDOT:PSS were inkjet printed on photo paper and sheet resistance of printed structures was $\sim 115 \text{ k}\Omega/\square$. Bare nanotubes on PET substrate showed poor adhesion and high sheet resistance ($>4 \text{ M}\Omega/\square$) (13).

Carboxyl functionalized CVD MWCNTs (10-70nm diameter and 1-5 μm long) - based aqueous ink was used to print patterns on paper and plastic surfaces. Electrically conductive patterns were obtained after 30 overprints. The sheet resistivity dropped to $40 \text{ k}\Omega/\square$ after 90 overprints (14).

Electrically conductive patterns were also obtained with SWCNTs of 5nm diameter and $10\mu\text{m}$ length dispersed in dimethylformamide. The inkjet-printed line with a width of 1.3 mm, corresponding to 8 overwriting steps, had a resistance of $5.7 \text{ k}\Omega$ (15).

Inkjet printing of the water soluble MWCNTs-polyaniline composite with a 32% content of MWCNTs resulted in conductive structures: 3 overprinted layers had sheet resistivity of $\sim 1.1 \text{ k}\Omega/\square$ (16).

Our result for the evolution of sheet resistance (R_{\square}) for CNTs-SU8 composite 2C thin film deposits as a function of CNT content is plotted in Figure 6.17. The results are plotted in the form of a box plot, where thick black line correspond to the median values, the boxes indicate the interquartile ranges (IQR), with the bottom and the top of the boxes corresponding to the lower (cuts off lowest 25% of data) and upper (cuts off highest 25% of data) quartiles, respectively, whiskers denotes the resistance ranges, which included 99.3% of data, and the circles indicate outliers. From the presented data it is possible to conclude that the electrical resistance decreases drastically with the increasing CNT content, as compared to film deposits of the same thickness prepared from unloaded SU8. The corresponding sheet resistance for such unloaded SU8 films could be of $1 \times 10^{17} - 1 \times 10^{18} \Omega/\square$, since the surface resistivity of SU8 is of $\sim 10^{14} \Omega\text{m}$ (17). It can be noticed that for the content of 0.8 wt% of CNT, the surface resistance decreased by ten orders of magnitude as compared to the unloaded SU8, which points to a percolation phenomenon.

Generally, materials can be classified concerning their electrical properties as follows (18): insulating materials are defined as those that have a surface resistance of at least $1 \times 10^{11} \Omega/\square$, conductive materials are those that have a surface resistance of less than $1 \times 10^4 \Omega/\square$, and the materials that have a surface resistance of greater than or equal to $1 \times 10^4 \Omega$

sq^{-1} , but less than $1 \times 10^{11} \Omega/\square$, are classified as dissipative materials. The CNTs-SU8 inks with various CNTs contents studied in this work fall in the latter category. These materials are very important when static electricity dissipation is required (5). The results of electrical characterisation of the inkjet-printed structures showed that our composite ink is indeed suitable for applications that require the control of electrostatic discharge. Actually, adding of only 0.8 wt% of CNTs was enough to obtain a composite ink suitable for applications that require electrostatic discharge.

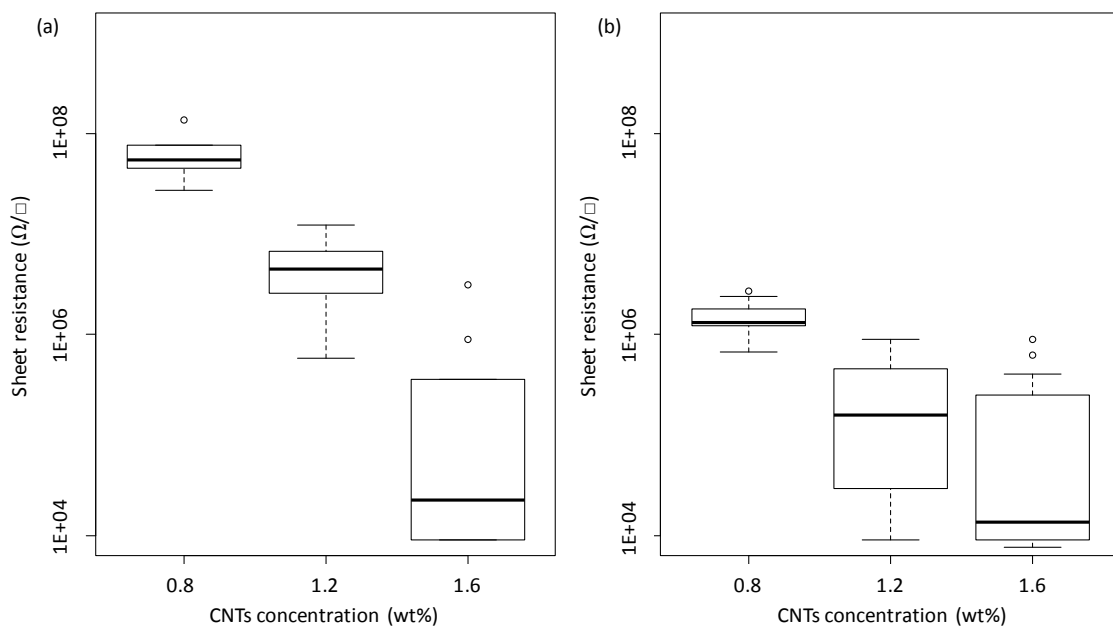


Figure 6.17: Sheet resistance of the native (a) and polished (b) surfaces of CNTs-SU8 inkjet-printed structures as a function of CNTs concentration (CNTs weight percent) (see the ref. [MM13]).

For 0.8 wt% and 1.2 wt% CNTs content an insulating layer of polymer forms on the top of the droplets, as observed by several samples to have resistivity above 200 MΩ in the native state. For the highest concentration batch, only one sample had such a high resistance. Removing the insulating layer has dramatically decreased the measured resistance of the samples with 0.8 wt % and 1.2 wt% of CNTs for two orders of magnitude. In contrast, the sample with 1.6% CNT content did not show any significant change upon removal of the insulating layer (Fig. 6.17).

The obtained values for sheet resistivity were higher than expected. The reasons could be numerous. In particular, since the CNTs suspension is stabilised by surfactant, the necessary inter-tube contact required for high conductivity is precluded by the presence of surfactant layers on the surface (10). Another reason for the obtained high sheet resistance might be due the observed phase separation, which was inferred from the difference in sheet resistance of the top-most and polished surfaces (see Fig. 6.17). In principle, one cannot exclude that similar phase separated regions do exist in the bulk on a very fine scale.

They are certainly not predominant, because the overall resistance has considerably decreased upon CNTs loading.

Surprisingly, in some applications, the appearance of the phase separation in inkjet-printed structures and devices might be considered as an advantage. Therefore it is very important to know which parameters induce phase separation and change printed structures. In fact, besides the drying temperature, which is known to affect mechanism of phase separation in printed structures, also the heating rate is very important (19). It was found that rapid drying of the inkjet-printed structures also resulted in a fine phase separation. The devices obtained this way showed better performances than the devices prepared by other printing techniques, because the fine phase separation resulted in formation of smaller domains than the practical sizes of the printed droplets or lines (19). This approach, in combination with the elevated substrate temperature, yielded 2D features of hundreds of nanometres in size (19). Clearly, the films produced in this way may suffer from a non-uniform thickness (12).

Our mono-layered inkjet-printed constructs showed semiconductor behaviour and fine phase separation. They might find applications in various types of devices, where semiconducting active layers are required. An additional advantage is the difference in sheet resistivity between the topmost layer and the bulk of printed features. This could give rise to new possible applications as encapsulated semiconductors, what would eliminate the need to protect and insulate printed semiconductors. Moreover, the actual size of a semiconducting element printed this way would be smaller than the printed structure itself, because of the phase-separated-insulating-topmost layer.

6.2.3 Conclusions

We successfully prepared CNTs-SU8 composite 2C ink by the choice of the appropriate solvent, surfactant and CNTs. The ink with optimized parameters is highly suitable for inkjet printing on various substrates. Straight flexible conductive lines and regular arrays of 150 μm dots were successfully printed, with sheet resistances corresponding to the class of dissipative materials. The printed structures showed excellent adhesion to glass and even to unmodified polyester sheets (transparencies). The highest processing temperature used during the entire process was of 95°C, which is low as compared to the temperatures used in standard inkjet processes aiming to create conductive structures by sintering of metallic particles. Fully processed printed composite structures are flexible and show good performances at elevated temperatures (SU8 itself can be heated up to 250°C, during which its chemical resistance further increases). The printed structures are not subject to chemical modification or degradation upon exposure to harsh chemicals like hydrofluoric acid. This is in contrast to organic conductive polymers and

metallic nanoparticles known to be unstable in most environments, even at atmospheric conditions, such as moisture or oxygen.

6.3 Screen printing

Over the last decades, the technologies of printing have been rapidly developing. Notwithstanding, the further improvement of printing techniques, with the aim of bringing new functions to the materials, still remains in the focus of interests of industrial and scientific communities. For applications on the industrial scale, screen printing is often considered as the most suitable printing technique because of many advantages, like low cost mass production and simplicity of the process. Furthermore, the screen printing method is one of the most effective techniques for rapid covering of large surfaces. In the context of printing applications, the most remarkable ones are related to the development of patterned electronic circuits with new functions, like flexible electronics, low cost conductors, sensor properties and smart materials. These new exciting properties do not arise from the printing technique itself. In fact, they are also consequences of new ink generations especially designed to have desired properties by adding nano-sized fillers into polymers. The vast majority of the reported results in this field are related to composite pastes where CNTs are used as filler (20; 21; 22; 23; 24; 25; 26; 27). The screen printing method enables us to cover large surfaces with CNTs where other deposition methods cannot be used (like the electrophoresis which cannot be used for rapid large scale coverage and direct CNTs' carpet growth which is unsuitable for most of the processes owing to the growth temperatures above 150°C).

The screen printing of pastes containing CNTs is facing several difficulties in achieving a bigger outcome. One of the main shortcomings of screen-printed CNTs-based pastes is the weak adhesion of CNTs to a substrate (21). Some attempts to overcome this problem are accomplished through a special thermal treatment in controlled atmosphere (22), which is not suitable for all kind of substrates and processes. Other solutions to better fix CNTs to a substrate consist on adding binding materials. These latter methods have also some drawbacks, including:

- binders require sintering at temperatures above 350°C (20; 21; 22; 23; 24; 25; 26),
- out-gassing of the binders' components cause undesirable effects in certain applications (24; 26)
- binders often cover the surface of printed CNT films after sintering and might degrade the film properties.

In order to remove these residuals, different methods were used (like mechanical rubbing of surface (22), adhesive taping (24) or crushing the printed film by mechanical pressure (25)). Unfortunately, all these methods are causing secondary contamination and damage of the film. Another problem of the screen printing technique is a limitation in resolution of

printed structures, which is related to the rheological properties of the paste (24). This problem can be overcome by the use of photosensitive CNT paste in conjunction with a photolithographic process (26; 27; 28). Consequently, suitable pastes for advanced applications would be photosensitive ones.

6.3.1 Process description

The screen printing process involves using of screens, inks, squeegees and substrates (Fig. 6.18). In simple terms, the screen printing process consists of placing substrate under the printing screen and forcing ink to pass through the screen mesh with a squeegee (Fig. 6.18 (a)).

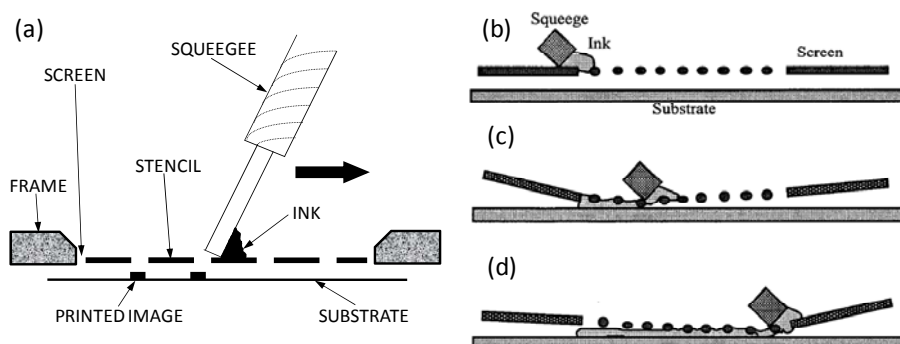


Figure 6.18: Screen printing set-up (a) and process (b), (c) and (d), (From the ref. (29)).

The screen, one of the most important components of screen printing, is a complex system for itself and has to be prepared prior to the printing process. The screen consists of a stencil which defines the pattern to be printed, a mesh which carries the stencil and a frame which holds the mesh. The screen printing process is illustrated in Figure 6.18. In the first step, the ink has to be placed on the upper surface of the screen which is parallel to the substrate at the “snap off” distance (Fig. 6.18 (b)). Subsequently, the squeegee travels over the screen and presses it down in order to obtain contact with the substrate (Fig. 6.18 (c)). Simultaneously, the ink, a thick film paste, is forced to pass through the holes of the screen by pressure of the squeegee. After the squeegee passed over the screen, the deposited paste wets the substrate’s surface (Fig. 6.18 (d)). In such a way, desired shapes can be obtained on diverse substrates.

6.3.2 Results and discussions

Our CNTs-SU8 composites could successfully be prepared in form of a paste that was suitable for screen printing applications, if the weight percent of CNTs was of 3 wt% or higher. Standard screen printing was performed on an alumina substrate with composites containing 3 wt%, 5 wt% and 10 wt% of CNTs in SU8, under different squeegee force and

printing speed. Changes of printing speed did not influence printing outcome, but squeegee force appeared to be a crucial printing parameter. In fact, higher pressures enabled structures with well defined edges without blurring.

The rod coating of composite pastes through the stencil pattern was carried out on glass slides, on paper or on absorbent fabric. Obtained structures were very well defined without blurred edges. Excellent adhesion was achieved for all used substrates, which confirmed that the usual screen-printing problems of fixing CNTs to a substrate have been solved.

The important difference between printing onto fabric, paper and plastic foil is in that fabric is more absorbent than paper, while plastic foil is not absorbent at all. This would mean that, when we pass a squeegee over fabric, it will absorb ink more than paper. In contrast, plastic foil would tend to let ink segregate on top of it. Absorption of ink into the printing substrate is essential for the quality. Namely, if the ink cannot be absorbed at all or if it is absorbed too intensively by the substrate, the printed design might be blurred. In order to avoid this problem, printing is usually done “off-contact”. This means that the screen and the substrate are separated by the “snap off” distance (Fig. 6.18 (b)). We could print our CNTs-SU8 composites both “in contact” and “off-contact”. Surprisingly, printing “in contact” on a plastic foil (a non-absorbing substrate) resulted in printings, which were not blurred (Fig. 6.19 (a) and (b)).

Screen printing of CNTs-SU8 composites on a standard white paper was expected to have problems of blurring, because the liquid phase of a composite system can be very easily absorbed by the paper substrate, which would leave traces around printed structures. Unexpectedly, however, printing on paper substrate resulted in structures with very well defined edges (Fig. 6.19 (c) and (d)). There were no traces of composite’s liquid phase absorption (or/and drying) outside of structures’ edges.

For printing on a fabric, an absorbent fabric was intentionally chosen. This type of fabric, due to its strongly absorbing properties, corresponds to the most difficult conditions for successful screen printing. Moreover, for such sort of a fabric, with very high surface roughness, one could expect difficulties in achieving printed structures with defined edges. Astonishingly, as can be seen in Figure. 6.19 (e) and (f), the printed composites’ structures were without blurred edges.

Additionally, it is worth of noting that all our screen-printed deposits showed considerable flexibility (Fig. 6.19 (b), (d) and (e)). CNTs-SU8 composite layers were flexible regardless of the layer thickness. We also found excellent adhesion of these deposits to atypical substrates, like plastic foils, paper or fabrics. Adhesion and flexibility of composite layers are preserved even in the case of layers deposited on flexible substrates. Furthermore, no case of cracking or fracture formation on CNTs-SU8 layers could be observed, even after numerous bending of the substrate.

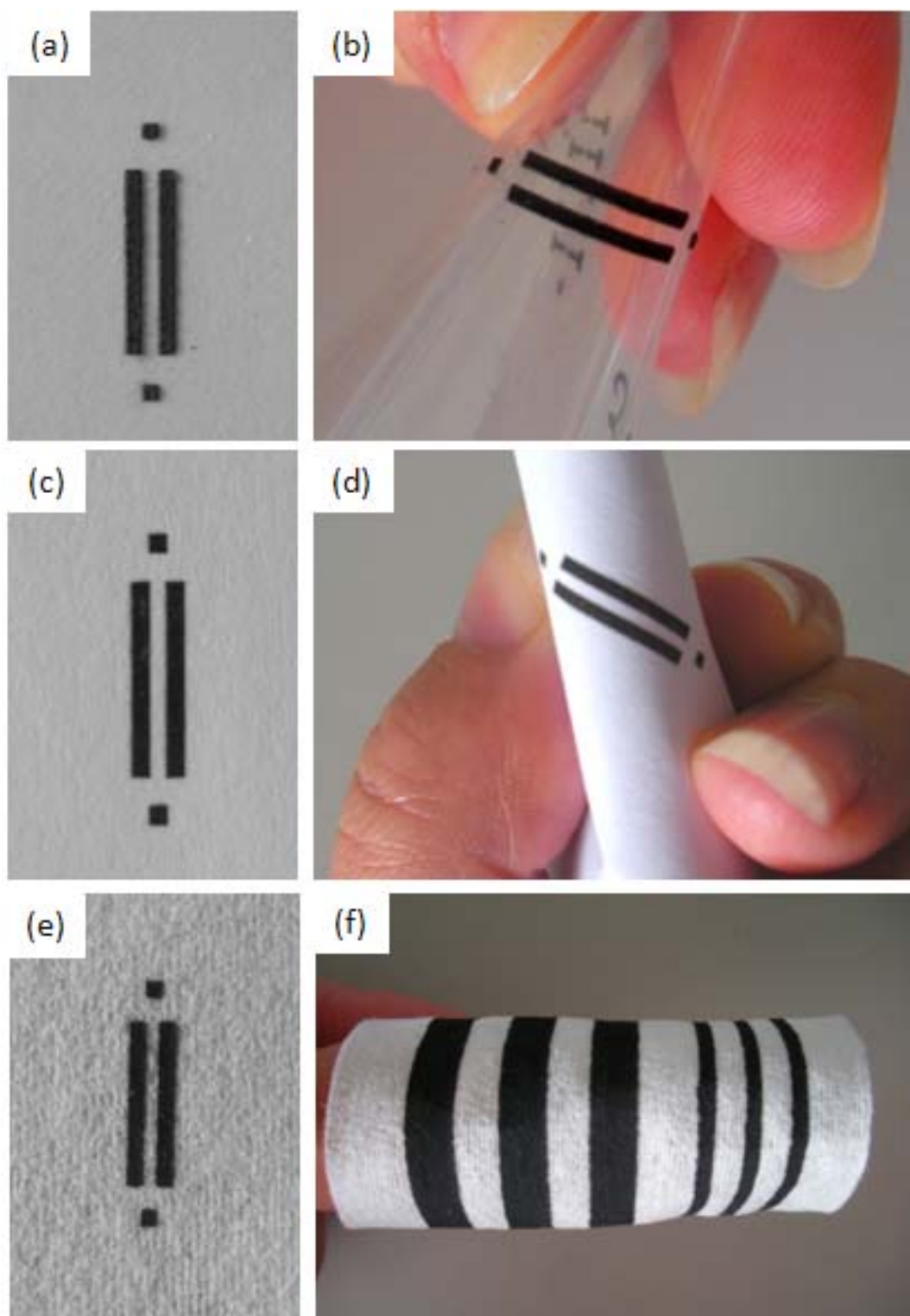


Figure 6.19: Example results of CNTs-SU8 composites 2 screen-printed on: (a, b) a plastic foil, (c, d) paper and (e, f) fabric. Printed structures did not have blurred edges. Moreover, traces of solvent spreading into absorbing substrates (paper (c) and fabric (e)) put aside of the pattern were not observed. Interestingly, all printed structures showed considerable

flexibility and preserved adhesion, without cracks formation, even after multiple bending (b, d, f).

The overall results indicate that composites obtained in this work could find attractive applications in flexible electronics. Moreover, it could be very promising to have electric circuits printed on a standard paper, which would make electronics even lighter and cheaper. Another fascinating application would be to make sensors directly printed on cloths in order to monitor desired performance, like, for instance, the heart beat or temperature. The obtained results are already good achievement, but the big potential applications have to be checked.

References

1. **Gersteltec**. [Online] [Cited: 5 June 2011.] <http://www.gersteltec.ch/su-8-Photoresists/>.
2. *SU-8: a photoresist for high-aspect-ratio and 3D submicron lithography*. **A. del Campo and C. Greiner**. 17, 2007, *Journal of Micromechanics and Microengineering*, p. R81.
3. **Y. Leterrier, M. Sangermano, H.-A. Klok, and E. Nouzille**. *Science and Technology of UV-induced Polymerization*. EPFL. 2008.
4. *Reduction of diffraction effect of UV exposure on SU-8 negative thick photoresist by air gap elimination*. **Y.-J. Chuang, F.-G. Tseng and W.-K. Lin**. 2002, *Microsystem Technologies*, Vol. 8, p. 308.
5. *Antistatic Epoxy Coatings With Carbon Nanotubes Obtained by Cationic Photopolymerization*. **M. Sangermano, S. Pegel, P. Pötschke and B. Voit**. 5, 2008, *Macromolecular Rapid Communications*, Vol. 29, p. 396.
6. *In Situ Synthesis of Silver-Epoxy Nanocomposites by Photoinduced Electron Transfer and Cationic Polymerization Processes*. **M. Sangermano, Y. Yagci and G. Rizza**. 2007, *Macromolecules*, Vol. 40, p. 8827.
7. **G. Genolet**. *New photoplastic fabrication techniques and devices based on high aspect ratio photoresist*. thesis no. 2421. Lausanne : EPFL, 2001.
8. **E. Nouzille**. *Dark curing kinetics of UV printing inks by real-time ATR-FTIR spectroscopy*. Lausanne : EPFL, 2007. Thesis No. 3780.
9. *Self-Organization of Ink-jet-Printed Triisopropylsilylethynyl Pentacene via Evaporation-Induced Flows in a Drying Droplet*. **J. A. Lim, W. H. Lee, H. S. Lee, J. H. Lee, Y. D. Park and K. Cho**,. 2, 2008, *Advanced Functional Materials*, Vol. 18, p. 229.
10. *Inkjet Printing for Materials and Devices*. **P. Calvert**. 13, 2001, *Chemistry of Materials*, p. 3299.
11. *Highly conductive paper for energy-storage devices*. **L. Hu, J. W. Choi, Y. Yang, S. Jeong, F. L. Mantia, L. Cui and Y. Cui**. 512, 2009, *PNAS*, Vol. 106, p. 21490.
12. *Inkjet printing as a deposition and patterning tool for polymers and inorganic particles*. **E. Tekin, P. J. Smith, and U. S. Schubert**. 4, 2008, *Soft Matter*, p. 703.
13. *Inkjet printing of transparent and conductive patterns of single-walled carbon nanotubes and PEDOT-PSS composites*. **T. Mustonen, K. Kordas, S. Saukko, G. Toth, J. S. Penttila, P. Helisto, H. Seppa and H. Jantunen**. 244, 2007, *Phys. Status Solidi B*, p. 4336.
14. *Inkjet Printing of Electrically Conductive Patterns of Carbon Nanotubes*. **K. Kordas, T. Mustonen, T. Geza, H. Jantunen, M. Lajunen, C. Soldano, S. Talapatra, S. Kar, R. Vajtai and P. M. Ajayan**. 2, 2006, *Small*, p. 1021.

15. *Inkjet printing of single-walled carbon nanotubes and electrical characterization of the line pattern.* **J. W. Song, J. Kim, Y. H. Yoon, B. S. Choi, J. H. Kim and C. S. Han.** 19, 2008, *Nanotechnology*, p. 095702.
16. *Inkjet deposition and characterization of transparent conducting electroactive polyaniline composite films with a high carbon nanotube loading fraction.* **W. R. Small, F. Masdarolomoor, G. G. Wallace and M. in het Panhuis.** 17, 2007, *Journal of Materials Chemistry*, p. 4359.
17. [Online] [Cited: 18. 7. 2011.] <http://www.microchem.com/pdf/SU-8-table-of-properties.pdf>.
18. **Electrostatic Discharge Association.** *ESD Association Standard ANSI/ESD S541-2008 for the Protection of Electrostatic Discharge Susceptible Items - Packaging Materials for ESD Sensitive Items.* s.l. : Electrostatic Discharge Association, 2008. An American National Standard Approved September 29, 2008.
19. *Controlled Phase Separation of Polyfluorene Blends via Inkjet Printing.* **Y. Xia and R. H. Friend.** 38, 2005, *Macromolecules*, p. 6466.
20. *Highly Efficient Field Emission from Carbon Nanotube Nanohorn Hybrids Prepared by Chemical Vapor Deposition.* **R. Yuge, J. Miyawaki, T. Ichihashi, S. Kuroshima, T. Yoshitake, T. Ohkawa, Y. Aoki, S. Iijima and M. Yudasaka.** 12, 2010, *ACS Nano*, Vol. 4, p. 7337.
21. *Field emission properties and stability of thermally treated photosensitive carbon nanotube paste with different inorganic binders.* **J.H. Park, J.S. Moon, J.W. Nam, J.B. Yoo, C.Y. Park, J.M. Kim, J.H. Park, C.G. Lee and D.H. Choe.** 14, 2005, *Diamond & Related Materials*, p. 2113.
22. *Large area screen-printing cathode of CNT for FED.* **Y. Shi, C. Zhu, W. Qikun and L. Xin.** 12, 2003, *Diamond and Related Materials*, p. 1449.
23. *Field emission characteristic of screen-printed carbon nanotube cathode.* **J. Li, W. Lei, X. Zhang, X. Zhou, Q. Wang, Y. Zhang and B. Wang.** 220, 2003, *Applied Surface Science*, p. 96.
24. *Effects of bonding materials in screen-printing paste on the field-emission properties of carbon nanotube cathodes.* **H. Shin, W. Chung, K. H. Kim, Y. Cho and B. Shin.** 6, 2005, *J. Vac. Sci. Technol. B*, Vol. 23.
25. *The fabrication and operation of fully printed Carbon nanotube field emission displays.* **F. Zeng, C. Zhu, W. Liu and X. Liu.** 37, 2006, *Microelectronics Journal*, p. 495.
26. *Effects on the field emission properties by variation in surface morphology of patterned photosensitive carbon nanotube paste using organic solvent.* **W. Cho, Y. Lee, J. Choi, J. H. Han and B. Ju.** 257, 2011, *Applied Surface Science*, p. 2250.
27. *Fabrication of triode-type field emission displays with high-density carbon-nanotube emitter arrays.* **J.E. Jung, Y.W. Jin, J.H. Choi, Y.J. Park, T.Y. Ko, D.S. Chung, J.W. Kim, J.E. Jang, S.N. Cha, W.K. Yi, S.H. Cho, M.J. Yoon, C.G. Lee, J.H. You, N.S. Lee, J.B. Yoo and J.M. Kim.** 323, 2002, *Physica B*, p. 71.
28. *Carbon nanotube electron emitters with a gated structure using backside exposure processes.* **D.S. Chung, S.H. Park, H.W. Lee, J.H. Choi, S.N. Cha, J.W. Kim, J.E. Jang, K.W. Min, S.H. Cho, M.J. Yoon, J.S. Lee, C.K. Lee, J.H. Yoo and J.-M. Kim.** 80, 2002, *Appl. Phys. Lett.*, p. 4045.
29. **J. Muller.** *Processing and electrical properties of screen-printed PZT thick film.* Lausanne : Thesis, EPFL, 2002.
30. *Inkjet printed water sensitive transparent films from natural gum-carbon nanotube composites.* **M. in het Panhuis, A. Heurtematte, W. R. Small and V. N. Paunov,** 3, *Soft Matter*, p. 840.

Chapter 7

Conclusions

In this work I have studied the synthesis of CNTs, their chemical and physical modification with the aim to prepare CNT-SU8 composites with good electrical and thermal conductivity, as well as improved mechanical properties.

From the study of preparation and treatment of supported catalysts and CVD synthesis conditions, we concluded that fine tuning of the catalyst support, the base used for the precursor formation and precipitation, and the precursor drying procedure, all together, can provide a fairly good control over the diameter of large-scale CVD synthesised CNTs. Furthermore, we could see that the diameter of produced CNTs cannot be correlated with the size of the catalyst precursor with the exception of catalyst 6 (see Chapter 4).

Considering the quality of synthesized CNTs, the best graphitized CNTs were obtained from the uniformly amorphous precursor of catalyst 7. Interestingly, in this case the average diameter of CNTs was 13.3 nm, which could not be correlated with the micrometer-range sizes of the catalyst precursors.

Considering the CNTs growth mechanism, we concluded that there were two main mechanisms related to the growth of CNTs: (i) the CNTs growth proceeds from the previously formed precursor grains (if the catalyst precursor is dried by heating and its grains are formed prior to the CNTs growing process), and (ii) the CNTs growth proceeds firstly through the stage of *in-situ* precursor grain formation, which is then followed by the direct CNTs growth from these grains (if the catalyst precursor did not pass heat treatment (lyophilisation only), and it was in amorphous phase prior it has been introduced into furnace). Moreover, our experiments confirmed different functions of Fe and Co precursors, thus if they form bimetal catalysts, their nano-clusters differently respond in CNTs growth. This is similar, in fact, to multiphasic catalysts where different phases might

have complementary functions. Consequently, bimetallic catalysts can have higher catalytic activity than their monometallic counterparts.

We noticed that under the certain experimental conditions CVD synthesis yielded well graphitized, perfectly straight CNTs, which resembled CNTs obtained by the arc-discharge method. Further study of this phenomenon and its better understanding might open up new avenues for large-scale synthesis of arc-discharge-like CVD CNTs, thus overcoming the challenging problem of scalability of high-quality CNT production. We also synthesized single- and few-layered graphene by CVD method in the absence of transition metal catalysts or specially prepared highly crystalline metal surfaces. Purification process did not require oxidizing acids and thus, the graphene surface could be preserved without altering its properties. The reported graphene synthesis method is very simple, scalable and inexpensive.

We studied which parameters influence the average length of ground CNTs for the cutting process by planetary ball milling. Average length of CNTs ground by planetary ball milling was found to depend only on the number of hits defined as product of grinding time and rpm. As a result, the required length can be achieved by simple choosing the value of 'RPM*grinding time' for the planetary ball milling process according to the dependence presented in Figure 4.30. The only limitation of this process was found to be 400 rpm above which degradation of the employed milling balls takes place.

Composites were prepared by three different methods. First, native and functionalized CNTs were dispersed in different solvents and mixed into SU8 (composites 1). In order to improve dispersion, surfactants were used and compatible photoinitiators selected to make composites 2. Finally, oriented carpets of CNTs were impregnated in order to archive best possible electrical and thermal conductivity in a preferential direction. We refer these systems as composites 3.

Nanoindentation of CNTs-SU8 composites 1 showed a modest increase of mechanical properties (an increase in E_V of $\sim 100\%$) with respect to unloaded SU8, due to the random and strongly clustered CNTs network which cannot carry the load. The impedance measurement showed the presence of percolating CNTs network in composites 1F. However, microscopy of microtome composites and measurement of the resistivity and thermopower as a function of temperature revealed presence of CNTs aggregates separated by SU8 rich areas. Therefore, conduction is limited by inter-tube hopping.

Microscopy on microtomy slices of composites 2 showed well-dispersed CNTs for different CNTs concentrations, what was confirmed by four-point resistivity measurement which has shown percolation for the CNTs content of ~ 0.1 wt%. Threefold increase of thermal conductivity, with respect to the unloaded SU8, was achieved for composites 2 with 10 wt% of CNTs in SU8. Threefold increase of hardness, with respect to the unloaded SU8, was achieved for composites 2 with only 0.8 wt% of CNTs in SU8. However, measurement of

the resistivity as a function of temperature pointed to the mechanism of hopping conduction, thus meaning that CNTs were still separated by the polymer and/or by the surfactant molecules.

For the composites 3, room temperature thermal conductivity parallel to the orientation of the CNTs was found to be 13 times higher than that of SU8. Due to the high anisotropy of CNTs-SU8 composites, we can tailor material's functionality in the required direction.

In this thesis, we report on the successful optimisation of thermo- and UV-curable CNTs-SU8 composite formulations, where the best photo-curable properties showed composites 2 containing new PI, surfactant 1 and standard long CNTs. In this work, by applying the *state-of-the-art* photolithographic processing, photo-patterned films of CNTs-SU8 composites 2 suitable for various applications were obtained. These films offer a plethora of tuneable features, including transparency, flexibility, electrical conductivity and variable mechanical properties.

We successfully prepared CNTs-SU8 composite 2C ink by the choice of the appropriate solvent, surfactant and CNTs. The ink with optimized parameters is highly suitable for inkjet printing on various substrates. Straight flexible conductive lines and regular arrays of 150 μm dots were successfully printed, with sheet resistances corresponding to that of the class of dissipative materials. The printed structures showed excellent adhesion to glass and even to unmodified polyester sheets (transparencies). The highest processing temperature used during the entire process was of 95°C, which is low compared to the temperatures used in standard inkjet processes aiming to create conductive structures by sintering of metallic particles. Fully processed printed composite structures are flexible and show good performances at elevated temperatures (SU8 itself can be heated up to 250°C, during which its chemical resistance increases even further). The printed structures are not subject to chemical modification or degradation upon exposure to harsh chemicals like hydrofluoric acid. This is in contrast to organic conductive polymers and metallic nanoparticles known to be unstable in most environments, even at normal moisture or oxygen levels.

The overall results indicate that composites obtained in this work could find attractive applications in flexible electronics. In particular, a possibility of using CNTs-SU8 composites for printing electronic circuitry on fabrics or a standard paper, to make electronics lighter, cheaper and user-friendly, sounds very appealing. Another fascinating application would be to design sensors deposited directly on cloths to perform bio-medical sensing, like, for instance, the heart beat or temperature.

The obtained results in this work are already good achievement, but the big potential of CNTs-SU8 composites for further applications remains to be explored.

Appendix 1

Statistical analysis of the length distributions of cut CNTs

This Appendix presents the statistical analysis of the length distributions for cut CNTs (see Chapter 4). From each batch, we have usually manually determined the lengths of 1000 tubes (from SEM micrographs like the one shown in Figure 4.27 (b)). Observation of the raw data histograms (Fig. A1.1) shows that the tubes get shorter if ground at higher rpm-s (Fig. A1.1 (a)) or for longer times (Fig. A1.1 (b)). In order to go beyond this trivial observation and to quantify the size reduction we have searched for an adequate distribution and tried to determine the evolution of its parameters with the physical variables like the grinding time or the speed of the mill.

Very often particle size distribution of powders (1), and cut CNTs as well (2), follows Weibull law. However, particle sizes in powders can also follow the log-normal distribution (1). Densities of these distributions are very similar, thus one cannot tell which one suits better only looking at the histograms of the measured data (Fig. 4.1). This is why we tested these two possibilities by the following graphical techniques.

The most powerful methods for deciding whether a given dataset follows a certain distribution are graphical techniques, where suitable transformation of the data yields a straight line plot if the data follow that particular law. Then, by Gan and Koehle (3): “the fit of the hypothesized model is assessed by judging the degree of linearity of the plotted points”. Furthermore, stronger deviations from straight line signify bigger inadequacy of the

tested distribution. This allows comparing different potentially fitting distributions, like log-normal or the Weibull distributions here. We will give a short overview of these methods and for detailed information see (4) or (5).

Two of the possible tools are quantile plots and probability plots. The probability density, $f(x)$, means the probability that the random variable, x , takes a value between x and $x+dx$ is equal to $f(x)dx$ (Fig. A1.2 (a)). Several techniques exist to approximate the probability density, for example histograms or kernel density estimators.

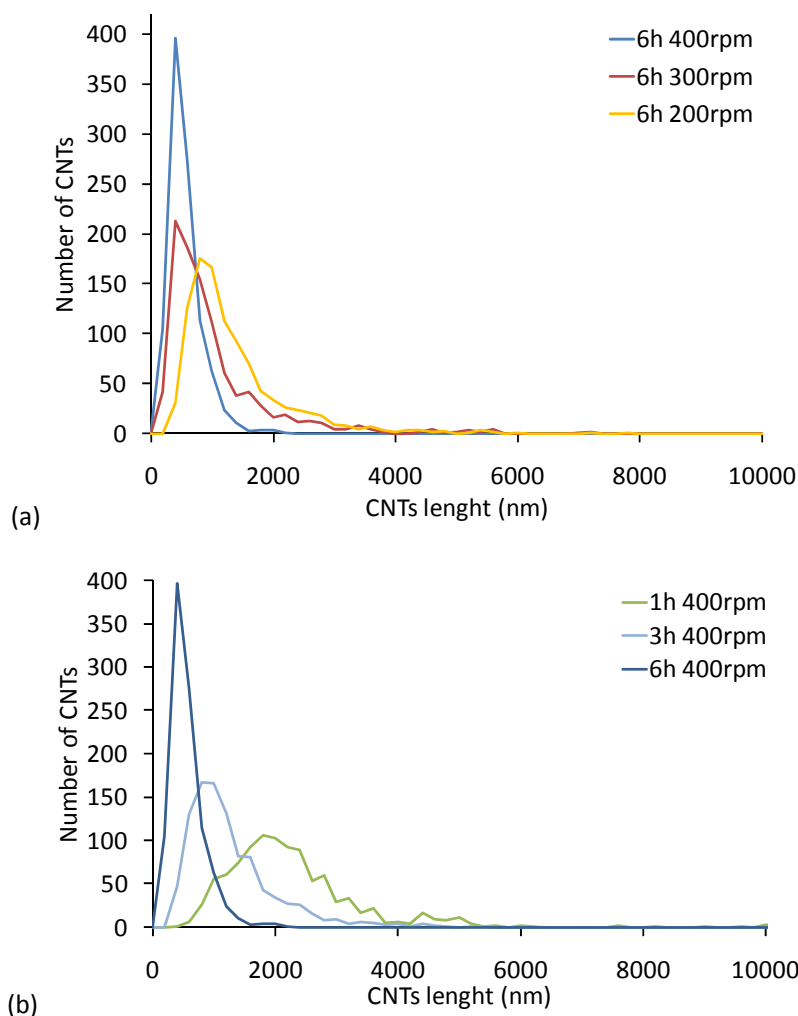


Figure A1.1: Histograms of raw data for CNTs length after ball milling under the five different conditions: (a) for fixed time, 6h, and three different speeds and (b) for fixed speed and three different times (all five distributions were for 1000 CNTs).

The probability that the value x_0 is smaller than x is given by the function $P(x_0 < x)$, which is just the integral of the probability density from minus infinity to x . By nature of its definition, $P(x)$ takes values between 0 and 1, and is monotonically increasing. This function is shown in Figure A1.2 (b). The advantage of it is that it can be inverted to yield the quantile function (Fig. A1.2 (c)). For experimental data, the quantile function can be approximated by

plotting the values against the empirical probabilities, which is determined from the rank of the point i and the total number of observations n : $\hat{P}(x_0 < x) = \frac{i-a}{n+1-2a}$. The constant a is between 0 and 1, and its exact value depends on the distribution one wants to test for. For large number of data points its actual value is quite irrelevant.

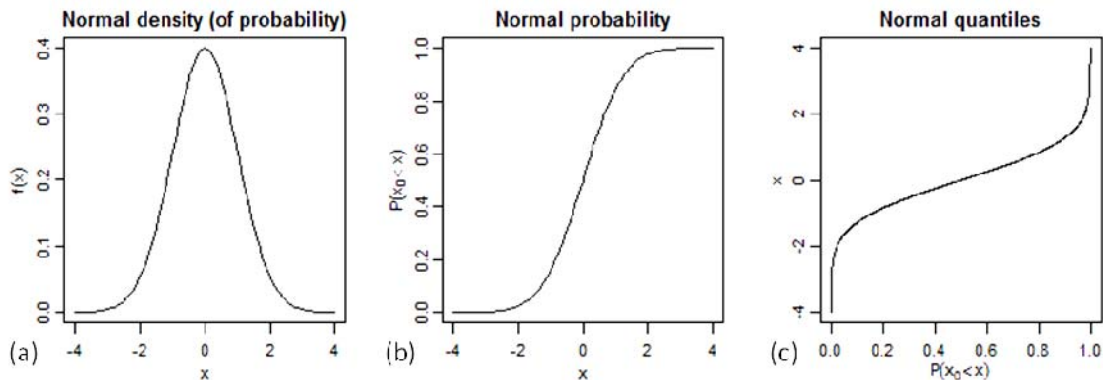


Figure A1.2: (a) The normal probability density (the “bell” curve), (b) the normal probability function $P(x_0 < x)$ and (c) the normal quantile function, the inverse of the one shown in (b).

We have used the probability plot to decide whether the Weibull law describes the length distribution of our tubes. The Weibull probability is given by $P(x_0 < x) = 1 - e^{-\left(\frac{x}{\lambda}\right)^k}$, what after rearrangement can be written in a more convenient form: $\ln(-\ln(1 - P(x_0 < x))) = k \ln x - k \ln \lambda$. As x variable we use the ordered observed lengths, and as probability the empirical probability $\hat{P}(x_0 < x) = \frac{i-0.3}{n+0.4}$ suggested in the literature.

We plot its transformed values against $\ln(x)$, and if this plot shows a straight line, we know that the data follow the Weibull distributions, and the slope and the intercept of the straight line fit allow the determination of k , the shape parameter, and λ , the scale parameter. On the other hand, if the points show systematic deviation from the straight line, we can be certain that our data do not follow this law. As an illustration of the procedure, Figure A1.3 (a) shows the Weibull plot for 1000 simulated variables following this law. One can see that the bulk of the data are on a straight line, and shows what sort of deviations from linearity we should be prepared for, even if our data follow this law.

The other practical tool is the quantile-quantile plot, also called qq-plot, where the observed values are plotted against the theoretical quantiles calculated at the empirical probabilities. This test is particularly efficient for the normal distribution, since if the observed values follow a normal distribution, and we plot them against the quantiles of the standard normal distribution, we will observe a straight line, independently of the mean and the standard deviation of the actual dataset. To illustrate this, the Figure A1.3 (b) shows the normal qq plot of 1000 simulated normally distributed points with mean=2, sd=3. The data

are on a straight line, and the intercept and the slope of a straight line fit could give an estimation of the mean and the standard deviation of the underlying distribution.

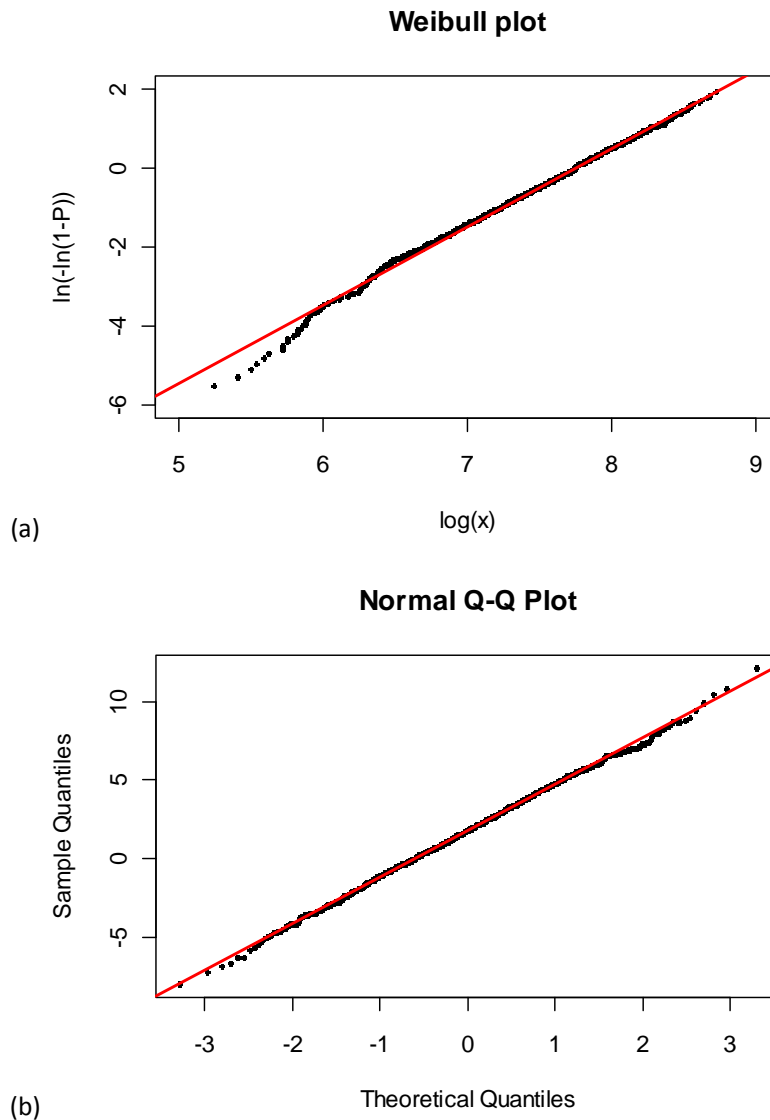


Figure A1.3: (a) The Weibull plot and (b) the normal qq plot of 1000 simulated variables following the respective laws.

We have made the Weibull plots and normal qq-plots of the logarithm of the tube lengths for all of our datasets. As an example, Figures A1.4 (a) and A1.4 (b) shows one of the pairs of plots for the same dataset (time and rpm). While the Weibull plot is curved, indicating the inadequacy of this model, the points of the normal qq-plot follow rather closely a straight line. Although some points deviate from the distribution along a straight line, essentially all of them are within dashed lines delimiting the 95% confidence interval (Fig. A1.4 (b)). Consequently, our data can be adequately described by lognormal distribution and we will use it in further analysis. In this sense, we followed the argument of

W. Weibull: “the only practicable way of progressing is to choose a simple function, test it empirically, and stick to it as long as none better has been found” (6).

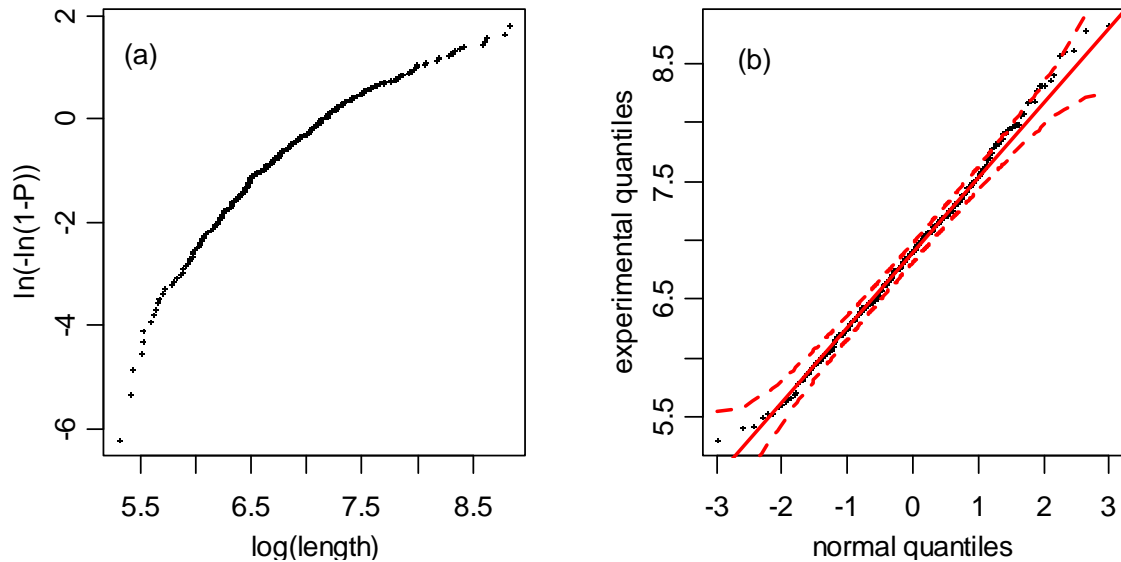


Figure A1.4: (a) The Weibull plot of one of the data sets. If the data followed the Weibull-distribution, the set of data points would be distributed along a straight line, whose slope and intercept would yield the two parameters of the distribution. (b) Normal quantile-quantile plot of the logarithm of tube lengths for the dataset shown in panel (a). The points follow rather closely a straight line, and essentially all of them are within the dashed lines delimiting the 95% confidence interval. This shows that the length distribution of the original data can be modeled by log-normal law.

As the next step of our analysis we have determined the location and scale parameter of the lognormal distribution (which is the mean and standard deviation of the logarithm of the lengths, noted by meanlog and sdlog), and made linear regression on them using the grinding time, the rpm, the product of the two and the square of rpm as explanatory variables. The choice of the first two is natural as the preliminary histograms (Fig. A1.1) have already shown that the average length decreases both with increasing grinding time and increasing rpm. The product ‘RPM*grinding time’ was chosen because this is proportional to the total number of collisions (ball-wall and ball-ball) the material is subjected to. We can see that the probability densities presented in Figure A1.5, are grouped by the product ‘RPM* grinding time’, what also indicates the importance of this variable.

The square of the rpm was included because in ball milling the energy of ball collisions is proportional to it (7; 8). Possible correlation of this variable with the others could reveal if there is threshold energy in the cutting process within the studied range of variables.

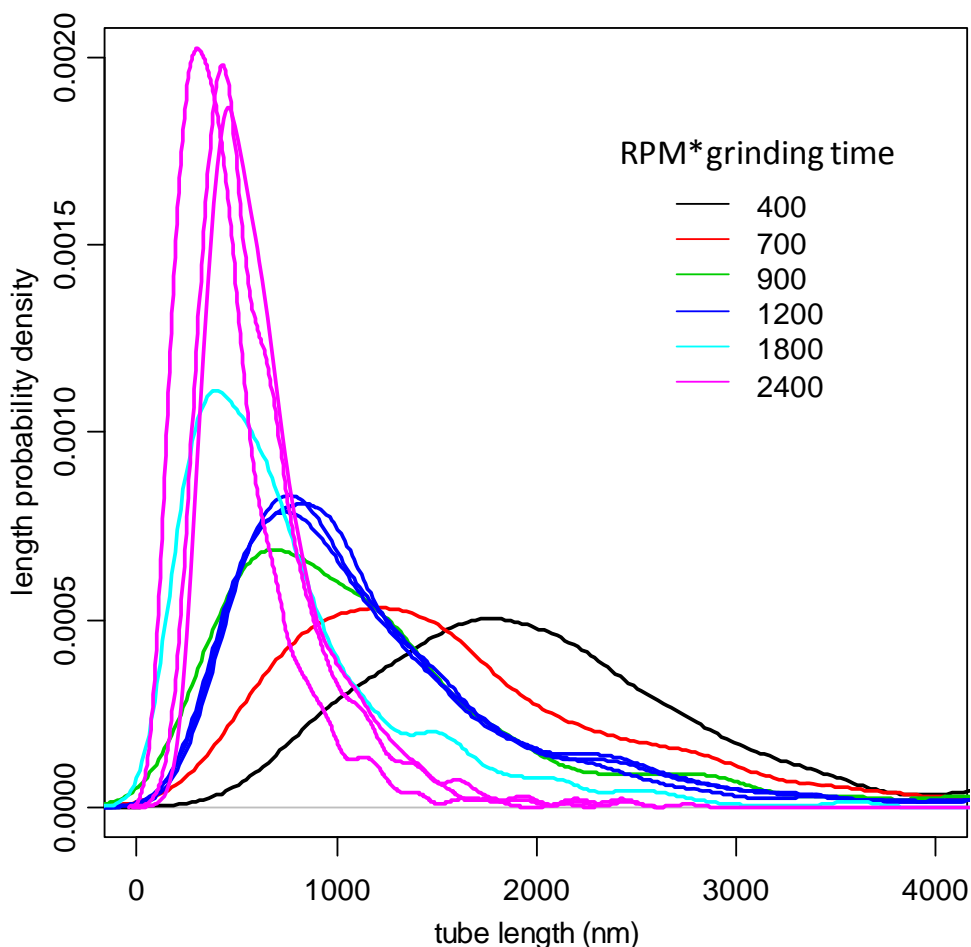


Figure A1.5: Kernel density estimates of the measured tube lengths. As it can be seen, the data are grouped according to the product 'RPM*grinding time', to which the total number of grinding events is proportional.

As a first attempt, we have plotted sdlog and meanlog against the prospective explanatory variables. Figure A1.6 shows these plots for scale parameter (the variance of the the logarithm of the lengths). No systematic dependence could be noticed, and thus, the variance seems to be independent of any of the assumed explanatory variables.

We have also checked whether there is any correlation between the two parameters of the log-normal distribution. The corresponding graph is shown on the fifth panel of Figure A1.6. The data show no correlation.

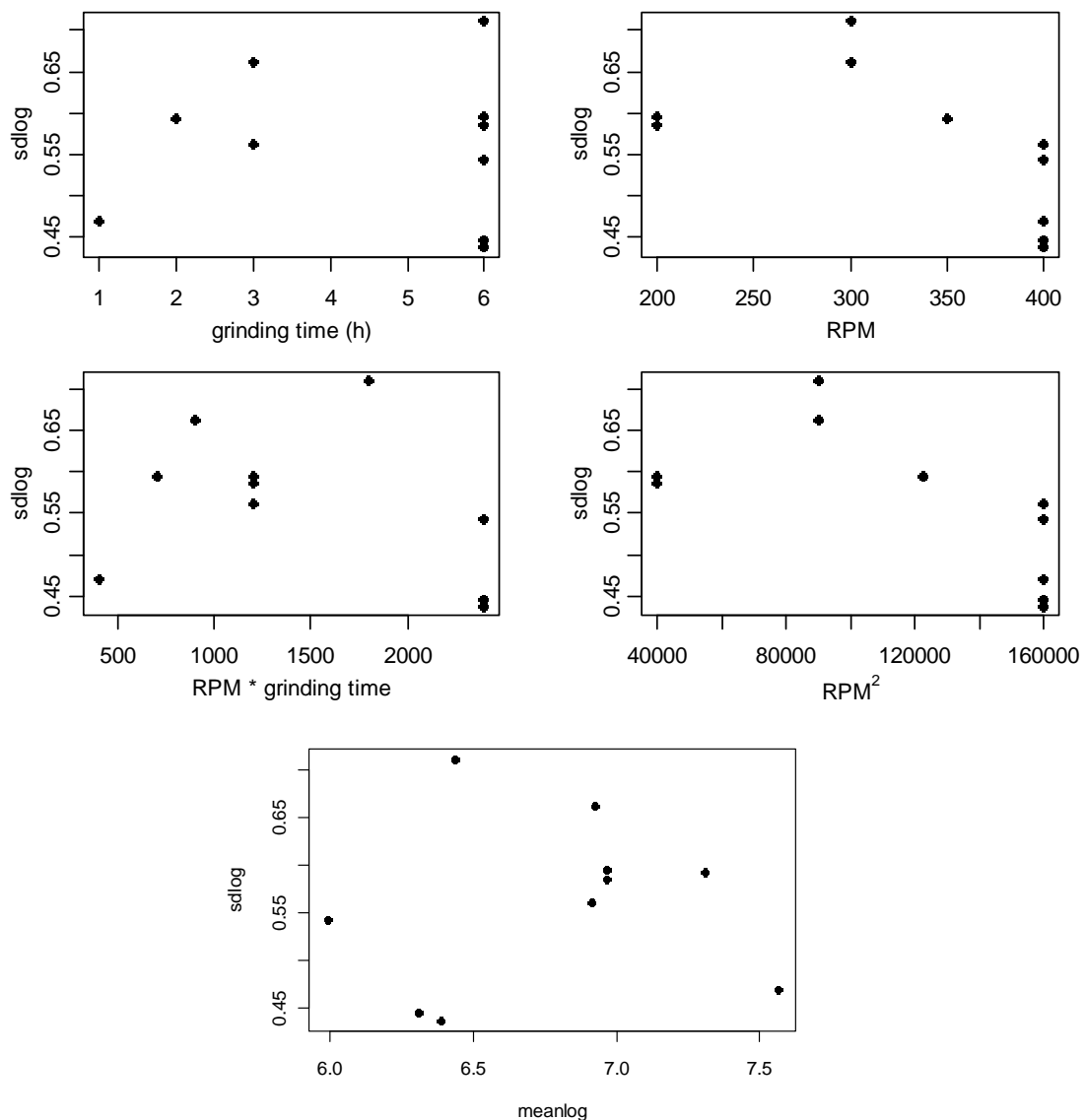


Figure A1.6: Scale parameter of the distributions as a function of the different independent variables. The scattering of the parameter is too big to show any significant dependence on any of studied variables.

The location parameter, which is the mean of the logarithm of the lengths, is shown on Figure A1.7 as a function of the different independent variables. Clearly, there is no dependence on the RPM or the square of the RPM. There is correlation between the length and the grinding time, however, data points collect at 6h grinding time where several experiments were done with very different RPMs. The use of the product 'RPM*grinding time' allows separating them, and yields a rather straight line, as shown on the third panel of Figure A1.7 (the third panel) and Figure 4.30 where the linear decrease of the location parameter with the product 'RPM*grinding time' is obvious. We have systematically tested possible linear models consisting of more than one explanatory variable but it did not bring about any significant increase in the fit quality.

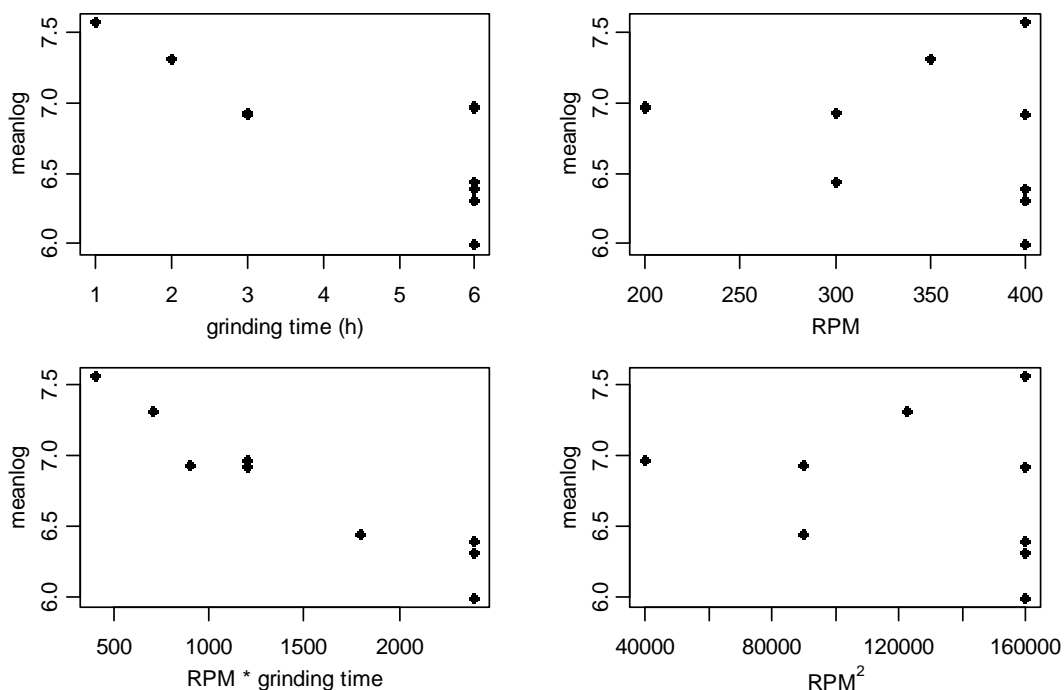


Figure A1.7: The location parameter (the mean of the logarithm of the lengths) as a function of the different independent variables.

Neither of the parameters shows systematic dependence on the speed of the grinding (RPM) or its square, *i.e.* the energy of grinding. This shows that there is no explicit energy dependence in the range of RPMs we have studied. In other words any hit of the ball cuts, regardless of the rpm, meaning that there is no threshold energy value. This is in line with the fact that we did not find the Weibull distribution for lengths since this usually arises from models where the failure is due to the breaking of the weakest link.

In conclusion, we have studied CVD CNTs cut in a planetary ball mill using a wide range of different cutting times and speeds. SEM images were used to determine the length distribution of the cut CNTs, which was found to be lognormal. The location parameter was found to vary linearly with the product 'RPM*grinding time', which is proportional to the number of ball-wall and ball-ball collisions. The scale parameter of the distribution did not show any significant systematic variation with any of the tested independent variables.

References

1. **A. Jilavenkatesa, S. J. Dapkunas and L.-S. H. Lum,** *Particle Size Characterization*. Washington : National Institute of Standards and Technology, 2001. Special Publication 960-1.
2. *Statistical characterization of single-wall carbon nanotube length distribution*. **S. Wang, Z. Liang, B. Wang and C. Zhang,** 2006, *Nanotechnology*, Vol. 17, p. 634.

3. *Goodness-of-Fit Tests Based on P-P Probability Plots*. **F. F. Gan and K. J. Koehler**. 3, 1990, Technometrics, Vol. 32, p. 289.
4. **W. Nelson**. *Applied Life Data Analysis*. New York : Wiley-Interscience, 2004.
5. *Probability Plotting Methods for the Analysis of Data*. **M. B. Wilk and R. Gnanadesikan**. 1, 1968, M. B. Wilk and R. Gnanadesikan, Biometrika 55, 1 (1968), Vol. 55, p. 1.
6. *A Statistical Distribution Function of Wide Applicability*. **W. Weibull**. 3, 1951, J. Appl. Mech.-Trans. ASME, Vol. 18, p. 293.
7. *A mathematical analysis of milling mechanics in a planetary ball mill*. **P. P. Chattopadhyay, I. Manna, S. Talapatra and S. K. Pabi**. 1-3, 2001, Materials Chemistry and Physics, Vol. 68, p. 85.
8. *Contributions to the modelling of the milling process in a planetary ball mill*. **Gy. Kakuk, I. Zsoldos, A. Csanady and I. Oldai**. 2009, Adv. Mater. Sci., Vol. 22, p. 21.

Appendix 2

Optimization of photolithography processing of CNTs-SU8 composites 2 and 2C

This Appendix deals with a detailed description of each step of the photolithographic process. In particular, in the following, we will discuss both difficulties in processing CNTs-loaded SU8 composites as well as possible ways to overcome them.

A2.1 Spin-coating

In the spin-coating step, a certain predetermined amount of relatively viscous solution of the photoresist is firstly deposited in the centre of the wafer. Subsequent spinning of the wafer induces radial spreading of the photoresist and coating of the surface of the wafer with the resist layer. The resist's spreadability on a given substrate depends on the wetting properties of the substrate by that resist. This, in turn, is determined by the substrate surface energy or the contact angle of the liquid on the particular substrate (1). In general, poor wetting, that is low surface energy and high contact angle, results in formation of beads and leads to discontinuity of the film thickness. On the other hand, good wetting and low contact angle provide continuous and uniform coating, even for layers with a lower thickness (2). We studied the wetting mechanisms of glass substrates by SU8 and CNTs-SU8 composites having different CNTs concentrations and we found that CNTs loading does not

change the wetting properties of these composites (see Appendix 3). In fact, it was found that the CNTs-SU8 composites have the same contact angles as the unloaded SU8. Consequently, our composites can be deposited on all commonly used substrates for processing of the unloaded SU8 resin. Therefore, in this study, we used quartz, Pyrex and float glass as substrates for the photolithographic processing of CNTs-SU8 composites.

The main goal of the spin-coating step is to obtain a composite layer with the required uniform thickness. The overall thickness of the obtained layer is determined by the spin-coating parameters, such as speed/time of spinning and plateau's acceleration/deceleration, as well as by the properties of the photoresist. Moreover, for thick layers, the thickness is also determined by the amount of the resist initially placed on the substrate (3). Therefore, the quantities of the deposited composites were the same for all coated samples (they were controlled by a graduated pipette).

Some difficulties may accompany the spin-coating of SU8 on substrates. One of them is connected to the appearance of beads formed by a build-up of the photoresist on the wafer's edges. If beads are formed on the back side of the wafer (the side without spin-coated layer), they can be easily removed by a stream of solvent, like, *e.g.* acetone, in the case of SU8. Nowadays, systems with new spinning technologies are designed to minimize undesired effects of coating resulting in improved uniformity of SU8 layers. In this study, we used one of such systems, a Sawatec LMS200 coater for negative resist, which has a closed chamber around the chuck of the spin coater resulting in more uniform coatings. Yet, even while using such spin-coating system, the deposited films can have edge beads on the front side of the wafer (side with spin-coated layer). This represents a serious problem, which might lead to the planarization defects. Other possible shortcomings are: unintentional tilt, dirt particles, curvature of the substrate, etc., which contribute to a reduced surface flatness of the coated layer. This might result in a cross-section profile given by a black marked curve presented in Figure A2.1. Surface unevenness appears to be bigger if the viscosity of resist is higher (3), which was typical for our composites. The common way to partially solve this problem is by leaving the coated layer to relax in a very flat-levelled position for several minutes to several hours (depending on the viscosity of coated liquid). This enables the liquid deposit reflow (in the case of low viscosity) and yields thinner layers. Otherwise, edge beads need to be removed by solvent spraying, which is neither always possible nor recommended (1). For unloaded SU8, typical flatness errors, reported to appear in this way, are 10% (1) or 20% (3) in resist thickness on the distance $2R/3$ from the centre of the wafer, where R is the radius of the wafer (Fig. A2.1) (3).

In the case of spin coated CNTs-SU8 composites, obtained layers have a thickness profile which corresponds to the unloaded SU8 in the outer region of the wafer. However, in the central region of the coated wafer a hill-like feature appeared which was not reported for spin-coated unloaded SU8. A series of attempts has revealed that the height of the hill in the middle of the wafer corresponds fairly to the height of the initially deposited composite

on that place. In fact, prior to spin-coating, the height of the composite is quite large in the wafer centre. For the composite spin-coating step, this has to be avoided in order to prevent a hill-like formation in the middle of the wafer. To avoid formation of hill-like structures, while working with CNTs-SU8 composites, we tried different ways of deposition. It turned out that the best thickness profile could be obtained when we deposited the composite by slowly forming a spiral from the centre of the wafer towards the outer edge of the wafer.

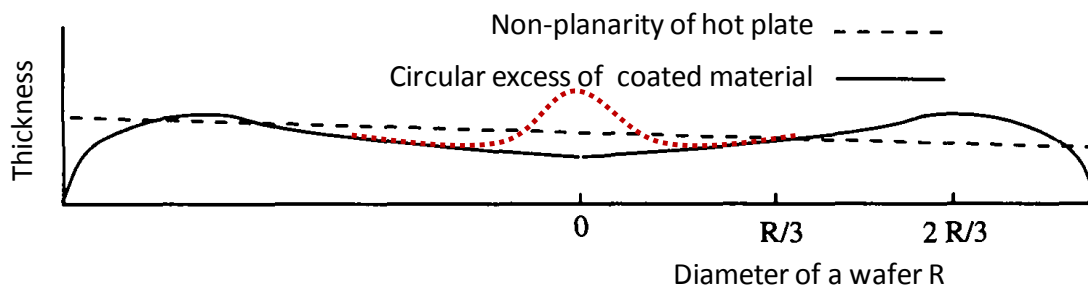


Figure A2.1: Influences of the possible non-planarity of the hot plate and the excess of the coated material in form of a ring on the edge of the wafer on the thickness profile (the black marked curve) of the SU8 spin-coated layer on the wafer's surface (From the ref. (3)). In the case of CNTs-loaded SU8 additional deviation in planarity of coated composite layer appeared in the centre of the wafer. Typically obtained thickness profile of a CNTs-SU8 composite layer in the central region of wafer is indicated by the red dotted line.

In this way, a formation of a hill-like structure in the middle of the wafer was avoided or markedly diminished, in the case of composites with CNTs concentrations up to 1.2 wt% or above, respectively. Regardless of the concentration, the planarization of the surface of the composite layer appeared to be significantly improved by the new deposition method which could be used for all resist formulation with high viscosity.

The noticed phenomena of the formation of hill-like profile can be understood as a natural consequence of rotation. Namely, if a disk rotates around an axis perpendicular to the disk and passing through the centre of the disk, every point on the disk has the same angular velocity. Clearly, the tangential velocity in each point of the disk is a function of its distance from the axis of rotation and linearly increases with the distance from the centre of the disk (Fig. A2.2 (a)). Therefore, a highly viscous resin with a great thickness in the centre of the rotating disk cannot move from its initial position, leaving behind a hill-like thickness profile in the middle of the wafer.

The described motion additionally gives rise to entanglement and aggregation of CNTs in the plane of rotation (Fig. A2.2 (b)). Namely, CNTs have a finite size which causing that a CNT is not in all its points in the same distance from the centre of wafer. Therefore, different parts of a CNT are exposed to different tangential velocities.

Moreover, in the plane perpendicular to the wafer, spreading of the liquid composite from the centre of the wafer towards edges causing CNTs entanglement and aggregation in

this plane, as well. This is a consequence of the spreading process itself. To be precise, according to fluid mechanics when liquid spreads over the solid surface, velocity of liquid is not the same over the cross-section of the layer. In general, a velocity profile of the spreading liquid in the cross-section of the liquid in the plane perpendicular to the surface of stationary wafer is given in Figure A2.3. Without going too much into details, it should be mentioned that the substrate movement and the presence of solid objects (CNTs) in the progressing fluid induce complex changes in the given velocity profile, yielding a quite complicated picture. Simultaneously, the shear rate and the shear stress are also evolving over the cross-section of the progressing resist layer, and the liquid moves much faster in the upper parts of the layer than towards the bottom (Fig. A2.3). In fact, this enables spreading of the resin on the surface of the wafer in such a way that the top of the obtained layer is flat and uniform. Nevertheless, gradient of velocity simultaneously induces CNTs entanglement, because different CNTs segments are exposed to different velocity and shear stress.

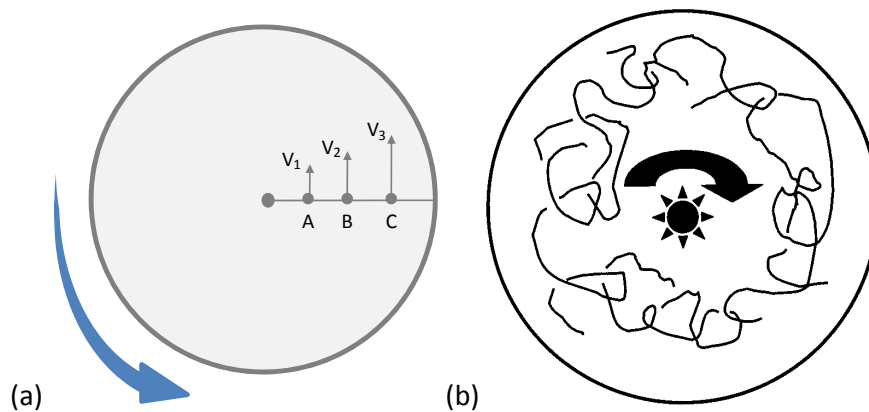


Figure A2.2: (a) The intensity of tangential velocities of points A, B and C (V_1 , V_2 and V_3 , respectively) is increasing towards the outer edge of the disk, e.g. $V_1 < V_2 < V_3$; (b) When exposed to the rotational motion, CNTs, as high aspect ratio objects, undergo orientation and entanglements in the direction of motion (From the ref. (4)).

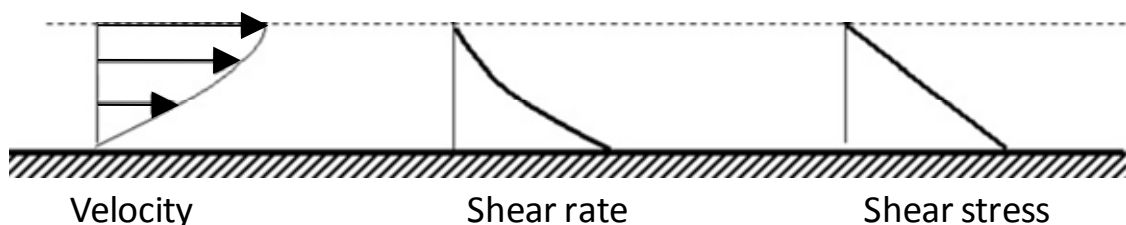


Figure A2.3: Velocity, shear rate and shear stress profiles for liquid flow over the solid surface (From the ref. (2)).

In fact, during spin-coating, CNTs are simultaneously exposed to the tangential velocity gradient in the plane of the wafer, due to the rotation, and to the velocity gradient in the plane perpendicular to the wafer, due to the fluid progressing over the solid surface.

The combination of these exposures unavoidably yields in a shear induced aggregation typical for this type of system, *i.e.* filler-loaded dissolved polymer (5). CNTs tend to aggregate rapidly also in the absence of flow. On the other hand, the effect of shear on colloidal stability in the presence of inter-particle interactions is poorly understood. The existing theory (5) predicted a dependence of the aggregation rate upon the size of the colliding bodies, but this dependence is highly nontrivial and not applicable to all possible interactions and systems. In any case, aggregation is considered as typical for strongly anisotropic building blocks such as rod-like fillers, like CNTs.

In order to minimize shear induced aggregations we studied the influence of spin-coating parameters, speed and time on the plateau and acceleration/deceleration. The standard SU8 process parameters are 40 s time on the plateau and 100 rpm/s for acceleration and deceleration (6). At first, for composite coating, we kept these standard values constant for the SU8 processing and we changed only the spin-coating speed on the plateau from 500 rpm to 2000 rpm. The result was clearly noticeable macroscopic aggregations of CNTs for all obtained composites layers, regardless of the coating speed. The outcome indicates that time on the plateau or acceleration/deceleration, rather than speed on the plateau, has bigger influence on the filler aggregation. When only time on the plateau was changed, CNTs aggregation became more pronounced with the increase of time on the plateau, while it showed a reducing tendency in the opposite case. The change of only acceleration/deceleration towards lower values resulted in a more obvious aggregation, whereas higher values yielded aggregation decrease. Combined change of the coating parameters gave us information that the crucial parameter which influences filler aggregation is the total duration of coating and not the coating speed on the plateau. As a result, the final optimal parameters for significant diminishing of filler aggregation during spin-coating processing step are:

(1) acceleration and deceleration have to be higher than the standard 100 rpm/s and at least 500 rpm/s for speeds on the plateau higher than 1500 rpm, but the value should be adjusted according to the hereby experimentally obtained rule that duration of acceleration part of the coating should not longer than 5 s;

(2) the time on the plateau has to be approximately from 1 s to 5 s, depending on the formulation viscosity, where a lower viscosity composite requires a shorter period, but the period should just exceed the time which is required to cover the entire wafer surface by the composite;

(3) in this study the experimentally obtained rule is that the total duration of spin-coating (what includes the period of acceleration, time of the plateau and period of deceleration) should not exceed 10 s. The latter point is an advantage for industrial applications where the efficiency of the process is crucial.

As an example, optical microscope images of one composite spin-coated using two different protocols are shown in Figure A2.4, where the right image is spin-coated under the previously described 'good conditions' and under the coating conditions which are 'standard' for SU8. The images show clearly a strong influence of this processing step on the final morphology of the CNTs-SU8 composite layers due to the possible shear stress-induced aggregations of CNTs.

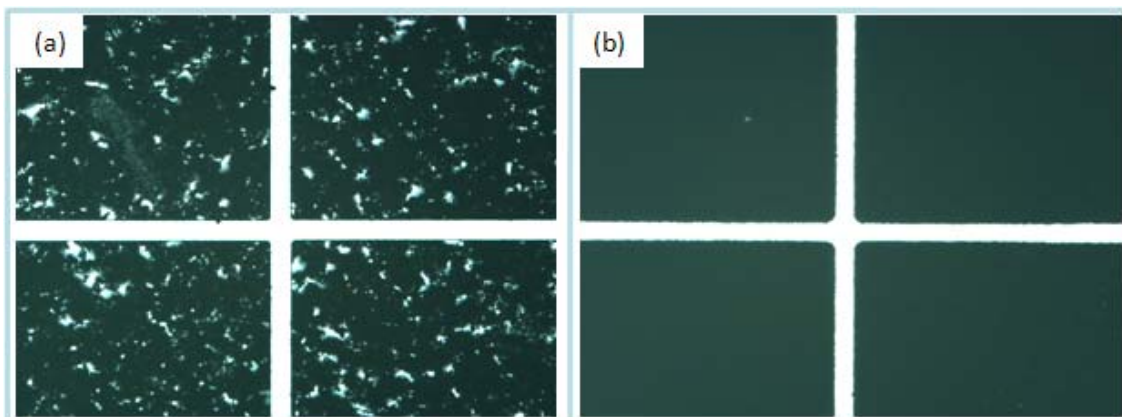


Figure A2.4: Optical microscope images of square structures of composite 2 spin-coated using two different spin-coating protocols. (a) Protocol (i): distinct, shear stress-induced aggregations of CNTs (dark regions) and SU8 rich (bright regions) can be seen. (b) Protocol (ii): homogeneous structures.

A2.2 Soft baking

After the spin-coating step, the substrate and the deposited resist layer are baked in order to remove the solvent in the SB step. SB has to be performed on a hot plate, because in the case of SB in convection ovens or lyophilisation, a 'skin' forming on the surface of the resist layer prevents solvent evaporation, and thus prevents the inner part of the composite layer from complete drying (7). Therefore, the only recommended way to remove the solvent is by heating on a hot plate under a good temperature control and uniform heating over the whole surface of the hot plate.

The usual temperature for SB of unloaded SU8 formulations containing GBL solvent is of 95°C (6). This temperature is much higher than the glass transition temperature of SU8 (~50°C (8)). Therefore, at the beginning of the SB process SU8 can reflow. This reflow can reduce the edge beads on the outer perimeter of the resin layer, as well as any other surface unevenness which is a consequence of the spin-coating step. Obviously, in this context, the flatness of the hotplate is crucial for obtaining films with uniform thickness and smooth surface (9). Hence, SB is typically performed on a well levelled hotplate. For certain more viscous SU8 formulations, SB has to be performed on higher temperature, typically at

120°C (6). However, the increase of the SB temperature has to be done with precaution, because higher SB temperatures can initiate thermal cross-linking (see Chapter 2).

The duration of SB which is sufficient for the solvent removal, is determined by the thickness of resist layer, which is in turn determined by the parameters of previous processing step, spin-coating. For instance, SB for 6 min is sufficient for 5 μm thick SU8, while 200 μm thick SU8 requires 3 h of SB (9). However, SU8 can be used for ultra high aspect ratio structures, what implies quite thick SU8 layers. In such a case, for a SU8 layer of thickness for example from 1mm to 3 mm, the required minimum period of SB is from 30 h to 45 h, respectively (1). Even then, the remaining solvent content is around 12% (10). The duration of SB itself has strong impact on further processing steps and thus, on the properties of the final structures. Although some experiments showed that over-baking is much less critical than under-baking (9) both cases can induce further problems. For instance, over-baking can induce crack formation (Fig. A2.5), while under-baking leaves higher solvent content which provides higher mobility of initiator species during the exposure and post-exposure bake and hence, causing widening of the cross-linked area comparing to the UV-exposed area. Moreover, the excess of solvent on the end of SB can be partially removed during the post-exposure bake and then induce high stress in the obtained structures resulting again in cracks (Fig. A2.5 (b)). Furthermore, simultaneously, bubbles are very likely created (Fig. A2.5 (b)). An additional problematic consequence of the higher solvent content is the reduced mechanical stability often resulting in a collapse of the final structures. In that sense, the SB processing step has a strong influence on the layer adhesion. Taking into account all above, the SB procedure has to be carefully optimized for each resin thickness and application, and especially for each filler concentration, since the last one can have huge impact on the solvent removal process.

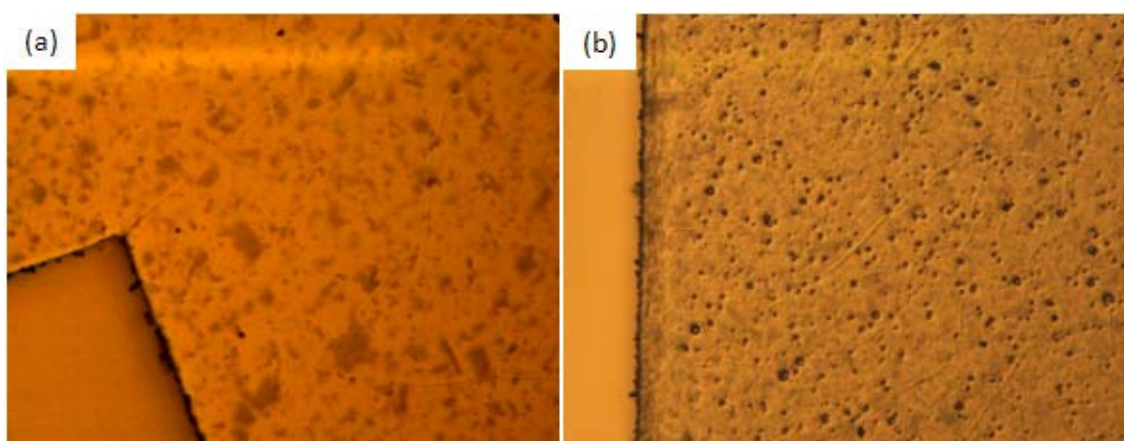


Figure A2.5: (a) Cracks or (b) bubbles and cracks formed on the surface of composite layer (spin-coated using inappropriate coating conditions) due to the (a) over-baking or (b) under-baking in the SB processing step.

The solvent removal in the SB process is naturally followed by volume shrinkage of the resin layer that is causing film stress. Barber et al. show that the thickness of the resin layer has the greatest impact on internal stress (11). Moreover, internal stress increases with the increase of layer thickness and can be even so high to induce de-bonding of the resist film from the substrate (1). From the perspective of SU8 processing, studies show that SB has the largest contribution of all processing steps to the overall film stress with even 50% (11). Additionally, the heating and cooling rate can significantly contribute in building up film stress and even induce crack formation. Therefore, in order to minimize crack formation and to reduce internal stress, very slow progressive heating and cooling down is shown to be necessary (9).

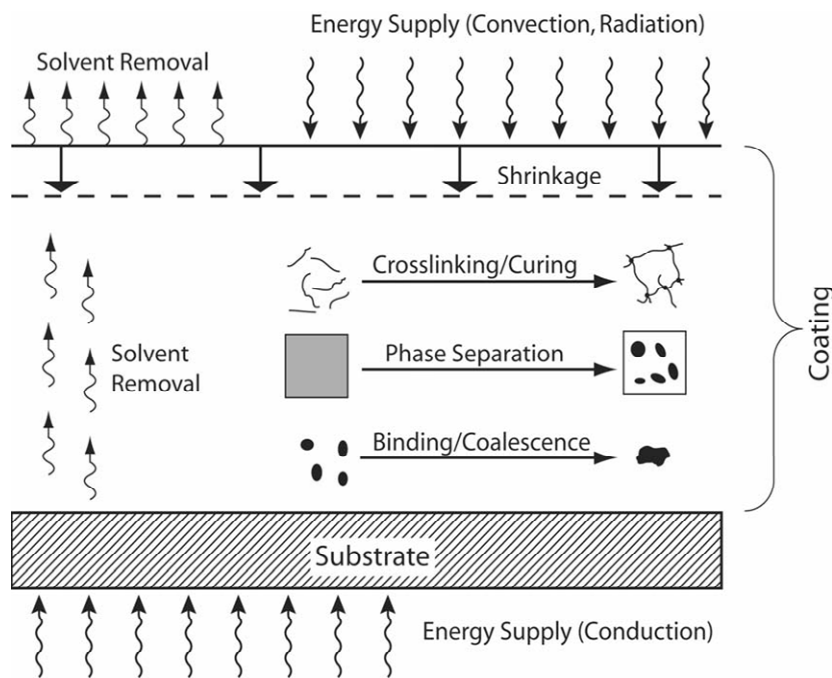
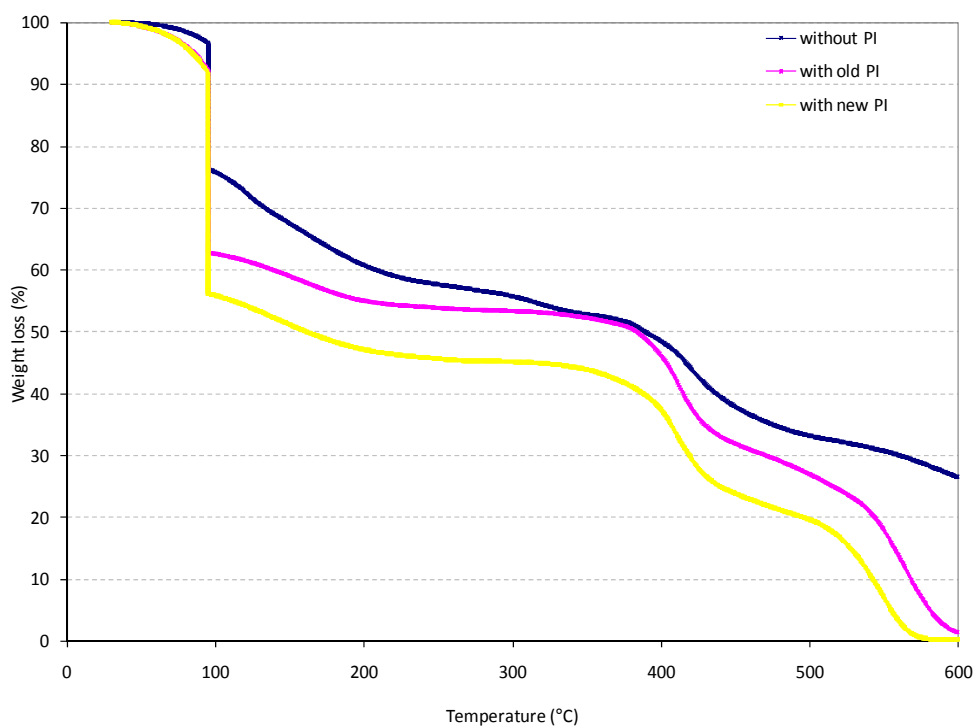


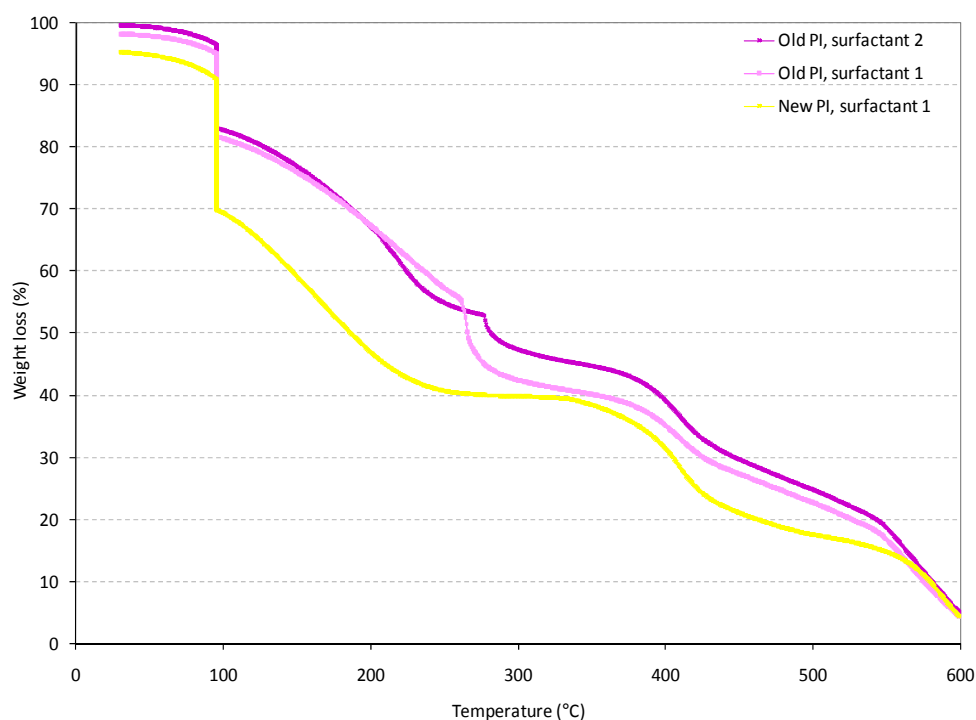
Figure A2.6: Composite's volume shrinkage and possible accompanying processes during soft baking step of the photolithography (From the ref. (12)).

Besides internal stress, the volume shrinkage can additionally induce some undesired consequences, like, for instance, phase separation or coalescence of the filler in the case of composites (Fig. A2.6). Moreover, the presence of reinforcement elements in composites, as well as a rigid substrate, represent constraints for shrinkage. Therefore, these factors contribute to an increase of the overall internal stress in the film coating (12).

In order to optimize the SB process for CNTs-SU8 composites, we had to study the influence of all composite components on the solvent removal. To facilitate photolithography processing, we studied CNTs-SU8 composites 2 with different compositions (surfactant 1 and 2; 'old' and 'new' PI; see Chapter 3). All composites contain the same ratio of SU8 and GBL, but not the same ratio of volatile parts, since 'old' PI and both surfactants contain solvents. For details about compositions see the reference [MM1].



(a)



(b)

Figure A2.7: TGA curves for: (a) unloaded SU8 samples differing with respect to PI and (b) CNTs-SU8 composite samples prepared with different surfactants and PI.

A study was performed by TGA (see Chapter 3). As a reference, we firstly monitored the change in weight of the unloaded SU8 samples: without any PI, with old PI and with new PI (Fig. A2.7 (a)). This was done in order to test if new PI influences the process of solvent

evaporation. From the Figure A2.7 (a) we can see that the dynamic of solvent evaporation follows the same pattern in the presence of both PIs. However, weight loss after the isothermal part is higher for the samples with new PI, what can be related to the presence of propylene carbonate (boiling point 240°C (13)) in the old PI and thus, higher content of volatile components in the overall weight.

TGA of CNTs-SU8 composite samples prepared with new PI and surfactant 1, and with old PI and surfactants 1 and 2 is given in Figure A2.7 (b). The tendency which could be observed for unloaded SU8, that sample with new PI have lower solvent content after isothermal bake, can also be seen for the composite sample. However, TGA of samples with old PI and with different surfactants show no essential difference due to the surfactants' nature. Therefore, an important conclusion is that these two surfactants do not significantly influence the solvent removal process.

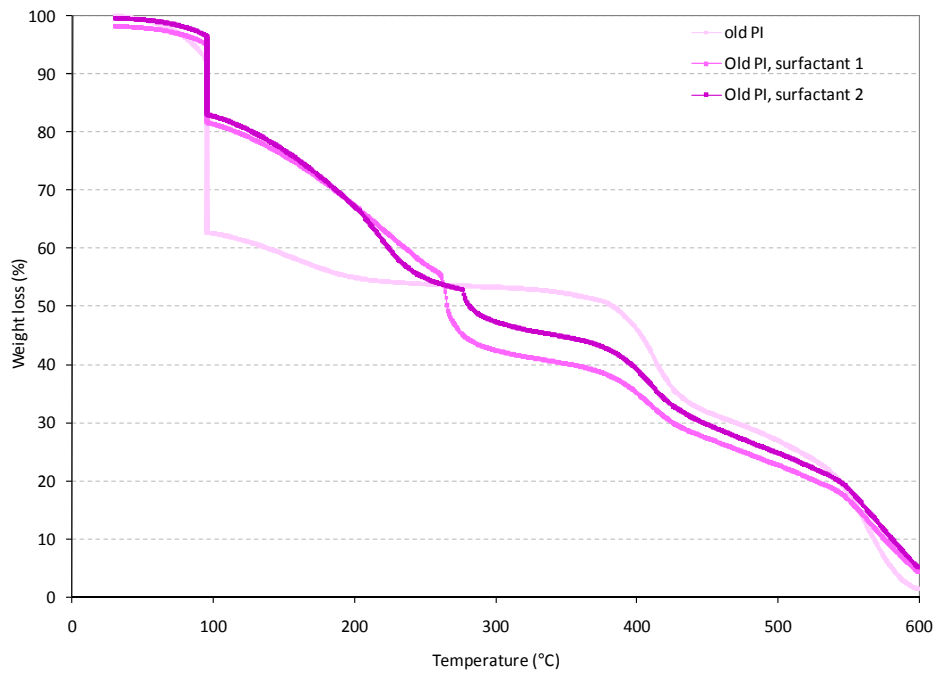
In order to clearly see the influence of CNTs, we plotted together the results for all samples containing old PI, that are unloaded SU8 prepared with old PI, and CNTs-SU8 composites with old PI and two surfactants (Fig. A2.8 (a)). Weight loss for both samples with CNTs, which is fairly the same, is obviously much lower than for the unloaded SU8 until 260°C. At higher temperatures, it is the opposite. TGA curves for all samples prepared with new PI are given in Figure A2.8 (b). Comparing to the unloaded SU8 sample containing new PI, weight loss of the sample with CNTs and new PI is higher at lower temperatures up to 195°C, but lower afterwards.

Sample	Temperature (°C)							Char Content (%)
	10% wl	20% wl	30% wl	40% wl	50% wl	60% wl	70% wl	
without PI	95	95	133	207	389	437	561	26.52
with old PI	95	95	95	139	384	415	471	1.56
with new PI	95	95	95	95	162	388	419	0.33
Old PI, surf. 2	95	128	187	224	282	396	447	5.15
Old PI, surf. 1	95	117	186	237	266	355	426	4.43
New PI, surf. 1	95	95	95	147	186	281	405	4.42

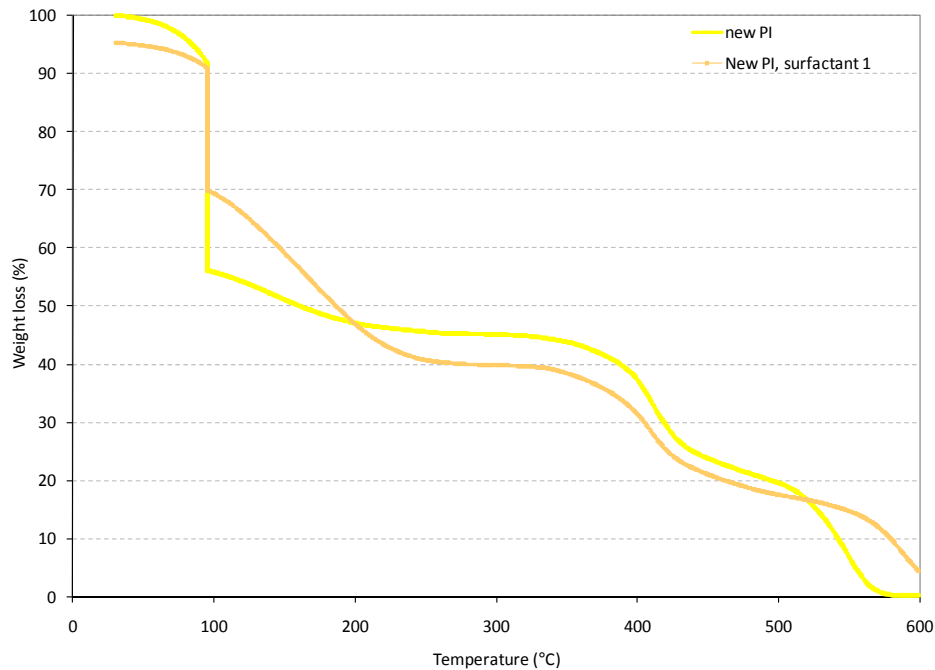
Table A2.1: TGA data of unloaded SU8 and CNTs-SU8 composites.

Besides the graphs presented in Figures A2.7 and A2.8, TGA values for the 10% up to 70% weight loss and for the char content are reported in Table A2.1. The data quantitatively support our previous conclusions. It is interesting to observe that a sample containing only SU8 and GBL (in Figure A2.7 and Table A2.1 this sample is denoted as “without PI”) is

showing a higher thermal stability above 400°C than all other samples, including SU8 with PI or composite samples. Moreover, char content at 600°C is surprisingly high 26.52% and for even an order of magnitude higher than for all other samples. Simultaneously, weight loss up to 350°C is higher for the SU8 with PI than for SU8 without PI.

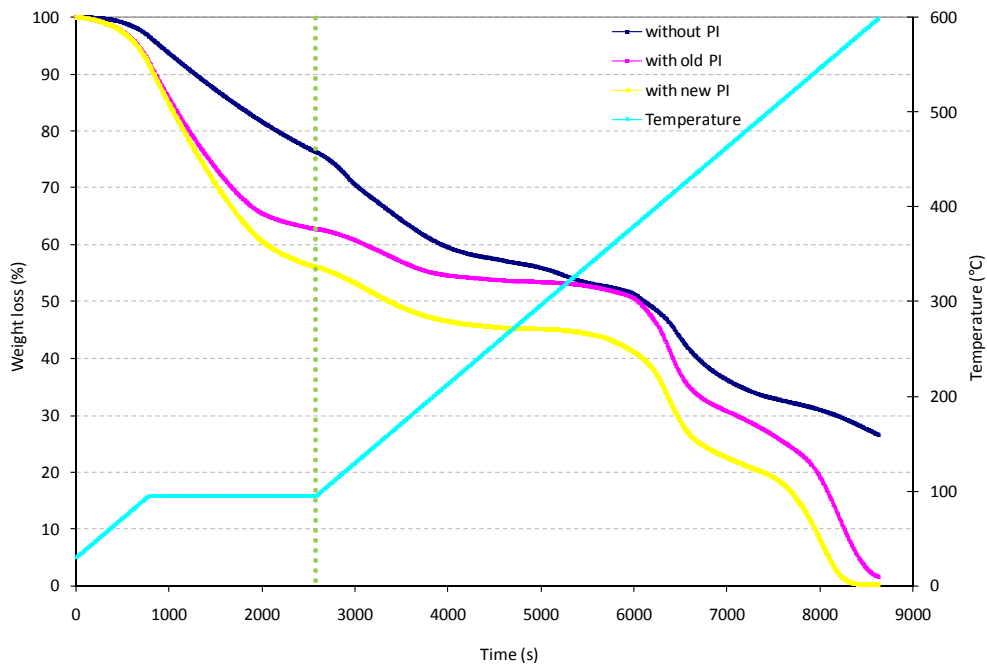


(a)

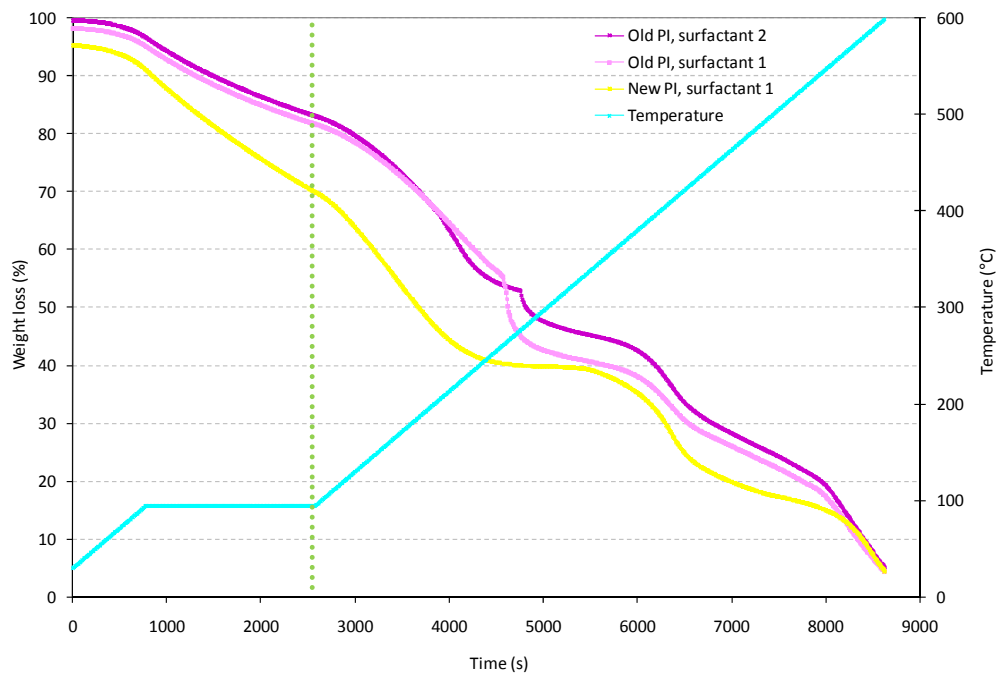


(b)

Figure A2.8: TGA curves for: (a) samples with old PI without and with CNTs (with two surfactants) and (b) samples with new PI without and with CNTs.



(a)



(b)

Figure A2.9: Weight loss rate of: (a) unloaded SU8 samples differing with respect to PI and (b) CNTs-SU8 composite samples prepared with different surfactants and PI (the green dotted line indicate end of the isothermal part of the heating process).

Weight loss from the beginning of the TGA measurement until the weight loss corresponding to the solvent content (see the ref. [MM1]), is actually the solvent weight loss. This as a function of time could be seen as solvent removal rate. Therefore, curves of

weight loss as a function of time for all samples are given in Figure A2.9. Comparing the SU8 samples with different surfactants (Fig. A2.9 (a)) we can see that the rate of solvent removal is almost the same during the first 25 minutes. The end of this period corresponds to 30% of weight loss. After that, solvent removal is faster in the presence of new PI. If we compare the samples containing CNTs (Fig. A2.9 (b)) it is clear that the fastest solvent removal is for the sample with new PI, while for samples with old PI and CNTs and just changed surfactant a significant difference cannot be noticed. This again confirms that there is no influence of the nature of surfactants on the general dynamic of solvent weight loss for the composites containing old PI. Based on this results and data in Table A2.1 and Figure A2.7 (b), we can see that from all formulations containing CNTs, composites containing surfactant 1 and new PI responded the best on SB, meaning that the solvent removal was the most efficient in that case.

The overall conclusion related to SB is that the presence of CNTs slowed down solvent removal, like it was expected. However, this can be overcome by increasing the duration of SB for the composite comparing to the unloaded SU8 sample of the same thickness containing the same PI. Simultaneously, the isothermal part of SB of the composites can remain at the same temperature as for the unloaded SU8 containing the same solvent.

A2.3 UV-exposure

After the solvent removal by SB, obtained composite films had to be structured in a form of predetermined pattern. The structuration (patterning) is provided by exposure to UV light through a mask, which is basically a square glass plate having a metallic film with a pattern on one side. The main exposure methods are: contact, proximity, and projection (Fig. A2.10).

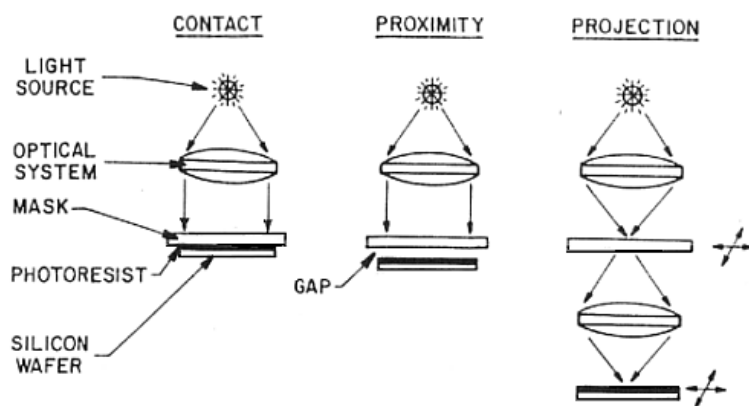


Figure A2.10: Schemes of the three methods of mask alignment based on (a) contact, (b) proximity and (c) projection exposure (From the ref. (14)).

In contact printing, a resist film is placed into the direct physical contact with the mask. This exposure method is widely used because of the possibility to obtaining a high resolution. However, this method is followed by problems induced by the direct contact itself. Actually, the simultaneous contact of the complete surface of resist and mask is almost impossible because the resist surface is never perfectly flat. Moreover, any surface unevenness can very easily damage the mask and cause defects on the patterned structures (14). In a typical direct contact of mask and resist, the gap nonuniformity of 10-100 μm is very common for the unloaded resist due to the unevenness of the surface of the film caused by spin-coating (15). This variation of the mask-to-resist distance, as well as the thickness of the resist between the mask and the wafer, may significantly influence patterning.

The proximity printing is quite similar to contact printing except the difference that mask and resist film are now on a distance of 10-25 μm during exposure. This gap reduces the damage of the mask, but does not eliminate it. The biggest drawback of this method is the problem of diffraction due to the gap (16).

The projection printing is a method where the pattern on the mask is projected in decreased dimensions onto the layer of resist, which is at a centimetre distance away. Comparing to this method, in previous two modes (whether a mask and resist layer are in direct contact or on a proximity gap) the image on the mask is reproduced on the resist without reduction in size of the features.

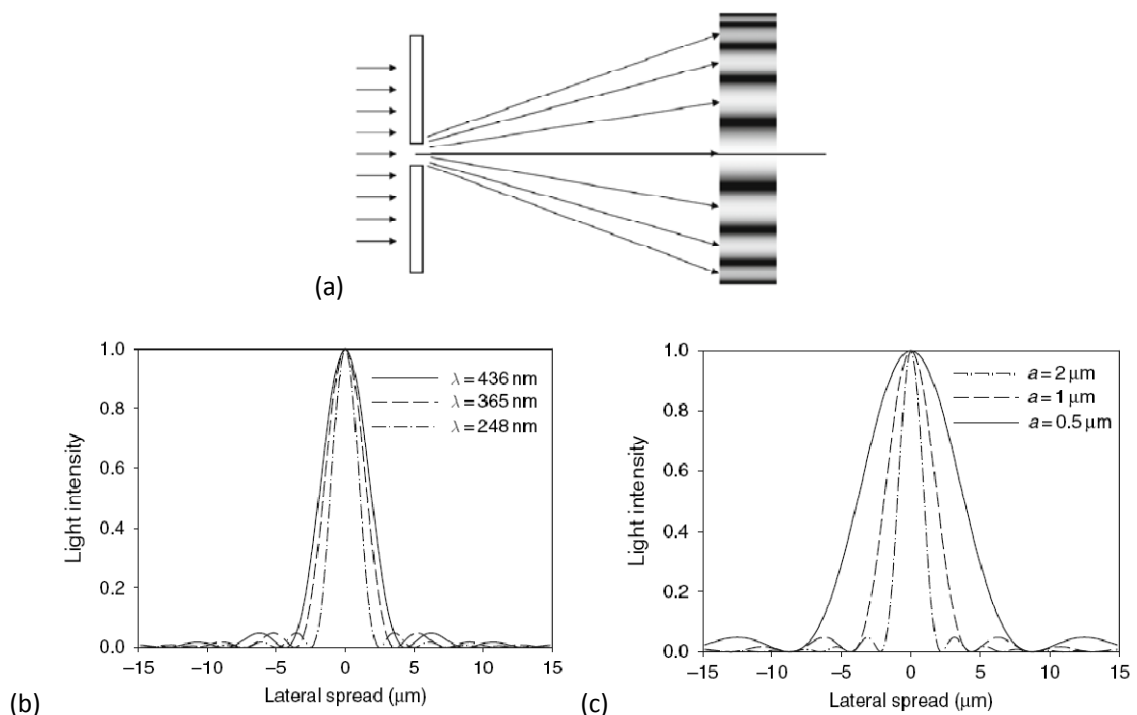


Figure A2.11: (a) Single-slit diffraction; (b) Light intensities of three single-slit diffractions for 1-mm slit width, and (c) at 436-nm wavelength (From the ref. (17)).

Regardless of which exposure method is used, light has to pass through the mask in order to obtain a patterned film. While UV light is passing through the transparent openings of the mask during exposure, they behave like a slit causing light diffraction (the bending of waves around obstacles) just as a Young's single-slit diffraction. In fact, according to the Huygen's principle every point on a wave front acts as a source of tiny wavelets which interfere with each other, causing variations of light intensity through maxima and minima visible as bright and dark fringes (Fig. A2.11 (a)) (17). The angle of each dark fringe relative to the source (ϑ , the diffraction angle of light passes through the slit) can be determined by the equation:

$$\sin \vartheta = m\lambda/d, \quad m = 1, 2, 3, \dots \quad (\text{A2.1})$$

where λ is the wavelength of light, and d is the width of the slit. Therefore, the diffraction angle ϑ , which signify the spread or expansion of light, is a function of wavelength and the width of the slit is in such a way that a narrower distribution of diffraction can be obtained with a shorter wavelength light (Fig. A2.11 (b)). However, for a fixed λ , the spread of light is wider for the smaller slit (Fig. A2.11 (c)) meaning that the obtained image occupies a much larger area than the original features of the mask. Consequently, if two of such slits are placed on the mask close to each other, their images can merge and become irresolvable. In general, the minimum resolvable detail of two images is, by the Rayleigh criterion, diffraction-limited when the first diffraction minimum of the image of one light spot coincides with the maximum of another light spot image (Fig. A2.12 (a)). If the distance between two adjacent light spots is greater than that, the two points are well resolved otherwise points are unresolved (17). In the case of single slit, according to the Eq. A2.1, the angle at which the first minimum intensity at the image plane occurs (ϑ_R), depends on the wavelength (λ) and the diameter of the circular aperture (a) as expressed by the equation:

$$\sin (\vartheta_R) = \lambda/a \quad (\text{A2.2})$$

Then, the minimum separation of the two images (Fig. A2.12 (a)), would be half of the distance between the two minimums of the diffractive image of the single spot. This would mean that the resolution limit (R) for single slit is given by the equation:

$$R = 0.5 \lambda / \sin (\vartheta_R) \quad (\text{6.2.3})$$

In optical projection lithography there is a more general expression for the resolution of a lens at the diffraction limit:

$$R = k_1 \lambda / \text{NA} \quad (\text{6.2.4})$$

where NA is and numerical aperture of the exposure tool (proportional to the index of refraction of the medium and the sine of half the angle of the image-forming cone of light at the image), and k_1 is an empirical constant related to a specific imaging process ($k_1 < 1$). The value of k_1 is known for well defined theoretical systems, like 0.61 for the diffraction

through a circular aperture, and 0.5 for the single slit (Eq. A2.3). In reality, k_1 depends on lots of parameters, like lens aberrations, illumination conditions, mask, geometrical shapes, exposure tool conditions, resists, process and operator (18). From Eq. (A2.4) apparently follows that a shorter wavelength results in a narrow distribution of light diffraction, like we can see in Figure A2.11 (b) (17). Moreover, besides shortening the exposure wavelength, the resolution can be also improved by increasing the numerical aperture and by decreasing the value of k_1 .

In standard photolithography the light passes through the mask's features which have to be separated enough that their images are resolvable. In the case of imaging high density features of the periodically repetitive pattern of equal-line-and-space features, the half-pitch (which is equal to the linewidth) is considered to be the minimum feature which can be imaged (17). The light intensities (so called "aerial image") of two-line features having 0.2 μm linewidth on a mask, as a function of their separation is given in Figure A2.12 (b). When the separation is half of the linewidth or "half-pitch", (what is in this example $D=0.1 \mu\text{m}$) line features are becoming irresolvable (17). Generally speaking, for the resist of thickness t , which is on certain distance from the mask (air gap is s), exposed to the light of the wavelength λ , the theoretical resolution (R_{min}) of line/space is given by the equation (15):

$$R_{min} = \frac{3}{2} \sqrt{\lambda \left(s + \frac{1}{2} t \right)} \quad (\text{A2.5})$$

which provides simple practical calculation of the resolution.

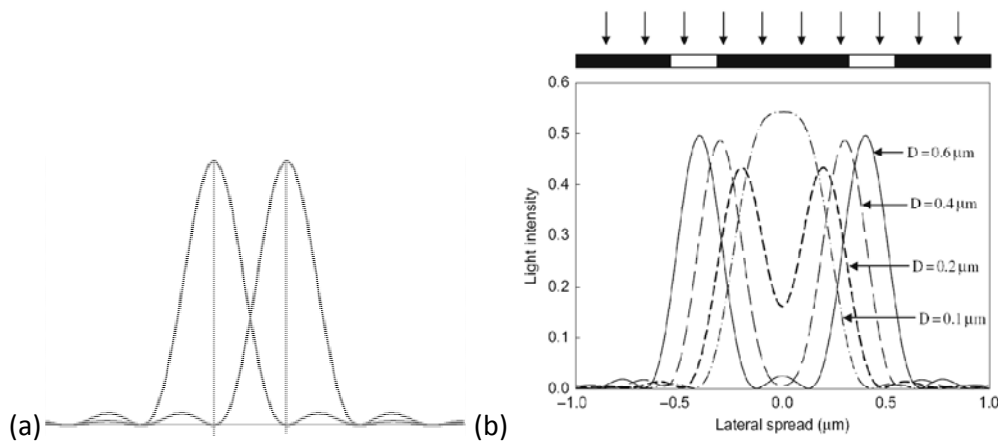


Figure A2.12: (a) Light intensities of diffraction from separated slits giving resolvable image. (b) The images of two separate lines (D is the separation distance between the centres of two-line opening) (From the ref. (17)).

Besides resolution, another important requirement for high-quality optical lithography is the depth of focus (DOF), or depth of field, expressed by equation (18):

$$DOF = k_2 \frac{\lambda}{NA^2} = \frac{k_2 R^2}{k_1^2 \lambda} \quad (A2.6)$$

where k_2 is an empirical constant determined for each tool in practice ($k_2 \leq 1$) related to a specific lithography system and photoresist process. The DOF is extremely shallow because of its inverse square dependency on NA. Therefore, the use of high-NA lenses for an improved resolution is followed by very small DOF, what means that the optical imaging would only be in focus in a very small range of height variations. This is one of the reasons for the strict requirement for planarization of surface of resist film. In practice, an absolutely flat surface cannot be obtained and thus many places on a wafer would not be in focus because of the surface irregularities, usually coming from spin-coating, presence of filler or wafer bowing. The effect would be more pronounced on the larger size wafers, used for industrial applications where DOF is thus actually one of the most important lithographic parameters (17).

The exposure can provide structuration of the resist by initiating its cross-linking in the predetermined regions. The most common way to cross-link SU8 is by exposure in the near-UV range, due to its quite high transparency in that region. In fact, SU8 shows much higher absorbance at shorter wavelengths (below ~ 400 nm) than for longer wavelengths. Consequently, the exposure wavelength has to be chosen according to the SU8 transparency. The SU8 exposure in our experiments was performed with MA6 containing a mercury lamp which has the strongest emission in the required spectral range with peaks at wavelengths of 365nm, 404nm and 435nm, corresponding to *i*-, *h*- and *g*- lines, respectively (3). Indeed, the choice of exposure wavelength is crucial for the optimisation of all lithographic parameters, like resolution and DOF, for which it is necessary to use light with a lower wavelength. Besides this influence of light wavelength on mentioned parameters of lithography, there is an additional influence on the cure depth. This arises from the resist's UV absorption at the exposure wavelengths and thus a non-uniform light intensity distribution across the resist film. Therefore, the photo-initiated curing process follows a surface to depth gradient due to the limited penetration of light in the resist layer. In fact, the intensity (I) at a certain distance in the vertical direction from the film's surface (z) is given by the Lambert-Beer's law of absorption (15):

$$I = I_0 e^{-\alpha z} \quad (A2.7)$$

where α is the absorption coefficient and I_0 is the intensity of incident light. The transmission is then defined as (15):

$$T = I/I_0 = e^{-\alpha z} \quad (A2.8)$$

and the absorbance would be:

$$A = -\ln(I/I_0) = \alpha z \quad (A2.9)$$

Thus, due to the light absorption by SU8, the light intensity gradually decays as a function of the coating's thickness. Therefore, the coating layers oriented towards the incident light are more exposed than the deeper ones (15). Clearly, the UV-exposure induces structural changes in the SU8 material due to the photoactivation of photoinitiator and initiation of the polymerisation process. This, in turn, changes locally the absorption coefficient of the resist, and SU8 becomes less transparent in the required spectral region (1). In addition, this change of the local absorption coefficient during the UV-light exposure will affect more the thicker coatings. Since SU8 can be used as a layer of thickness in the range of three orders of magnitudes (from less than 100 nm to more than 1 mm), the absorption of light with the increased thickness is becoming crucial for thick layers. The light transmission through SU8 is also wavelength dependent. Yang et al. measured transmission of light as a function of thickness of unexposed SU8 for the two different wavelengths and showed that the intensity light of shorter wavelengths (*i*-line) decayed significantly faster with the coating thickness (15). This means that the light with the longer wavelength can penetrate deeper into the resist and expose the thicker layers. Moreover, also the unexposed SU8 is more transparent for light of longer wavelengths.

However, the exposure to light of longer wavelengths is accompanied by problems of decreased resolution (Eq. A2.5) and decreased DOF (Eq. 6.2.6). But definitely the most problematic consequence of choosing longer wavelength light is the diffraction effect (Eq. A2.1) which is important, because the edges of the aerial image of patterns are defined by the edges of diffraction pattern. The diffraction effects are even more pronounced for the exposure with air gap between the mask and the resist, which as we said, can be significant due to the surface imperfection and unevenness caused mainly by the standard spin-coating. An additional factor which can significantly increase surface roughness is the presence of the filler in the case of composites, like we have. By increasing gap distance notable T profiles could be seen, because the pattern edges were irradiated with higher doses resulting in pattern enlargement at the top of the features making T-profile instead of vertical walls. Simultaneously, the diffraction effects are becoming more pronounced with increasing resist thickness and gap distance at a fixed exposure dose. The T-profile sidewalls can be partially compensated by an increase of the exposure dose, but in that case with the drawback of widening the lateral dimensions of the final structures comparing to the dimensions of pattern on the mask.

For the exposure of our CNTs-SU8 composites we chose *i*-line (365nm) dominant lithography, because the shorter wavelength light (*i*-line), which is usually recommended for the advanced optical lithography (19), is less affected by diffraction and favourable for a good resolution and DOF. On the other hand, the light intensity in that case drops too fast with the depth what could cause a difficulty in cross-linking the composite at the film's side opposite to the incident light. Moreover, the shorter wavelength light is mostly absorbed by the surface part of SU8 film oriented towards incident light, causing over-exposure of that

part of the film (15). This could result in pronounced T-profiles and non-vertical sidewalls, due to the irradiation of the one part of the resist with higher dosage (1).

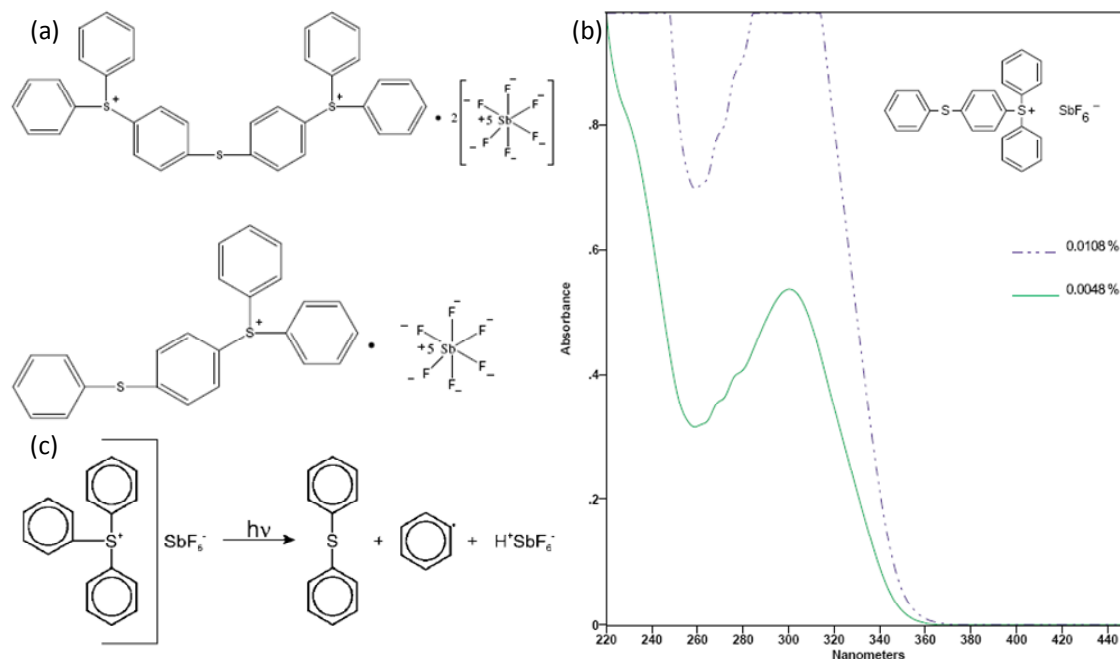


Figure A2.13: Chemical structure (a) (From the ref. (20)) and UV absorption spectra (b) (From the ref. (21)) of usually employed SU8 PI containing mixed Triarylsulfonium hexafluoroantimonate salts in propylene carbonate. (c) Generalised basic schema of protolysis of these salts which generates an acid that induces the cross-linking (From the ref. (9)).

The irradiation itself or the UV exposure processing step has the main function to initiate polymerisation of negative tone polymers, in this case of SU8, in the regions determined by the openings of the patterns on the mask. In fact, upon irradiation, the PI decomposes to form a Brønsted acid (in the case of SU8 usually hexafluoroantimonic acid), which act like a catalyst for the initiation of the cross-linking reactions (see Chapter 2). In order to successfully proceed with UV exposure, the first requirement is that the spectral absorption range of PI has to fit the spectral range of the light source. Therefore we need PI which absorb in the near-UV range where the mercury lamp has its strongest emission, especially in the *i*-line (365nm) dominant range which we chose. The second requirement is that PI should be a combination of different PI. This is necessary for a simultaneous surface and in-depth curing needed for successful cross-linking of SU8 films of different thicknesses (22). Due to suitability to both listed requirements (Fig. A2.13), the PI containing mixed Triarylsulfonium hexafluoroantimonate salts in propylene carbonate ('old' PI), is the most often used PI for SU8 cross-linking (23; 24). Especially important is that this PI does not have too large light absorption at 365nm (Fig. A2.13 (b)) because SU8 patterning requires a very good compromise between cure speed and cure depth. Hence, the main requirement for a PI to be compatible with SU8 is "not to have excessive absorption at 365nm" (25).

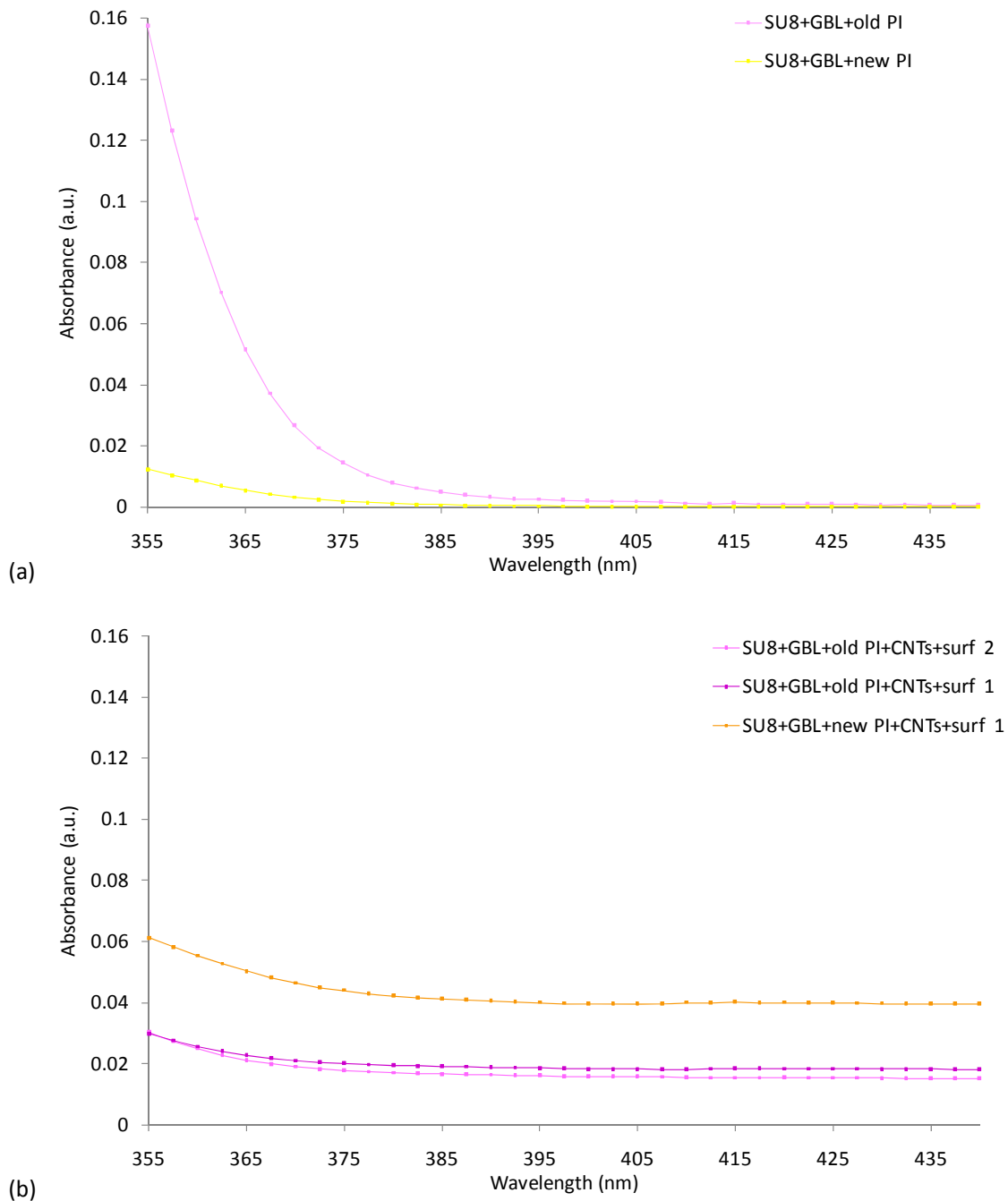


Figure A2.14: UV absorption spectra of: (a) unloaded SU8 with the old and new PIs and (b) CNTs-SU8 composites prepared with different surfactants and the old and new PIs.

Besides the mentioned requirement for photopatterning of the resist that the emission spectra of the light source correspond to the absorption of the PI, an unexposed resin has to be simultaneously transparent in this spectral range. In other words, the only absorbing species of the exposure wavelength should be PI, while all other components in the resin formulation should ideally be completely transparent for that wavelength (here 365nm). Therefore we measured the absorption by ultraviolet and visible (UV-vis)

absorption spectroscopy. The spectral region of interest for this work was around 365 nm and up to 440 nm in order to identify if the choice of exposure wavelength is also suitable for the composites. Absorption measurement results in that range are presented here. All samples for this measurement were prepared in the same way (spin-coating and soft baking on a quartz wafer). Initially, we measured the absorption of unloaded SU8 prepared with old and new PI (Fig. A2.14 (a)) in the concentrations (see the ref. [MM1]) which were previously experimentally determined to be sufficient for the cross-linking of unloaded SU8 with the standard exposure doses (6). The results showed a 9.4 times higher absorption at 365 nm by old PI comparing with new PI, while at *g*-line (435 nm) samples showed the same trend just with a lower ratio of absorbance (3.9). This would make the new PI more suitable for cross-linking of unloaded SU8 at *i*-line (365 nm) dominant range.

In order to observe the influence of the other components of CNTs-SU8 composites, we measured the absorbance of three types of composites containing 1.2 wt% of CNTs in SU8, but prepared with different surfactants and PI (Fig. A2.14 (b)). It is evident that composites prepared with old PI had almost the same absorption over the wavelength range of interest, meaning that surfactant's nature did not significantly influence the absorption properties of composites and that PI has a dominant effect. The same conclusion as the last one can be drawn from the comparison of two composites prepared with the same surfactant (here surfactant 1) and with two different PI (Fig. A2.14 (b)), where the sample with the new PI had two times higher absorption than the one with the old PI.

Furthermore, we were especially interested in the influence of CNTs on the composite overall absorption, since it is known that in UV curing the presence of fillers can, besides providing complementary properties, significantly influence the ability of UV rays to penetrate the composite film (22). Hence, we measured the absorbance of the composite containing only SU8, GBL and CNTs without adding any PI or surfactant (Fig. A2.15). The result was an almost constant absorbance in the spectral range of interest for this work. This result was firstly compared with the absorbance of unloaded SU8 with new PI and with the composite containing new PI and surfactant 1 (Fig. A2.15 (a)). The comparison showed that the absorbance at 365nm of the composite containing new PI and surfactant 1 is just the sum of the individual absorbances of the composite containing only SU8, GBL and CNTs (without PI and surfactant) and with the sample of unloaded SU8 with new PI, like it was expected. The result was secondly compared with the absorbance of the composite containing old PI and surfactant 1 or 2, and with unloaded SU8 with the same PI (Fig. A2.15 (b)). On the contrary, the absorbance of the final composites with PI and CNTs was not the sum of the constituents, like it would be expected, because absorbance is additive. Surprisingly, the absorbance of final composites with PI and CNTs was lower than each of both absorbances of the constituents or in other words, the sample become more transparent when we added CNTs, what is contra intuitive. This showed a significant influence of CNTs-old PI combination on the overall composite absorption, what could lead to the problem with the initiation process.

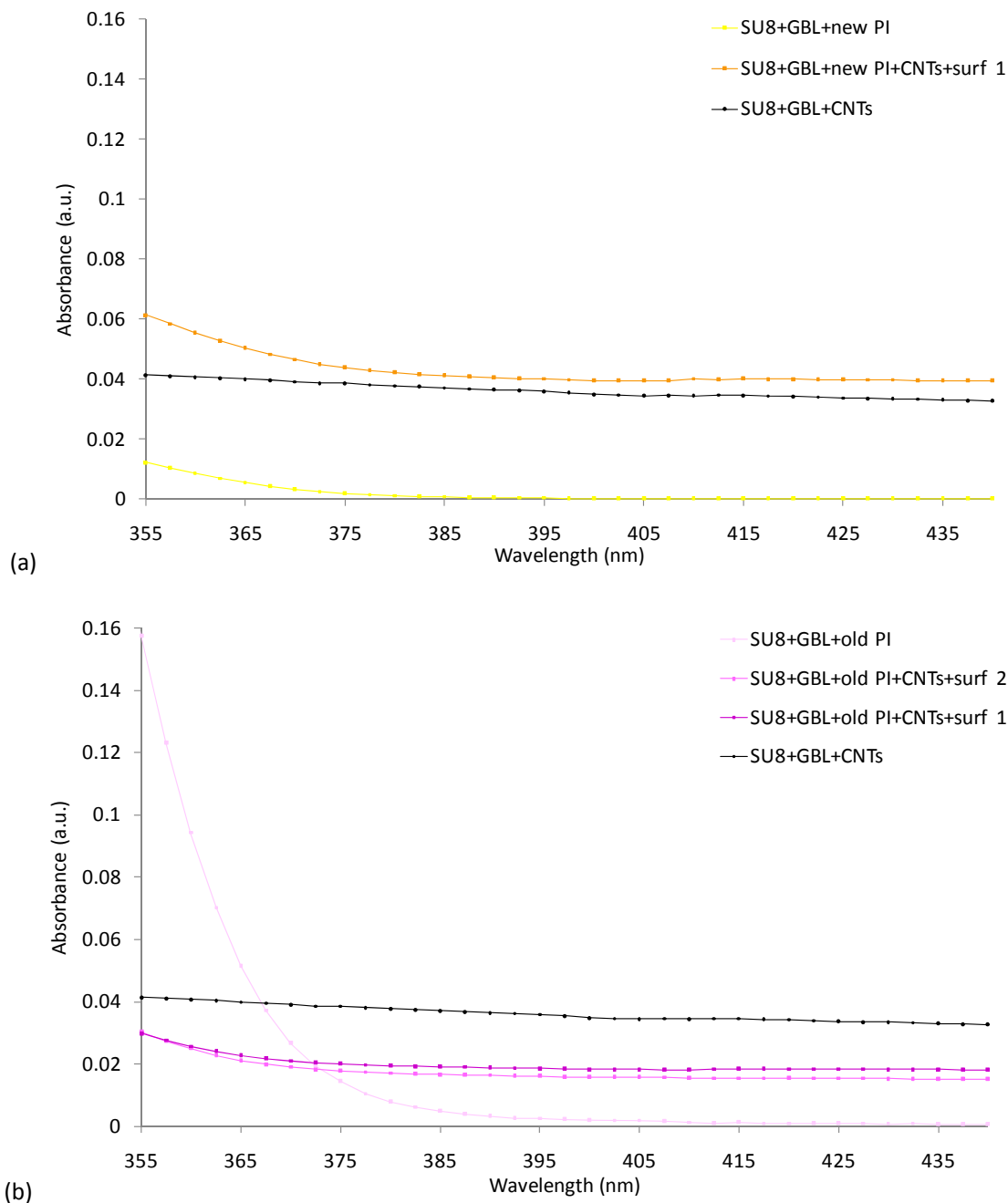


Figure A2.15: UV absorption spectra of the composite containing CNTs without any PI or surfactant and: (a) samples with the new PI with and without CNTs (b) samples with the old PI, with and without CNTs (with two surfactants).

Based on presented results for the absorbance of all samples, the conclusion is that composites prepared with new PI and surfactant 1 are most appropriate for the cross-linking initiation by UV exposure in *i*-line dominant range. Whereas composites containing old PI and CNTs showed interference of effects of individual components, resulting in a complex and unpredictably response of these composites on the exposure step.

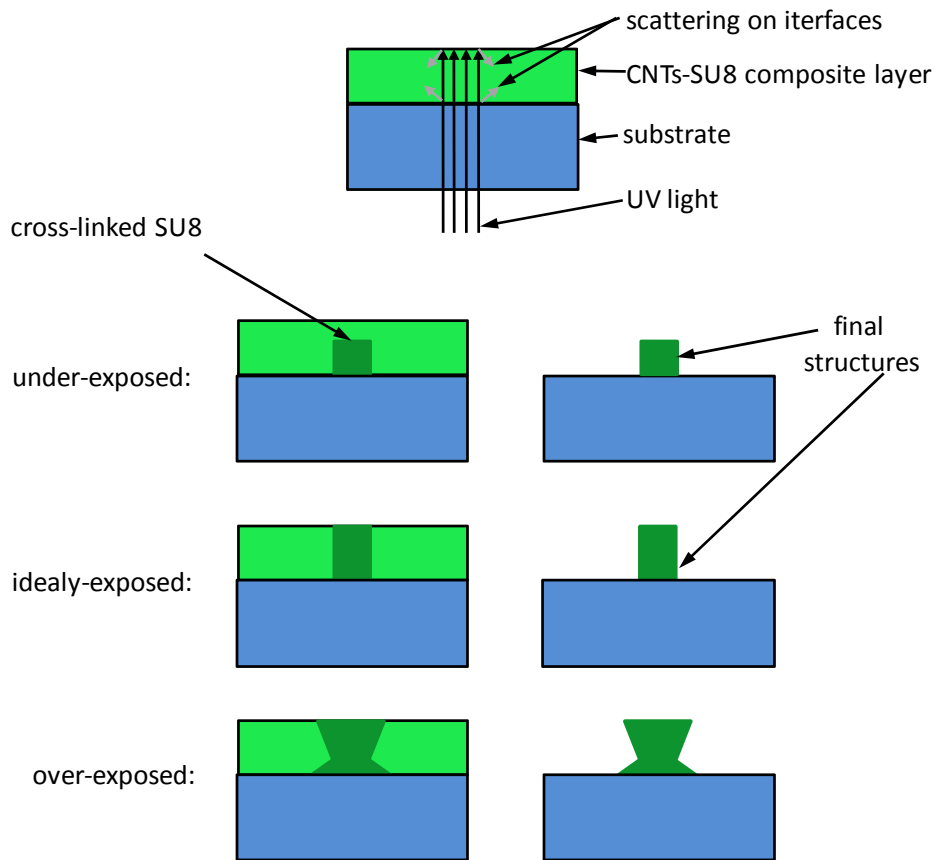


Figure A2.16: Schematic representation of the back side exposure mode and in that case obtained final structures depending on the exposure dose.

Upon conforming that composites can be exposed at chosen wavelength, we needed to establish an exposure dose, which is actually threshold energy necessary to cure SU8 inside the targeted region. The exposure dose in general has to be found for each particular resist thickness and CNTs concentration, because it depends on the quantity of SU8 which changes with the thickness and with filler concentration. The standard way to find the exposure dose for one specific thickness is to expose the layer of such thickness with different doses by slowly increasing the exposure dose. This has to be done in so called “back side” exposure mode, where the exposure is in such a way that incident light enters the resist layer on the resist-wafer interface (Fig. A2.16). It means that light is passing through the mask and the quartz wafer and then through the resist layer. Naturally, incident light can be scattered on the interfaces, what can be an additional reason for the broadening of the aerial image of pattern comparing to the original dimensions of pattern on the mask. This exposure mode is particularly convenient for finding the appropriate exposure dose because the thickness of the cross-linked resist layer gradually increase with the increase of the exposure dose (under-exposure), until the entire resist thickness is cross-linked in the ideally exposed resist layer (Fig. A2.16). A further increase of the exposure dose (over-exposure) cannot result in a thickness increase, but can induce

significant deviation of structures' walls from the vertical side profile (Fig. A2.16). Therefore the standard curve of cross-linked resist thickness as a function of exposure dose in back side mode is showing a linear increase followed by the saturation plateau when full thickness is reached.

We followed the presented standard procedure which is necessary to obtain the appropriate exposure dose for different thicknesses of composite layers and different CNTs concentrations. All samples used in this study were prior to this spin-coated on quartz wafers of 100 mm diameter and soft baked under appropriate conditions (for the details see ref. [MM1]). All samples were exposed to a gradual increase of the exposure dose, where step size was tuned according to the thickness of the composite layer. Surprisingly, the expected standard curve of thickness of the cured composite as a function of the exposure dose could not be observed for any of treated samples. In fact, in many cases, the thickness of the composite layer was even decreasing at the beginning of the increase of the exposure dose, while a further dose increase had almost no effect on it. Unexpectedly, if the layer was under-exposed surface roughness was dramatically high varying from almost bare wafer to the thickness of overexposed layers. On the other hand, if the layer was over-exposed, the aerial dimensions of the projection image were rapidly spreading resulting in a widening of the structures comparing to the patterns on the mask. Therefore, the right exposure dose was established as the value in between these two regions. However, the full thickness of the composite layer could not be cured in this exposure mode, no matter how high the exposure dose was chosen. Actually, from a certain exposure dose, the exposure through the mask resulted in a continuous layer like in the exposure without any mask, and an even further increase of the dose did not result in an increase of the cured thickness. Hence, the full thickness of the exposed layer could not be cross-linked in the back-side exposure mode regardless of the exposure doses.

Besides the back side exposure mode, the resist layer can be exposed in the front side mode, when incident light is entering the resist layer on the resist-air interface (Fig. A2.17). This exposure mode is not usually used for finding the exposure dose appropriate for a certain thickness of the resist layer. Namely, under-exposure of the resist layer means that the light intensity is lower than the threshold energy required for cross-linking the full thickness of the exposed resist layer. Moreover, in the front side exposure mode, this means cross-linking of the topmost part of resist layer, while the bottom part of the same layer underneath remains uncured (Fig. A2.17). As a result, such under-exposed structures would be washed out during the development step, because the bottom of the layer would not be cross-linked. Therefore, in the range of under-exposure doses, a gradual increase of the exposure dose can bring an increase of cured thickness but that effect on thickness cannot be registered because all of these under-exposure doses would appear exactly the same after the development step; they would be all washed out. For that reason, it does not make sense to study the dependence of the cured thickness on the exposure dose, like for the back side exposure mode. On the contrary to the under-exposure, when resist layer is

exposed to the ideal exposure dose, which would correspond to enough energy to cross-link throughout the entire thickness of the exposed layer, final structures would remain on the wafer surface after the development step. A further increase of thickness would not be possible. Consequently, a further increase of the exposure dose or over-exposure, would appear in the same way like over-exposure in the back-side exposure mode, by inducing deviation of walls of the structures from the vertical side profile (Fig. A2.17).

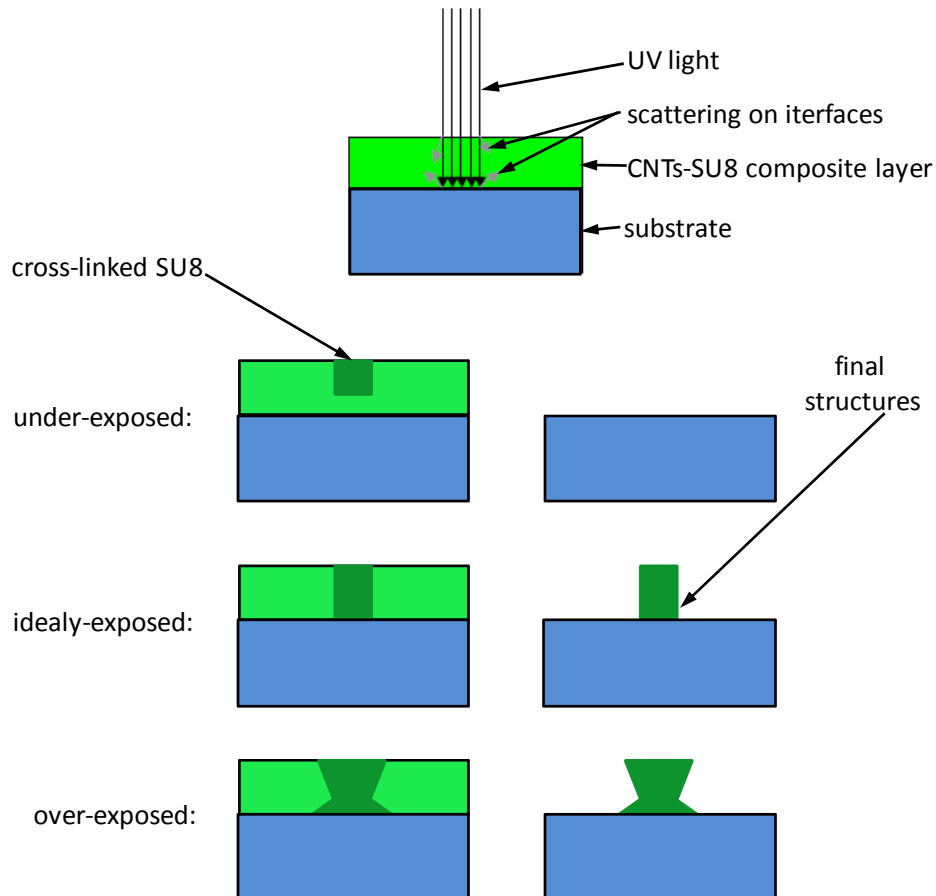


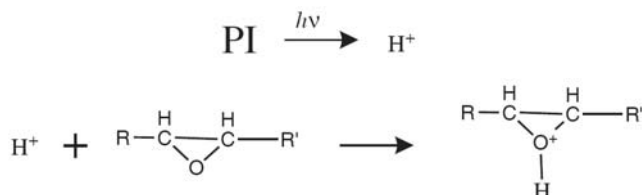
Figure A2.17: Schematic representation of the front side exposure mode and the resulting structures as a function of the exposure dose.

All samples which were previously exposed in the back side mode were also exposed in the front side exposure mode with the same exposure doses, in order to verify our previous choice of the appropriate exposure doses. On that way obtained ideal exposure doses were approximately the same like in the back side exposure mode. However, a slight difference could be noticed in the broadening of the edges of the structures which appeared to be more rapid with the dose increase than in the back side exposure mode. This could be attributed to the expected diffraction problem. Namely, the exposure in front side mode was performed either through an air gap of 25 μm or through direct contact of the mask and the surface of the composite film. In both cases, diffraction could be caused by surface roughness resulting from the spin-coating induced surface imperfections and unevenness

(see section about spin-coating) or from higher CNTs concentrations what goes along with shear induced aggregation and hence higher surface roughness.

A2.4 Post-exposure baking (PEB)

A strong acid that is generated in low concentrations by UV-exposure, acts as a catalyst in the successive cross-linking process, which is activated by heating in the subsequent step of PEB (1). In principle, the UV-exposure step just defines the starting points of a chemical reaction that is actually driven by temperature (26). The cross-linking is initiated by the cationic ring opening of epoxy groups by the acid. In fact, in the presence of a photo-generated acid, the ring-opening polymerisation of epoxides proceeds through the oxonium ion (26):



In order to provide propagation of polymerisation, reactive species have to be mobile enough to diffuse in regions with uncross-linked SU8. However, considering the size of active species, anions are quite large comparing to tertiary oxiranium ion what can affect their diffusion in the CNTs-SU8 network. When the new monomer adds to the oxonium ion in propagation of polymerisation, the anion flows to the new position. In the case of our composites, the CNTs network could reduce mobility of active species and thus affect the propagation step of polymerisation.

The propagation occurs by the reaction of protonated oxonium ions with neutral epoxides in a series of cross-linking reactions activated by the heat (1). The final result of the cross-linking process is a dense, stable network where each SU8 oligomer is connected to 7 others on the average (9).

All PEB were performed under the same ambient conditions in clean room (CMI, EPFL) with 45% (± 1 point) of relative humidity. This is important because the relative humidity has strong influence on the cationic polymerisation by decreasing the polymerisation rate and inducing loose of physical properties (22). In fact, in the cationic curing the presence of groups containing a hydroxyl end groups (-OH) leads to a softer polymer network because the mechanism of polymerization changes from a typical active chain-end mechanism to an activated monomer mechanism (27).

In essence, cross-linking implies that intermolecular bonding, hydrogen bridges and van der Waals forces are replaced by covalent bonds (22). As a result, during PEB the

properties of the resist film change. Firstly, shrinking necessarily occurs because of the densification of SU8 network through the cross-linking. In addition, shrinkage in PEB is enhanced also by outgassing of the remaining solvent (9). This volume shrinkage induced by cross-linking is significant and therefore contributes a lot to the overall internal stress of the film with 45% (30% originate in the exposure and 15% in the post-exposure bake) (1). On the other hand, the positive side of shrinkage during polymerisation is induced excess free volume which allows a redistribution of the reactive species within the system and hence diffusion of PI into regions of unreacted bonds (22). In fact, as the cross-linking further proceeds, the shrinkage is no longer able to keep up with conversion. In this way resulting excess volume allows additional mobility of the reactive species. Hence, a higher polymerization rate creates more temporary excess volume, resulting in higher crosslink densities and final maximum conversions (12). Besides shrinkage which is induced by chemical reactions, the overall internal stress can be also significantly influenced by exposure to an elevated temperature in PEB followed by thermal contraction during cooling down (12). Therefore, in order to minimize the internal stress in the PEB step, it is necessary to heat up the wafer very slowly from room temperature until PEB temperature, which is typically 95°C, and to “naturally” (without employment of cooling systems) cool the wafer back to room temperature.

The presence of CNTs can influence the volume shrinkage during PEB since CNTs can by themselves be an obstacle for SU8 oligomers to approach close to each other in order to cross-link. Consequently, this could reduce cross-link density and hence, epoxy conversion, what was confirmed experimentally (28). Simultaneously this could create additional excess free volume comparing to the usual one, which would provide even higher mobility of the reactive species. Accordingly, PI could easier diffuse into the unexposed regions of the composite causing broadening of aerial dimensions of the structures. The other problem which may appear due to the presence of CNTs is the formation of cracks on the topmost composite layer. The reason can be surface roughness of the obtained films which can be significant (see Chapter 6) and which increases with the increase of CNTs concentration, due to the shear induced aggregation. The edges of bumps and dents of the surface roughness are prone to cracking, because of the stress concentration in these points (Fig. A2.18). Therefore, composite films with high surface roughness, what would mean composite with high CNTs concentration and/or spin-coated under inappropriate coating conditions, could have poor mechanical properties.

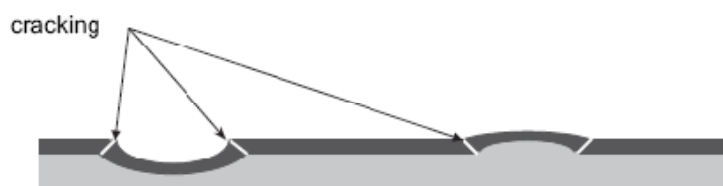


Figure A2.18: Schematic view of bumps and dents which may lead to stress concentration and thus, to cracking of the top-most composite layer (From the ref. (2)).

In order to study thermal behaviour and to observe if cross-linking of SU8 can proceed in the presence of CNTs in composites, we used DSC. In our DSC study the most important parameter is temperature from which start the appearance of the exothermal peak or to be more precise, from which stops the endothermal slope. The appropriately long PEB at this temperature is considered as suitable for the cross-linking. It is very important to observe the lowest possible temperature, because on higher temperatures the cure speed would be too high for patterning. Consequently, in the case of chemically amplified resist, such as SU-8, pattern broadening would occur as a consequence of the diffusion of the PI during PEB (1). Therefore, for each specific application, the best compromise must be found between the cure speed and depth (26).

A technique often related to DSC, is the already mentioned technique of TGA, where the weight of the sample is recorded continuously as the temperature is raised. By this technique chemical reactions related to weight change, like volatilization, dehydration or oxidation can be recorded (4). On the other hand, simple transitions are missed, because they are not followed by weight changes, but they are followed by changes in heat capacity what can be seen by the results of DSC measurement. For that reason, TGA and DSC are often combined due to the complementary information which they can give. This combination is especially important for detecting transitions like cross-linking, which would appear as an exothermic peak on the DSC curve, but which would simultaneously not appear as a weight loss on the TGA curve.

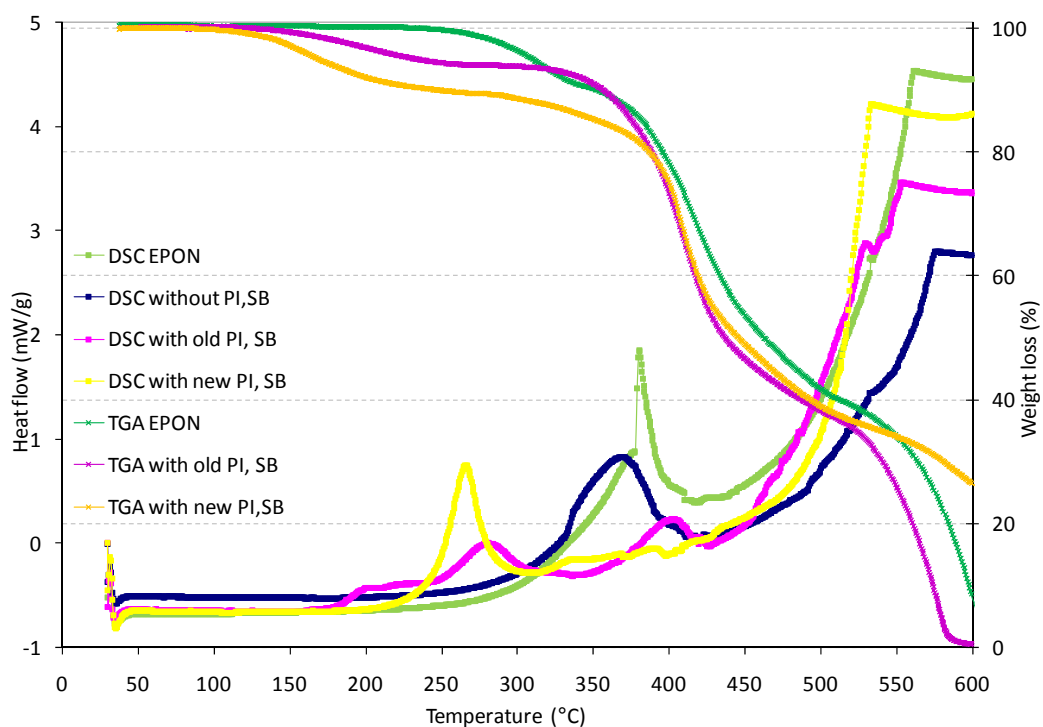


Figure A2.19: DSC and TGA curves of the previous SB SU8 samples with or without solvent (EPON), but with different PIs (old or new) or without PI.

Firstly, we measured TGA and DSC curves for the SU8 samples without CNTs, as a reference (Fig. A2.19). DSC of samples with PI shows clearly exothermic peak between around 200°C and 300°C, which is not followed by weight loss in the corresponding TGA curves. Since these samples were only soft baked and not exposed, observed peaks are confirming that the polymerisation is thermal cross-linking. In the case of the SU8 sample with old PI, the lowest temperature where exothermic slope start to occur is at 150°C, what correspond to PEB temperature used for thermal cross-linking for this reason. In the case of SU8 with PI, this value is higher, 170°C. To confirm that the noticed peak originates from the cross-linking reaction, we measured DSC of the SU8 resin without PI and of the SU8 without any solvent or PI (in the form of pure EPON) (Fig. A2.19). Both DSC curves show the first exothermic peak at around 380°C, what matches with SU8 degradation temperature (see Chapter 2) followed by expected dramatic weight loss on the corresponding TGA curves. The last degradation stage of all samples occurs at around 550°C, but surprisingly the SU8 resin with new PI shows a much lower degradation rate above 500°C, comparing to the other samples. This is most obvious in the high char content of this sample, which is at 600°C unexpectedly high, 27%.

In order to observe the influence of CNTs presence in composites, we measured TGA and DSC of the composites containing one of the two surfactants and old or new PI (Fig. A2.20). All samples were SB, like the previously examined samples (showed in Fig. A2.19). Comparing the DSC results for SU8 (Fig. A2.19) and composite (Fig. 6.2.20 (a)) both containing new PI, we can see that thermal cross-linking starts at lower temperature (at 150°C) in the presence of CNTs. However, the previously observed high char content for the SU8 sample with new PI did not appear on the TGA curve of the composite (Fig. A2.20 (b)). On the contrary, the char content was only 1.1% of initial sample's weight. This indicates that simultaneous presence of CNTs and surfactant 1 together with new PI and SU8 supports high temperature thermal decomposition of the composite. Moreover, weight loss noticed on the TGA curve of SU8 with new PI (Fig. A2.19) in the region from 100°C to 250°C which corresponds to evaporation of remaining traces of solvent, did not appear in the case of a composite with new PI (Fig. A2.20 (b)), signifying that solvent was surprisingly easier removed from the composite with CNTs than from unloaded SU8 alone.

Considering the DSC results of all SB samples with the old PI, which are SU8 and composites with two different surfactants, a significant difference in the region of interest was not noticed. Nevertheless, TGA curves of these samples show a difference in the temperature range from 95°C to 250°C, where remaining solvent which continued to evaporate can be seen (Fig. A2.20 (b)). Corresponding weight loss is 18% of the weight at the beginning of the TGA measurement, but this is equivalent to 10% weight loss normalised to the sample weight before SB (the last can be seen in the Figure A2.20 on the curves marked with "relative" indicating weight loss relative to the sample weight before SB). Accordingly, in the composites containing old PI, CNTs interfered in the solvent evaporation

by being an obstacle to solvent removal from the network of CNTs and SU8, regardless which surfactant was used.

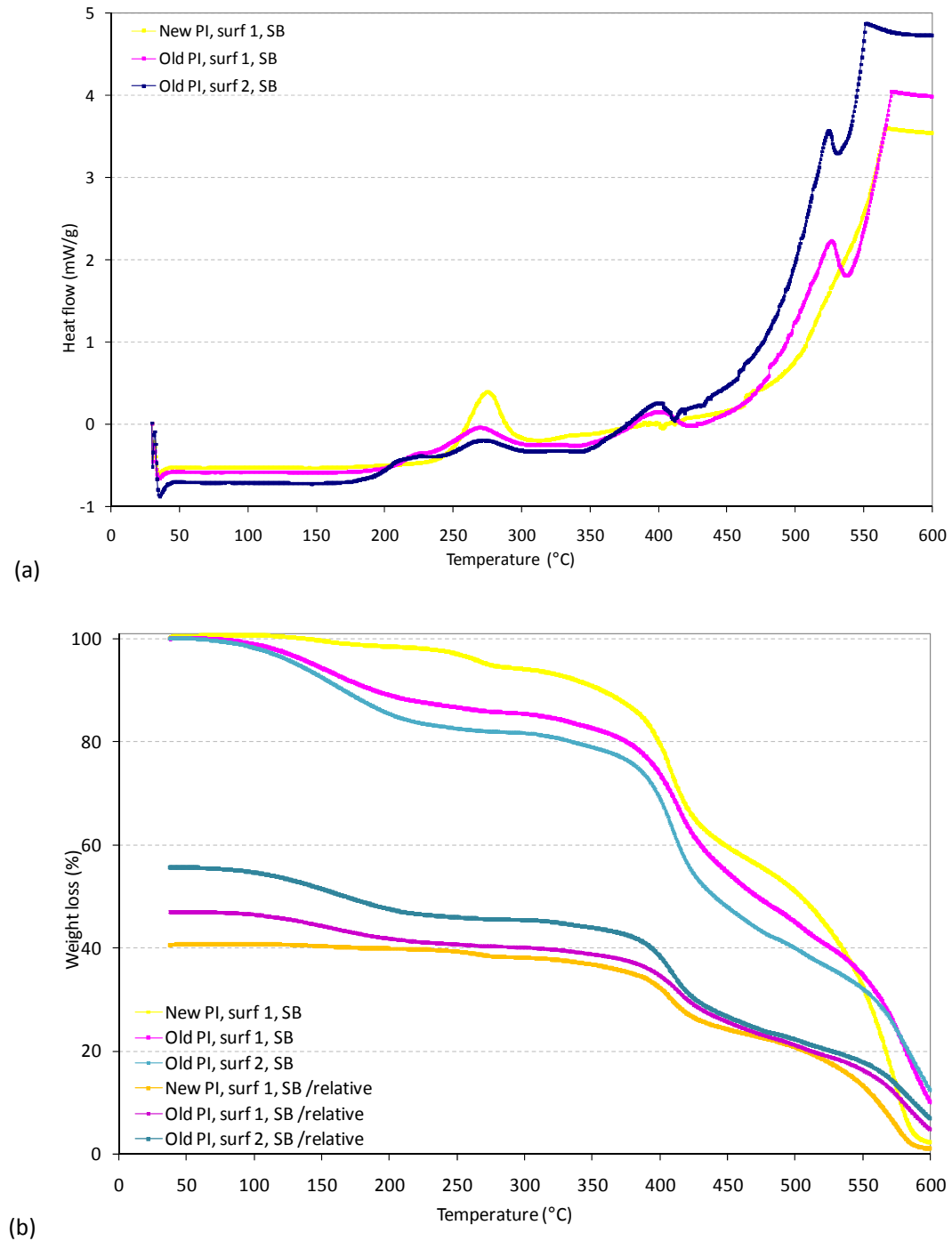


Figure A2.20: (a) DSC and (b) TGA curves of CNTs-SU8 SB composites with different PI and surfactants. TGA curves marked as “/relative” indicate the same measurement just with all weight losses expressed relative to the samples weight before SB.

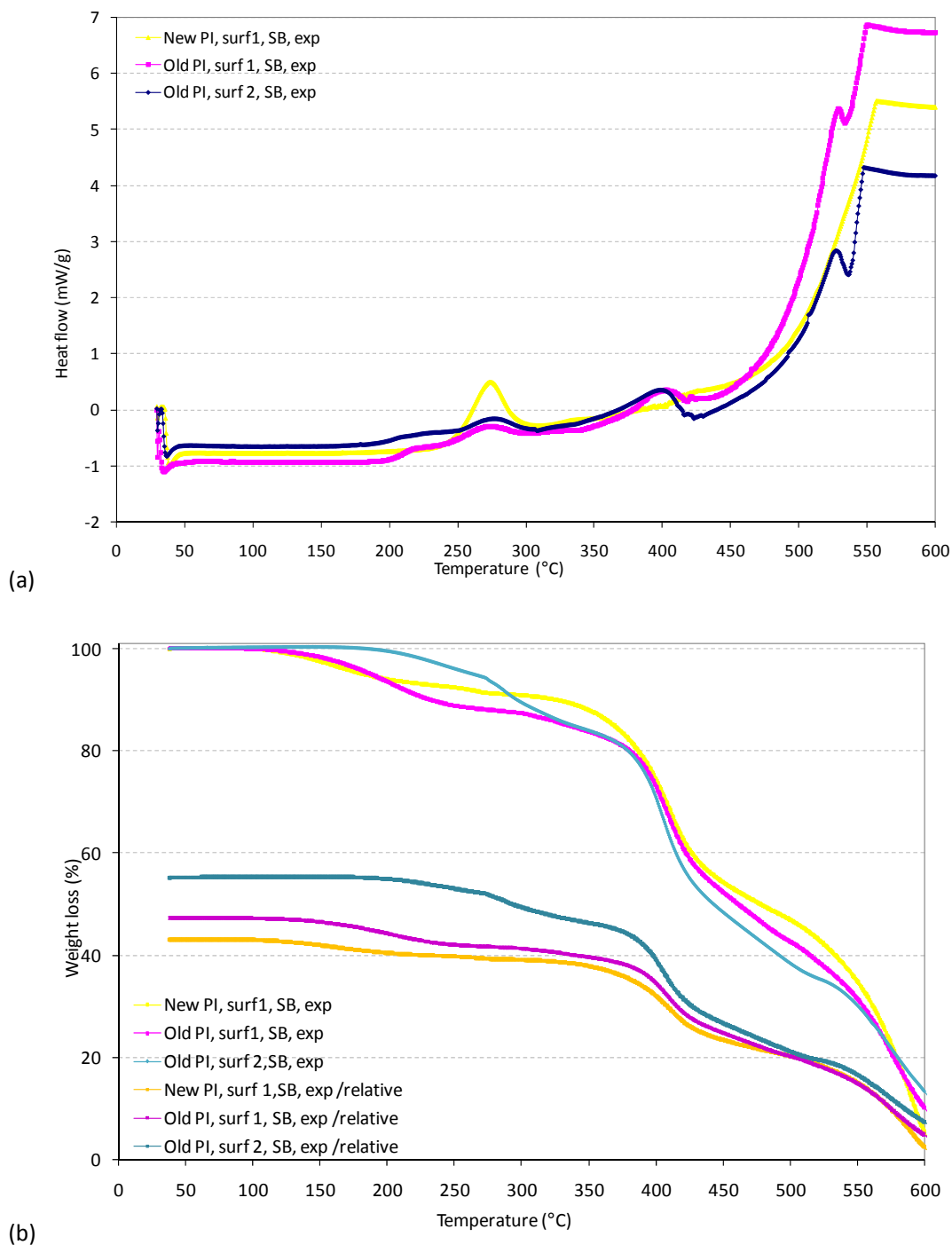


Figure A2.21: (a) DSC and (b) TGA curves of CNTs-SU8 composite samples with different PI and surfactants. All samples were first SB and then UV-exposed (exp). TGA curves marked as “/relative” have the same meaning as on previous Figure.

On the other hand, for the PEB itself it is of particular importance to combine the interpretations of the DSC-TGA curves of the composites which were UV exposed after the SB (Fig. A2.21). At first, we compared the results for the samples with old PI, because this PI is a commonly used SU8 PI with well known properties. For SU8 containing standard PI, PEB

is usually performed at 95°C (6). Fortunately, the composite samples with old PI (Fig. A2.21 (a)) both showed that PEB temperature can be kept as in the standard SU8 processing, what was also confirmed experimentally in this study. Additionally, UV exposed composites with old PI (Fig. A2.21 (b)) showed higher thermal stability comparing to the same samples which were just SB (Fig. A2.20 (b)).

In contrast, DSC of composite with new PI after UV exposure (Fig. A2.21 (a)) showed that PEB in that case have to be performed at 120°C what was experimentally confirmed to be the appropriate PEB temperature, while TGA (Fig. A2.21 (b)) showed a retained thermal stability of this type of composites.

Commonly, at the beginning of the standard PEB process, the image of the patterns from the mask was very rapidly becoming visible on the surface of the SU8 film, if the exposure dose was appropriate for the exposed SU8 thickness and the PEB temperature was suitable for SU8 cross-linking. The same phenomenon remains to appear in the case of PEB of CNTs-SU8 composites, regardless of employed PI, surfactants, exposure mode or CNTs concentration.

The main consequence of PEB is cross-linking in the previously UV exposed regions what makes them stable against the action of solvents during the subsequent development step (1).

A2.5 Development

In the case of negative tone resists, like SU8, the function of the development step is to remove non-illuminated regions of SU8, since its UV light-exposed parts become insoluble in the developer after PEB (26). Removal of the non-exposed SU8 is initiated by diffusion of the developer molecules into the regions composed of non-cross-linked SU8. This process is then followed by solvation of the polymer chains into the developer solution (1). The SU8 development is usually performed by immersing the wafer with SU8 film in PGMEA, used as SU8 developer, at room temperature. Subsequent rinsing in isopropanol (IPA) can yield a clear solution indicating that all unexposed SU8 is removed. On the contrary, a blurry isopropanol bath or the presence of whitish traces signify non terminated SU8 development and thus, the wafer has to be again immersed in a PGMEA bath until the complete removal of unexposed SU8.

The duration of development, if possible at all, can be from a few minutes to many hours. Such a broad possible time interval of development originates in the complex influence of lots of processing parameters, like “the exposure dose, soft-baking time and temperature, the temperature and agitation during development and the geometry of the pattern” (1). Longer development times are normally needed for structures with high aspect which are more difficult to develop or in the case of composites, where the filler may have

stronger adhesion towards substrate than the bare resist. On the other hand, the long-lasting development process may induce substantial damage of structures, especially fine features, due to swelling of cross-linked regions or debonding of the resist (1). The developing time can be reduced by agitation and stirring of the PGMEA solution during the development (9). This can enhance diffusion of the developer molecules, resulting in a faster and more efficient development. But, a drawback of the stirring is the pressure gradient which may cause structures' deflection, collapse, deformation or even debonding and pattern loss (1). Additional improvement of the development can be achieved by the downward orientation of the wafer during stirring (29). In this downward-development process, established by Chang et al. removal of development products is accelerated via a gravity-induced pulling force and better convective transport (29).

In the case of our composites containing old PI and surfactant 2, the study showed a surprising adhesion towards substrate and that unexposed regions could not be removed even after the quartz wafer was 17 hours immersed in the PGMEA bath. Nevertheless, the uncross-linked composite with old PI and surfactant 1 could be removed after 30 minutes to 2 hours (depending on the thickness of composite film) immersion in PGMEA bath accompanied by agitation and manual stirring, and followed by PGMEA spraying. However, the most efficient development was achieved with a composite containing new PI and surfactant 1. In that case the development was terminated after only a few minutes (between half minute and 5 minutes, depending on the thickness of composite film) of immersion in PGMEA bath accompanied by manual stirring, and subsequent PGMEA spraying.

One of the possible problems which may appear in this processing step is the collapse of the structures during rinsing (30), which could have two sources. Most commonly, this appears as a consequence of the capillary forces during drying after PGMEA and isopropanol baths (31). Namely, during solvent evaporation its volume decreases and drying front shifts from the top of the structures. Accompanying surface tension at the resist-liquid interface pulls against any structure in contact with liquid causing the collapse of the photoresist features (1). Capillary forces which act on the resist walls during drying increase with increased wetting of the resist by the liquid. Therefore, one of the possible ways to avoid structure collapse in development is to use a liquid which is not wetting well SU8 (32) (what is not compatible with all processes and system components) or to use freeze drying with the disadvantage of long processing time (33).

The other possible reason for pattern collapse can be the stronger adhesive forces between the features in contact rather than the forces required for bending them. In this case the pattern collapse depends on Young's modulus of the resist material, its surface energy and the pattern geometry (aspect ratio, lateral size and distance between structures) (34). Therefore, increasing Young's modulus of the SU8 may prevent the collapse of the pattern. As presented in Chapter 5, the presence of CNTs in the composite significantly

increases Young's modulus of composites, even with very low CNTs concentrations. Consequently, we could expect that Young's modulus enhancement can enable avoiding of structure collapse. The experiments confirmed our expectation and we did not observe any collapsed features, regardless of the composite type (different PI and surfactants). Drying of all samples was performed in a wet bench with an appropriate air flow which promoted liquid removal. In this regard, we do not recommend nitrogen blow-drying, because the detachment of some features was noticed under such drying conditions.

A2.6 Hard baking

The function of the hard baking is to: achieve complete cross-linking (9), remove residual solvents, restore adhesion after development and increase resistance to etchants by film hardening (26). This processing step is optional and is usually recommended if obtained structures are a part of a final device (1). This step is especially important if the structures have to be exposed to thermal treatment during the operation of a device, where the structures are going to be integrated. In that case, the hard baking should be done at a 10°C higher temperature than the operating temperature of the device (7). Still, the temperature range for hard baking is from 150°C to 250°C (for 5 to 30 minutes), depending on the degree of cure required (7). In the case of CNTs-SU8 composites, the hard baking can be performed, if necessary, up to 300°C, without SU8 degradation (see Fig. A2.20 (b) and A2.21 (b)). Moreover, the hard baking can be used for removal of small cracks (<5 µm) by annealing (6). The main restriction for hard baking is that it can be done only for thin layers (<10 µm), because of easy structure detachment from the wafer. This is due to the temperature-induced stress resulting from the difference between thermal expansion coefficients of the wafer and the already structured resist (9).

A2.7 Conclusions

All photolithographic processing steps and their parameters were optimised to yield planar, well photo-patterned, composite films with tuneable transparency, flexibility, electrical conductivity and mechanical properties. In summary, the optimised processing steps for photolithography of CNTs-SU8 composites 2 with the use of the new PI and surfactant 1 are:

- (1) **spin-coating**: - the most critical processing step. The minimization of aggregation of CNTs can be achieved by employment of all listed instructions (the procedure can be applied for all composites containing any filler, when these composites have to be spin-coated): (a) composite deposition have to be done by slowly forming spiral from the centre of the wafer towards the outer edge of the wafer and the composite amount should be enough that the spirally deposited composite

uniformly covering a circle with the radius of at least the half of the wafer's radius; (b) acceleration and deceleration have to be higher than the standard 100 rpm/s and at least 500 rpm/s for speeds on the plateau higher than 1500 rpm, but the value should be adjusted according to the here experimentally obtained rule that the duration of acceleration part of the coating is not longer than 5 s; (c) the time on the plateau have to be approximately from 1 s to 5 s, depending on the formulation viscosity, where a lower viscosity composite requires a shorter period, but the period should just exceed the time which is required to cover the entire wafer surface by the composite; (d) the experimentally obtained rule in this study was that the total duration of spin-coating should not exceed 10s (this time includes period of acceleration, time on the plateau and the deceleration time).

- (2) **soft baking:** the SB temperature of the composites can remain the same as for the conventional SB processing of SU8 with the same solvent. However, while keeping all other technological parameters (*i.e.* solvent, deposit's thickness) the same as for the conventional SB processing of SU8, the duration of the process has to be longer.
- (3) **UV-exposure:** CNTs do not considerably interfere in the initiation of the polymerisation, and thus, transparency of composite films is not significantly affected by CNTs presence within the range of exposure. However, the exposure doses for thick films have to be higher than the ones needed for the SU8 films of the same thickness.
- (4) **post exposure baking:** the recommended PEB temperature is of 120°C, while using the post exposure baking time on the plateau of 15 min (the same as for conventional processing of SU8).
- (5) **development:** standard PGMEA bath with downward wafer orientation accompanied by stirring for 0.5 to 5 minutes (depending on the deposit thickness), followed by obligatory PGMEA spraying, isopropanol bath and natural drying in the laminar flow box (*not* by nitrogen blow-drying).

References

1. *SU-8: a photoresist for high-aspect-ratio and 3D submicron lithography*. **A. del Campo and C. Greiner**. 17, 2007, Journal of Micromechanics and Microengineering, p. R81.
2. **J. R. Wagner Jr.** *Multilayer Flexible Packaging*. Kidlington : Elsevier Inc., 2010.
3. **H. Lorenz.** *Nouvelles Technologies de Microstructuration de Type UV-LIGA et Fabrication de Composants Micromécaniques*. Lausanne : EPFL, 1998. Thesis no. 1770.
4. **L.H. Sperling.** *Introduction to Physical Polymer Science*. Fourth Edition. Hoboken : John Wiley & Sons, Inc., 2006.

5. *Theory of activated-rate processes under shear with application to shear-induced aggregation of colloids*. **A. Zaccone, H. Wu, D. Gentili and M. Morbidelli**. 2009, *Physical review E*, Vol. 80, p. 051404.
6. **Gersteltec**. [Online] [Cited: 5 June 2011.] <http://www.gersteltec.ch/su-8-Photoresists/>.
7. **MicroChem**. Processing guidelines for:SU-8 2000.5, SU-8 2002, SU-8 2005, SU-8 2007, SU-8 2010 and SU-8 2015. [Online] [Cited: 15 June 2011.] http://www.microchem.com/pdf/SU-82000DataSheet2000_5thru2015Ver4.pdf.
8. *Micromachining applications of a high resolution ultrathick photoresist*. **K.Y. Lee, N. La Bianca, S.A. Rishton, S. Zolgharnain, J.D. Gelorme, J. Shaw, and T.H.-P. Chang**. 6, 1995, *Journal of Vacuum Science and Technology B*, Vol. 13, p. 3012.
9. **G. Genolet**. *New photoplastic fabrication techniques and devices based on high aspect ratio photoresist*. thesis no. 2421. Lausanne : EPFL, 2001.
10. *Ultra-deep x-ray lithography of densely packed SU-8 features: I. An SU-8 casting procedure to obtain uniform solvent content with accompanying experimental results* . **C. Becnel, Y. Desta and K. Kelly**. 6, 2005, *Journal of Micromechanics and Microengineering*, Vol. 15, p. 1242.
11. *Optimisation of SU-8 processing parameters for deep X-ray lithography*. **R. L. Barber, M. K. Ghantasala, R. Divan, K. D. Vora, E. C. Harvey and D. C. Mancini**. 2005, *Microsystem Technologies*, Vol. 11, p. 303.
12. **L. E. Schmidt**. *Low stress acrylated hyperbranched polymers*. Lausanne : EPFL, 2006. Thesis No. 3627.
13. **Sigma-Aldrich**. *Material Safety Data Sheet: Propylene carbonate*.
14. **T. E. Price**. *Introduction to VLSI Technology*. s.l. : Prentice Hall International (UK) Ltd, 1994.
15. *A numerical and experimental study on gap compensation and wavelength selection in UV-lithography of ultra-high aspect ratio SU-8 microstructures*. **R. Yang and W. Wang**. 2, 2005, *Sensors and Actuators B: Chemical*, Vol. 110, p. 279.
16. **C. Y. Chang and S. M. Sze**. *ULSI Technology*. s.l. : The McGraw-Hill Companies, Inc., 1996.
17. **Z. Cui**. *Nanofabrication: Principles, Capabilities and Limits*. New York : Springer Science+Business Media, 2008.
18. *High-numerical-aperture optical designs*. **R. N. Singh, A. E. Rosenbluth, G. L.-T. Chiu and J. S. Wilczynski**. 1/2, 1997, *IBM Journal of Research and Development*, Vol. 41, p. 39.
19. *Pushing the limits of lithography*. **T. Ito and S. Okazaki**. 2000, *Nature*, Vol. 406, p. 1027.
20. *Kinetics study of the UV-initiated cationic polymerization of cycloaliphatic diepoxide resins*. **V. Y. Voytekunas, F. L. Ng and M. J. M. Abadie**. 2008, *European Polymer Journal*, Vol. 44, p. 3640.
21. **Sigma Aldrich**. [Online] [Cited: 30. 08. 2011.] http://www.sigmaaldrich.com/etc/medialib/docs/Aldrich/General_Information/photoinitiators.Par.0001.File.tmp/photoinitiators.pdf.
22. **E. Nouzille**. *Dark curing kinetics of UV printing inks by real-time ATR-FTIR spectroscopy*. Lausanne : EPFL, 2007. Thesis No. 3780.
23. **L. M. Brown, J. D. Gelorme, J. P. Kuczynski and W. H. Lawrence**. *Method for patterning cationic curable photoresist*. 4,940,651 United States Patent, 10. Jul 1990.
24. **R. W. Angelo, J. D. Gelorme, J. P. Kuczynski, W. H. Lawrence, S. P. Pappas and L. S. Simpson**. *Photocurable epoxy composition with sulfonium salt photoinitiator* . 5,102,772 United States Patent, 7. April 1992.
25. *Improving the Process Capability of SU-8, Part III*. **D. W. Johnson, D. J. Nawrocki and R. Ruhmann**. 5, 2002, *Journal of Photopolymer Science and Technology*, Vol. 15, p. 749.

26. **Y. Leterrier, M. Sangermano, H.-A. Klok, and E. Nouzille.** *Science and Technology of UV-induced Polymerization*. EPFL. 2008.
27. **G. Odian.** *Principles of Polymerization*. Fourth Edition. Hoboken : Wiley-Interscience, A John Wiley & Sons, Inc., 2004.
28. *Antistatic Epoxy Coatings With Carbon Nanotubes Obtained by Cationic Photopolymerization.* **M. Sangermano, S. Pegel, P. Pötschke and B. Voit.** 5, 2008, *Macromolecular Rapid Communications*, Vol. 29, p. 396.
29. *Development behaviours and microstructure quality of downward-development in deep x-ray lithography.* **C.-M. Cheng and R.-H. Chen.** 2001, *Journal of Micromechanics and Microengineering*, Vol. 11, p. 692.
30. *Why optical lithography will live forever.* **T. A. Brunner.** 6, 2003, *Journal of Vacuum Science and Technology B*, Vol. 21, p. 2632.
31. *Mechanism of Resist Pattern Collapse.* **T. Tanaka, M. Morigami and N. Atoda.** 7, 1993, *Journal of Electrochemical Society*, Vol. 140, p. L115.
32. *Reduction of capillary force for high-aspect ratio nanofabrication.* **T. Kondo, S. Juodkakis and H. Misawa.** 2005, *Applied Physics A: Materials Science & Processing*, Vol. 81, p. 1583.
33. *Freeze-Drying Process to Avoid Resist Pattern Collapse.* **T. Tanaka, M. Morigami, H. Oizumi and T. Ogawa.** 1993, *Japanese Journal of Applied Physics*, Vol. 32, p. 5813.
34. *Constraints on Microcontact Printing Imposed by Stamp Deformation.* **C. Y. Hui, A. Jagota, Y. Y. Lin and E. J. Kramer.** 2002, *Langmuir*, Vol. 18, p. 1394.

Appendix 3

Optimization of inkjet printing of CNTs-SU8 composites 2C

Inkjet printing is considered as a material-conserving deposition technique used predominantly for liquid phase materials. These materials are inks consisting of a solute dissolved or dispersed in a solvent. Basically, the process involves the ejection of a fixed quantity of ink from a nozzle in a chamber through a sudden reduction of the chamber volume. The ejected drop falls governed by gravity and exposed to air resistance until it impinges on the substrate and spreads under momentum acquired in the motion (1). Surface tension supports flow along the surface and finally, the drop dries through solvent evaporation (2).

Inkjet printers operate either in a continuous or in a drop-on-demand (DOD) mode (3). Continuous inkjet printers appeared first on the consumer markets (in the late 1970s). They used electrostatic plates to deflect the motion of drops (4). In the continuous printing mode a stream of drops is ejected under pressure through a small nozzle. In order to direct and position these drops, the nozzle is maintained at a potential which passes on a small charge on each drop as it is formed. Individual drops in the stream are directed by applying a further potential to deflector plates. A schematic diagram of continuous inkjet printing is shown in Figure A3.1 (left panel). Diameters of formed drops are generally larger than the nozzle diameter (5). In the continuous mode, ink is pumped through a nozzle to form a continuous stream of liquid drops, even when no printing is required. Unwanted drops are deflected by the electric field to a gutter, from where the unused ink can in principle be

recycled (Fig. A3.1, left panel). However, ink recycling is done in rare cases. In fact, exposure to the environment can easily contaminate the ink, which thus cannot be reused. Therefore continuous inkjet printing is usually considered as a wasteful process (5).

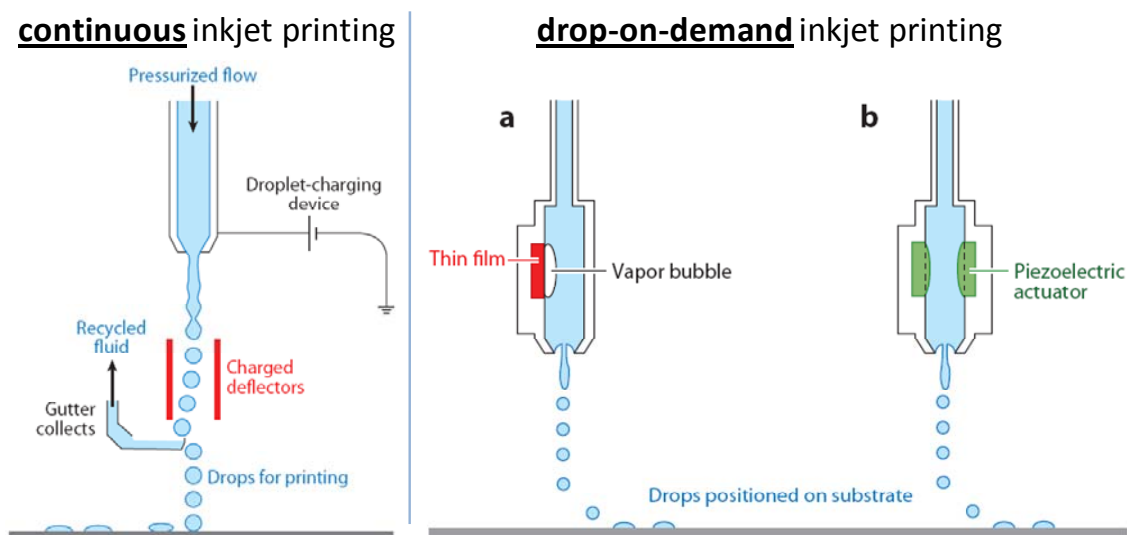


Figure A3.1: Schematic diagram showing the operating principles of continuous and drop-on-demand (DOD) inkjet printing systems. In DOD systems drops are ejected by a pressure pulse generated (a) by a vapour bubble (thermal inkjet) or (b) from a piezoelectric transducer (piezoelectric inkjet) (From the ref. (5)).

Compared to continuous inkjet printing, the DOD printing mode is more efficient in using of ink because DOD inkjet systems print individual drops only when it is required (5). Prior to drops ejection, the printer nozzle can be manually positioned over any location on the substrate, above required landing place. In the beginning of the DOD process, fluid ink in a reservoir behind the printing nozzle is exposed to pressure pulse. Propagation of pressure pulse causes formation and ejection of an ink droplet through the nozzle. When printing is not required, pressure pulse is not applied. Consequently, liquid is not ejected and it is kept static by surface tension at the nozzle. The pressure pulse that promotes drop formation and ejection can be generated by two methods, either thermally or piezo-electrically (5).

In thermal DOD printing, a thin film heater is placed in the fluid reservoir (Fig. A3.1 (a)). The heater's temperature rises to about 300°C when current passes through it (4). As a consequence, the fluid ink which is in direct contact with a heater is heated to above its boiling temperature to form a vapour bubble. The formed vapour bubble rapidly collapses if current is not passing through the heater. The pressure pulse is formed by this rapid expansion and collapse of the vapour bubble (5).

In piezoelectric DOD inkjet printing, the pressure pulse is generated by deformation of a piezo-electric membrane (Fig. A3.1 (b)) (5). More precisely, voltage applied on the piezoelectric actuator causes sudden volume change which is forming the pressure pulse.

The pressure waves propagate throughout the capillary and in this way push fluid outwards, thus causing drop ejection (6). If the pressure pulse is sufficient and well-shaped, liquid can be ejected from the nozzle and a drop can be generated (7).

A3.1 Applications and related problems

Over the last two decades inkjet printing became one of the key technologies in the field of defined material deposition (3). In particular, it became a main technological approach in a number of manufacturing processes, such as micro-engineering, lubricants delivery to micromechanical parts or dispensing of UV-curable resins for the fabrication of micro-optical parts (4). Different inkjet printing modes support a variety of applications. Continuous inkjet printing allows for high speed printing. Therefore, it is widely used in industrial branches where speed is essential, like coding, marking and labelling (3). Nevertheless, drawbacks of this printing mode are: wasting of ink and inability to employ particle suspensions in volatile solvents which are very sensitive to even slight changes of concentration.

In contrast, major activities in nowadays inkjet printing are poised towards the DOD mode because of its numerous advantages (efficient ink using, smaller drop size, higher accuracy, and less restrictions on ink properties) (3). Thermal DOD printers are widely used as desktop or domestic printers, but they are not that often used for industrial applications. The main reason is the limitation of solvents which can be used. In other words, to create vapour bubbles necessary for thermal DOD printing, only fluids with a high vapour pressure under ambient conditions can be used (5). Therefore, thermal DOD is mostly restricted to water as a solvent. This, in turn, severely limits the number of polymers and solutes which can be used (3). Another crucial problem presents clogging of the nozzle by dried ink (4). In contrast, piezoelectric DOD technology is commonly used in industrial printers and it is subject of the majority of scientific studies (5). Popularity of this technology originates in the possibility to use a variety of solvents (3) and to control drop size and velocity (5).

Piezoelectric DOD inkjet printing already became a fabrication tool for a wide range of materials science applications, like in ceramic component manufacture (8), polymer electronic devices (3) or organic transistors (4). Inkjet printing of polymers and metal particles is particularly attractive due to growing research efforts into the development of plastic electronic devices. Major advantages of these devices are flexibility, low weight, easiness to process them and low manufacturing costs (6). Tunable electrical conductivity of such devices is essential for various applications. Conductivity of inkjet-printed structures is usually obtained by using ink solutions or suspensions containing conductive particles or polymers (9; 10). However, the inkjet printing process with such inks encounters numerous difficulties and we will mention in brief the most important ones.

The most crucial part of inkjet printing technology is probably the ink and its physical properties (11). In particular, the surface tension should be high enough to prevent dripping of the ink from the nozzle (3). The viscosity must also be sufficiently low to allow the channel to be refilled fast (4). Therefore, inks containing polymers and/or particles have to be in form of a dilute solution or a colloidal dispersion (4). Studies showed that the main factor that appears to affect printability of inks is their vapour pressure (not viscosity or surface tension) (6). The solvent volatility should be sufficiently low in order to avoid clogging of the print head nozzle (3). Given that inkjet printing is very susceptible to blockage due to solvent drying, printing of inks with rapidly evaporating solvents is considered as being essentially impossible (4).

An additional problem related to solvents appears during drying of a droplet. Namely, solvent evaporation induces flow formation in the droplet, hence controlling morphology of the dried droplet (Fig. A3.2) (10). Due to the surface tension gradient between the edge of the drop and its centre, the solvent evaporation proceeds faster at the droplet's edges. As a result, a convective flow is established from the centre toward the drying edge of the droplet (10). On the other hand, this surface tension gradient creates also an opposing Marangoni flow, which results in recirculation of the solvent in the droplet (10). These flows are not in balance. For that reason, inkjet printing frequently leads to the formation of ring stains, *i.e.* the familiar “coffee ring” effect. Some studies showed that the formation of ring stains can be eliminated by using a two-solvent system where one of the solvents has a much higher boiling point than the other (2). However, this might be problematic in general applications since both the choice and the exact ratio of solvents needs to be optimized for each particular system (6).

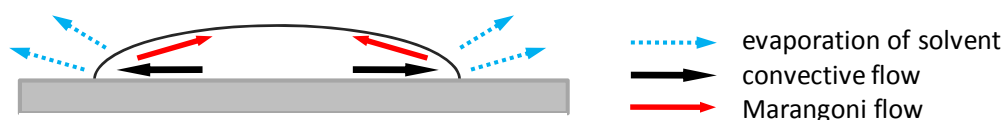


Figure A3.2: Flow directions in the drying droplet induced by solvent evaporation (From the ref. (2)).

Another problem concerning particle-based inks is related to particles size. In order to avoid particles' sedimentation particles size should be well below a micrometer (4). To obtain reliable jetting of the printing head and more stable particle dispersion, as small as possible particles have to be used. For instance, Kodak Research Labs reported that commercially available pigmented inks contain pigments with an average particle size in the range of 100–200 nm (12). Bigger particles lead to channel or nozzle clogging (12). On the other hand, when very small (<100 nm) particles are used, the maximum particle volume fraction is strictly limited to very low values due to the increase of viscosity (4). Therefore, the particles in the ink must be very well dispersed to avoid any agglomeration and aggregation that would additionally increase viscosity (4).

The processing temperature appears very often as a problem in inkjet printing whose aim is obtaining electrically conductive structures. In order to provide electrical conductivity of printed features, ink solutions containing various particles (usually metal nanoparticles) or organic conductive polymers have been used. It is also possible to form conductive structures by printing a solution of a metal precursor. This process is then followed by conversion of metal precursors to metal. This latter technological step, usually based on thermal treatment, is also the main challenge in printing metal-containing inks (6). Typically, the temperatures required for sintering can be higher than 500°C (4). The lowest sintering temperature of 200°C (for an hour) was reported for silver (13). Therefore, the sintering step is incompatible with printing structures on polymers or organic materials-containing substrates. Laser densification is possible, but it is often too slow for large area printing (4). For that reason, research in the field of conductive inkjet printing is focused on lowering the temperature needed to convert the metal precursor to metal, thus allowing for application of polymeric substrates (6).

In other words, the main goal of this field is to obtain conductive features on flexible polymeric substrates. Therefore, the thermal stability of the substrate has to be matched with the effective sintering temperature of the ink (6). Moreover, when metal nanoparticles are used for conductive inks, an additional problem appears due to the surface oxidation of metal particles. In principle, due to marked influence of surface oxides on conductivity, particles with the thinnest possible oxide layers are required. An additional difficulty stems from the prevention of post oxidation during post synthesis processes, such as ink preparation, printing and annealing during sintering (14). Oxidation stability could be in principle achieved by introducing shell layer around metal nanoparticles, but such layers are unstable under the elevated temperatures required for the sintering process (14).

In order to avoid the sintering problem, several strategies were tried. On the one hand, a polymer solution could be printed onto a solid substrate and then externally doped. On the other hand, a polymer could be printed onto a layer of a dopant to induce conductivity (4). The general drawback of these strategies consists of chemical treatment (like dipping or rinsing with aggressive solutions) which is usually incompatible with most of the substrates and processes (10).

All mentioned problems with metal containing inks or doped polymers can be overcome by using organic conductive polymers inks to obtain conductive structures. But, this may pose other problems. They are often unstable towards atmospheric moisture, intolerant for wide temperature range and they can be expensive due to the complex multi-step synthesis whose product is in the form of salt (what is reason for very limited solubility) (4). The best results with conductive polymers are obtained by surface-energy-assisted inkjet printing. This type of printing is based on the dewetting of solute-containing inks of a repulsive surface-energy barrier (15). The difficulties of this process are its high complexity and requirement for careful controlling of ink concentration and viscosity, surface-energy

contrast and the amount of deposited liquid (15). Moreover, the required temperatures were not favourable for some flexible substrates and supplementary solution needed to be used, which led to an inhomogeneous thickness and non uniform lines (6).

A3.2 Inkjet printing process optimization

In order to inkjet print CNTs-SU8 composite inks we needed to obtain at first drops at the nozzle tip. For inkjet inks other than standard inks, especially for nanoparticles loaded inks, the whole process of drop formation and impaction is particularly important since the ink's properties and behaviour are very different from usual inks (7). This process involves much more than simply ejection of liquid from the nozzle exit. The DOD drop formation process is significantly influenced by pulse properties (e.g. amplitude of the major pulse of driving signal), liquid properties (e.g. surface tension, viscosity, presence of additives), geometry of printing head (chamber and nozzle) and the interaction of liquid and the nozzle's walls (7).

Thus, due to the complexity of the whole process of the drop formation and impaction during DOD printing, we needed to optimize conditions for inkjet printing of CNTs-SU8 composites.

Ink

In order to prepare composite ink suitable for inkjetting we had first to choose appropriate ink components which could fulfil the requirements for successful inkjet printing.

One of the necessary conditions for inkjet inks is low viscosity (6). This is typically fulfilled by adding solvents in order to obtain a sufficiently diluted liquid. However, this cannot be applied in the case of nanoparticle loaded inks because suspensions are normally stable in a very narrow range of concentrations and conditions. Therefore, any change in concentration of components could significantly affect or even completely eliminate a good dispersion. This poses a serious problem for nanoparticle loaded inkjet inks, since such inks are generally very viscous. Our CNTs-SU8 composite inks undergo the same problems. In other words, we had very viscous inks whose properties varied rapidly with the concentration of components and therefore lowering inks' viscosity could not be achieved by simple dilution. Consequently, we had to find the other possible solution. Besides dilution, the other ways to lower ink viscosity are the choice of an appropriate solvent and heating of the nozzle.

The class of solvents which can be used for inkjet printing are restricted to low viscosity solvents. Therefore, water is used very often as solvent for inkjet inks (water

viscosity at 25°C is of 0.454 cp). Other frequently used solvents are organic ones, like chloroform, xylene or toluene, (9; 6) but they are highly toxic. Thus, we had to choose the SU8 solvent which has high solvency, low cost, low toxicity and low viscosity. Therefore, we chose GBL, having viscosity of 1.738 cp at 25°C. Note, that the GBL's viscosity markedly depends on temperature and drops to 0.951 cp already at 70°C (16). Therefore, we used the strategy to heat up the nozzle to 70°C, in order to sufficiently reduce the viscosity of the CNTs-SU8 composite inks to enable drops ejection. However, heating of ink was followed by so-called the "first drop problem" (FDP), caused by the evaporation of ink at the nozzle exit (7). Such ink evaporation can prevent stable printing or can even cause nozzle clogging. The FDP is considered as serious for inks whose properties vary rapidly with the concentration of suspended materials (7), like in our case. This is why we tried to avoid long lasting jetting interruptions. It is worth to mention that the drop formation process was not possible when nozzle was at the room temperature, even when voltage of 120 V was applied.

Another solvent's property crucial for the inkjet printing process is vapour pressure. Specifically, solvents with a very high vapour pressure are quickly evaporating leaving fillers' particles to block the printer's nozzle, so these solvents easily clog the nozzle. An additional problem which is usually caused by high vapour pressure is the appearance of the "donate" cross-section profile of printed droplets. When a droplet evaporates most of the solute is deposited as a perimeter ring. In such cases, uniform deposition could be obtained by using very low vapour pressure solvents (9). At this point, the second advantage of choosing GBL as a solvent for our composite would be its very low vapour pressure of only 0.3 mmHg at 25°C (17).

Upon choosing appropriate solvent for our polymer, we had to examine the filler. CNTs synthesised with an average length of ~10 micrometers cannot be used for inkjet printing because commonly used nozzles are up to 100 µm. Even in the cases when particle size becomes of the order of 1 µm, problems with inkjet printing start to occur and printability limit is usually reached (9). In order to meet this requirement we decided to work on printability limit by choosing CNTs with average length of 1 µm as filler in CNTs-SU8 composites 2C especially designed for inkjet printing applications. Using of CNTs much shorter than 1 µm would require very high CNTs concentration to obtain conductive structures. But, a higher concentration means higher viscosity and therefore a lower possibility for inkjet printing of such inks.

Applied voltage and the pulse shape

Due to above-mentioned disadvantages of the continuous and thermal DOD inkjet processes we decided to use the piezo-driven DOD mode for inkjet printing of CNTs-SU8 composites 2C.

At the beginning of inkjet printing we needed to optimize applied voltage what included the choice of maximal voltage and appropriate waveform. In fact, creating an appropriate pulse which provides stable drop ejection for a particular ink is regarded as critical know-how (5). For instance, even slight variations in a driving signal wave form may result in a significant change in the DOD drop formation (7). Studies have shown a significant effect of pulse voltage on droplet morphology, drop velocity, droplet breakup time from the nozzle and droplet size (10). It was demonstrated that higher voltage is required for inkjetting of more viscous particle loaded inks (18). This requirement is explained by Tsai *et al.* (18) in the following way. During the flow the particle interactions influence interparticle distances and consequently frictional forces and viscosity (19). Therefore, a lot of energy dissipates by suspended particles as the wave propagates in the printhead and flow during the droplet formation. As a result, a higher driving pulse voltage is required to extrude a liquid column and to form droplets for the particle suspension (18). This could be as well applicable for our CNTs-SU8 composites because of their high viscosity. Indeed, for our inks, stable condition with single droplet jetting was obtained for a maximum voltage of 80 V. At such a high voltage splitting up of the liquid column into two and formation of the main droplet and a satellite is typically observed in nanoparticle loaded inks (10). In the case of silver nanoparticles-loaded ink the occurrence of satellite formation was observed above 44 V (18). We did not observe such satellite drop formations. This can be explained by the presence of elongated tubular CNTs which increase ink viscosity. In this way, propagation of residue waves is eliminated and a stable printing process is obtained. The optimum operation range of the single droplet was only 1 V. This was not surprising, because a similar behaviour was observed for other nanoparticle loaded inks (10; 18).

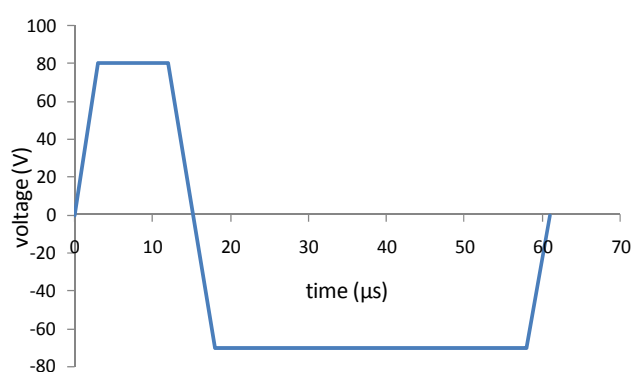


Figure A3.3: A schematic diagram of a biphasic trapezoidal pulse waveform used for stable inkjet printing of CNTs-SU8 composite inks (see the ref. [MM13]).

In order to obtain stable single drop printing conditions we used a customised waveform, which had a maximum voltage of 80 V and a pulse width of 61 μs . A schematic diagram of a typical bipolar pulse waveform employed in this study is shown in Figure A3.3. The biphasic trapezoidal pulse waveform was set to be 3 μs for rise time, 9 μs for dwell time

(first plateau in the diagram), 6 μs for fall time, 40 μs for echo time (the second plateau in the diagram), and 3 μs for final rise time. Initially, the voltage increases, causing the ink to retreat from the nozzle. The voltage subsequently decreases which causes ink to move towards and through the nozzle. In order to force our inks to move through the nozzle, we had to use pulse with rather large width of 61 μs . Such large width of the pulse was obtained by extension of the echo time, which is typically of few microseconds in standard inkjet printing conditions. In fact, the echo time was set to such a high value in order to push ink forward through the nozzle. This necessity appeared due to the high viscosity of inks and elongated shape of fillers in our inks. These are as well the reasons for the very high maximal voltage used because the voltage magnitude must be adequate to generate droplet ejection. In fact, droplet ejection and formation are quite complex processes. The key issues which influence droplet formation and resultant morphology are solvent choice and polymer or/and additive concentration (6). They have to be optimized, because above a certain concentration of polymers or/and additives, the capillary force is not able to break the filament and to overcome the decelerating action of ambient air, so the ejected droplet retracts back into the nozzle (6). We faced the problem of the droplet retraction for the maximal voltage values below 80 V and for pulses shorter than 61 μs . However, when excessive waveform voltages, like 80 V, are used drop ejection becomes chaotic. Since the liquid drips from the printhead due to gravity, a back pressure of 9.65 Pa was applied using the pneumatic console to control ejection of the liquid. In the same way we could control the liquid level near the orifice and prevent the CNTs-SU8 ink meniscus from wetting the nozzle.

Wetting of the nozzle surface

Wetting the surface of the nozzle by ink is a typical problem when nanoparticles-loaded inkjet inks are used (10). Namely, good dispersion without particle aggregation is very difficult to obtain for most of the particles and macromolecules. Their suspensions are likely to be unstable in most solvents. Hence, chemical functionalisation of particles or adding of stabilizers are required. The use of surfactants, however, frequently causes wetting the faceplate around the nozzle by ink (4). This can prevent the formation of a stable droplet stream due to the presence of residual liquid on the nozzle plate (Fig. A3.4 (a)). For standard inkjet inks, the liquid column broke up into a liquid droplet at the exit of the nozzle (Fig. A3.4 (b)). However, for the nanoparticle suspension the particles often adhere on the nozzle plate in form of a residual liquid layer. When the next liquid column extrude, the residual liquid layer cannot be extracted back to the liquid column. Therefore, the separation of the liquid column occurs below the nozzle (Fig. A3.4 (c)) and the separation time from the nozzle is prolonged (18). The unwanted residual liquid is formed because of local wetting around the nozzle exit (18). Since our composite inks contain surfactant, it was likely that we could face the common problem of nozzle wetting. As

expected, during the printing process, wetting of the jetted liquid on the surface of the nozzle around the orifice could be observed. This ink flow on the nozzle plate of inkjet printhead was extensively studied (18; 20). The origin of such behaviour was found to be the actuation of the piezoelectric printhead (20) in addition to the presence of the surfactant in inkjet ink (4).

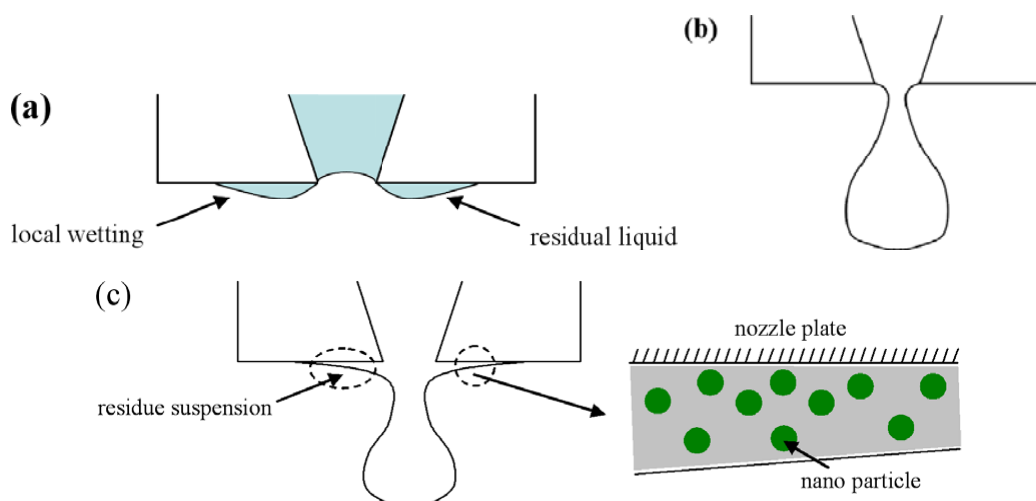


Figure A3.4: (a) A schematic illustration of the residual liquid layer due to the local wetting of the jetted liquid on the nozzle plate. (b) A schematic illustration of a liquid column breaking up at the nozzle if ink does not contain nanoparticles. (c) A schematic illustration of the liquid column of the nanoparticles suspension breaking up below the nozzle (From the ref. (18)).

Besides standard expected symmetrical wetting of the nozzle faceplate, asymmetrical wetting often appeared (Fig. A3.5 (a)). At first, this could be attributed to printing under ambient conditions in the box with one open side, what could induce air flow. Actually, asymmetrical wetting was usually on the same side of the nozzle (opposite to the open side of the printing box) indicating strong influence of ambient conditions on printing possibilities. Some studies have shown that even the air flow induced by the jet itself can cause lateral deviations of horizontal moving droplets (20). We could observe the same behaviour when the printing box was closed from all sides. In that case ambient flow could be excluded as a reason for deviations in droplet trajectory (Fig. A3.5 (b)). Stable drops were formed even under the condition of asymmetric wetting of nozzle faceplate (Fig. A3.5 (c) and (d)). In our case, the control of ambient conditions in combination with the choice of appropriate back pressure (9.65 Pa) enabled us to prevent wetting of the nozzle surface by the CNTs-SU8 ink meniscus. In this way we could obtain stable droplet ejection without deviations in droplet trajectory and without wetting of the nozzle (Fig. A3.5 (e) and (f)).

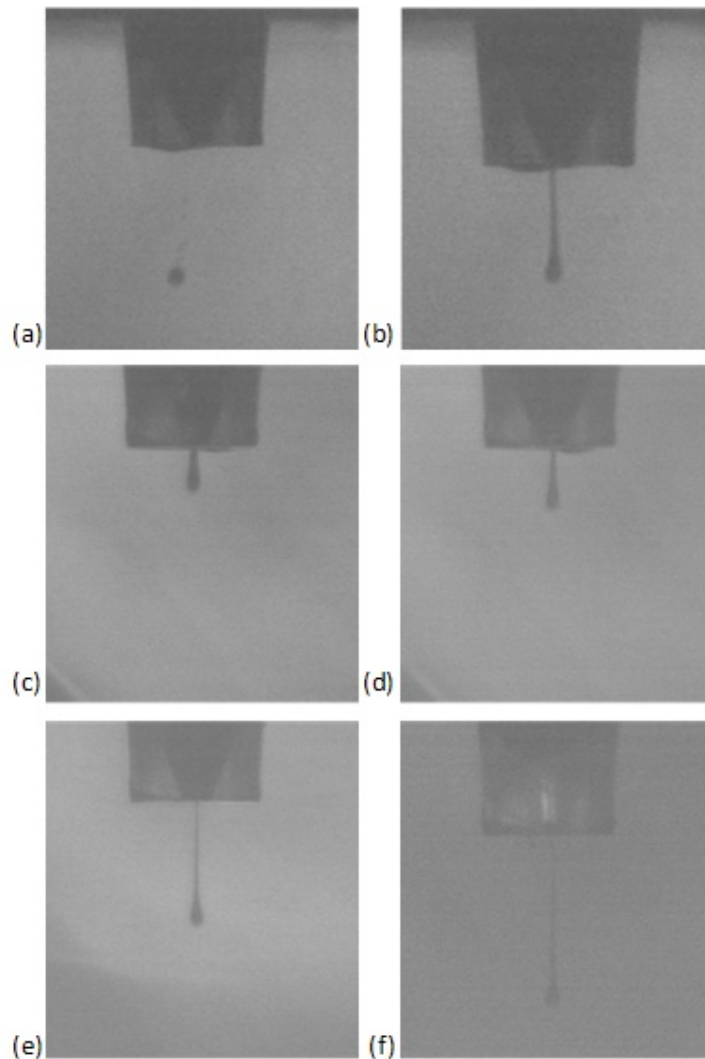


Figure A3.5: Stroboscopic image of CNT-SU8 droplet being ejected from the 80 μm diameter inkjet nozzle: a) and b) drop deviations from the vertical trajectory when ink locally wetting the nozzle faceplate; stable drop formation: (c) and (d) even under the asymmetric wetting and (e) and (f) when wetting of nozzle faceplate was prevented by choice of appropriate back pressure and by controlled ambient conditions (see the ref. [MM13]).

Drop formation

In general, the drop formation process consists of pushing the liquid out of nozzle, necking of the liquid column near the nozzle until the surface tension cannot longer sustain the liquid column. At the end, the free liquid column contracted to form microdroplets. If inkjet ink contains polymers or macromolecules, this process is influenced by their molecular weight, their concentration and structure (6). In fact, polymer segment length, which is directly related to molecular weight and, hence, viscosity, has a critical impact on ink flow properties in inkjet printing (10). The most common fluid behaviour during the

inkjet printing of polymer and macromolecule solutions is non-Newtonian. Typically, a droplet of solution remains attached to the nozzle by an elongating filament (6). This often encountered behaviour is additionally influenced by the shape of the polymers and additives. For instance, elongated linear shape of molecules gives rise to substantially long filaments (6). For all these reasons, during drop formation of the nano-suspension inks, the liquid column broke up far away below the nozzle (18). This behaviour of polymer and macromolecule solutions is attributed to the elastic stresses associated with extensional flow in the nozzle (6). Due to the commonly present particle interaction, the nano-suspension inks favour to expand more in the axial direction than the radial direction. Since the nanoparticle suspensions usually have a relatively low surface tension, relatively small energy it required to form the extra surface. Consequently, particle interactions can be considered as responsible for the formation of the long and thin liquid column (18). Our composite inks contains SU8 polymer which is a very rigid high molecular weight molecule and CNTs which are elongated linear macromolecules with very high aspect ratio. Therefore, we could suppose that elongating filaments can appear during inkjetting of our inks. As expected, a considerably long filament was following each droplet formation (Fig. A3.5 (e) and (f)).

The drop formation process is followed by impaction on the substrate surface. The impaction of a liquid drop on a solid surface is controlled by numerous physical processes and can be driven by inertial forces, capillary forces and gravitational forces (5). The initial impact stage is governed by kinematic behaviour followed by impact-driven spreading, recoil and oscillation. The surface tension forces and the capillary forces become more important in controlling behaviour during spreading. The viscous forces damp the spreading and oscillations until the system approaches true equilibrium (5). Furthermore, drop volume and velocity in impacting can be significantly influenced by acoustic resonances from the fluid-filled chambers used to generate drops (5). Therefore, the shape and amplitude of the actuating pulse can also in this way considerably influence printing behaviour.

The impaction of a liquid drop on a substrate

The impaction of a liquid drop on a substrate and the spreading of the printed drop strongly depend on the wettability of the substrate and the interaction of ink components and the material of the substrate surface (10). In general, wetting is the ability of a liquid to establish contact with a solid substrate surface. In order to obtain good coating uniformity, the coating liquid must to wet well the substrate surface and to spread uniformly. Wettability or spreading of a liquid over a flat rigid solid surface is determined by the interaction of the cohesive and adhesive forces as described by Young in 1805 (21). The cohesive or adhesive forces are attractive intermolecular forces between like or unlike molecules, respectively. Wetting of the solid surface by a liquid takes place if the adhesive forces at the liquid-solid interface are stronger than the cohesive forces. This would mean

that the molecules of the liquid have a stronger attraction toward the molecules of the solid surface than toward each other. Otherwise, if the cohesive forces are stronger than the adhesive forces, that is to say the liquid molecules are more strongly attracted toward each other than toward the molecules of the solid surface, the wetting of the solid surface does not occur (21).

One of the methods to quantify wettability of certain solid surface by certain liquid is to measure contact angle θ at the point of interface of three phases: liquid, solid and gas (Fig. A3.6 (a)) (22). Then contact angle correspond to the angle between solid surface and the tangent line on the liquid-gas interfacial line in the point of three phase contact. The contact angle is always measured from the liquid side and can have value from 0° to 180° . Generally, a liquid wet the solid surface if the contact angle has value less than 90° and such liquids are termed hydrophilic. Otherwise, liquids are hydrophobic for the contact angles higher than 90° . Examples of good wetting liquid and poor wetting liquid are given in Figure A3.6 (b) and (c), respectively (23).

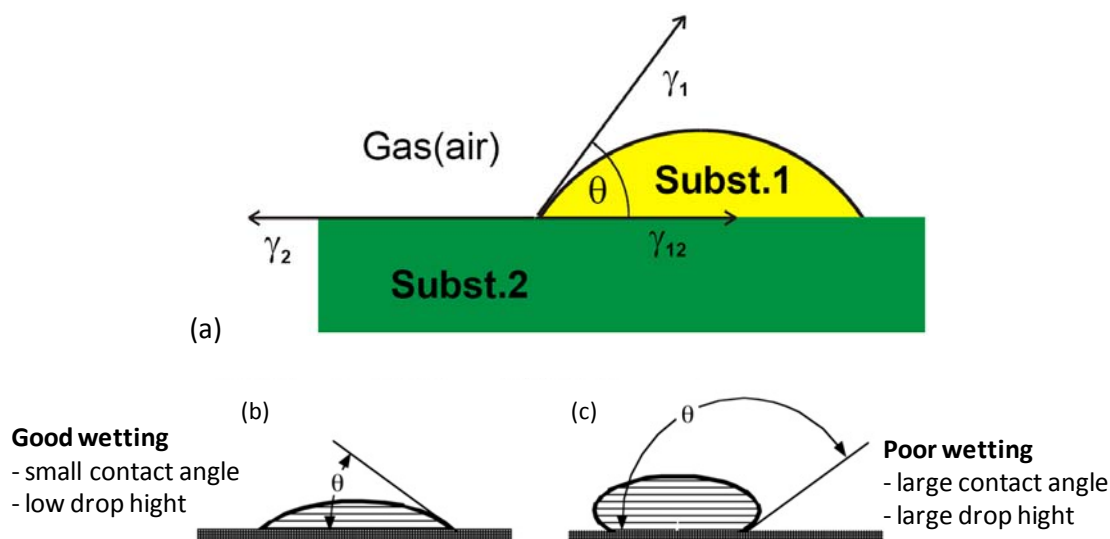


Figure A3.6: (a) Contact angle, θ , of a liquid droplet of substance 1 wetting a flat rigid solid surface of substance 2. (b) Generalised example of good and (c) poor wetting (From the ref. (23; 24)).

In fact, contact angle examine from the qualitative point of view provides information of the interfacial energies between phases. Due to the presence of three phases, three interfacial energies have to be taken into account: liquid-gas interfacial energy γ_1 (i.e. surface tension of liquid, that is force involved in stretching the liquid interface for the unit length), solid-gas interfacial energy γ_2 (usually termed surface energy, that is work involved in increasing the surface by the unit area) and solid-liquid interfacial energy γ_{12} (Fig. A3.6 (a)). The relation between these energies and the contact angle is defined by Young's equation:

$$\gamma_2 = \gamma_{12} + \gamma_1 \cos \theta \quad (\text{A3.1})$$

In this sense, the good wetting requirement to have contact angle lower than 90° can be understood as requirement that the force to the right in Figure A3.6 (a) (the surface tension or the surface energy of the solid) should exceed the sum of forces to the left, the solid–liquid interfacial tension plus the liquid surface tension times the cosine of the contact angle (23).

In order to quantitatively relate contact angle with the adhesion (24), we can first describe work of cohesion of a single substance in the terms of interfacial energies defined according to Dupré as (Fig. A3.7):

$$W_{11} = \gamma_1 + \gamma_1 - 0 = 2 \gamma_1 \quad (\text{A3.2})$$

In the same way, the work of adhesion between two substances is (Fig. A3.8):

$$W_{12} = \gamma_1 + \gamma_2 - \gamma_{12} \quad (\text{A3.3})$$

Substituting equation (A3.1) into equation (A3.3) one can obtain the Young - Dupré equation (22):

$$W_{12} = \gamma_1 (1 + \cos \theta) \quad (\text{A3.4})$$

Zisman (25) used this relation and studied wetting of various liquids on the one solid surface. Resulting “Zisman plot” presents $\cos \theta$ as a liner function of the surface tension of liquids. Consequence of this empirically found connection is that different liquids with the same contact angles on the same solid substrate have the same surface tension γ_1 .

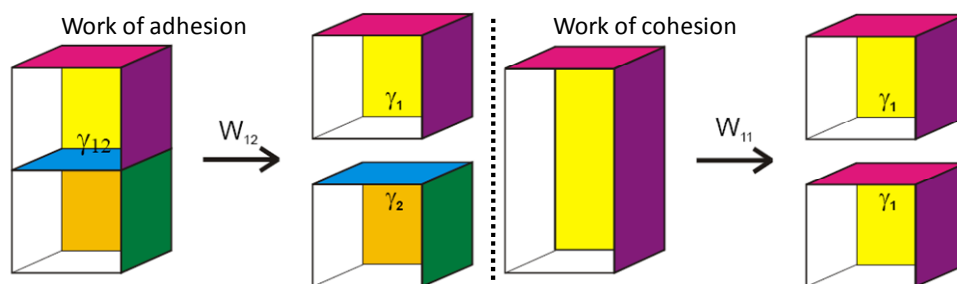


Figure A3.7: Schematic representation of work of adhesion and cohesion (From the ref. (24)).

In order to obtain information on wettability of our inks, upon obtaining stable droplet ejection we measured a contact angle of CNTs-SU8 composite inks on the glass substrate. Particular importance was devoted to substrate cleaning, because some studies showed a significant influence of surface cleaning techniques on the contact angle behaviour (26). First, we measured the contact angle of the SU8 solution with the same concentration of photo-initiator, surfactant and SU8 in GBL like in CNTs-SU8 composite inks. In that case, the equilibrium contact angle measured on the glass slide was $(49.4 \pm 1.7)^\circ$, which was then used as a reference for the other contact angle measurement. Afterwards we measured the contact angles for the CNTs-SU8 composite inks with four different CNTs

concentrations: 0.4, 0.8, 1.2 and 1.6 wt% of CNTs in SU8. Figure A3.8 shows optical microscopy images of the representative contact angles of CNTs-SU8 composite drops on the previously cleaned glass slide surface. Almost no difference was observed between the samples. Therefore, we could consider the contact angle of CNTs-SU8 composites inks as constant and independent of CNTs concentration. This can be interpreted in the framework of the already mentioned Zisman's plot.

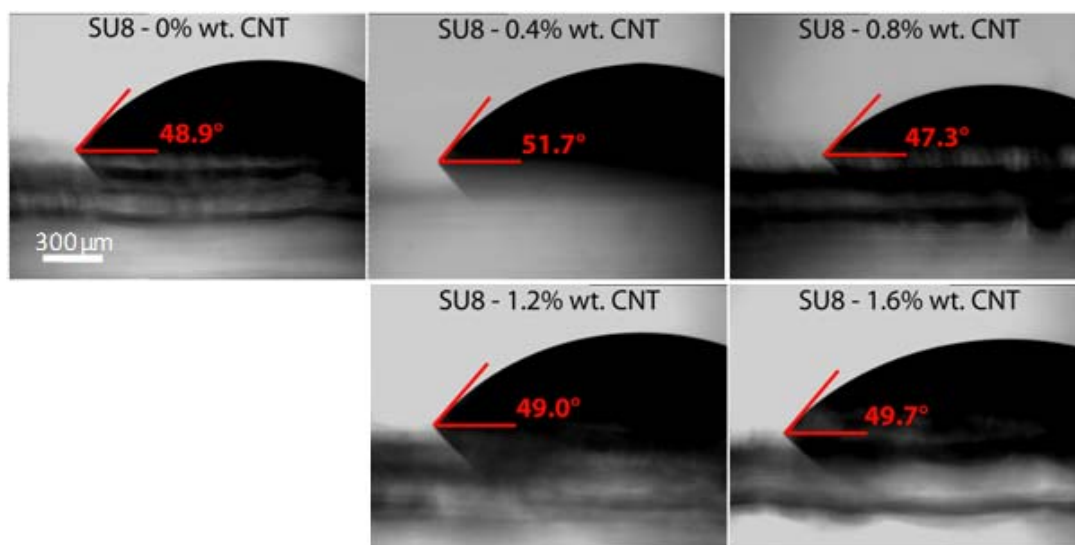


Figure A3.8: Optical microscope images of the contact angles of CNTs-SU8 composites. CNTs concentration of each sample is indicated above the drop on each image (see the ref. [MM13]).

Taking into account that all CNTs-SU8 composite inks have almost the same value of contact angle on the glass slide substrate we can conclude that they all have the same surface tension. That would mean that the surface tension of composite inks is independent of the CNTs concentration. This can be understood by comparing the composites' contact angles with the value of contact angle for the SU8 formulation without CNTs. All these values are the same indicating partial SU8 rich phase separation on the air side (i.e. the side of the drop in the contact with air), that is to say partial CNTs rich phase separation on the glass side (i.e. the side of the drop in the contact with the glass substrate). Observed behaviour pointed out a distinctive compositional modification of the external layers of the drops. This kind of phenomenon is typical for polymer and surfactant containing solutions. In fact, polymers and surfactants are usually absorbed on the solid/liquid (and/or on the liquid/gas) interface governed by the difference in their surface tensions (22). Even from the seminal work of Gibbs it is known the reduction in surface tension in polymer solution is caused by the polymer adsorption to the surface (27).

We can examine our system from the perspective of surface tensions. Firstly, our glass substrate is considered as a relatively high energy substrate because of its surface tension of $\sim 1 \text{ J/m}^2$ (28). In contrast, all the CNTs-SU8 composites' components have surface

tension of the same order of magnitude, being two orders of magnitude lower than that of glass. The corresponding surface tensions are: $\sim 47 \text{ mJ/m}^2$ for epoxy resins (28), $27.04 - 45.3 \text{ mJ/m}^2$ for CVD MWCNTs (29; 30), and $35.4 - 43.44 \text{ mJ/m}^2$ for GBL (31; 16). Due to the relatively similar values for the surface tensions of ink components (compared to the surface tension value for the glass substrate), there should not be an ink component with the dominant surface tension, capable of driving the phase separation. Therefore, the most probable phase separation would occur for these two components: CNTs and SU8 molecules. Clearly, even if there is no considerable difference in the surface tensions of these components, there is certainly a significant difference in their molecular size. This might govern the surface activity of SU8, thus allowing for easier surface migration of the smaller SU8 macromolecule in the liquid state of the composite. Therefore, after cross-linking and solidification, the previously occurred surface segregation might become permanent. This leads to increased SU8 content on the air side surface of the final composite films. In the same time, longer molecular structures with high aspect ratio, like CNTs, are usually associated with the reduced mobility and higher propensity to self organisation (32). Actually, the latter tendency often leads to a partial or full phase separation of CNTs. As a result, the selective migration of the SU8 toward the air interface allowed us to keep the same properties of the pure resin on the outer side of printed composite inks. This fact is very important from the point of view of applications, because coating lines are usually designed and optimized for a particular substrate. Our finding enabled us to print CNTs-SU8 composite inks on all type of substrates commonly used for SU8 ink without any substrate modifications. Therefore, our CNTs-SU8 composite inks can be used in all inkjet processes, like standard SU8, without the need to physically or chemically modify the surface of the substrate. This represents a great advantage for future applications of our composites, since they can be easily integrated in existing processes.

The next step in the inkjet printing process was the achievement of patterns formed from directional and controlled drop arrangement. Therefore, in order to print collections of single droplets and lines, substrate was continuously moved under the fixed inkjet head. This allowed successful printing of single droplet groups with a very well defined droplet size and spacing. An example is shown in Figure 6.14 (a) in Chapter 6.

The reproducibility of the inkjet-printed drops strongly depends on the reproducibility of the drop impaction and formation processes (7). Due to the obvious complexity and impossibility to fully control the influence of all process parameters, the successful printing reproducibility is achieved in practice by establishing satisfactory experimental printing conditions (7). In this manner, we achieved a number of inkjet-printed single droplets with very good reproducibility. In particular, we could obtain a group of single droplets which were extending over relatively long distances. Moreover, we could observe that these single droplets were perfectly aligned along one direction. An example of such printing over the length of more than a millimetre is shown in Figure A3.9.

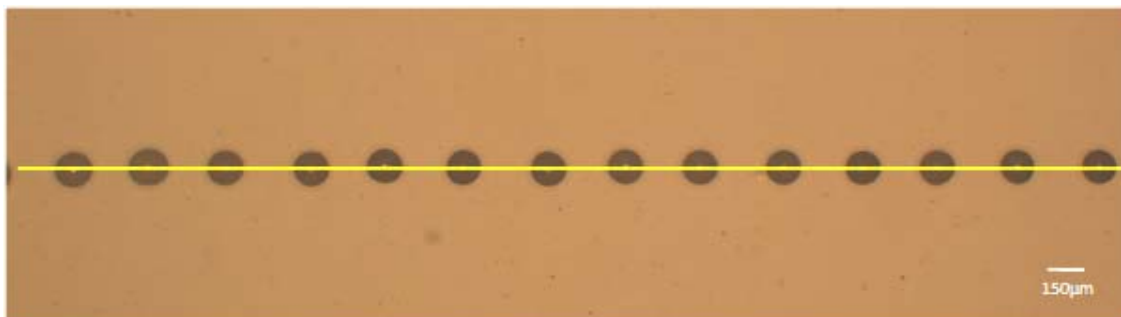


Figure A3.9: Optical microscope image of inkjet-printed collections of single droplets with very good control of printing direction over a half millimetre length. Yellow line passing through the centres of printed droplets indicating their uniform alignment.

Another factor which affects the reproducibility of the drop impaction process is the flatness of the substrate. Since the substrate is moved to provide a fresh surface, the substrate's vertical coordinate varies within the space where the drop impacts (7). Additionally, reproducibility can be affected by the substrate wettability. The inkjet printing process is often not totally reproducible because the wettability of substrates varies from impact to impact (7). Therefore, variations of the substrate's vertical position and of the wettability of the substrate could affect printing reproducibility. This was observed in rare cases during inkjet printing of our CNTs-SU8 composites, like the one shown in Figure A3.10 (a). Even still rarer, we could observe satellite drops beside the main drop on the substrate (Fig. A3.10 (b)). This was surprising because no satellite drops were visible during the drop formation and falling. In addition, the diameter of satellite drop was notably smaller than the diameter of the main drop. Consequently, we assume that impaction on the substrate surface was responsible for the small satellite drop formation and not the usual splitting of the liquid column.

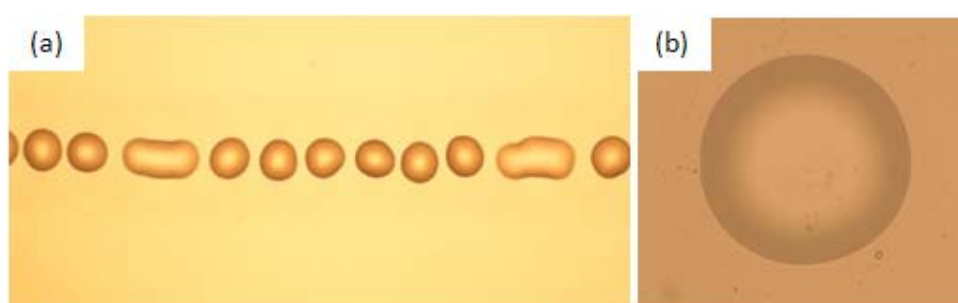


Figure A3.10: Optical microscope images of inkjetted droplets (the droplet diameter is of 150 µm) show: a) irregularities in the droplets' shape and deviation from the directional printing in the collections of single droplets and b) satellite drop formed beside the main drop.

During stage movement, the droplet spacing was controlled by print frequency. Lower frequencies lead to lower droplet ejection rate. This enables better drop positioning, but result in a decrease of production efficiency. However, operating piezoelectric DOD printheads at high frequencies result in chaotic droplet ejection. The reason for this ejection

is an interaction of earlier pressure waves which have not decayed completely, with the next generated pressure waves (6). The decay time of residual waves depends on ink's composition and in this way on ink viscosity (6). Inks with higher viscosity have a greater damping effect (6). Therefore, due to the high viscosity of our CNTs-SU8 composite inks, we expected that chaotic droplet ejection at high frequencies can be suppressed. Indeed, inkjet printing of our inks was stable at high frequencies up to 200 Hz, as well as at low frequencies from 1 – 10 Hz. However, in some cases in DOD systems resonances within the chamber behind the nozzle are observed (5). These resonances strongly influence pressure pulse propagation and drop generation (5). We did not notice such a resonance.

Upon obtaining very well controlled collections of single droplets we aimed to print lines. Inkjet printing of thin lines is limited by the size of the drop (10). Intuitively smaller nozzle would promote formation of the smaller droplets. But smaller nozzles have tendency to clog easier, thereby reducing the reliability and repeatability of the jetting process (10). This is especially the case if inkjet ink contains suspended particles. Both experimental and theoretical investigations have shown that droplet size does not depend only on the printhead's nozzle diameter (6). In fact, drop size additionally depends on jetting conditions (e.g. driving voltage), ink (e.g. viscosity), surface energy of the substrate and printhead geometry (e.g. the length of the fluid cavity) (10; 6). The major influence on drop size has definitely the process of DOD drop formation which has even recently been termed "black magic" (7). In reality, general rules which would relate the optimal operating performance with driving signal, liquid properties and printhead geometry are not available. Currently, finding satisfactory working conditions is a trial-and-error process (7), even though considerable research has been performed into understanding how the droplet ejection process works and how to tailor droplet size (6). As previously mentioned, the droplet forms from an initial liquid column, that thins to define a leading droplet and the elongated tail. The rupture of the elongated tail can lead to the formation of satellite drops. These drops may catch up and merge with the leading drop in flight. To facilitate drop merging in flight and to avoid satellite drops formation, it is usual to print at a stand-off distance from the substrate which is typically 2–3 mm. This can considerably influence drop placement accuracy because drag from air currents in the printing environment can deviate drops from their desired trajectory (5). To minimize this effect, the stand-off distance was set at the minimum value of 0.5 mm.

The process of line formation by inkjet printing typically passes through following phases. If the drops are inkjet-printed at large values of drop spacing, where no overlap of the spread drop footprint occurs, a train of discrete droplets can be observed (Fig. A3.11 (a) and (e)). If the spacing between the printed drops is slightly smaller than the diameter of the footprint, drop coalescence can be observed, but the resulting liquid line does not show parallel sides (Fig. A3.11 (b)). At slightly smaller deposited drop spacing, a stable liquid line with smooth parallel sides can be found (Fig. A3.11 (c) and (f)). At final stage when the drop spacing is too small, bulging instability occurs (Fig. A3.11 (d) and (g)) (5). As we can see in

Figure A3.11 (from (e) to (f)), line printing with our CNTs-SU8 composite inks went through the characteristic phases of inkjet lines formation.

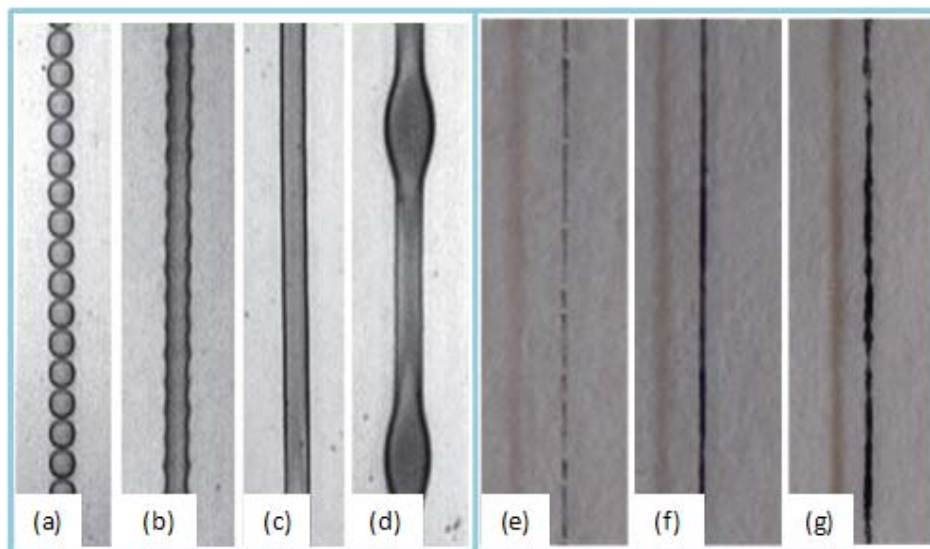


Figure A3.11: From (a) to (d) is shown typical way how a liquid line can form when a row of spread drops coalesce (From the ref. (5)). From (e) to (g) our printed lines are shown. (a) and (e) Drop spacing is too large for drop coalescence. (b) Initial coalescence leads to a line with a periodic irregularity. (c) and (f) After a sufficient overlap a parallel-sided line occurs. (d) and (g) If drop spacing is too small, a bulging instability forms.

Inkjet printing of drops or lines which starts with stable drop ejection followed by the liquid drop impact on a substrate, ending with phase change which transforms the liquid into solid. This phase change generates the final desired product. The mechanisms of solid formation through evaporation from a solution are of particular importance, especially for inkjet printing of nanoparticle suspensions in order to obtain conducting and semiconducting structures (5). Namely, the shape of a printed drop can be strongly influenced by solute distribution during drying through the well-known coffee stain effect, when solute strongly segregates to the initial contact line (5). In brief, the rate of solvent evaporation is higher toward the contact line because of an easy vapour transport in the surrounding “dry” substrate (33). Therefore, precipitation occurs first at the contact line and fluid flow occurs from the centre of the drop to replace the evaporating fluid from close to the contact line (33). This peripheral flow continuously feeds the solidification at the contact line, and the final deposit will show a characteristic ring where the solute has segregated during the drying process (33). This phenomenon of an unequal distribution of dried solute called coffee staining is often reported for inkjet printing of polymers and macromolecules loaded inks. Moreover coffee staining is considered as a typical problem of printing on unmodified substrates (6). Some studies have shown that for inks which display coffee staining after printing on a low-temperature substrate, the staining effect could be eliminated by a higher-temperature substrate, even though evaporation of solute occurred at a greater rate (5). Therefore, to print onto a heated substrate is considered as a strategy

to minimize or eliminate the coffee staining effect. However, this approach only works for certain systems and it runs the risk of causing nozzles to clog as a result of radiant heat arising from the substrate (6).

Considering that we print nanoparticle loaded polymer suspension onto an unmodified substrate, we needed to prevent the very probable appearance of the coffee staining effect. Additionally, we had to take into account that our nanoparticles are CNTs with all their specificities. In that sense, quite useful was research of Song et al. who studied morphology of inkjet-printed CNTs as a function of drying conditions. Namely, SWCNTs of 5nm diameter and 10 μ m length, dispersed in dimethylformamide were inkjet-printed on substrates with various drying conditions. It was shown that faster drying (60 °C vs. room temperature) enabled a more even density distribution of the CNTs (34). Consequently, we used the strategy of printing onto a heated substrate. In order to print lines, the stage with substrate was heated up to 100°C. With this approach we could successfully obtain a straight line (Fig. A3.12 (a)). The pattern resolution is limited by the extent to which a liquid drop spreads on a substrate and how spreading changes with the overlap of adjacent drops to form continuous features (5). In fact, the side alignment, resolution and accuracy of printed lines are strongly affected by the interactions between individual drops and the substrate as well as between adjacent drops (5). These interactions can be influenced and even tuned in the desired direction by temperature. Heating of the substrate enhanced solvent evaporation and additionally prevented axial liquid transport along the line, which resulted in the rare formation of beads (Fig. A3.12 (b)). Sporadic beads formation could be also caused by jetting conditions and properties of the ambient which affect falling of the drops (10).

Droplet volume reduction and phase separation

The transition from a liquid ink to the final desired solid material in the final step of the printing process is almost always accompanied by a reduction in volume (5). In the cases when solidification occurs by solute evaporation, the volume change can be considerable because only low viscosity inks, that would mean only dilute solutions of polymers and low volumes of particles in suspension, are normally inkjet printable (5). Volume change in general, in particular drastic volume change, can strongly affect final morphology of printed structures. This volume change can even completely deform printed features. Taking into account that in our inks solvent content is always more than half of the volume, volume shrinkage due to solvent evaporation during solidification must be significant. Indeed, we could notice surface structuring of printed lines which appeared after solidification by solvent evaporation (Fig. A3.12 (c)). In fact, such behaviour is also observed in other inkjet inks. Actually, Singh et al. studied the drying conditions of nanoparticle loaded ink droplets and morphological properties of films in order to determine the critical drying temperature for optimal film formation (10). It was found that by increasing the drying temperature, film

formation changed from hill-like to ring profile resulting in poor film quality. It appeared that the parameter which has the strongest impact on the critical drying temperature is the volume of the drop (10). In fact, the critical drying temperature increases with volume increase. Our results are in agreement with these studies.

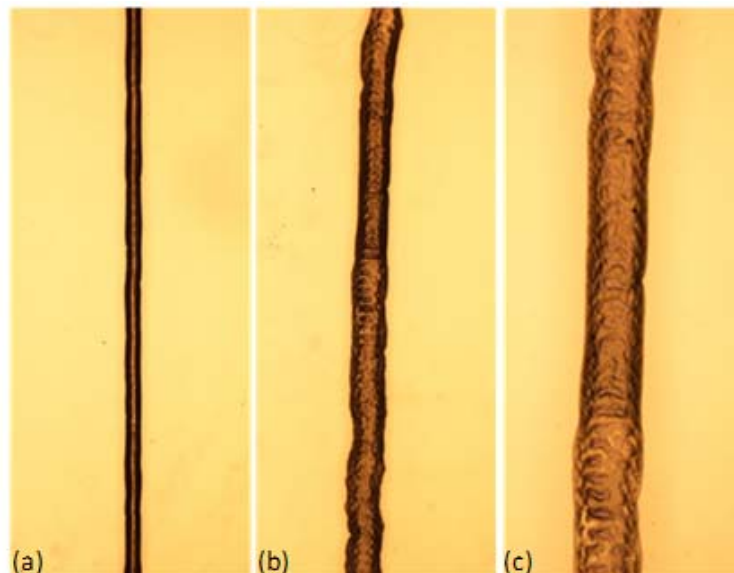


Figure A3.12: Optical microscope images of inkjet-printed linear patterns on the substrate preheated to 100°C. Most of the printed lines were straight even after drying (a), but rare deviations and bead formations could be observed as well (b). A closer look on the line's surface (c) showed clear signatures of volume-shrinkage-induced surface deviations. The line width was 130 μm . Droplet spacing was set at 200 μm .

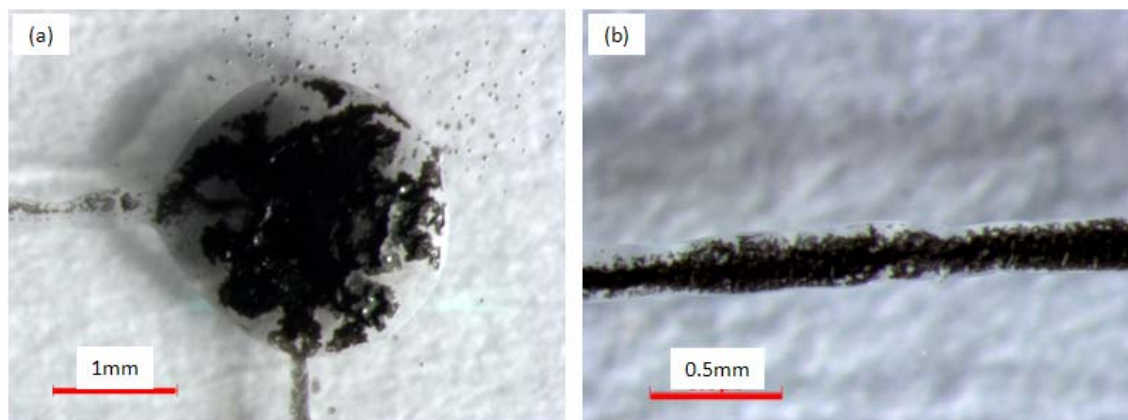


Figure A3.13: Phase separation of CNTs and SU8 could be noticed on inkjet-printed objects of large size after solidification by solvent evaporation.

Since solidification of inkjet-printed ink occurs after deposition, the printed pattern must remain stable in the liquid state prior to solidification (5). Moreover, the increased likelihood for phase separation of nanoparticles is the reason why they behave differently from polymers during printing (10). For instance, in some cases larger particles can pack

closer to the centre of the droplet when the contact angle is high, while smaller particles under the same conditions can migrate closer to the contact line at the edge of the droplet (10). This kind of packing of nanoparticles strongly depends on lots of parameters, like nature of the substrate and particle surface, ambient conditions or process temperature (10). Moreover, capillary forces can be considerable during the drying of nanoparticle suspensions. Particularly, it was shown that CNTs are strongly affected by fluid flows within drying drops that are causing CNTs phase separation (5). CNTs in our study undergo the same type of behaviour (Fig. A3.13). Namely, phase separation of CNTs and SU8 could be noticed on inkjet-printed lines after the solidification process through solvent evaporation.

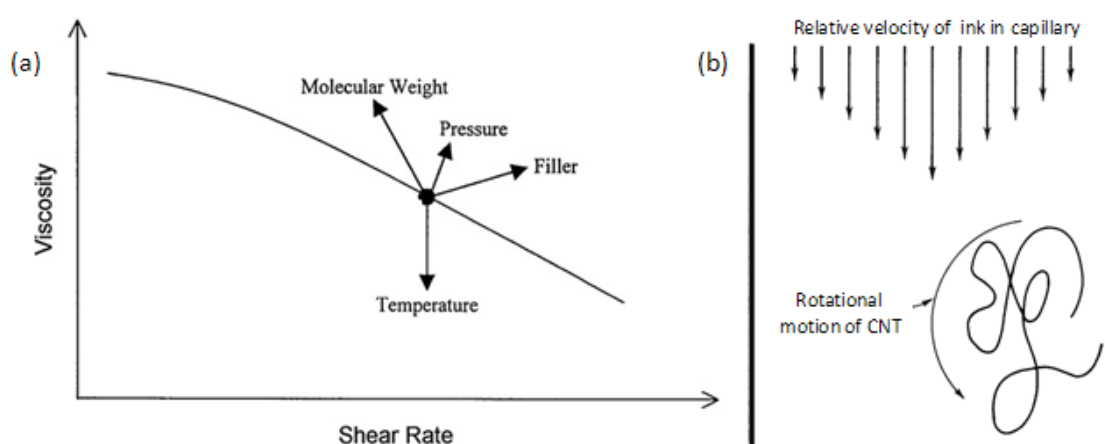


Figure A3.14: (a) Schematic presentation of general influence of various parameters on polymer solution viscosity and shear rate (From the ref. (23)). (b) The effect of velocity (and shear rates) gradient on CNTs chain rotation (adopted from the ref. (35)).

The origin of this partial CNTs phase separation can be in numerous possible processes which are part of overall inkjet printing process. The most probable one is related to the fluid flow in the inkjet tube before drops are ejected. Generally, in the case of unidirectional flows of solution in the capillary tube, the flow rate is different depending on the distance from the edge of the capillary. Consequently the shear rate and the shear stress are also changing over the perpendicular cross section of the capillary tube. Commonly, velocity profile of a liquid in a capillary is in the shape previously shown in the Figure A2.3 in Appendix 2. Situation becomes much more complicated in the presence of polymer molecules, surface active agents and additives or fillers. For instance, surfactants often change interaction of liquid with the capillary walls. The effects of factors such molecular weight, pressure, filler and temperature on viscosity related to shear rate are summarized in Figure A3.14 (a). Naturally, increase of temperature decreases both viscosity and shear rate. On the other hand, polymer molecule with high molecular weight, high pressure or presence of the filler can significantly increase viscosity and shear rate. Our CNTs-SU8 composite inks are exposed to all listed parameters which result in increase of shear rate. This is greatly affecting properties of inkjetted inks, mainly because any finite size object in the capillary tube would “see” a different shear rate in its different parts (Fig.

A3.14 (b)). Presence of shear rate gradient results in an increase in the frictional drag and rotational forces on the molecule. This would more affect bigger size objects, especially flexible fibrous ones with high aspect ratio, like CNTs. In this way, CNTs in tube exposed to the frictional drag and rotational forces are becoming more and more entangled by passing through the capillary tube of usually macroscopic length (more than few centimetres). Overall process yield in pronounced CNTs entanglement, aggregation and very probable phase separation towards middle zone of the cross section of the capillary tube (23; 35).

Furthermore, phase separation could also appear due to other process conditions. For instance, when the droplet hits the substrate, it expands with an accompanying swift fluid flow, which is radially outwards, and in the end the fluid comes to rest after an initial rebound and a series of inertial oscillations that are dampened by viscous dissipation (6). This rebounding and oscillations of the liquid on the substrate can induce phase separation in nanoparticle suspensions. Another reason for observed phase separation could lie in possible traces of acetone. To be precise, before and after use, inkjet nozzles were cleaned in an ultrasonic bath while filtered acetone was aspirated through the nozzle. Before using, the inkjet nozzle was dried by passing a constant stream of filtered air through it from the pneumatic console. If there were any traces of acetone remaining in the system tubes, this would strongly destabilize our composite inducing phase separation.

A3.3 Conclusions

All inkjet printing processing steps and its parameters were optimised to yield patterned composite films with tuneable transparency, flexibility, electrical conductivity and mechanical properties.

References

1. *Marangoni Effects in the Spreading of Liquid Mixtures on a Solid*. **D. Pesach and A. Marmur**. 3, 1987, *Langmuir*, p. 519.
2. *Self-Organization of Ink-jet-Printed Triisopropylsilylethynyl Pentacene via Evaporation-Induced Flows in a Drying Droplet*. **J. A. Lim, W. H. Lee, H. S. Lee, J. H. Lee, Y. D. Park, and K. Cho**. 2, 2008, *Advanced Functional Materials*, Vol. 18, p. 229.
3. *Inkjet Printing of Polymer Micro-Arrays and Libraries: Instrumentation, Requirements, and Perspectives*. **B. de Gans and U. S. Schubert**. 11, 2003, *Macromolecular Rapid Communications*, Vol. 24, p. 659.
4. *Inkjet Printing for Materials and Devices*. **P. Calvert**. 13, 2001, *Chemistry of Materials*, p. 3299.
5. *Inkjet Printing of Functional and Structural Materials: Fluid Property Requirements, Feature Stability, and Resolution*. **B. Derby**. 40, 2010, *Annual Review of Materials Research*, p. 395.
6. *Inkjet printing as a deposition and patterning tool for polymers and inorganic particles*. **E. Tekin, P. J. Smith, and U. S. Schubert**. 4, 2008, *Soft Matter*, p. 703.

7. *Visualization of drop-on-demand inkjet: Drop formation and deposition.* **H. Dong, W. W. Carr and J. F. Morris.** 77, 2006, Review of Scientific Instruments, p. 085101.
8. *Ink-jet printing of wax-based alumina suspensions.* **K. A. M. Seerden, N. Reis, J. R. G. Evans, P. S. Grant, J. W. Halloran and B. Derby.** 84, 2001, Journal of the American Ceramic Society, p. 2514.
9. *Inkjet Printing of Polymers: State of the Art and Future Developments.* **B.-J. de Gans, P. C. Duineveld and U. S. Schubert.** 3, 2004, Advanced Materials, Vol. 16, p. 203.
10. *Inkjet Printing—Process and Its Applications.* **M. Singh, H. M. Haverinen, P. Dhagat and G. E. Jabbour.** 22, 2010, Advanced Materials, p. 673.
11. *Water-based ink-jet ink I. Formulation.* **H. R. Kang.** 35, 1991, Journal of Imaging Science and Technology, p. 179.
12. *Particle generation and ink particle size effects in pigmented inkjet inks – Part II.* **J. Mendel, D. Bugner and A.D. Bermel.** 1, 1999, Journal of Nanoparticle Research, p. 421.
13. *Inkjet Printing of Narrow Conductive Tracks on Untreated Polymeric Substrates.* **T. H. J. van Osch, J. Perelaer, A. W. M. de Laat and U. S. Schubert.** 20, 2008, Advanced Materials, p. 343.
14. *Stable Aqueous Based Cu Nanoparticle Ink for Printing Well-Defined Highly Conductive Features on a Plastic Substrate.* **S. Jeong, H. C. Song, W. W. Lee, S. S. Lee, Y. Choi, W. Son, E. D. Kim, C. H. Paik, S. H. Oh and B. Ryu.** 27, 2011, Langmuir, p. 3144.
15. *Dewetting of conducting polymer inkjet droplets on patterned surfaces.* **J. Z.Wang, Z. H. Zheng, H.W. Li,W.T.S. Huck and H. Sirringhaus.** 2004, Nature Materials, Vol. 3, p. 171.
16. *Mixture Properties of the Water + γ -Butyrolactone + Tetrahydrofuran System. 2. Viscosities and Surface Tensions of γ -Butyrolactone + Water at 303.15-343.15 K and γ -Butyrolactone + Tetrahydrofuran at 278.15-298.15 K.* **D. H. S. Ramkumar and A. P. Kudchadker.** 4, 1989, Journal of Chemical and Engineering Data, Vol. 34.
17. *Improving the process capability of SU-8.* **M. Shaw, D. Nawrocki, R. Hurditch and D. Johnson.** 10, 2003, Microsystem Technologies, p. 1.
18. *Effects of pulse voltage on inkjet printing of a silver nanopowder suspension.* **M. H. Tsai, W. S. Hwang, H. H. Chou and P. H. Hsieh.** 33, 2008, Nanotechnology, p. 335304.
19. **C. W. Macosko.** *Rheology: Principles, Measurements, and Applications.* s.l. : New York: VCH, 1994. p. 449.
20. *Flows on the nozzle plate of an inkjet printhead.* **B. Beulen, J. de Jong, H. Reinten, M. van den Berg, H. Wijshoff and R. van Dongen.** 42, 2007, Experiments in Fluids, p. 217.
21. *An Essay on the Cohesion of Fluids.* **T. Young.** 1805, Philosophical Transactions of the Royal Society of London, Vol. 95, p. 65.
22. *Wetting: statics and dynamics.* **P. G. de Gennes.** 3, 1985, Reviews of Modern Physics, Vol. 57, p. 827.
23. **J. R. Wagner Jr.** *Multilayer Flexible Packaging.* Kidlington : Elsevier Inc., 2010.
24. **F. K. Hansen.** *The Measurement of Surface Energy of Polymers by Means of Contact Angles of Liquids on Solid Surfaces.* Oslo : University of Oslo, 2004.
25. **W. A. Zisman.** Relation of the Equilibrium Contact Angle to Liquid and Solid Constitution. *Contact Angle, Wettability, and Adhesion.* s.l. : American Chemical Society, Advances in Chemistry, 1964, Vol. 43, 1.
26. *Molecular dynamics simulation and measurement of contact angle of water droplet on a platinum surface.* **S. G. Kandlikar, M. E. Steinke, S. Maruyama and T. Kimura.** New York : s.n., 2001. Proceedings of IMECE.01: International Mechanical Engineering Congress and Exposition. pp. Paper # 2-8-3-2.
27. **A. W. Adamson.** *Physical Chemistry of Surfaces.* New York : Wiley, 1976.

28. **A.J. Kinloch.** *Adhesion and Adhesives.* New York : Chapman and Hall, 1987.
29. *Superhydrophobicity of a material made from multiwalled carbon nanotubes.* **Y. C. Honga and H. S. Uhm.** 24, 2006, Applied Physics Letters, Vol. 88, p. 244101.
30. *Direct measurement of multiwall nanotube surface tension.* **S. Nuriel, L. Liu, A.H. Barber and H.D. Wagner.** 404, 2005, Chemical Physics Letters, p. 263.
31. [Online] [Cited:] <http://www.guidechem.com/products/96-48-0.html>.
32. *Fluorinated Alcohols as Surface-Active Agents in Cationic Photopolymerization of Epoxy Monomers.* **M. Sangermano, R. Bongiovanni, A. Priola and D. Pospiech.** 2005, Journal of Polymer Science: Part A: Polymer Chemistry, Vol. 43, p. 4144.
33. *Capillary flow as the cause of ring stains from dried liquid drops.* **R. D. Deegan, O. Bakajin, T. F. Dupont, G. Huber, S. R. Nagel and T. A. Witten.** 389, 1997, Nature, p. 827.
34. *Inkjet printing of single-walled carbon nanotubes and electrical characterization of the line pattern.* **J. W. Song, J. Kim, Y. H. Yoon, B. S. Choi, J. H. Kim and C. S. Han.** 19, 2008, Nanotechnology, p. 095702.
35. **L.H. Sperling.** *Introduction to Physical Polymer Science.* Fourth Edition. Hoboken : John Wiley & Sons, Inc., 2006.

Curriculum Vitae

Name Marijana Mionić
Date of birth 08.04.1973
Place of birth Kraljevo, Serbia
Nationality Serbian

EDUCATION

- 2007 – 2011 **Doctoral Studies in Physics** (specialization in nanotechnology, preparation and characterisation of new materials) at EPFL, Institute of Condensed Matter Physics, Laboratory of Nanostructures and Novel Electronic Materials (now Laboratory of Physics of Complex Matter), Lausanne, Switzerland
- 2004 – 2006 **Master's Degree in Technical Science (Master of Science in Engineering)**, specialization in heat engineering and environmental protection, heat and mass extending; University of Kragujevac, School for Mechanical Engineering, Department for Thermodynamic, Kraljevo-Serbia
- 1992 – 2001 **Diploma in General Physics** at University of Kragujevac, School of Science and Mathematics, Department for Physics, Kragujevac-Serbia
- 1988 – 1992 **Grammar School** for Natural Sciences and Mathematics, Kraljevo-Serbia

PROFESSIONAL EXPERIENCE

- 2006 – 2007 **Internship**: Studying mechanical properties of proteins and single cells by atomic force microscopy, EPFL, Institute of Condensed Matter Physics, Laboratory of Nanostructures and Novel Electronic Materials (now Laboratory of Physics of Complex Matter), Lausanne, Switzerland

(Swiss Government scholarships for university for foreign students for the academic year 06-07)
- 2001 – 2006 **Teacher of physics** in various Primary and Secondary schools in Kraljevo and its surrounding (Serbia)

LANGUAGES

Serbian, English, French and German

List of publications and patent

PATENTS

[MM1] M. Mionic, A. Magrez, L. Forro, S. M. Jiguet, M. P. Judelewicz and T. Stora, Carbon nanotubes/SU-8 nanocomposites for microfabrication applications, Patent pending No. WO/2011/061708

SCIENTIFIC PUBLICATIONS

[MM2] M. Mionić, D.T.L Alexander, L. Forró, and A. Magrez, Influence of the Catalyst drying Process and Catalyst Support particle size on the carbon nanotubes produced by CCVD, *Physica Status Solidi B*, 2008, 245, 1915

[MM3] M. Mionić, S. Jiguet, M. Judelewicz, L. Forró, and A. Magrez, Preparation and characterization of SU8-carbon nanotubes composites, *Physica Status Solidi B*, 2009, 246, 2461-2464

[MM4] M. Mionić, S. Jiguet, M. Judelewicz, A. Karimi, L. Forró, and A. Magrez, Study of the mechanical response of carbon nanotubes-SU8 composites by nanoindentation, *Physica Status Solidi B*, 2010, 1–4, DOI 10.1002/pssb.201000305

[MM5] L. Ćirić, A. Sienkiewicz, B. Náfrádi, M. Mionić, A. Magrez, and L. Forró, Towards electron spin resonance of mechanically exfoliated graphene, *Physica Status Solidi B*, 2009, 246, 2558-2561

[MM6] R. Smajda, M. Mionić, M. Duchamp, J.C. Andresen, L. Forró, and A. Magrez, Production of High Quality Carbon Nanotubes for Less than \$1 per Gram, *Physica Status Solidi B*, 2010, 3-4, 1236-1240

[MM7] A. Magrez, J. W. Seo, R. Smajda, B. Korbely, J.C. Andresen, M. Mionić, S. Casimirius, and L. Forró, Low-Temperature, Highly Efficient Growth of Carbon Nanotubes on Functional Materials by an Oxidative Dehydrogenation Reaction, *ACS NANO*, 2010, 4 (7), 3702-3708

[MM8] Z. Micković, D.T.L Alexander, A. Sienkiewicz, M. Mionić, L. Forró, and A. Magrez, Synthesis of Nanosized Mn-Doped ZnO by Low Temperature Decomposition of Hydrozincite Precursors, *Crystal Growth&Design*, 2010, 10, 4437-4441

[MM9] M. Duchamp, R. Meunier, R. Smajda, M. Mionic, A. Magrez, J. W. Seo, L. Forró, B. Song, and D. Tománek, Reinforcing multiwall carbon nanotubes by electron beam irradiation, *Journal of Applied Physics*, 2010, 108, 084314

[MM10] A. Magrez, J. W. Seo, R. Smajda, M. Mionić, and L. Forró, Catalytic CVD Synthesis of Carbon Nanotubes: Towards High Yield and Low Temperature Growth, *Materials*, 2010, 3, 4871-4891

[MM11] R. Sangines, M. D. Abad, Cr. Vaju, R. Smajda, M. Mionic, and A. Magrez, Electrical Properties and Applications of Carbon Based Nanocomposite Materials: An Overview, *Surface and Coatings Technology*, 2011, doi:10.1016/j.surfcoat.2011.01.025

IN PREPARATION:

[MM12] A. Magrez, M. Mionic, and L. Forro, Calcite CaCO_3 Hollow Nanorods, *submitted*

[MM13] M. Mionić, R. Gaal, A. Magrez, L. Forró, K. Pataky and J. Brugger, Carbon nanotube-SU8 composite for flexible conductive ink-jet printable applications, *submitted*

[MM14] R. Gaál, A. Karsa, M. Mionić, R. Smajda, A. Magtez, and L. Forró, Thermal conductivity of CNTs-SU8 composites

[MM15] M. Mionić, V. Lukovac, R. Gaál, R. Smajda, A. Magrez and L. Forró, Cutting of Carbon Nanotubes by Planetary Ball Milling

[MM16] M. Mionic, L. Brocher, R. Gaál, T. Stora, S. Jiguet, M. Judelewicz, A. Magrez and L. Forró, Thermo-electric power and electrical resistivity of carbon nanotube-SU8 composites

[MM17] M. Mionić, T. Stora, R. Gaál, A. Karimi, S. Jiguet, M. Judelewicz, and L. Forró, Carbon nanotubes-SU8 composites

[MM18] M. Mionić, P. Bowen, D. T. L. Alexander, A. Magrez, and L. Forró, Role of CaCO_3 as a support for CVD catalyst

[MM19] M. Mionić *et al.* Mechanical properties of SU8 composites with long and short CNTs

Acknowledgements

During the last few years that I have spent on the EPFL, many people me to finish the work which is presented in this thesis. Without all these people, presented thesis would not be possible.

First of all, I would like to acknowledge the financial support from the National Centre of Competence in Research (NCCR) "Nanoscale Science" of the Swiss National Science Foundation grant No. NSF 200020-121814, NSF 113723 and NSF 121814.

I would also like to thank to my Professor, László Forró, for his confidence in my abilities and for giving me the opportunity to work my thesis in the prestigious scientific institution like EPFL. I thank Prof. O. Schneider, Prof. D. Damjanovic, Prof. K. Harnadi and Prof. J. W. Seo for accepting to participate on the jury of this thesis.

Many, many thanks to Dr. Richárd Gaál, who was my supporting advisor through most of my thesis work, for his endless patience, for the numerous discussions and for listening and finding solution of my scientific problems. Moreover, Dr. Richard Gaal was personally doing numerous measurement of transport properties of my composites and all statistical analysis given in Appendix 1.

Many, many thanks to Dr. Andrzej Sienkiewicz, who was carefully reading and correcting this thesis in its all versions (often all night, when it was necessary). Without him, this thesis would never be like you can see it!

I am grateful:

To Andrzej Kulik, who introduced me to the world of experimental physic, and especially of the AFM technique, but also of the life in Switzerland. Andrzej and Gerit Kulik, were patient and helpful friends not only in the lab, but also in private.

To Vladimir Lukovac, who introduced me to the world of CNTs in the first month of my thesis, and also for presenting me the equipments and explaining his research results on which I could build up my research.

To Thierry Stora (CERN), who introduced me to the magic world of making nanocomposites and dispersing nano-objects in liquid medium. I am eternally grateful for the knowledge this he transferred on me. Without him, I would never achieve to make composites 2, which were the best result of my thesis work.

To Alexander Duncan from CIME (EPFL) for HR SEM of calcite powders, HR TEM and EDX of catalyst precursors, TEM of produced CNTs, lots of different attempts to find suitable characterisation of the materials and definitely for numerous fruitful discussions and listening to my various ideas; also for performing TEM and HR TEM measurements of

catalyst precursors and synthesis products, especially for the remarkable observation of perfectly straight CVD CNTs, and for numerous fruitful discussions.

To Paul Bowen from LTP (EPFL) for calcite powders characterisation (BET, XRD and the secondary particle size distributions) and interpretation of their results, and for being patient in listening my ideas, giving advices, discussing about work strategy, interpretations and teaching me basics of powders and article writing.

To Prof. Helmut Cölfen (University Konstanz) for giving me the honour and devoting his time to discuss with me my work and the state of CaCO_3 calcite powder surfaces, as well for making images given in Figure 4.1.

To Stéphane Casimirius, former member of LPMC (EPFL), for giving me his recipe for the bimetallic Fe-Co catalyst preparation.

To Fabien Bobard from CIME (EPFL) for HR SEM of calcite powders (inserts in Figure 4.5).

To Arnaud Magrez from LPMC (EPFL) for SEM micrographs in Figure 4.3.

To Primoz Rebernik Ribic for Raman spectroscopy measurement and interpretation.

To Rita Smajda for HR TEM images.

To L. Brochet for measurement of R and phermopower as a function of temperature.

To Anita Karsa for measurement of thermal conductivity of composites 2 and 3.

To Ayat Karimi for teaching me nanoindentation technique and helping me in indentation measurement and interpretation.

To Juan Carlos Andresen for growing carpets which were used for preparation of CNTs-SU8 composites 3, (and to Rita Smaida for growing carpets which unfortunately could not be impregnated with SU8 due to the collapsing of CNTs).

To CMI/EPFL for access to the equipment in their Clean Room and to the whole CMI staff for trainings, fruitful discussions and great readiness to help, especially to: Michaël Pavius for introducing me to numerous devices and explaining me each photolithographic step, Georges-André Racine, Jean-Baptiste Bureau, Boris Lunardi, Michel Jeanneret, Cyrille Hibert, Philippe Langlet, Guy Clerc, Kevin Lister, Samuel Clabecq, Philippe Flückiger and Claudia D'Agostino.

Many, many thanks to Sébastien Jiguet from Gersteltec for his generous help in performing TGA, DSC and UV-vis spectroscopy measurements and for numerous discussions. Moreover, thanks to Gersteltec S.A., Moshe Judelewicz and Sébastien Jiguet for providing SU8 materials.

We gratefully thank the LTP for the access to the TGA, DSC and UV-vis spectroscopy equipment.

To Prof. Jürgen Brugger and Dr. Kristopher Pataky from LMIS 1 Department as well as the whole crew of the LMIS 1 Department for inkjet-printing.

To the whole team of researchers from the LPM Department at the EPFL for using their labs and, in particular, to Nathalie Serra and Thomas Maeder from this Department for screen printing, as well as for numerous fruitful discussions.

To Monique Bettinger and Ludi Evelyn for their friendly administrative support.

To all current and former members of NN group: to Zlatko Mickovic (without whom I would never find where to come in Switzerland); to “nase malo, ali jako srpsko udruzenje” in NN group: Luka Ciric, Stevan Arsenijevic, Dejan Djokic and Jacim Jacimovic; to Gerit Kulik, Juan Carlos Andresen, Vladimir Lukovac, Alexander Duncan, Katarzyna Pierzchala, Kathrin Gloystein, Stéphane Casimirus, Kyumin Lee, Mireille Crittin, Lenke Horváth, Massimo Spina, Markus Bonda, Martial Duchamp, Axel Fanget, Flavio Mor, Nissanka Wickremasinghe and lot of others...

Most of all I want to thank very much to my Steff for always being there for me for better and for worse, for sharing our lives and for having so incredibly wonderful son Max!!! And finally, many thanks to my family in Serbia, to my “mama Vera, tata Zujo, brat Marko i moj bratanac Vukasin Mionic”-they always had understanding and unconditional support for me and my choices in life-thank you for all!!!